UNIVERSITÉ CATHOLIQUE DE LOUVAIN

INSTITUTE OF CONDENSED MATTER AND NANOSCIENCES

(IMCN)

Laboratory of Physical Chemistry

Prof. Tom Leyssens

Nefiracetam Solid Forms: from Physicochemical Properties Enhancement by Cocrystallization to Chiral Resolution through Preferential Crystallization

---

Thèse présentée en vue de l'obtention du grade

de docteur en Sciences par

Buol Xavier

Louvain-la-Neuve

November 2020

I dedicate this doctoral thesis to my beloved and mourned grandfathers,

Jean Buol and Maurice Blomme

Jury Members

Prof. J. Wouters
UNamur

Prof. S. Hermans
UCLouvain

Dr. L. Aerts
UCB Parma

Dr. K. Robeyns
UCLouvain

Dr. V. Dupray
Université de Rouen-Normandie

Prof. Y. Garcia (President)
UCLouvain

Prof. T. Leyssens (Supervisor)
UCLouvain

Acknowledgments

I would like to express my warm appreciation to the following persons who made my thesis journey memorable:

My promotor **Prof. Tom Leyssens**. Four years ago, you made possible this journey and you allowed me to live the best moments of my life. I thank you for your humanity, understanding, kindness, humour and the autonomy and education you gave me that have made me, I believe, a better scientist. I will miss a boss like you.

Prof. Johan Wouters who was my MSc promotor and gave me the opportunity to perform an internship at UCB Pharma and indirectly a Ph.D. thesis.

My lab buddy who became one of my closest friend **Dr. Michael Guillot**. We started together with the Ph.D. and I could not imagine a better person to spend this trip with. We shared so many funny moments and sometimes sad ones but the thesis is made of both of it. I am fortunate to have spent those last four years with a great human being like you who supported me, laughed at my jokes, and gave me personal and scientific advice. I cannot thank Michael without thanking **Dr. Vanessa K. Seiler**, my other lab buddy and friend. You were the German touch in our team and we really miss you since you took the degree. Next year, reunion guys!

Dr. Andrea Carletta, my eternal master thesis supervisor who became my best friend. You inspired me and gave me the desire to pursue research with this thesis. Your guidance was a great help along with the thesis. Since 2015, we have spent countless hilarious moments wherever we were. Shall we plan a post-COVID trip for next year? You cared for me years ago and now you have to take care of Anaëlle and la mia bellissima nipote. I am grateful to **Dr. Anaëlle Tilborg** for making him happy and to be a good friend to me. Congrats to you, guys!

One of my greatest and gratifying achievements was to supervise and to share my humble knowledge with my master students **Camila Caro Garrido** and **Sarah Huynen**. You were not just students but friends and you made me grow socially and professionally. I am also so glad you decided both of you to start a Ph.D. thesis as well. Science has something to gain with you in the field!

To my past and present colleagues/friends in the Lavoisier: **Benjamin**, **Bram**, **Carole**, **Chloé**, **François**, **Fucheng**, **Fuli**, **Gabriel**, **Jean-Baptiste**, **Joséphine**, **Kevin**, **Lixing**, **Marie-Claire**, **Martin**, **Max**, **Nicolas**, **Ousam**, **Paolo**, **Ricky**, **Sylvia**, **Timothy** and **Véronique**. A particular thanks to **Aurore Becquevort**, the pack's mother, who was always taking care of us and sharing her good mood. Thank you for the memories.

I would like to thank my thesis jury members i.e. **Prof. Tom Leyssens, Prof. Sophie Hermans, Prof. Yann Garcia, Prof. Johan Wouters**, **Dr. Valerie Dupray, Dr. Luc Aerts**, and **Dr. Koen Robeyns** for their expertise, their advice and the time they spent in the reading/correction of my thesis. I would like to express my gratitude to my midterm committee members: **Prof. Yaroslav Filinchuk** and **Prof. Patricia Luis Alconero**.

To the co-authors of our articles **Prof. Tom Leyssens**, **Prof. Johan Wouters**, **Dr. Koen Robeyns**, **Camila Caro Garrido**, **Dr. Nikolay Tumanov**, **Laurent Collard** and **Laurie Bodart** for the great collaboration. A particular thanks to **Dr. Koen Robeyns** for measuring and solving the single crystal structures.

I thank **Pascal Van Velthem** for the DSC/TGA technical support and **Dr. Céline Rougeot** for her advice in our early experiments on preferential crystallization.

I am grateful to the "**Fonds Européen de Développement Régional"** (FEDER) and the «**Région Walonne**» for the financial support.

To my friends: **Arianna** and **Matthieu**, **Benjamin B.**, **Giulia**, **Kevin** and **Cecilia** (congrats guys!), **Laurie**, **Marie**, **Poldo**, **Phu**, and **Thomas.** Thank you for the memories.

Je remercie chaleureusement mes parents, **Guillaume** et **Laura**, mes défunts grands-pères, **Jean** et **Maurice**, et ma grand-mère **Anne-Marie** pour l'amour, l'éducation et les valeurs qu'ils m'ont apportés au fil des années.

Un grazie di cuore alla mia famiglia italiana **Caterina**, **Enrico**, **Bruno**, e **Clara** per la loro gentilezza e per avermi accolto calorosamente in famiglia.

L'ultima ma non meno importante, l'amore della mia vita **Fabiana** che mi sopporta giorno dopo giorno e che mi ama nonostante tutto. Tu hai fatto di me una personna migliore, completa e felice. Grazie per la felicità che mi doni tutti giorni, la tua dolcezza, la tua pazienza, la tua comprensione, la tua intelligenza, il tuo coraggio e ovviamente la tua cucina.

List of Publications

1. Buol, X.; Caro Garrido, C.; Robeyns, K.; Tumanov, N.; Collard, L.; Wouters, J.; Leyssens, T., Chiral Resolution of mandelic acid through Preferential Cocrystallization with nefiracetam. *Cryst. Growth Des.* **2020**.
2. Bodart, L.; Derlet, A.; Buol, X.; Leyssens, T.; Tumanov, N.; Wouters, J., Combining two antitubercular drugs, clofazimine and 4-aminosalicylic acid, in order to improve clofazimine aqueous solubility and 4-aminosalicylic acid thermal stability. *J. Pharm. Sci*. **2020**.
3. Buol, X.; Robeyns, K.; Caro Garrido, C.; Tumanov, N.; Collard, L.; Wouters, J.; Leyssens, T., Improving Nefiracetam Dissolution and Solubility Behavior Using a Cocrystallization Approach. *Pharmaceutics* **2020,** *12* (7), 653.
4. Buol, X.; Robeyns, K.; Tumanov, N.; Wouters, J.; Leyssens, T., Identifying, Characterizing, and Understanding Nefiracetam in Its Solid State Forms: A Potential Antidementia Drug. *J. Pharm. Sci.* **2019,** *108* (11), 3616-3622.
5. Carletta, A.; Buol, X.; Leyssens, T.; Champagne, B.; Wouters, J., Polymorphic and Isomorphic Cocrystals of a N-salicylidene-3-aminopyridine with Dicarboxylic Acids: Tuning of Solid-state Photo-and Thermochromism. *J. Phys. Chem. C.* **2016,** *120* (18), 10001-10008.

List of Abbreviations

A	Solid Surface/Membrane Surface Area
ACE	Angiotensin Converting Enzyme
ADMET	Absorption, Distribution, Metabolism, Excretion and Toxicity
API	Active Pharmaceutical Ingredient
AS3PC	Ideal Auto-Seeded Polythermic Programmed Preferential Crystallization
ATR	Attenuated Total Reflection
AUC	Area Under the Curve
BA	Bioavailability
BCS	Biopharmaceutical Classification System
BPD	Binary Phase Diagram
CD	Cyclodextrin
CEC	Capillary electrochromatography
CH_3CN	Acetonitrile
cHPLC	Chiral High Performance Liquid Chromatography
CINV	Chemotherapy-Induced Nausea and Vomiting
CIP	Cahn-Ingold-Prelog
CPC	Coupled Preferential Crystallization
CSP	Chiral Stationary Phase
D	Diffusion Coefficient
DSC	Differential Scanning Calorimetry
DVS	Dynamic Vapor Sorption
EtOAc	Ethyl Acetate
EtOH	Ethanol
FaSSIF	Fasted State Simulated Intestinal Fluid
FDA	U.S. Food and Drug Administration
FeSSIF	Fed State Simulated Intestinal Fluid
GABA	γ-aminobutyric acid
GERD	Gastroesophageal Reflux Disease
GC	Gas Chromatography
GI	Gastro-Intestinal
GRAS	Generally Recognized As Safe
H_2O	Water
H_3PO_4	Phosphoric acid
HLB	Hydrophilic-Lipophilic Balance
HMWP	High Molecular Weight Polymers
HPC	Hydroxypropylcellulose
HPH	High-Pressure Homogenization
HPLC	High Performance Liquid Chromatography
HPLC	High Performance Liquid Chromatography

HPMC	Hydroxypropylmethylcellulose
HT	High Temperature
HTS	High-Throughput Screening
ICC	Ionic Cocrystal
IDR	Intrinsic Dissolution Rate
IEC	Ion-Exchange Chromatography
IR	Infrared
IV	Intravenous
LAG	Liquid-Assisted Grinding
LC	Liquid Chromatography
LFCS	Lipid Formulation Classification System
MZW	Metastable Zone Width
N	Nefiracetam
NCA	2:1 Nefiracetam-Citric Acid Cocrystal Form I
NCA1	2:1 Nefiracetam-Citric Acid Cocrystal Form II
NCE	New Chemical Entities
NMR	Nuclear Magnetic Resonance
NNRTI	Non-Nucleoside Reverse Transcriptase Inhibitor.
NOA	2:1 Nefiracetam-Oxalic Acid Cocrystal
NRMA	1:1 Nefiracetam-(R)-Mandelic Acid Cocrystal
NRSMA	1:1 Nefiracetam-(RS)-Mandelic Acid Cocrystal
NSAID	Nonsteroidal Anti-Inflammatory Drug
NSMA	1:1 Nefiracetam-(S)-Mandelic Acid Cocrystal
NZC	1:1 Nefiracetam-Zinc Chloride Ionic Cocrystal
NZCW	1:1 Nefiracetam-Zinc Chloride Ionic Cocrystal Monohydrate
O	Oral
PC	Preferential Crystallization
PDA	Photometric Diode Array
PK	Pharmacokinetics
Pr	Productivity
PSR	Particle Size Reduction
Pu	Purity
PVP	Polyvinylpyrrolidone
Q	Matter Flux/Passive Diffusion
RESS	Rapid Expansion of a Supercritical Solution
RH	Relative Humidity
rHPLC	Reverse High Performance Liquid Chromatography
RI	Resolution Index
RMA	(R)-Mandelic Acid
RSMA	(RS)-Mandelic Acid
RT	Room Temperature
S3PC	Ideal Seeded Polythermic Preferential Crystallization
SCXRD	Single Crystal X-Ray Diffraction

SEC	Size-Exchange Chromatography
SGF	Simulated Gastric Fluid
SHG	Second Harmonic Generation
SIPC	Ideal Seeded Isothermal Preferential Crystallization
SMA	(S)-Mandelic acid
SOAT	Second-Order Asymmetric Transformation
THF	Tetrahydrofuran
TLC	Thin-Layer Chromatography
TPD	Ternary Phase Diagram
USP	U.S. Pharmacopia
UVS	Ultra-Violet Spectroscopy
VHP	Via Humida Paratum
VT-XRPD	Variable Temperature X-Ray Powder Diffraction
XRPD	X-Ray Powder Diffraction
$ZnCl_2$	Zinc Chloride

Abstract

The pharmaceutical industry has always faced challenges. Some of these challenges relate directly to the physicochemical properties of the drug compounds. Poor water-solubility, dissolution rate, and permeability are among the main issues encountered during drug development. Issues related to these may ultimately result in failure during drug development. A second well-known issue relates to the chirality of the drug compound, with both enantiomers often presenting different biological effects. It is therefore recommended to aim for single enantiomer formulations of drug forms to avoid a crisis such as encountered for thalidomide. Classical approaches to produce single enantiomers involve asymmetric synthesis or chiral resolution of a racemate.

In this work, we aim at resolving both issues through a crystal engineering approach, more precisely focusing on cocrystallization. On one hand, we use cocrystals to improve the physicochemical properties of nefiracetam, a target drug compound, and on the other, we use cocrystals of nefiracetam to develop a resolution process of mandelic acid through preferential cocrystallization.

Nefiracetam is a lipophilic, nootropic drug of the racetam family. We attempted to tune the solubility of this compound using a cocrystal approach. Prior to doing so, a preliminary polymorph screening was performed as this was absent in the literature. To our surprise, we were able to identify polymorph FII, stable at higher temperatures, and thus enantiotropically related to form FI, stable at low temperatures. A third metastable form was also discovered recrystallizing nefiracetam from the melt. Finally, a monohydrate form was identified working in water saturated conditions. These novel solid forms of nefiracetam were structurally and thermodynamically analyzed, with the solubility of the monohydrate evaluated as reference, since we showed a rapid solvent-mediated conversion to this form in solution. We then set out, to explore the potential of nefiracetam cocrystals screening 133 coformers among which carboxylic acids, amino acids, profens, racetams and sugars. Seventeen of these led to successful cocrystal formation, with a high success rate for carboxylic acid containing coformers. Among the cocrystals, three are biocompatible (citric acid, oxalic acid and zinc chloride) and more deeply studied. To be based on dissolution experiments, the nefiracetam-citric acid cocrystal appeared a potential candidate for formulation of nefiracetam.

During cocrystal screening, we stumbled upon a remarkable result. Indeed, a cocrystal between nefiracetam and mandelic acid was identified. Not only pharmaceutically interesting, as mandelic acid shows analgesic, antirheumatic and spasmolytic effects,

cocrystallization seemingly led to formation of a stable conglomerate, whereas mandelic acid forms itself a racemic compound. We fully characterized this system, to then develop a chiral resolution of mandelic acid by entrainment. Different modes of this process were developed such as the Seeded Isothermal Preferential Crystallization (SIPC) and the Seeded Polythermal Preferential Crystallization (S3PC) modes all leading to excellent entrainment results showing relatively good yields per cycle, and more importantly enantiopure outcome.

Contents

1. Importance of the Solid Dosage Form in the Pharmaceutical Field

1.1. Drug Discovery and Development: Challenges and Opportunities

Looking at the overall drug market of the past decade, one notices that a major part (40%) of drugs are practically insoluble or only slightly soluble in water (**Figure 1-1**).[1] Nowadays, one of the greatest challenges in the pharmaceutical field concerns the poor water-solubility of novel **A**ctive **P**harmaceutical **I**ngredients (APIs). With the important increase of **N**ew **C**hemical **E**ntities (NCE) due to the use of combinatorial chemistry (rapid synthesis route), virtual screening (selection of potential bioactive substances through computational models) and **H**igh **T**hroughput **S**creening methods (HTS),[2-3] numerous poorly soluble drugs (75%) appeared.

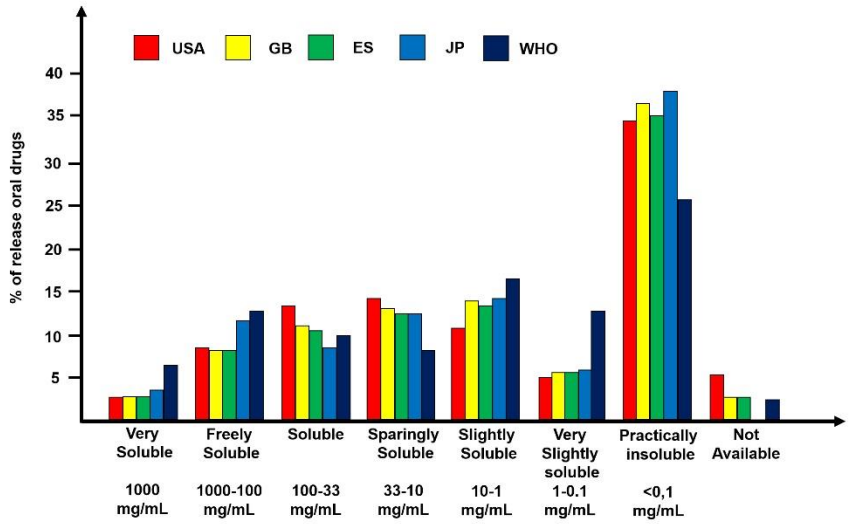

Figure 1-1. Distribution of the marketed drugs' solubility in United-States of America (USA), Great-Britain (GB), Spain (ES), Japan (JP) and according to the World Health Organization (WHO). Freely adapted from Takagi et al. (2006).[4] Values of solubility range are given according to the Handbook of Solubility Data for Pharmaceuticals (2009).[5]

HTS is wide-spread in the pharmaceutical and the biotechnology fields, and consists in a rapid method to find those compounds suitable or capable to interact with the

biological target through *in vitro* assays.[6-7] One of the pitfalls with new "positive hits" with potential efficient therapeutic effect is that they are mostly soluble in organic media with low water-solubility. These drug-like compounds must exhibit good pharmacokinetic properties (ADMET) and survive through different clinical trials (Phase I and II). Their low bioavailability is the main reason why most are discarded during the discovery and development processes. The "Lipinski's rule of 5"[8-9] is a relevant tool to predict if a drug may exhibit low bioavailability. A synthetic compound with more than 5 hydrogen bond donor groups, 10 hydrogen bond acceptor groups, a molecular weight > 500 $g.mol^{-1}$ and a log P > 5 (partition coefficient) is likely to exhibit poor bioavailability. In 1995, the **B**iopharmaceutical **C**lassification **S**ystem[10-11] (**Figure 1-2**), was introduced with the purpose to classify all drug substances on the market according to their *solubility* and *permeability* with respect to their dose required. This classification divides the drugs in 4 groups, reflecting the likeliness of how bioavailable a drug is/would be. The BCS I and III groups contain the substances with high water-solubility but with respectively high and low membrane permeation. BCS II and IV(40%)[1] gather up the drugs with low solubility and respectively high and low permeability. A logical pathway to handle the solubility issue of these latter two classes would be to decrease the lipophilicity of the drug, but a lack of permeation, hence potency, could potentially result.

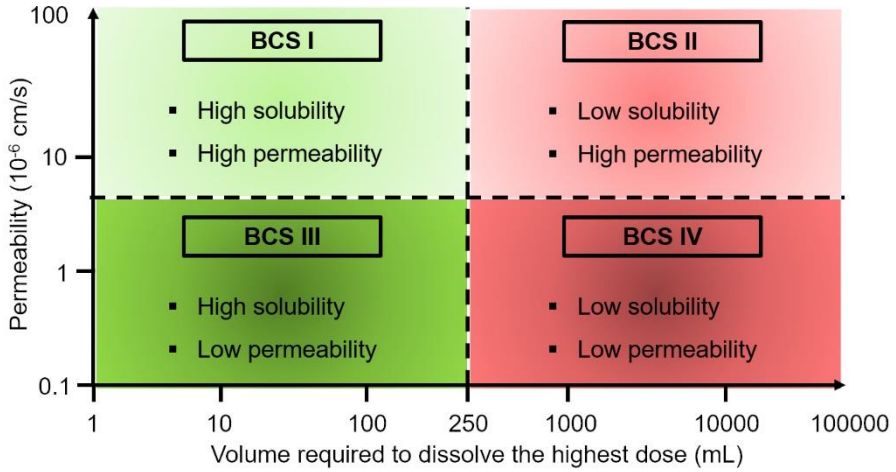

Figure 1-2. Schematic diagram of the Biopharmaceutical Classification System categorizing the drugs according to their permeability and solubility (for the highest dose). Freely adapted from Amidon *et al.* (1995).[10]

Therefore, alternatives were sought to counter the lack of solubility or dissolution rate without molecular alteration. As most drugs are administrated as oral solid dosage forms for patient convenience and cost-effectiveness, the focus was on these substances that are orally administered. The main techniques used are *lipid-based*

solubilization (co-solvent, surfactant and lipids), solid dispersion, particle size reduction, crystal engineering, salt formation and *cyclodextrin complexation*.[12-15] Furthermore, drug formulations became intellectual property assets underlying the importance of this branch for the pharmaceutical field.

1.2. Solubility, Dissolution Rate and Permeability

Solubility is a thermodynamic parameter and is defined as the maximum amount of solute that can been dissolved in a given volume of solvent under fixed temperature and pressure conditions having an equilibrium present between the solute and solid. This equilibrium between the solid API and the dissolved API (Eq. 1) depends on the solvent-solute and solute-solute interactions. A solute is likely to be soluble (**Figure 1-3**) in a solvent where solute-solvent interactions are energetically favored in comparison to solute-solute ones (Eq. 2). Generally, breaking the lattice bonds requires energy (endothermic process) while the solvation releases energy (exothermic process).[11, 16-17]

$$API_{solid} \leftrightharpoons API_{solution} \quad \text{(Eq. 1)}$$

$$\Delta H_{solution} = \Delta H_{solvation} - \Delta H_{solvent} - \Delta H_{lattice} \quad \text{(Eq. 2)}$$

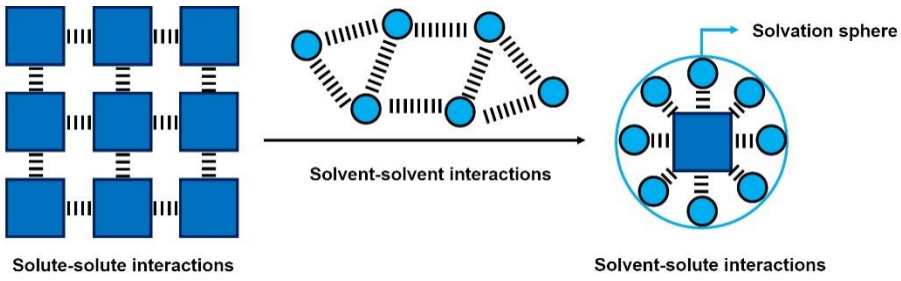

Figure 1-3. Solubilization steps from the solute-solute interactions at the solid state to the solute molecule solvation.

An FDA (U.S. **F**ood and **D**rug **A**dministration) guidance exists explaining how to properly measure the solubility and the dissolution profile of a given compound. Solubility is commonly measured at 37°C (physiologic temperature) in a water-based medium. The media used are SGF (**S**imulated **G**astric **F**luid), FeSSIF (**F**ed **S**tate **S**imulated **I**ntestinal **F**luid) and FaSSIF (**F**asted **S**tate **S**imulated **I**ntestinal **F**luid) and which simulate the different environments to which the drug is exposed in the body. While using those buffers, the pH-range goes respectively roughly from 1 to 8 (1.2,

4.5 and 6.8) to simulate the pH of the body. The drug is considered to be very soluble when its therapeutic dose is at least soluble in 250 mL whatever the pH value.[18-19] Practically, these solubility measurements can be managed in most cases using light scattering/turbidity or using a HPLC device (UV spectroscopy) if a chromophore is present on the molecule. The limiting step is to get a fully saturated solution. To do so, the shake-flask method is used. This method consists in preparing a suspension of excess amount of solute in a fixed volume of solvent (medium). Shaking of the suspension takes place for at least 24 hours, after which the suspension is filtered and the supernatant injected in a HPLC device to be dosed (vertical method).[20] This set-up may be performed at different temperatures in order to draw the solubility vs temperature profile. Another device useful in this context is the Crystal16™ (manufactured by Technobis Crystallization Systems), which takes benefit from the light scattering interaction with matter (horizontal method). Both methodologies are represented in **Figure 1-4**.

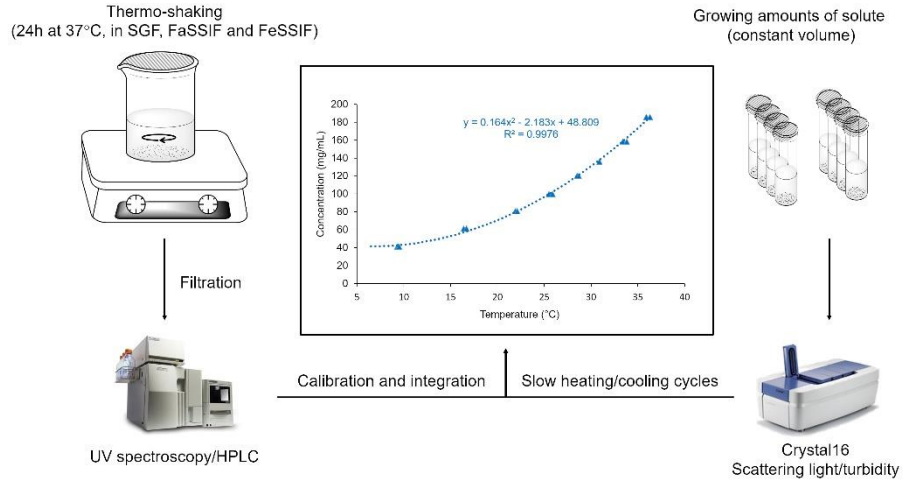

Figure 1-4. The two general methodologies to determine the solubility according to the FDA guidance. A typical solubility curve (concentration versus temperature profile) is illustrated as well.

Solubility is an equilibrium state between the solid and the solute and is therefore a thermodynamic parameter. *Dissolution*, on the other hand, is a kinetic process by which the drug (solute) goes from the solid state to solution (dissolved) over time. The dissolution phenomenon is commonly explained using the diffusion layer model of Noyes-Whitney[21] (**Figure 1-5** and Eq. 3) which is a matter flux-based model (Q).

$$Q = \frac{dW}{dt} = \frac{A \times D}{d}(C_S - C_B) \qquad \text{(Eq. 3)}$$

Where C_s is the concentration at the particle surface, C_{DL} the concentration in the diffusion layer, C_B the concentration in the bulk medium, A the solid surface, D the diffusion coefficient and d the thickness of the diffusion layer.

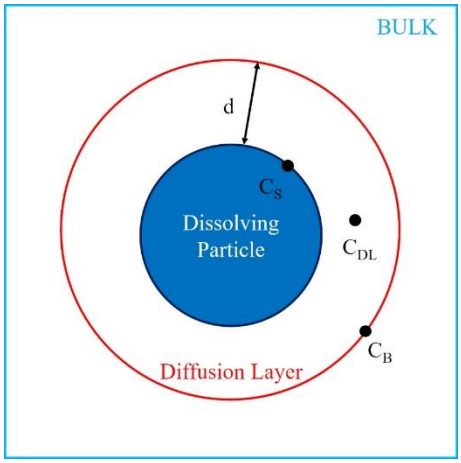

Figure 1-5. Diffusion layer model of Noyes-Whitney to explain the dissolution phenomenon.

As for the solubility evaluation, a guide exists to properly evaluate the dissolution of a drug (see http://www.accessdata.fda.gov/scripts/cder/dissolution/).[22]

The set-up is particular and has been ruled by the **U**nited **S**tates **P**harmacopeia. These devices are called an USP apparatus 1, 2 3 and 4 that are respectively operated with a basket apparatus, a paddle apparatus, a reciprocating cylinder and a flow-through cell.[23] Conventional USP apparatus 1 is generally made of a vessel, a motor equipped with a drive shaft, a cylindrical basket and a water bath while the USP apparatus 2 uses a paddle as stirring. Obviously, temperature and media used are generally the same as for solubility measurements.[24] A drug is considered rapidly dissolving when 85% of its solubility is reached in 900 mL of medium under 100 rpm within 30 min.[18] Stirring strongly impacts the dissolution rate as fast stirring tends to reduce the diffusion layer and increases the dissolution rate (Eq. 3). The dissolution rate is as important as the solubility, as dissolution needs to be fast enough to exceed the digestion time and render drug absorption possible. Generally, a dissolution profile plots the amount of drug dissolved versus time. The *dissolution rate* is defined as the slope (Eq. 4) of the curve, as shown in **Figure 1-6**. The steeper the slope, the faster the dissolution. Using a particular set-up (**Figure 1-6**) that consists in a reactor wherein a drug pellet is fixed on its holder and stirring is applied (through a paddle or a rotating holder) furthermore allows extracting the ***I**ntrinsic **D**issolution **R**ate* (IDR), which is the dissolution rate by surface unit (Eq. 5), compensating for the size and shape of the pellet.

$$DR = \frac{VdC}{dt} = \frac{dm}{dt} \quad \text{(Eq. 4)}$$

$$IDR = \frac{VdC}{dt} \times \frac{1}{A} = \frac{dm}{dt} \times \frac{1}{A} \quad \text{(Eq. 5)}$$

Where V is the medium volume, C the drug concentration, $dm.dt^{-1}$ the dissolution rate (mass per time unit) and A the surface area of the pellet.

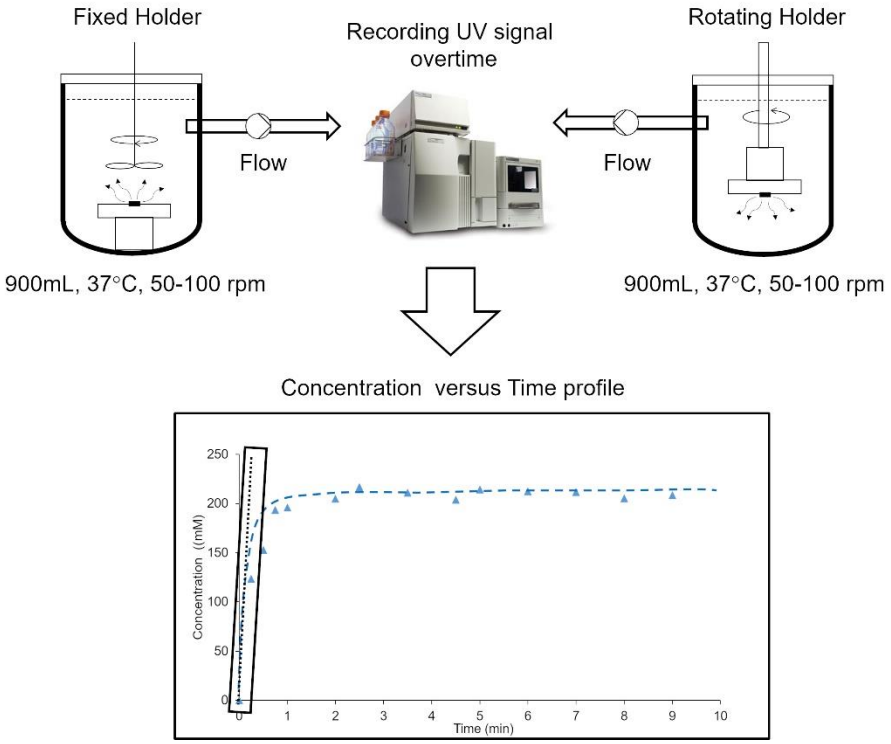

Figure 1-6. Two main IDR apparatus for IDR measurement and an example of a dissolution curve (concentration versus time profile).

Permeability is defined as the ability of a drug to diffuse through the cell membrane. A drug molecule should not be too large and lipophilic to diffuse passively (no energetic cost) through the membrane.[18] The lipophilicity (P or log P) or the partition coefficient (equilibrium) is generally used as a first tool to reflect the passive diffusion likeliness of a drug and depends on its molecular structure. Indeed, the more lipophilic the drug, the easier the diffusion across the membrane (Eq. 6 and 7). Generally, n-octanol is used to simulate an lipophilic (oily) environment. The partition coefficient is obtained by preparing a given drug concentration in water and mix it with an equal

volume of n-octanol (**Figure 1-7**). After phase splitting, the drug concentration is then dosed in each phase to get the partitioning.

$$D_{\text{n-octanol}} \leftrightharpoons D_{\text{water}} \quad \text{(Eq. 6)}$$

$$\text{LogP}\left(\frac{\text{oil}}{\text{water}}\right) = \text{Log}\left(\frac{C_{\text{n-octanol}}}{C_{\text{water}}}\right) \quad \text{(Eq. 7)}$$

Where $C_{\text{n-octanol}}$ is the drug (D) concentration in the oil phase and C_{water} in the aqueous phase. Passive diffusion is the main pathway for oral drug absorption i.e the drug passes from the **G**astro**I**ntestinal tract (GI) to the blood plasma going through the intestinal membrane. The mathematic model used to describe this passive diffusion (F or $\frac{dQ}{dt}$) is Fick's diffusion law[18] (Eq. 8) which is close to the Noyes-Whitney equation (Eq. 3) and driven by a difference in concentration (high vs low) between the two media.

$$F = \frac{dQ}{dt} = \frac{DAK}{d}\left(C_{GI}\text{-}C_p\right) = P\left(C_{GI}\text{-}C_p\right) = PC_{GI} \quad \text{(Eq. 8)}$$

Where D is the diffusion coefficient, A the membrane surface area, K the lipid-water partition coefficient of the drug, d the membrane thickness, C_{GI} the drug concentration in the GI tract and C_P the drug plasma concentration. Since D, A and K are constant in a human being, they may be combined in a permeability coefficient constant P. C_P can be neglected since it is very small compared to C_{GI}. Whereas the partition coefficient measurements give a first idea of the ease with which drugs pass cell membranes, the true drug permeability evaluation is harder to assess and requires advanced *in vitro* methods (or *in vivo* tests in animals) and cells from the GI to properly evaluate the permeability in the human body. To do so, Caco-2 cell (human colon adenocarcinoma) monolayers[25-28] are used to simulate the *in vivo* conditions since they are similar to the epithelial cells from the intestine and allow predicting permeability. This method has been used for classifying drugs according to their BCS class. A drug substance is considered as highly permeable when 90% of the dose is absorbed.

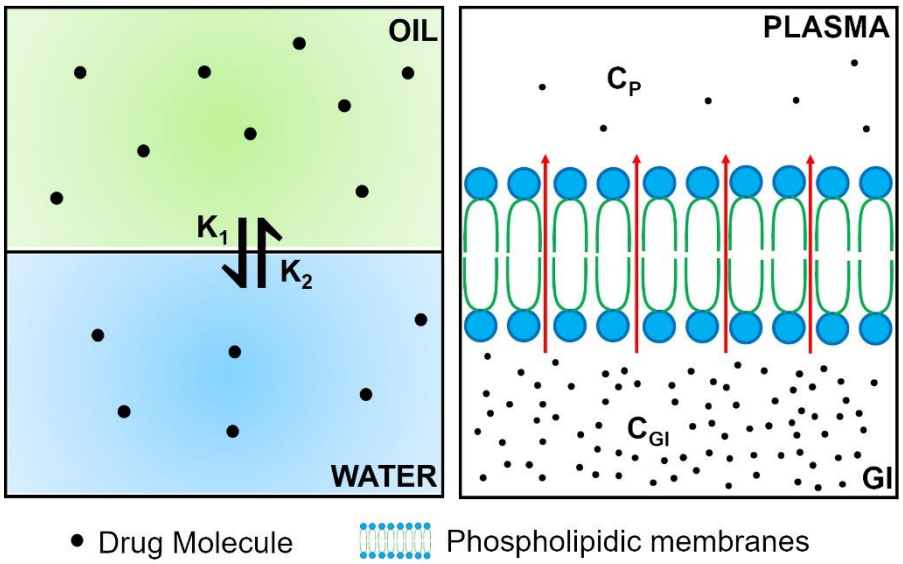

Figure 1-7. (left) Scheme of the coefficient partition of a drug in a biphasic (n-octanol and water) medium and (right) drug diffusion across a cell membrane through passive diffusion.

1.3. Pharmacokinetics and Pharmacodynamics

Pharmaco**k**inetics (PK) may be summarized as "the kinetic events that occur to the drug once administrated".[18, 29] On the other hand, pharmacodynamics deals with all the interactions between the drug and the body receptors also implying the biological response to the drug. Since most of the medication is administrated as an oral dosage, a total understanding of pharmacokinetics is required to design a suitable and efficient drug dosage that delivers the right amount (therapeutic) of a drug at the right moment in the body. A too high dose may lead to toxicity issues or on the other hand a too low dose, to a drug showing no effect at all. Please keep in mind that other routes of administration also exist but are not discussed here (intravenous, subcutaneous, intradermal, intramuscular injection, sublingual, intranasal or by inhalation).[24] Generally, the processes relating "what happens to the drug inside the body" are the so-called ADMET (**A**bsorption, **D**istribution, **M**etabolism, **E**xcretion and **T**oxicity) processes (**Figure 1-8**).

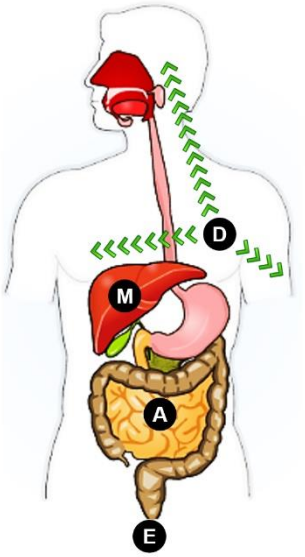

- **A**bsorption: the oral dosage releases the drug from the site of administration into the systematic circulation. It is the main property impacted by the type of oral dosage form.
- **D**istribution: the drug is delivered through the whole body after oral absorption.
- **M**etabolism: the drug is biotransformed by various organs (e.g. liver and kidney) into more hydrophilic substances to facilitate the excretion.
- **E**xcretion: the drug or the transformed form is expelled (as feces or urine) to avoid accumulation or toxicity.
- **T**oxicity: gathers up all the non-desired interactions that lead to toxicity (cytotoxicity or teratogenicity).

Figure 1-8. ADMET Properties

There are four main experimental PK parameters generally used to describe the performance of an oral dosage form.[30] The *volume of distribution* (Vd) is the ratio between the total amount of administrated drug (the dose) and the drug concentration in the plasma (Eq. 9). It may also be called the apparent volume wherein the drug is dissolved. The *Clearance* (Cl) is defined as the amount of unchanged or unaltered drug retrieved after elimination from the body (Eq. 10). The biological barriers that strongly impact this parameter are organs like the liver, the kidney, and the Gastro-Intestinal (GI) tract. The *half-life* ($T_{1/2}$), is the time required to halve the drug plasma concentration (Eq. 11). Finally, the *bioavailability* (BA or %F) represents the amount of drug that reaches its site of action without being altered (Eq. 12). It reflects the oral drug dosage efficiency. In case of intravenous injection (IV), the concentration in the plasma is considered maximum since it is directly injected into the general circulation. For an oral dosage (O), the BA is directly depending on the oral absorption and is lower due to the biological constraints but it may be improved with a suitable formulation. The performance comparison between an existing reference (formerly formulated form) and a new formulation is called *bioequivalence*.

$$Vd = \frac{D}{Co} \quad \text{(Eq. 9)}$$

$$Cl = \frac{D}{AUC\ (IV)} \quad \text{(Eq. 10)}$$

$$T_{1/2} = 0.693 \times \frac{Vd}{Cl} \quad \text{(Eq. 11)}$$

$$\%F = \frac{AUC\ (O)}{AUC\ (IV)} \times \frac{D\ (IV)}{D\ (O)} \times 100 \quad \text{(Eq. 12)}$$

Where D is the drug dose, C_0 is the plasma drug concentration after intravenous (IV) injection, and AUC the area under the curve. The oral dosage absorption depends on many parameters such as the physicochemical properties of the dosage, the kind of dosage, the biological barriers (GI tract, liver, etc), body environment (pH, enzymes, permeability), and the first-pass effect. Commonly, the bioavailability, which is the most important parameter to improve, is approached with the solubility and the dissolution rate (DR) or intrinsic dissolution rate (IDR). Since the drugs from the BCS II category (low solubility and high permeability) are the most spread drugs and the ones considered here, the permeability is not a restriction for the overall absorption. In **Figure 1-9**, considering an oral dosage, the solubility approximates the maximum on the drug concentration (C_{max}) versus time curve while the dissolution rate impacts the slope. The drug bioavailability (surface area under the curve) is improved when solubility and/or dissolution rate are enhanced through a suitable formulation. However, a fast enough dissolution rate is required even if the solubility is high in order for absorption to occur before complete digestion. In the opposite case, a too high dissolution rate and a low solubility may provide a low concentration level for the absorption flux through the membranes and may lead to inefficiency.[31]

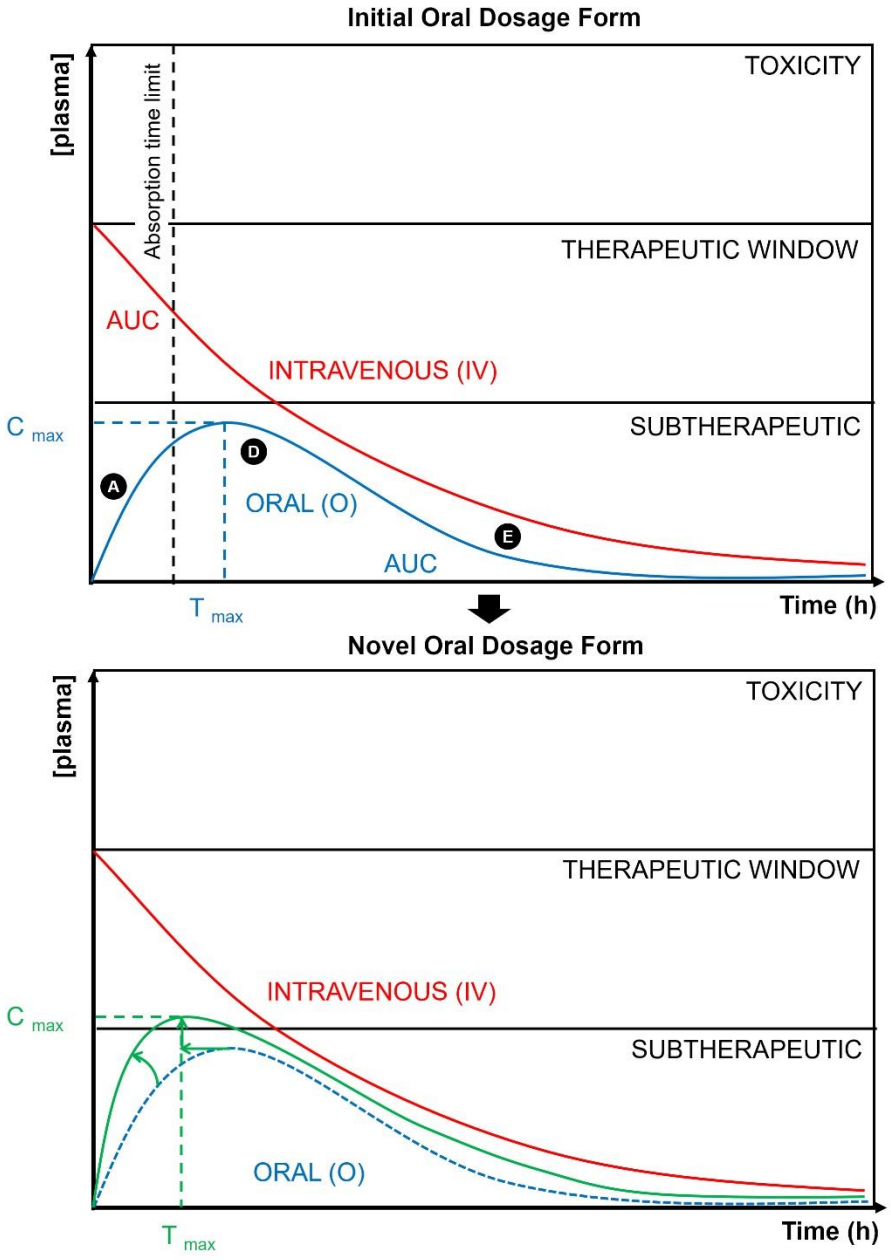

Figure 1-9. Drug plasma concentration versus time profile for intravenous (IV) and an oral route of administration (O). The bioavailability is given by the **A**rea **U**nder the **C**urve (AUC). The impact of a suitable formulation on the bioavailability profile is underlying as well. The letters A, D and E represent respectively the absorption, distribution and excretion periods.

1.4. Enhancing the Oral Drug Dosage Bioavailability

As mentioned, a suitable oral dosage form and a proper formulation are required for the best drug performance. However, other properties have to be considered as well during the preformulation of a new drug-like substance since they affect the final drug product performance. Among these are the particle size, the drug solid form (e.g. polymorphism), the hygroscopicity (moisture sorption), the partition coefficient (lipophilicity), the pKa, the chirality, the stability (pH, chemical, thermal, mechanical, electrical or in solution). [32-33] Basically, the formulation is simply defined as the preparation of a homogenous and stable material (drug substance and several excipients) which displays the desired properties. Excipients are used to help the drug release and stability. In case of a solid dosage, the final materials (formulated form) are generally hard/soft capsules or a tablet (70% of the final products). Pre-formulation mainly focuses on the physicochemical properties of the drug substance. Both in pre-formulation and formulation pathways exist to tune the physicochemical properties of the drug. Among the most spread oral formulation tools for oral solid dosage, there are *salt formation*, *lipid-based*, *particle size reduction (PSR)*, *crystal engineering*, and *cyclodextrin complexation (CD)*.[34] The selection for one or another depends on the drug, the carrier/matrix/host properties, and the desired drug performance. Obviously, all of these formulations led to countless pharmaceutical patents showing how important the formulation is in the pharmaceutical field.[35] A few marketed examples are mentioned for each formulation strategy in **Table 1-1**.

Table 1-1. Marketed drugs and literature examples with their therapeutic effect, their active pharmaceutical ingredient and their oral formulated form(s). NSAID: nonsteroidal anti-inflammatory drug; ACE: angiotensin converting enzyme; HPH: high-pressure homogenization; CINV: chemotherapy-induced nausea and vomiting; GERD: gastroesophageal reflux disease; NNRTI: non-nucleoside reverse transcriptase inhibitor.

Trademark	Therapeutic effect	API	Formulation
Voltaren®	NSAID	Diclofenac[36]	Sodium or potassium salt
Vasotec®	ACE inhibitor	Enalapril[37]	Maleate salt
Nurofen®	NSAID	Ibuprofen[38]	Lysinate salt
Agenerase®	HIV protease inhibitor	Amprenavir[39]	Lipid-based
Norvir®	HIV protease inhibitor	Ritonavir[40]	Lipid-based + solid dispersion
Neoral®	Immunosuppressant	Ciclosporin[41]	Lipid-based
Rapamune®	Immunosuppressant	Rapamycin[42]	PSR (HPH)
Emend®	Prevention of CINV	Aprepitant[43]	PSR (HPH)
Tricor®	Hypertriglyceridemia treatment	Fenofibrate[44]	PSR (HPH)
Sporanox®	Antifungal	Itraconazole[45]	Amorphous solid dispersion
Intelence®	HIV treatment (NNRTI)	Etravirine[46]	Amorphous solid dispersion
Omebeta®	GERD treatment	Omeprazole[47]	β-CD
Yaz®	Birth control	Drospirenone[48]	β-CD
/	NSAID	Ibuprofen[49]	Nicotinamide-based cocrystal
/	Anticonvulsant	Carbamazepine[50]	Saccharin-based cocrystal
/	Painkiller	Paracetamol[51]	Trimethylglycine-based cocrystal

1.4.1. Salt Formation

Since the major part of drug compounds contain acidic or basic moieties, salt formation is an obvious pathway to improve a formulation. Obviously, these compounds have to be ionizable in solution at a pH-range from 1 to 8 i.e. under relatively soft conditions. In an aqueous solution, at a fixed pH, a weak acid or basic

drug exists under two states (a monoprotic acid is considered here): the free acid/base and its dissociated form. The equilibrium (Eq. 13) is ruled by the pH and, commonly, the Henderson-Hasselbach relationships (Eq. 14), is used to express the pH-dependency on the ionization level of a weak acid or base.[16, 52]

$$HA + H_2O \leftrightharpoons H_3O^+ + A^- \quad \text{(Eq. 13)}$$

$$pH = pK_a + \log\left(\frac{[A^-]}{[HA]}\right) \quad \text{(Eq. 14)}$$

$$s = [A^-] + [HA] \quad \text{(Eq. 15)}$$

$$s = s_0 \times \left(1+10^{(pH-pK_a)}\right) \quad \text{(Eq. 16)}$$

The overall solubility of a weak acid can be approximated as the sum of the solubility of its free and ionized form (Eq. 15 and 16). At the solid state, salts are the outcome of the ionic interaction between ions e.g. a salt of an acidic or basic cation or anion and the corresponding counterion (**Figure 1-10**).[53-54] The merits of salt formation ($\left(XH^+A^-\right)_s$) is the significant solubility enhancement by conversion of the free drug form into an ion.

$$\left(XH^+A^-\right)_s \leftrightharpoons \left[XH^+\right] + [A^-] \quad \text{(Eq. 17)}$$

$$pK_s = -\log K_s = -\log\left([XH^+]\times[A^-]\right) \quad \text{(Eq. 18)}$$

Here, the solubility product (pK_s) of the salt is impacted by both the ionic drug [A^-] and its counterion [XH^+] (Eq. 17 and 18). In the body, the drug salt is exposed to fluids displaying different pH and ion populations. The common ion effect can decrease the solubility since salts with Na^+ or Cl^- are the most frequently encountered. The pH in the stomach (1-3) and the intestine (5-6.5), or broadly speaking the GI tract, rules the ionization state of the drug and thus its overall solubility. Solubility (Log S) vs pH curve may be drawn to underline this fact.[55-56]

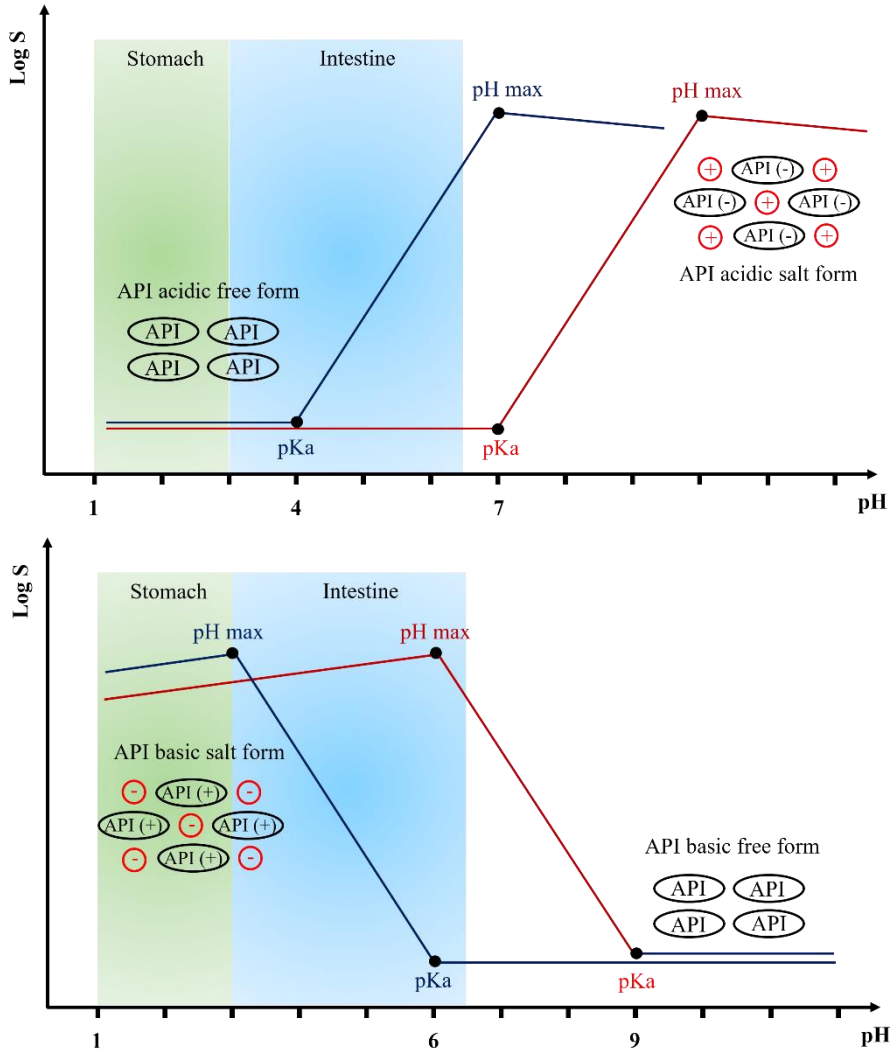

Figure 1-10. Solubility (Log S) versus pH profiles for (top) two weak acids (pKa = 4 and 7) and (bottom) two weak bases (pKa = 6 and 9). The stable solid state form depending on the pH is also noted.

Figure 1-10 illustrates the the use of a salt form of an acid is relevant when the purpose is to release at high pH since under this condition the drug will be stable under its ionized form and hence more soluble. On the opposite, making salt of a basic drug, is a smart route when the release has to occur at low pH i.e. in the stomach. The pK_a of the drug is important for the solubility profile of salts. However, one not only needs to consider the pH or the drug pKa, but also the salt nature i.e. its crystalline form including its counterion. In comparison to the free acid crystalline form, the salt often

shows strong ionic interactions resulting in an increased latttice energy. This often results in a high melting point, which is beneficial with respect to degradation (e.g. during compression) but often also implies a lower solubility. The high lattice energy can, however, be counterbalanced by the high solvation capacity of the ions in water.

$$\Delta H_{solution} = \Delta H_{solvation} - \Delta H_{lattice} = (\Delta H_{cation} + \Delta H_{anion}) - \Delta H_{lattice} \qquad \text{(Eq. 19)}$$

Moreover, the nature of the counter ion has a significant impact on the salt solubility as its capacity of solvatation depends on its size and charge. The most wide-spread counterions encountered in oral formulations are: chloride, sulfate, mesylate, maleate, citrate, phosphate, tartrate and maleate for the anionic ions and sodium, potassium, calcium, and zinc for the cationic ones. These counter ions must be GRAS i.e. **G**enerally **R**ecognized **A**s **S**afe or simply biocompatible to avoid any side effects. As the solubility, the dissolution rate is also impacted by the nature of the salt. In general, an improvement of the solubility leads to an increased dissolution rate as suggested by the Noyes-Whitney equation (C_S-C_{DL} parameter in Eq. 3). Even though salts seem promising, they also have issues related. Some important issues encountered when using salt forms are their high hygroscopicity in comparison to the non-ionized form, with potentially the issue of deliquescence, or their propensity to hydrate formation.

1.4.2. Lipid-based (Lipids, Cosolvents and Surfactants)

In this kind of formulation, the drug is combined with biocompatible excipients such as natural or synthetic *lipids* (oils, waxes, complex lipids), *solvents* (polyethylene glycol, ethanol or glycerin) and *surfactants* (polysorbates or polyoxyls).[57] These three sorts of excipients are commonly combined together and included in the "lipid-based" terminology. There are four different classes of lipid-based formulations according to the **L**ipid **F**ormulation **C**lassification **S**ystem (LFCS)[58-59]:

- Type I: purely oils
- Type II: oils and water-insoluble surfactants (HLB[a]<8-12)
- Type III: oils, surfactants and cosolvents (water-soluble or not)
- Type IV: surfactants and cosolvents (water-soluble)

Surfactants, cosolvents and lipids have the same general purpose i.e. to improve the solubilization of the drug making it more soluble in water. They mainly act by decreasing the aqueous bulk polarity and hence enhance drug-bulk interactions. Besides, these excipients (especially the lipid excipients) help the drug absorption and transport through permeability enhancement.[60-62] Considering the low melting point

[a] HLB: **H**ydrophilic-**L**ipophilic **B**alance. Higher is the HLB, more water-soluble is the surfactant.

of cosolvents, surfactants, and lipids, they are more applicable to parenteral formulation but are also often used for capsule filling (hard or soft). A surfactant (ionic or not) is frequently used to form micelles in water using surfactant concentrations above the CMC (**C**ritical **M**icelle **C**oncentration). A micelle (**Figure 1-11**) is characterized by a lipophilic core containing the drug and a hydrophilic outer layer in contact with the water-based bulk leading to an improved apparent drug solubility. In the market, lipid-based formulations are generally found as emulsions (self-emulsifying drug delivery system).[63] However, these lipid-based formulations may be converted into solid dosage forms using spray or freeze-drying or into solid dispersions using an appropriate polymer-based carrier. Moreover, surfactants and lipids provide a better wetting angle stabilizing the fine particles as nanocrystals.

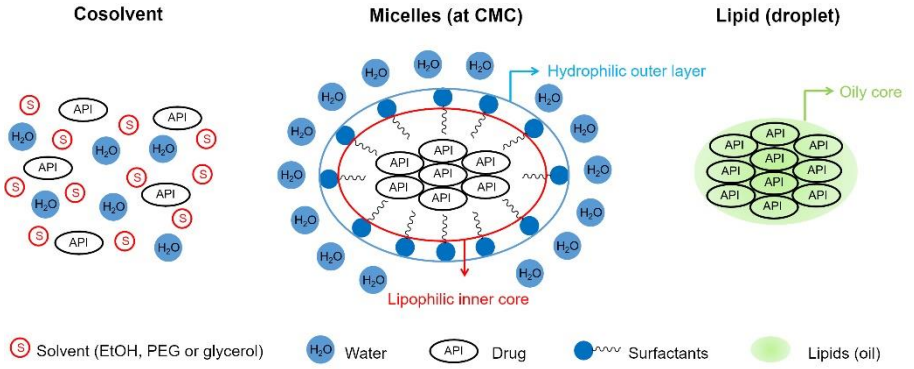

Figure 1-11. Cosolvent, surfactant and lipid-based approaches to address the low solubility and permeability of a drug (API).

1.4.3. Particle Size Reduction (PSR)

This technique is the most universal strategy used for oral drug formulation improvement (tablets, suspensions and capsules) of the dissolution rate of several orders of magnitude and by consequence the oral absorption. The purpose is to reduce the drug powder size to micrometer (micronization) or nanometer (nanonization, 100nm-1µm) size.[64-65]Micronization often suffices for poorly-soluble drugs while water-insoluble drugs require nanonization. Size reduction drastically increases the specific surface area of a drug and hence the surface available for solvation. The impact on the dissolution rate is explained using the Noyes-Whitney equation (Eq. 3). An increase of the solubility may be noticed as well, according to the Ostwald-Freundlich[16] equation which dictates that smaller particles have a higher solubility than larger ones.[66]

$$\log\left(\frac{s}{s_\infty}\right)=\frac{2\sigma V_m}{2.303RT\rho r} \qquad \text{(Eq. 20)}$$

Where s is the thermodynamic solubility, s_∞ the solubility of the solid made of large particles, σ the interfacial tension, V_m the molar volume, R the gas constant, T the temperature, ρ the volumic mass and r the particle radius. Besides, many particle size reduction methods cause defects or cavities in the crystal decreasing the solute-solute interactions leading to an increase of the overall solubility. However, the main parameter affected by PSR remains the dissolution rate. In case of nanocrystals, the fast dissolution and the high apparent solubility induced may cause a situation of supersaturation leading over time to recrystallization of a more stable form of the drug.[67] A similar type of behavior (described in the next section) is known to occur in case of an unstable polymorph, amorphous phase, cocrystal or a solvate. Generally, the nanocrystals-based formulation is combined with surfactants/stabilizers to avoid nanocrystal (high specific surface) aggregation or Ostwald Ripening.[68-69] Ostwald ripening or coarsening is the process wherein the particle size increases to reduce the interfacial tension and hence the overall energy of the system. For this purpose nanocrystals may be dispersed in a polymer carrier.

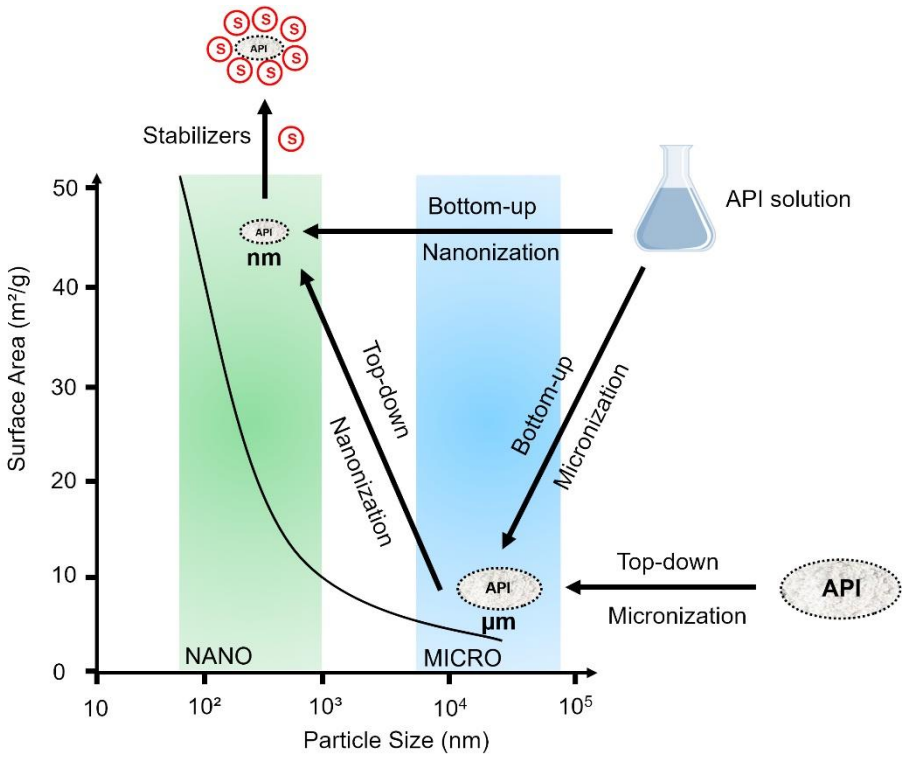

Figure 1-12. Bottom-up and top-down approaches to reduce the particle size of a drug and evolution of the surface area with the particle size.

Two main approaches are used in particle size reduction: the so-called *bottom-up* and the *top-down* approaches (**Figure 1-12**).[70] *Bottom-up*, or also called *via humida paratum* (VHP) gathers the methods exploiting the crystallization of microcrystals (or sometimes nanocrystals) from a supersaturated solution. A high degree of supersaturation is required to obtain fine nuclei formation.[71] Appropriate understanding of crystallization kinetics (nucleation and crystal growth) is required to achieve the desired size. More details about the crystallization process are given in the **Crystal Growth & Nucleation** section. To create the high supersaturation levels required, methods such as antisolvent addition (solvent shift), supercritical fluids (carbon dioxide), spray-drying (fast solvent evaporation) and freeze-drying (lyophilization) are used.[16] Spray-drying consists in dispersing the drug solution into a hot gas carrier leading to solvent evaporation and formation of small size particles.[72] Freeze-drying or lyophilization, involves freezing the solvent (generally water) and sublimate this latter under vacuum.[73] These last two methods are wide-spread and may be combined to a *top-down* approach. The *top-down* methods reduce larger crystals into smaller particles according to two main routes. *Pearl-milling* (or wet ball-milling)

is a slurry (suspension) wherein the drug, a medium (water), stabilizers and hard pearls are put together. A high milling-frequency is then applied on the system for a fixed duration causing collisions and a particle size reduction.[74-75] The duration varies from a couple of hours to several days depending on the drug stability and other parameters. Indeed, this kind of energetic milling is not appropriate in case of drugs that exhibit low thermal stability or a solid-solid transition (polymorphic transformation) below 100°C. The second *Top-down* method is called ***H**igh-**P**ressure **H**omogenization* (HPH). Its principle consists in the frontal collisions of two fluid streams (drug suspension) under high pressure leading to a particle size reduction. Many cycles are generally applied to reach the desired size. Several HPH technologies are found on the market using either a classical jet stream or a piston gap homogenizer.[76]

1.4.4. Solid Dispersions

Solid dispersion is the dispersion of a drug (crystalline or amorphous) into an inert matrix or carrier (crystalline or amorphous). There are six different kinds of combinations (**Figure 1-13**) between the drug and the carrier depending on their physical form and the manufacturing route[16, 77-78]:

- *Eutectic mixture:* wherein a crystalline drug form is suspended (partially dispersed) in a crystalline carrier. Such a situation is called a physical mixture that behaves like a pure solid with a single melting point for a fixed eutectic composition.
- *Amorphous solid suspension*: the drug is under amorphous form while the carrier remains crystalline.
- *Solid solution*: the drug is molecularly dispersed or dissolved into the crystalline matrix.
- *Glass suspension*: the crystalline drug is dispersed in the amorphous carrier. The material is characterized by a unique glass transition temperature (T_g).
- *Glass solution:* the drug is molecularly dispersed (dissolved) into the amorphous matrix.

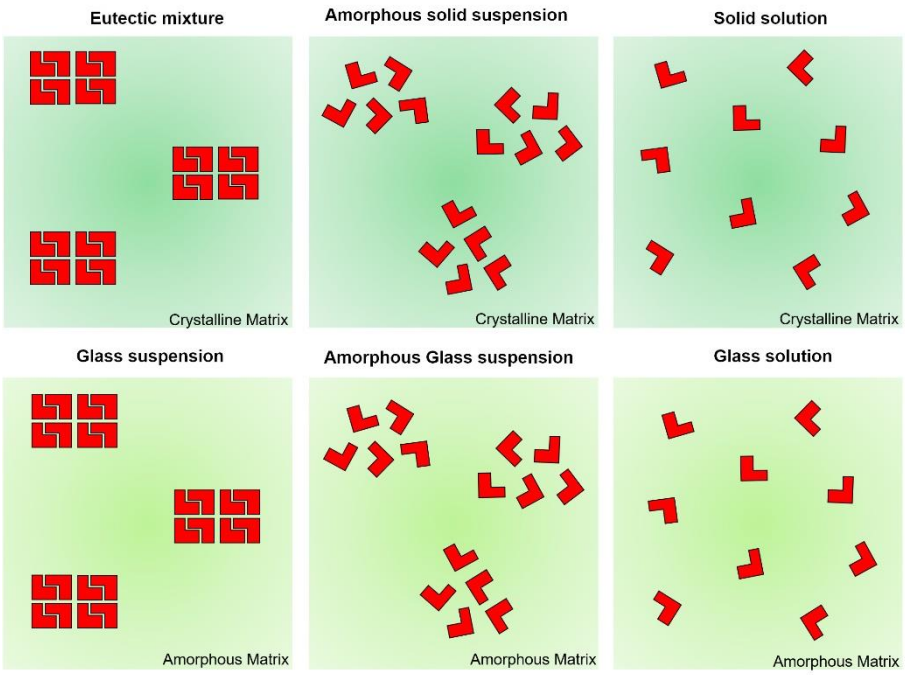

Figure 1-13. Type of solid dispersions according to the physical form of the drug and the carrier. Freely adapted from Williams *et al.*[16].

Currently, the matrix used are mainly **H**eight **M**olecular **W**eight **P**olymers (HMWP) which are water-soluble like natural polymers (cellulose or proteins), semi-synthetic polymers (HPMC and HPC)[a] or synthetic (PVP and PEG) ones[b]. The essential carrier properties are generally biocompatibility, thermal stability, high glass transition (T_g), water solubility and stabilization capacity. These polymers may also be combined with surfactants for additional solubilization enhancement. The interest for the pharmaceutical field in this method is the reduction of the drug particle size (in particular for the solid solution and the glass solution), the stabilization and the solubilization boost brought by wetting from the carrier.[79-80] The size reduction and stabilization in solution from the carrier lead to a better dissolution rate and oral absorption. Solid dispersion is well addressed to stabilize an amorphous drug by drug-carrier interactions and by decreasing the molecular motions required for nucleation and crystallization. In the dissolved drug vs time curve in **Figure 1-14**, an amorphous phase is stabilized through a solid dispersion (green dotted curve). Instead of recrystallizing rapidly (red curve) once the supersaturation is reached (spring), a softer crystallization occurs over time (parachute).[81-82] If a good enough carrier is chosen

[a] HPMC : **H**ydroxy**P**ropyl**M**ethyl**C**ellulose, HPC : **H**ydroxy**P**ropyl**C**ellulose
[b] PVP : **P**oly**V**inyl**P**yrrolidone

(dark blue line), the meta-stable situation might be maintained for a long time. However, the main drawback of this method still remains the potential crystallization of the amorphous form into a more stable one.[80] It is the reason why only a few examples based on this technique are found on the market.

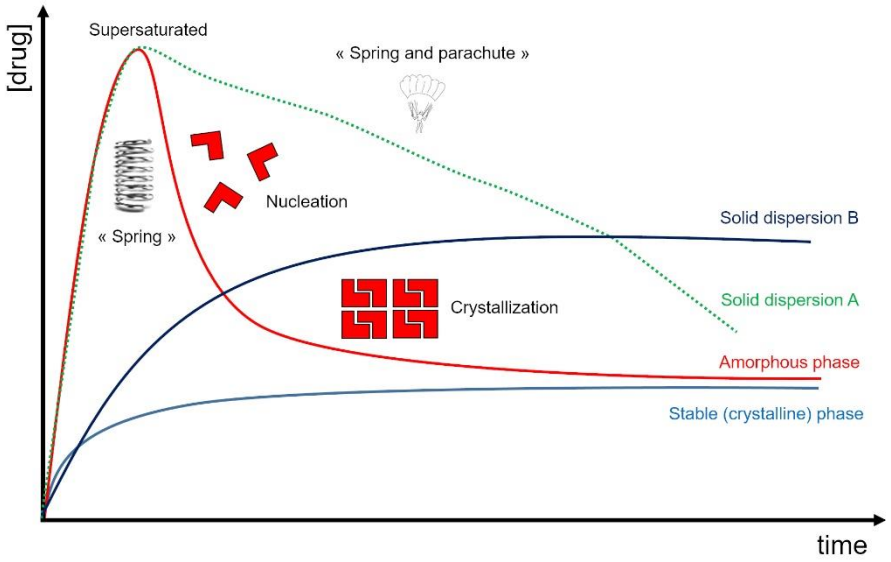

Figure 1-14. Drug concentration versus time profile in case of a crystalline drug (light blue), an amorphous drug (red), a solid dispersion A (green) and a solid dispersion B (dark blue). The "spring and parachute" concept is illustrated as well.

Many classical methods are used to prepare solid dispersions.[79, 82] Among them, the *melting method* consists of melting a physical mixture of the carrier and the drug followed by a fast enough cooling to avoid crystallization to occur. A rigorous stirring/mixing is also required to avoid heterogeneity in the dispersion. After solidification, the solid is crushed in order to get the desired particle size. The *hot-melt extrusion*, widely used in polymerization and formulation, is the method whereby melting is performed using an extruder. This method is limited to drugs that display suitable thermal stability and no polymorphic transition. On the other hand, the *solvent evaporation method* is based on the dissolution of a physical mixture in a suitable solvent followed by fast solvent evaporation. This method is tarnished with two issues. The difficulty of choosing a solvent that dissolves both the carrier and the drug (different polarity) and phase separation during drying. As aforementioned, *spray-drying* and *freeze-drying* are very popular and efficient methods, allowing good control over the physical properties of the solid form and no drug/matrix phase separation.[83] The most environmentally friendly method is the use of CO_2 as a supercritical fluid (exhibits both gas and liquid properties) through **R**apid **E**xpansion of a **S**upercritical **S**olution (RESS). In brief, both the drug and polymer are dissolved

in carbon dioxide and then sprayed to achieve fast cooling. Generally, nanosized particles are obtained. Recently novel methods such as *electrospinning* can also be encountered.

1.4.5. Cyclodextrin Complexation

Cyclo**D**extrins (CD) are part of the macrocyclic oligosaccharide family characterized by a lipophilic inner core and a hydrophilic outer layer. There are three main kinds of CDs: α-CD, β-CD and γ-CD with respectively 6, 7 and 8 glucopyranose moieties as shown in **Figure 1-15**. The inner core diameter (ID) varies from 4.7 to 5.3 Å (α-CD), 6.0 to 6.5 Å (β-CD) and 7.5 to 8.3 Å (γ-CD).[84] Generally, they are substituted on their inner and outer side with methyl or hydroxylalkyl groups for less toxicity and higher solubility. Many other modified CD may be found in the review by Rekharksy et al.[85]

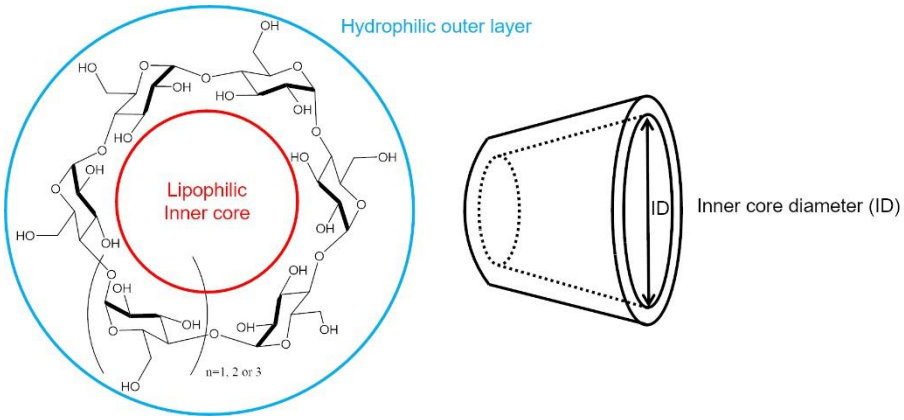

Figure 1-15. Molecular structure of cyclodextrins (α, β and γ) and their schematic cone representation.

They are used as vessels/host wherein the API/guest are associated/complexed in the lipophilic inner core (**Figure 1-16**). While apolar molecules association in water is linked to a positive enthalpy and entropy effect, this is not observed in the case of CD-drug inclusion. Indeed, the drug and the CD are associated through intermolecular interactions (vdW, hydrogen bonds, charge-transfer, etc) that energetically promote the complexation even if an entropy increment could appear due to the inclusion (enthalpy-entropy compensation).[86] The hydrophobic effect, that forces apolar molecules to aggregate together, may be used to explain this association but this terminology is still quite controversial.[87]

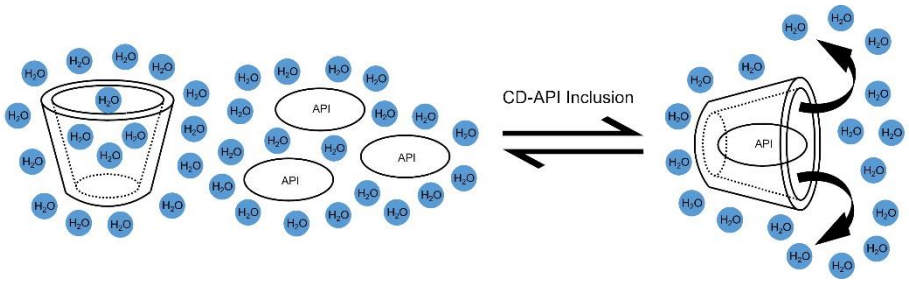

Figure 1-16. Cyclodextrin and drug association in aqueous solution.

The equilibrium constant (K_c), describing the association/dissociation of the CD-drug complex, has to be high enough to avoid using high CD concentrations. However, a too high binding constant leads to sub-optimal drug release. Using a CD carrier, the drug has an "apparent" solubility that is higher than that of the parent compound.

$$aAPI + bCD \leftrightharpoons aAPI \subset bCD \qquad \text{(Eq. 21)}$$

$$K_c = \frac{[aAPI \subset bCD]}{[API]^a \times [CD]^b} \qquad \text{(Eq. 22)}$$

The binding constant (K_c), as well as the stochiometry is usually determined by different spectroscopic technics such as NMR[a] or UVS. Many parameters affect the complexation : the nature of the drug, the CD inner core size, the ionized state and polarity of the drug, the presence of counterions, etc. Drug-CD inclusion is achieved using different methods.[16, 88] *Co-precipitation* starts by dissolving the CD in water and adding a suitable amount of drug under continuous stirring. The solution is then cooled to precipitate the complex. A more convenient method is *slurry complexation* which consists of a slurry (suspension) of CD and the drug in water. Once the equilibrium reached, the complex forms from the aqueous medium. *Paste complexation*, is the grinding of the CD with the drug with traces of water in order to achieve a paste. A variant of this method is *dry-mixing*, where no water is used. *Extrusion* is a kind of mixing between water, drug and CD with the use of an extruder using higher temperatures.

1.5. A Deeper Insight in Crystal Engineering

Before going deeper into the panel of different solid forms that exist, we start by reminding the definition of a crystal. A crystal is a solid characterized by a long-range

[a] NMR : **N**uclear **M**agnetic **R**esonance

and periodic organization of atoms or molecules (buildings blocks).[89] Such a 3D-arrangement maximizes the intermolecular interactions in the solid and stabilizes the crystal structure (Eq. 23). Frequently encountered interactions in the crystal structure are the van der Waals, π-π stacking, hydrogen bonds, halogen bonds, etc.[90]

$$\Delta G_{lattice} = \Delta H_{lattice} - T\Delta S_{lattice} \qquad \text{(Eq. 23)}$$

Crystal engineering might be defined as the design or the control of the crystal packing of a compound with the goal of reaching a solid form with enhanced properties.[91] Crystal engineering takes advantage from the rules of supramolecular chemistry i.e. intermolecular interactions, supramolecular synthon identification, geometry and directionality to build up new crystalline forms (multicomponent or not), also called supramolecular compounds.[92-95] A change in crystal packing leads to a change in free energy, and hence a variation of all physicochemical properties (density, refractive index, hygroscopicity, melting point, solubility, stability, hardness, tablet-ability, dissolution rate, …).[96] Among the solid phases that may be generated from a molecule, there are *polymorphs*, *solvates* (pseudo-polymorphs), *salts* (mentioned previously), *cocrystals*, *solid solutions*, *ionic cocrystals* and *the amorphous phase*.[97] A schematic representation of these solid forms is illustrated in **Figure 1-17**. From a pharmaceutical point of view, a particular interest relates to a difference in solubility and/or dissolution rate different solid forms presents and hence a potential change in bioavailability.

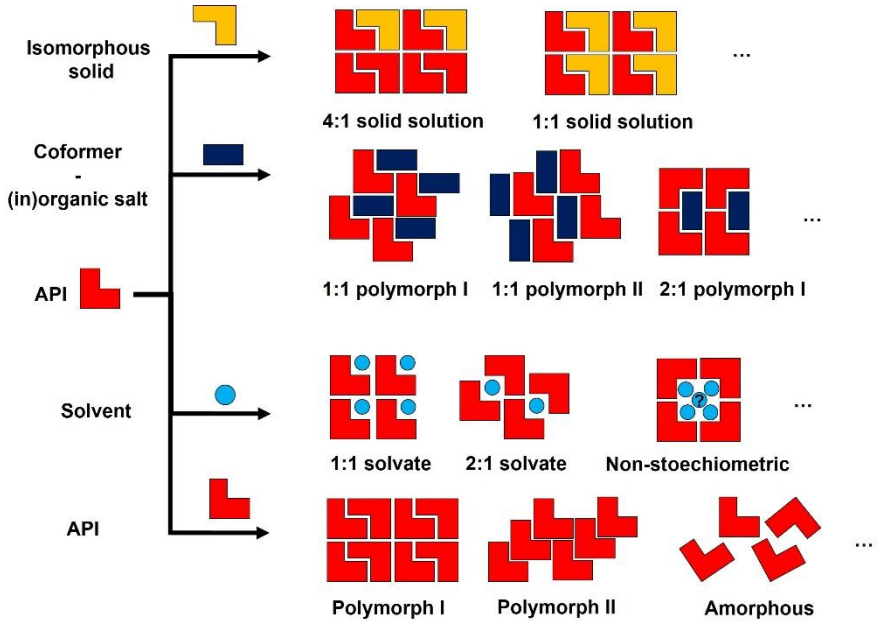

Figure 1-17. Schematic representation of the solid-state forms achieved through the crystal engineering approach.

1.5.1. Polymorphs

A given compound, inorganic or organic, may exhibit several crystalline forms, having the exact same chemical composition.[98] These forms are called polymorphs and the most famous case is likely the element carbon that may crystallize as graphite or diamond depending on the experimental conditions. These solid forms clearly exhibit different physicochemical properties at the solid state such as hardness, density, solubility, melting point.[99-100] The appearance of one polymorph over another depends on nucleation kinetics, and polymorph stability (thermodynamics).[101] The thermodynamic form is not always the one that crystallizes first, as Ostwald suggested with his rule of stages (**Figure 1-18**).[102] Indeed, starting with a supersaturated solution, a polymorphic system often evolves first to the state that is the easiest to reach (a metastable form, local minimum) even if it is not the most stable one. The equilibrium will be established once the overall stable form (least soluble) is reached. Generally speaking, two different polymorphic systems can be encountered, based on the Gibbs energy curves vs temperature.[103] In an *enantiotropic* system (**Figure 1-18**), there is a transition point (T_{trans}) below which a given polymorph is the most stable, and above which another form becomes the most stable. On the other hand, when a

given form is always the most stable up to its melting point, the system is called *monotropic*.

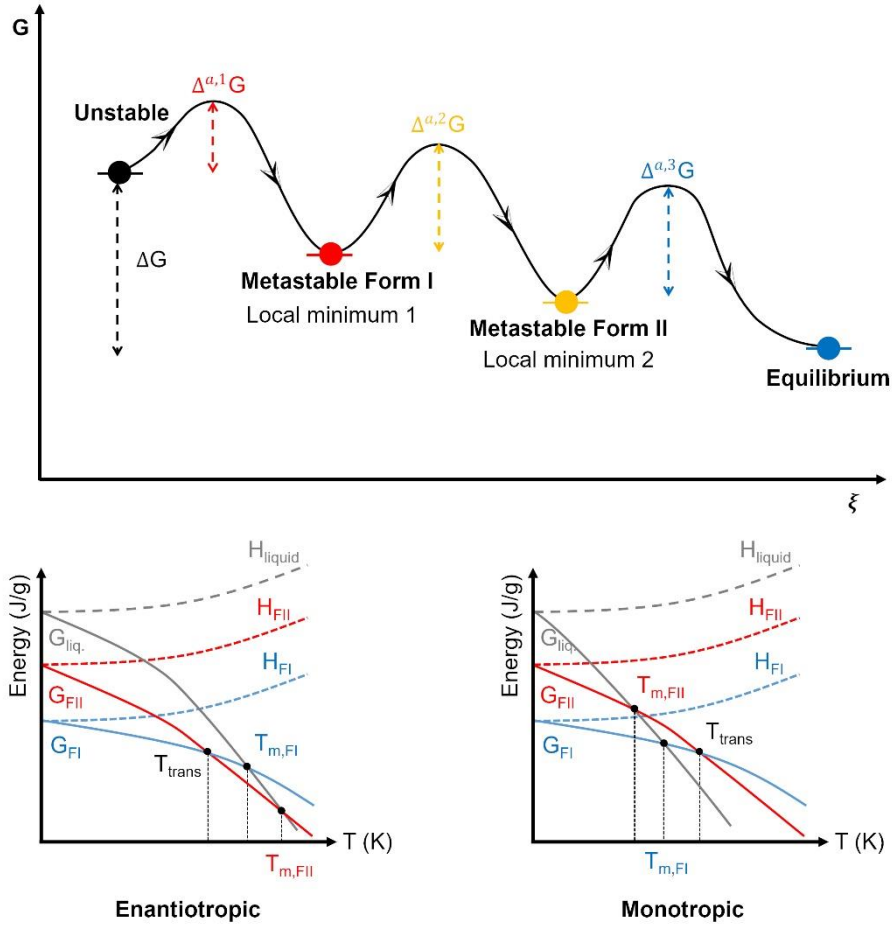

Figure 1-18. (top) The Ostwald's rule of stages in the case of two metastable states and (below) theoretical enantiotropic and monotropic system of two polymorphs.

The nature of a polymorphic system can be studied based on the melting enthalpies provided by a DSC[a] or by performing slurry conversion (or solvent-mediated transformation) experiments at different temperatures in a solvent. Unstable polymorphs, are higher-energy forms, display an increased dissolution rate and an increased apparent solubility, with the potential risk of these forms converting over time into the thermodynamic form (**Figure 1-14**). A complete understanding of the polymorphic forms as well as their transformation is required to avoid issues as those

[a] DSC : **D**ifferential **S**canning **C**alorimetry

encountered with the well-known case of Ritonavir (conversion over time from the unstable marketed form I into a new form II).[104]

1.5.2. Amorphous State

The amorphous phase is a solid phase showing only a short-range order contrary to the long-range organization of the crystalline state. The amorphous state is often easily accessible for those compound showing conformational flexibility and slow crystallization kinetics.[105] To obtain such a phase, many methods exist such as fast precipitation, melt quenching, milling, spray- and freeze-drying, dehydration of hydrate, etc. A pure amorphous phase, is characterized by a glass transition (T_g, kinetic parameter) which is the vitrification temperature of a liquid and may vary depending on the temperature scanning rate (thermal history). To avoid the relaxation (the arrows in the **Figure 1-19** from T_g to T_0) or physical aging which is the contraction of the glass phase into a lower energy crystalline state, the working temperature has to be lower than T_g but not too low as lower temperatures also promote transitions. In general, T_0 or T_K (Kauzman temperature) is used and defined as the temperature at which the relaxation time (τ) is infinite and there is zero mobility .[105-107] The Vogel-Tamman-Fulcher (VTF) equation is used to describe the glass phase relaxation.[16, 108]

$$\tau = \tau_0 \, e^{\left(\frac{DT_0}{T-T_0}\right)} \qquad \text{(Eq. 24)}$$

Where τ is the relaxation time, τ_0 the relaxation time constant, D the strength (fragility) constant, T the temperature and T_0 or T_K the Kauzman temperature. This temperature is theoretically the ideal temperature to store the unstable form as below this temperature, the amorphous phase converts into the crystalline one. The fragility of an amorphous form can be categorized according to the T_g - 50°C rule. Materials with a $(T_g-T_0) > 50$°C are considered as strong glass materials while materials with $(T_g-T_0) < 50$°C are considered fragile. An alternative is used when T_0 is unknown and it consists of a simple ratio between T_m and T_g ($T_m/T_g > 1.5$: strong glass material and $T_m/T_g < 1.5$: weak glass material). Such a strong/fragile appellation is used to discriminate fragile liquids that exhibit an important heat capacity variation (ΔC_p) at T_g while this variation is weak in case of strong liquids.[106]

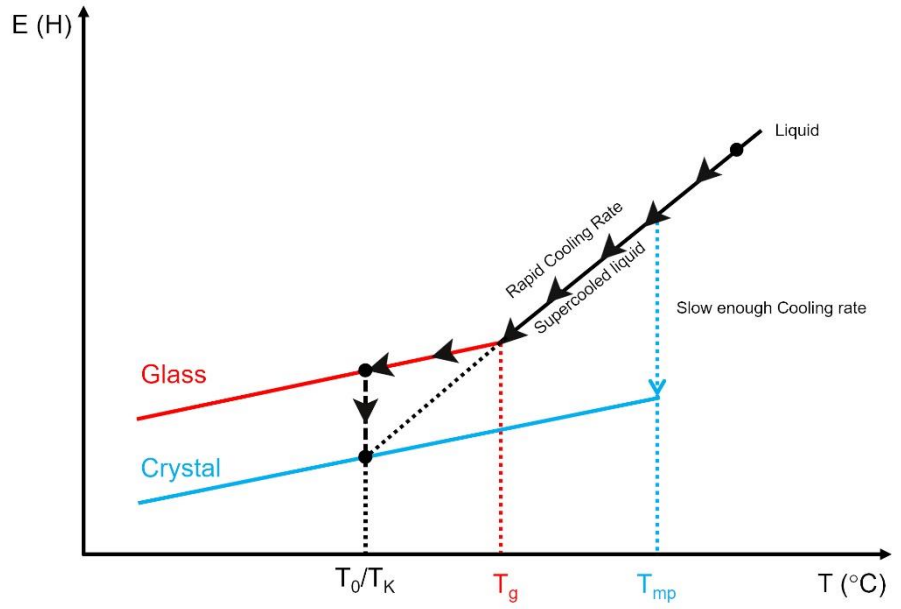

Figure 1-19. Enthalpy variation versus temperature curve from a liquid phase to a glass and crystalline phase.

Since it is a short-range arrangement, XRPD is less suitable to characterize the amorphous state. On the other hand, DSC is a very useful characterization method as it gives the T_g. In the pharmaceutical field, the amorphous phase is interesting, as its high-energy leads to rapid dissolution and hence oral absorption. However, recrystallization/precipitation in a more stable (crystalline) form is a potential pitfall.[109] In solution, the conversion from the amorphous state into the crystalline one is solvent-mediated. As mentioned previously, to avoid or reduce this risk, the amorphous phases are commonly stabilized through polymer-based solid dispersions. In a solid dispersion formulation, the polymer carrier reduces the kinetics of nucleation and crystal growth by interacting with the amorphous particle through the formation of a drug-polymer cluster (**Figure 1-14**).

1.5.3. Solvates

Polymorph screening as well as crystallization processes are often performed in solution. The compound may cocrystallize with the solvent molecule leading to a solvate or also called pseudo-polymorph.[110-111] As any different crystalline structure, different physicochemical properties are recorded for solvates. One distinguishes *stoichiometric solvates* from *non-stoichiometric* ones. In the case of a stoichiometric solvate, the solvent is present in a fixed ratio in the crystal structure (1:1, 1:2, 1:3, etc.)

and is usually strongly bonded to the parent compound. Solvent removal from the crystal structure leads to a collapse of the overall arrangement. Monohydrates are the most wide-spread hydrates (solvate with water) while occurrence of higher stoiochiometric solvates decreases with growing ratio.[101] In non-stoichiometric solvates, the solvent is not bonded as strongly as in a stoichiometric solvate but rather lies in voids or interstices. The solvent, however, remains crucial for the stability of the crystal structure. The ratio or the total amount of solvent is no longer fixed. In general, solvates are less stable than the anhydrous phase, since solvate stability depends on the temperature and partial pressure of the solvent in the atmosphere (which is usually 0 except for water due to the ambient moisture). Hydrates are therefore often the only stable observable solvates.[110] TGA[a], DSC, DVS[b] (moisture sorption) are well-known techniques to characterize and study solvates. Indeed, TGA informs about the amount of solvent lost upon heating and then allows determining the stoichiometry. DSC yields the desolvation point, desolvation enthalpy and potentially shows recrystallization phenomena. Finally, DVS shows great merit to study the stability or even the existence of other hydrates under different temperature/relative humidity conditions. Hydrates are of great interest for the pharmaceutical field.[112]

1.5.4. Cocrystals

Instead of crystallizing with a solvent molecule, a molecule of interest may "cocrystallize" with another solid molecule forming a so-called cocrystal. The definition of a cocrystal is quite a controversial matter but a generally accepted definition is that of a "crystalline multicomponent material made of at least two neutral components which are solid under ambient conditions and bonded to each other through intermolecular interactions e.g. hydrogen bonds".[113-115] The strategies in choosing the coformer are ruled by crystal engineering principles i.e. the identification of supramolecular synthons defined as the repetitive interactions pattern that lead to cocrystallization. Generally speaking, coformers are selected based on their donor/acceptor hydrogen bond moieties that are likely to exhibit supramolecular synthons and interactions with other such moieties as illustrated in **Figure 1-20**. However, other kinds of intermolecular interactions as halogen bonds and π-π stacking also need to be considered. The term *heterosynthons* is used when the molecular recognition comes from different moieties whereas similar moieties form *homosythons*. In 1990, Etter[116] proposed a notation called "Etter's Graph-sets" to discriminate and rationalize the different hydrogen bond motifs that may be found in

[a] TGA : **T**hermo**G**ravimetric **A**nalysis
[b] DVS : **D**ynamic **V**apor **S**orption

a structure. This notation (Eq. 25) dictates the amount of hydrogen bond donors and acceptors and the kind of network/pattern.

$$G_d^a(r) \qquad \text{(Eq. 25)}$$

G is the descriptor of the inter- and intramolecular hydrogen bond network. It can either be S-type (for intramolecular hydrogen bonds), C-type (infinite chain of intermolecular hydrogen bonds), R-type (for a ring pattern) and D-type (noncyclic dimer or any finite hydrogen bond pattern). The parameters a and d are respectively the number of hydrogen bond acceptors and donors in the considered set. Finally, the parameter r is the total number of atoms involved in the ring or repeated in a chain. Some examples are illustrated in **Figure 1-20**.

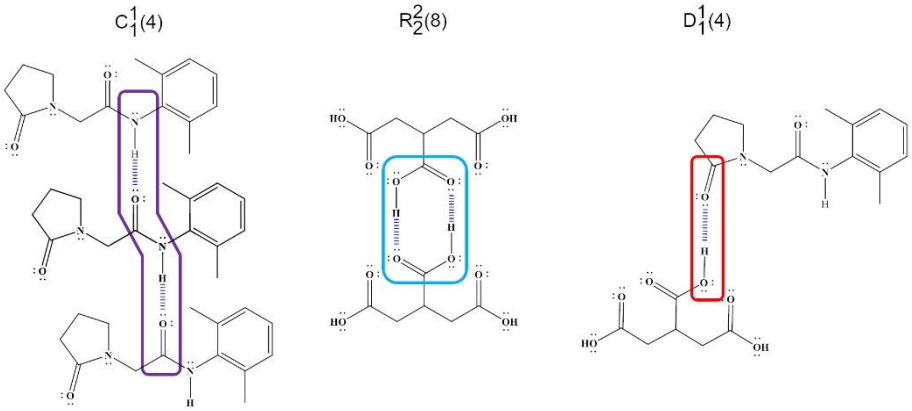

Figure 1-20. Illustration of some heterosynthons and homosynthons and their Etter's graph-set notation.

The main methods to achieve cocrystals remain the basic crystallization methods such as evaporative, cooling, and slurry crystallizations or alternatively using solid-state approaches (neat and liquid-assisted grinding). As for the other potential forms, cocrystals can be easily identified using analytical techniques such as XRPD, SCXRD[a] and DSC. Their interest in the pharmaceutical field is once more the potential to change physicochemical properties, with solubility and dissolution rate remaining the most interesting.[117-119] To fully grasp the dissolution profile of a cocrystal, ternary phase diagrams are required to understand the solid-liquid equilibria of a drug-coformer-solvent system. In the context of a cocrystal suspension in water (or any other solvent), two kinds of systems can be distinguished. A *congruent system*

[a] SCXRD : **S**ingle-**C**rystal **X**-**R**ay **D**iffraction

which means a cocrystal can be formed (i.e. its suspension is stable in solution) starting from stoichiometric conditions in that specific solvent. An *incongruent* system implies that a stoichiometric composition ultimately (thermodynamically) leads to either one of the pure components or a mixture of pure component and cocrystal to come out of solution. These two systems are illustrated in the **Figure 1-21**. A decrease or increase of the drug solubility may result from a cocrystal formation depending on the nature of the system.

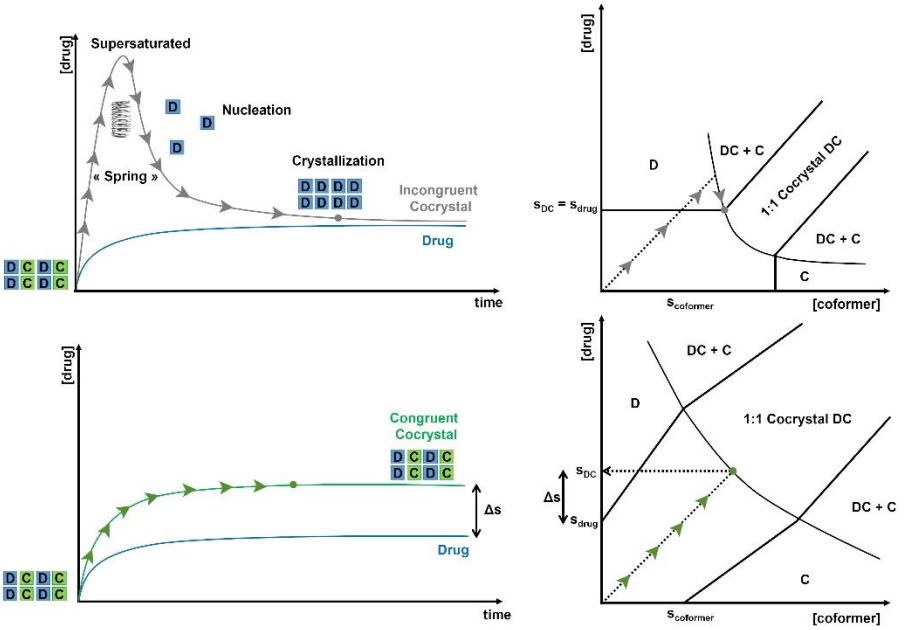

Figure 1-21. Drug concentration versus time profile (dissolution curve) and binary phase diagram in case of (bottom) a congruent cocrystal system (top) an incongruent cocrystal system.

In the pharmaceutical field, since the molecule of interest has a biological effect and has to be administrated to human beings, the cocrystal formers allowed must be GRAS (Generally Recognized As Safe) to avoid any side effects. A full list of acceptable food additives can be found online https://www.fda.gov/food/food-additives-petitions/food-additive-status-list. The new cocrystal forms may be combined with the previous formulations (PSR, solid dispersion, cyclodextrin inclusion or lipid-based formulation) for complementary performance. From a legal point of view, distinguishing between cocrystal and a salt is not always evident. As a general rule of thumb, a ΔpKa of 2 or 3 units (the pKa rule) between the acidic/basic drug and the base/acid leads to salt formation,[120-121] whereas a ΔpKa between 0 and 3, can lead to both a cocrystals or a salt, in a so-called salt-cocrystal continuum.[122]

1.5.5. Ionic Cocrystals (ICCs)

Metal-organic complexes may be included in the cocrystal definition. They can be seen as differing from the classical cocrystal as the coformer used is no longer a neutral organic molecule but an inorganic/metal salt.[123] While classical cocrystals are self-assembled through hydrogen bonds, the nature of the interaction in ICCs is the coordination (**Figure 1-22**) between the carbonyle/amine/amide moiety from the drug and the metal cation from the inorganic salt. As any other solid forms, ICCs show different solubility, hygroscopicity, dissolution rate, etc. They are particularly known to bring high thermal stability considering the nature of the interaction (covalent) between the salt and the drug.[124-126] They represent a great interest for industrial applications since many of the metal salts ($ZnCl_2$, $MgCl_2$, $CaCl_2$, etc) are biocompatible according to the FDA.

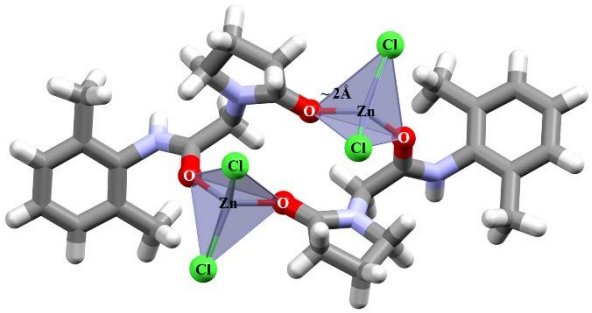

Figure 1-22. Example of interactions in the nefiracetam-zinc chloride ICC.

1.5.6. Cocrystal Solid Solutions

In terms of cocrystals, solid solutions differ from the ones explained previously in the **Solid Dispersion** section. In a substitutional cocrystal solid solution, some molecular species (drug compound) in the crystal structure are replaced with similar ones, only slightly affecting the crystalline structure.[127-128] The stoichiometry of the cocrystal is variable (= continuum) in this multicomponent crystal structure. This continuum in stoichiometry (Eq. 26) leads to variable properties from one extreme stoichiometry to another.

$$D + IC \leftrightharpoons D_{(1-x)}(IC)_x \qquad \text{(Eq. 26)}$$

Usually, solid solutions are observed for structurally very similar compounds with only slight chemical changes such as the substitution of polarizable halogen (Cl, Br or I) by another or hydrogen by a fluoride atom.[128]

2. Importance of Chiral Resolution

2.1. Chirality

Chirality is a 3D-property that exists when two mirror images are non-superimposable. The thus obtained items are called enantiomers, a type of stereoisomers. The common example used to illustrate this concept are the right and left hand (**Figure 2-1**). When an organic molecule is considered, it often exhibits at least one asymmetric atom (C, Si, S, P, B or N) i.e. substituted with all different substituents. A chiral molecule may display n chiral centers and then 2^n stereoisomers exist. This kind of chirality, which is the most spread, is called *central* chirality.[129] Chirality is not always caused by an asymmetric atom. Indeed, BINAP and ferrocene respectively display *axial* and *planar* chirality.[130]

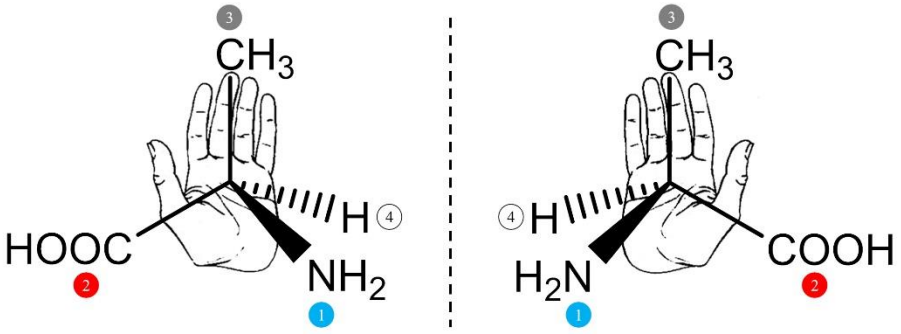

Figure 2-1. (D)-alanine (left) and its mirror image (L)-alanine (right).

The traditional R/S nomenclature of **C**ahn-**I**ngold-**P**relog (CIP), which dictates the absolute configuration of an asymmetric atom, is based on the CIP priority rules.[130-131] The substituent priority is attributed according to:

- Higher atomic number (Z) or High molecular weight (Mw) = higher priority.
- When substituents have the same following atoms (one or more), the atomic number of the next atom defines the priority.
- Double and triple bonds are considered respectively as two and three single bonds.
- *Cis* configuration has priority over *trans*.
- Lone pair electrons are viewed as an atom with atomic number 0.
- Close groups have higher priority than distant ones.

Once the attribution is set and the smallest priority group placed in the background, a clockwise or anticlockwise counting describes respectively an asymmetric atom with an R or S configuration. An example of this priority rule is applied to the alanine enantiomers (**Figure 2-1**). Fischer's nomenclature (D/L) is also used but mainly for carbohydrates and amino acids. Two enantiomers (R and S) behave in the same way when in achiral surroundings and their physicochemical properties (solubility, stability, etc) are identical, with exception to their interaction with polarized light. Indeed, an enantiomer has the ability to rotate the polarized light clockwise (+, dextrogyre *d*) or anticlockwise (-, levogyre *l*). Overall, a given amount of compound, can be comprised of a mixture of both enantiomers. The term *racemic* implies an equal amount of R and S and *nonracemic* when there is an excess in one enantiomer with respect to the other.[132] The enantiomeric excess (*ee*%) in solution is calculated using Eq. 27. The concentrations in each enantiomer required to calculate the enantiomeric excess may be obtained through polarimetry, chiral chromatography or NMR.

$$ee\%\ (S) = \frac{C_S - C_R}{C_S + C_R} \times 100 \qquad \text{(Eq. 27)}$$

Chirality is wide-spread in nature and, thus also in the human body, with proteins, enzymes, amino acids, nucleotides, all carrying asymmetric carbons. When a chiral molecule (drug) is placed in such an environment, its enantiomers exhibit different biological activities. Indeed, biological receptors, which are mainly proteins, have 3D structures able to select/recognize a single drug enantiomer and to interact specifically with it (drug-receptor model, **Figure 2-2**).

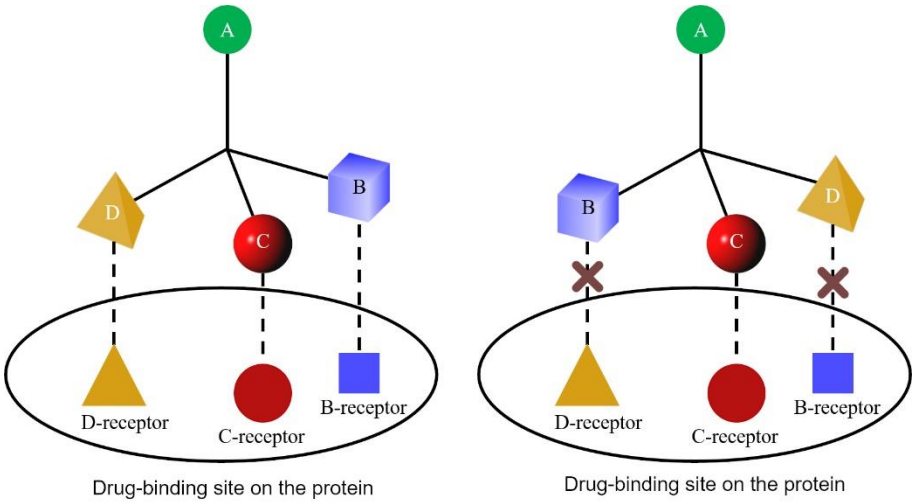

Figure 2-2. Stereoselective binding between two enantiomers and selective receptors on a protein. Freely adapted from Lin *et al.*[131]

These favored interactions lead to the desired therapeutic effect. The enantiomer that is responsible for the therapeutic activity is called *eutomer*. The opposite enantiomer, the *distomer*, may also show beneficial, no or unwanted side effects. The most famous example to underline the importance of the control and the understanding of the chirality of a drug, is the pitiful case of thalidomide. In 1950, thalidomide (R-enantiomer) was administrated as a sedative/anti-nausea drug to pregnant women. However, an increased percentage of deformations with new-borns was observed. This side effect orginated from the *in vivo* (plasma) racemization of the *eutomer* (S)–thalidomide displays a teratogenic activity that caused angiogenesis.[133-134] A similar chiral inversion in the human body has also been observed for some profens.[135] In the early 90's and to avoid future issues related to chirality, the FDA developed a regulatory guidance for the pharmaceutical field to prone the use of a single stereoisomeric drug (one single enantiomer).[133, 136] Since that moment onwards, the amount of racemic drugs on the market has constantly decreased (**Figure 2-3**). Many pathways exist to develop a single given enantiomer but the three main approaches are enantioselective synthesis of one single enantiomer (asymmetric synthesis), derivation from the chiral pool or finally the physical separation of both enantiomers from a racemic drug called chiral resolution. Amongst the synthetic routes, one finds dynamic kinetic resolution, enzymatic catalysis (biocatalysis), organometallic catalysis, organocatalysis and the roots based on the chiral pool.[131] These syntheses are generally costly since the use of a chiral pool compound, chiral auxiliaries and catalysts can be expensive and enantiopurity is not always reached up to the given requirement. The resolution route (separation of both enantiomers after synthesis of the racemate) also finds multiple techniques available such as *diastereoisomeric salt*

formation, *chiral chromatography* and *preferential crystallization* (PC). This last approach will be detailed further.

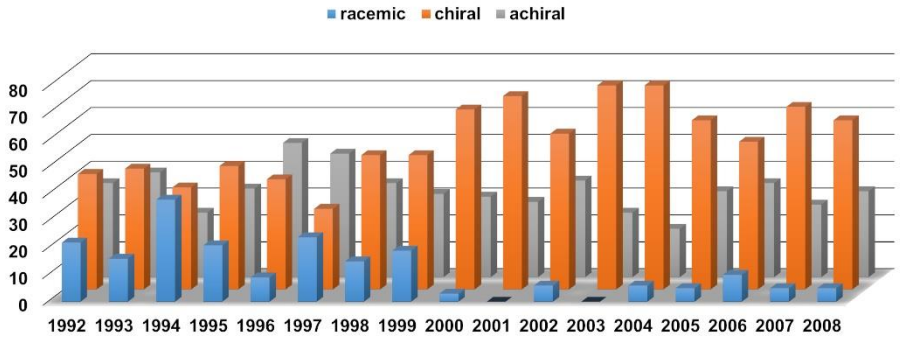

Figure 2-3. Annual distribution of chiral, achiral and racemic drugs (FDA-approved) from 1992 to 2008.

2.2. Chirality at the Solid State

When considering a chiral drug molecule instead of an achiral one different situations can occur at the solid state for a racemate. The crystallization outcome of a racemate (equal overall amounts of R and S) may lead to three different situations: a *racemic compound*, a *conglomerate* or a *solid-solution*. A racemic compound is a solid form wherein the enantiomers (R and S) are equally present in the crystal structure and well ordered. Most of the chiral molecules (90%) crystallize out as racemic compounds. A solid-solution also contains both (R) and (S)-enantiomer in a single given crystal, but in a completely arbitrary order. This situation is also called pseudoracemate and only occurs in about 1% of all cases. Last but not the least, one encounters *conglomerates* which are defined as a physical mixture of enantiopure crystals.[137] In this particular situation, the (R)-enantiomer crystallizes separately from the (S)-one. This is similar as physically mixing powders of both enantiomers. The occurrence of a conglomerate is about 5-10%.

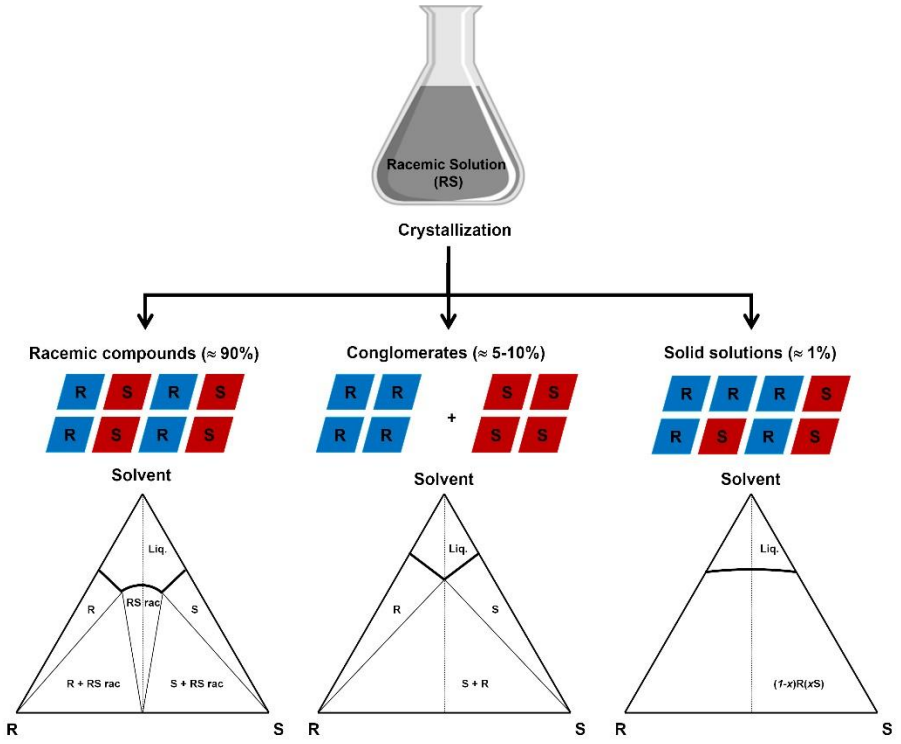

Figure 2-4. Possible crystallization outcomes of a racemate, their occurrence, and corresponding theoretical ternary phase diagram.

Generally, the solid-liquid equilibria related to each solid form are studied using a ternary phase diagram as illustrated in **Figure 2-4**. Preferential crystallization of only one enantiomer, can only be performed from a racemate, when a conglomerate behavior is observed. The identification of a such a conglomerate is commonly performed through XRPD, SCXRD, DSC, and chiral HPLC analysis. Besides, we want to point out that conglomerates (chiral crystals) crystallize out only under specific symmetries (65 space groups) with some symmetry operations not allowed. This chirality allows the use of the **S**econd **H**armonic **G**eneration[138] (SHG) to discriminate conglomerates from racemic compounds. SHG is a nonlinear optics technique based on the fact that centrosymmetric structures (most of the racemic compounds) cannot generate a SHG signal while non-centrosymmetric ones (e.g. conglomerates) do.

2.3. Chiral Resolution Routes

This section focuses on the physical ways to separate enantiomers from a racemic mixture. The four main methods used are *diastereoisomeric salt* formation, *chiral chromatography* and *preferential crystallization*.[139] This last method will be deeply studied in the following Section. The pitfall of those physical separations despite their efficiency is the loss of half of the matter i.e. the undesired enantiomer. However, the wrong enantiomer may be in some cases racemized through racemization methods in combination with the so-called physical resolution tools in order to achieve a nearly 100% yield.[140] **S**econd-**O**rder **A**symmetric **T**ransformation (SOAT) is such a tool that combines preferential crystallization and racemization.[141-142]

2.3.1. Chiral Chromatography

Like any other chromatography technique, this method consists in separating the components of a mixture (C) based on the intermolecular interactions between the components with the mobile (liquid or gas) and the stationary phase (solid). Depending on the affinity (Eq. 28 and 29) for one phase or the other (equilibrium), different elution times exist for each constituent. The higher the affinity for the stationary phase, the longer the retention time.[139]

$$\text{C (mobile phase)} \leftrightharpoons \text{C (stationary phase)} \qquad \text{(Eq. 28)}$$

$$K_a = \frac{[C]_{sp}}{[C]_{mp}} \qquad \text{(Eq. 29)}$$

Where K_a is the affinity constant, $[C]_{sp}$ and $[C]_{sp}$ are respectively the component concentration in the stationary and mobile phase. Many types of chromatography exist such as **G**as **C**hromatography (GC), **L**iquid **C**hromatography (LC), **T**hin-**L**ayer **C**hromatography (TLC), **C**apillary **E**lectro**C**hromatography (CEC), **S**ize-**E**xclusion **C**hromatography (SEC) and **I**on-**E**xchange **C**hromatography (IEC) according to the nature of the phases (mobile/stationary). In the context of this work, we used chiral **H**igh-**P**erformance **L**iquid **C**hromatography (HPLC), which comprises a chiral stationary phase.[143] The HPLC apparatus consists of:

- The *solvent tanks* containing the solvents of the mobile phase.
- The *pumps* allowing to mix the solvents and pushing the mobile phase through the column.
- The *injector* generally being an autosampler for automatic injection.

- The *column* which is the stationary phase. Its chemical nature dictates the effectiveness of the separation.
- The *UV-detector* recording the UV absorption of the eluted fractions over time.
- The *software* allowing to extract and treat data (chromatograms).

Different combinations between mobile and stationary phases exist according to their polarity. A stationary phase is called *normal-phase* when the mobile phase and the stationary phase are respectively apolar and polar. In the opposite case, one uses the term *reversed-phase*. Since the purpose here is to separate enantiomers the use of a **C**hiral **S**tationary **P**hase (CSP) is required. The basic material (support) for the column is in most cases a silica-based gel with chiral molecules (chiral selectors) grafted on the surface displaying specific interactions with each enantiomer.[131] **Figure 2-5** summarizes the most classical CSP used e.g.:

a) Brush-type (π-acidic or/and π-basic),
b) Polysaccharide-based (amylose/cellulose),
c) Chirobiotic-based (e.g. ristocetin)
d) Polyacrylamides
e) Ether crowns
f) Cyclodextrins

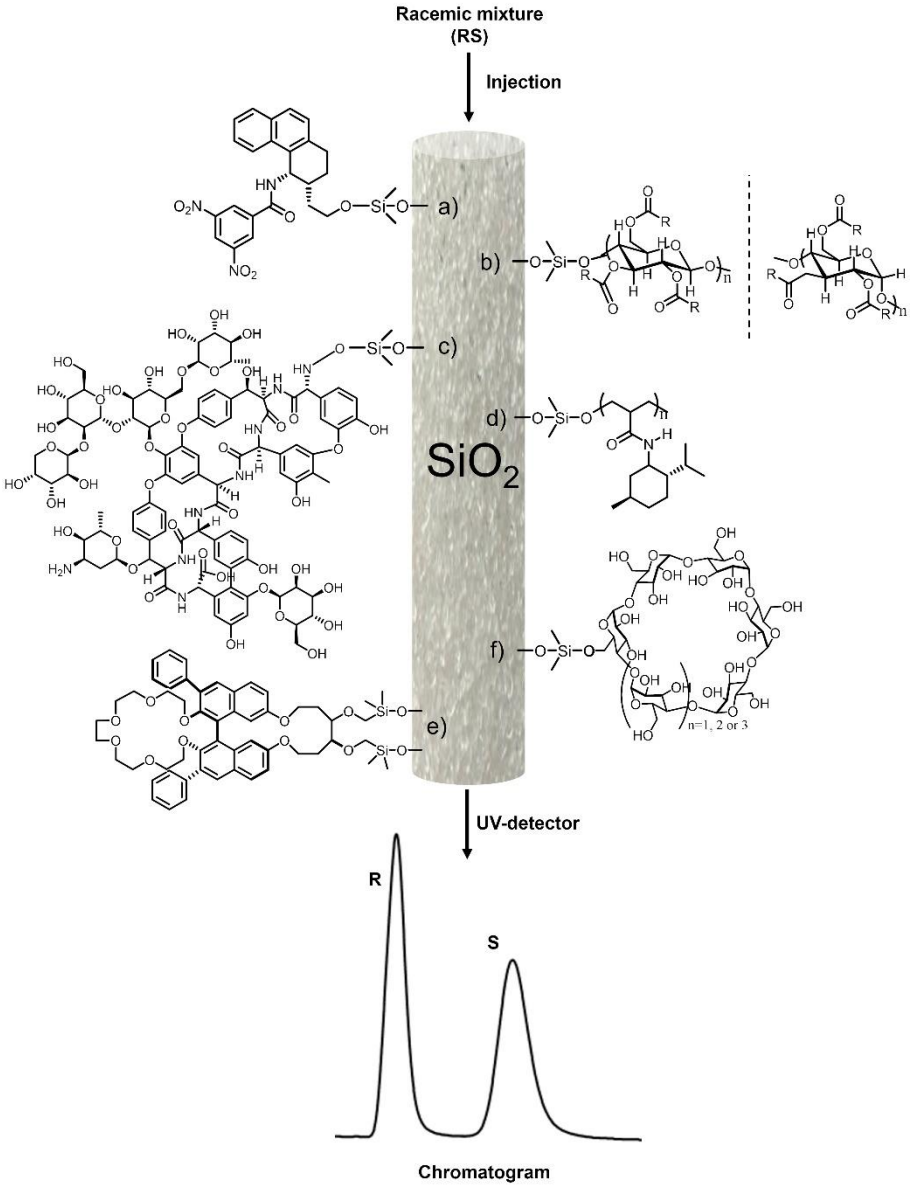

Figure 2-5. Examples of the main CSP grafted on a silica-based gel and the chromatographic separation principle.

2.3.2. Diastereoisomeric Salt Formation

This crystallization-based method is used to separate enantiomers from a racemic mixture and is wide-spread in industry. It is based on salt formation and hence only applicable to acidic/basic chiral molecules. The resolution is based on the fact that two diasteriomers have different properties. In practice, the acidic/basic racemic mixture reacts with a suitable resolving agent in order to form two diastereiosomeric salts as illustrated in **Figure 2-6**. The resolving agents are usually enantiopure acids or bases (carboxylic acids or amines) such as mandelic acid or amino acids derivatives. As diastereoisomeric salts (SR and RR) exhibit different physicochemical properties, they also have different solubilities. The principle behind the method is to crystallize the less soluble diastereoisomer only. The recovered salt can then be treated to recover the enantiopure target compound.[139, 144]

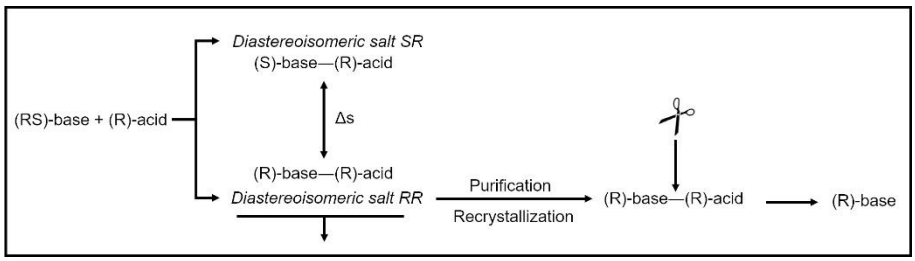

Figure 2-6. Schematic overview of a diastereoisomeric salt resolution process.

2.4. Emphasis on Preferential Crystallization as Chiral Resolution Tool

2.4.1. Crystal Growth and Nucleation

Prior to explaining PC we remind the basic concepts of any crystallization process from solution.[89] Crystallization is a process which consists in two parts. First of all, new crystals need to appear from solution, which is called nucleation. These nuclei then need to grow to full crystals. Two main types of nucleation exist as illustrated in **Figure 2-7**. Primary nucleation, where the first crystals appear spontaneously and secondary nucleation where nucleation is induced by other crystals of the same compound which are already present. For primary nucleation, one distinguishes, *heterogeneous nucleation* due to the presence of a foreign body (e.g. dust) from *homogenous* nucleation, where the nuclei appear in the bulk of the solution without any aid of external particles. *Secondary nucleation* is induced by nucleation spots

created by crystal seeds that act as a catalyst. Many mechanisms are proposed to explain this phenomenon as presented in **Figure 2-7** but they mainly relate to collisions of crystals between each other or with the paddle or the flask walls[145].

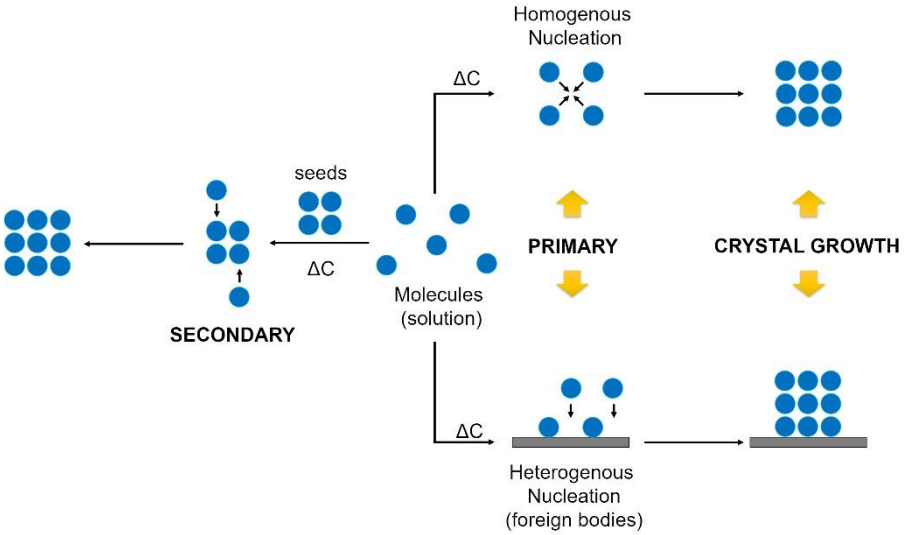

Figure 2-7. The different sorts of nucleation.

The nucleation rate as shown in **Figure 2-8** evolves exponentially with the temperature (T) and the supersaturation degree ($\beta = \Delta C$ or C/C^*) but once a too high ΔC reached, the solution viscosity becomes a constraint slowing down the nucleation rate. Turnbull and Fisher have proposed an additional free energy term in the exponential argument taking into account the viscosity.[146] A solution is supersaturated when the solute concentration overtakes its solubility limit. Indeed, depending on how important is the degree of supersaturation, many crystallization phenomena may occur as resumed in **Figure 2-8**.[147] A far too high supersaturated solution could lead to the amorphization or an oil formation due to the solution viscosity. The area of interest to work within is called the metastable zone width (MZW) and represents the zone between the spontaneous nucleation curve (kinetic event) and the thermodynamic solubility curve. In this region, the solution is able to keep its supersaturation (i.e. the solution remains homogeneous) but after a given time, called the induction time (inversely proportional to the nucleation rate), crystals are likely to appear from the supersaturation.[90] The MZW depends on the stirring route but mainly on the degree of supersaturation imposed to the system through evaporative and cooling rate or the use of antisolvent decreasing the overall solubility. In **Figure 2-8** the limit of spontaneous nucleation (primary) is called the Ostwald limit and depends on the working conditions (cooling and stirring). This meta-stable region may be divided in

two sub-regions according to the Ting and McCabe limit.[137, 148] The upper part is characterized by a high growth rate and secondary nucleation while the lower part is characterized by a slow crystal growth and low secondary nucleation. Having a kinetic control on a system (i.e. the supersaturation) is the key to manage properly a crystallization process which is very important from the industrial point of view.

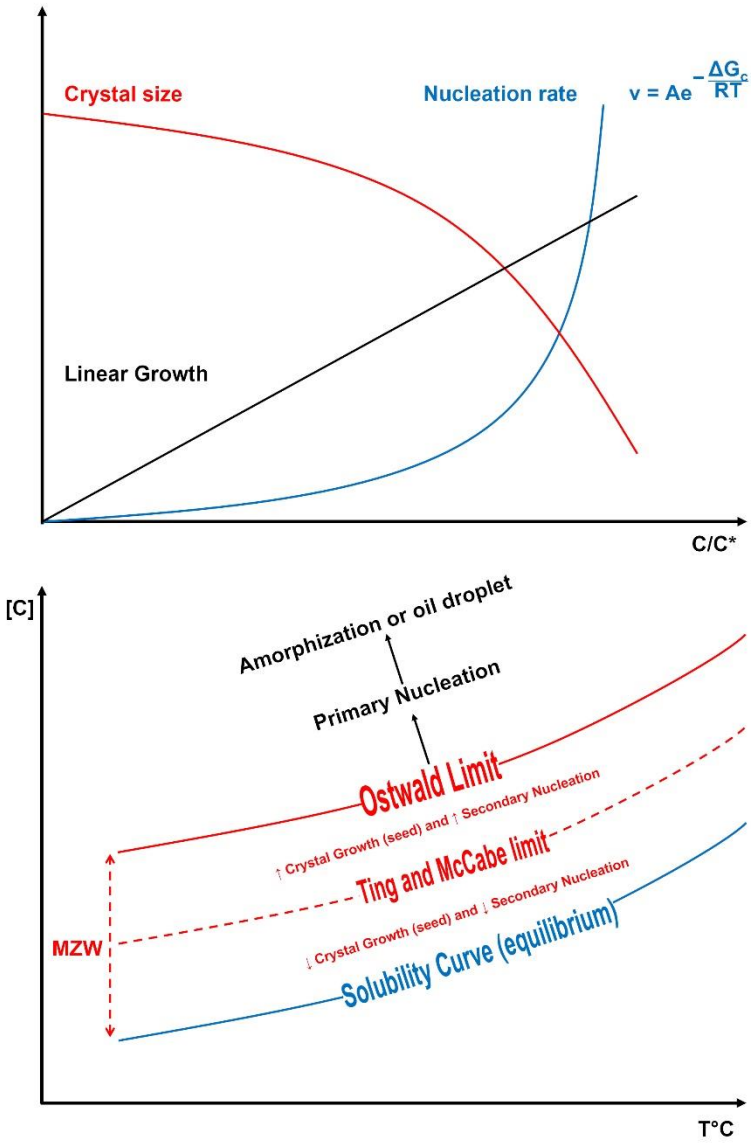

Figure 2-8. (top) Influence of the degree of supersaturation on the crystal size, the crystal growth and the nucleation rate and (bottom) effect of the degree of supersaturation on the possible crystallization events. ΔG_c is the critical free energy required to create the first nucleus.

2.4.2. Preferential Crystallization

To achieve chiral resolution through preferential crystallization (direct) or also called resolution by entrainment, the chiral molecule needs to crystallize out as a *conglomerate*.[131, 139] Practically, a supersaturated racemic solution achieved e.g. by cooling or solvent evaporation is seeded with the desired enantiopure crystals (R) in the metastable zone (STEP 1). Over time, the homochiral seeds grow and secondary nucleation leads to more crystals of the same enantiomer, leading to stereoselective crystallization (STEP 2) until the solubility of that enantiomer is reached. During STEP 2, filtration can be performed at any stage yielding a pure enantiomer. However, this process is not a thermodynamic process, as at any stage, the counter-enantiomer can also crystallize out considering the solution to be supersaturated with respect to this latter. In this case, the system evolves towards the equilibrium conglomerate suspension (STEP 3).[142, 149-150] An example of such a PC process is illustrated schematically on a ternary phase diagram (solvent, R and S enantiomers) in **Figure 2-9**.

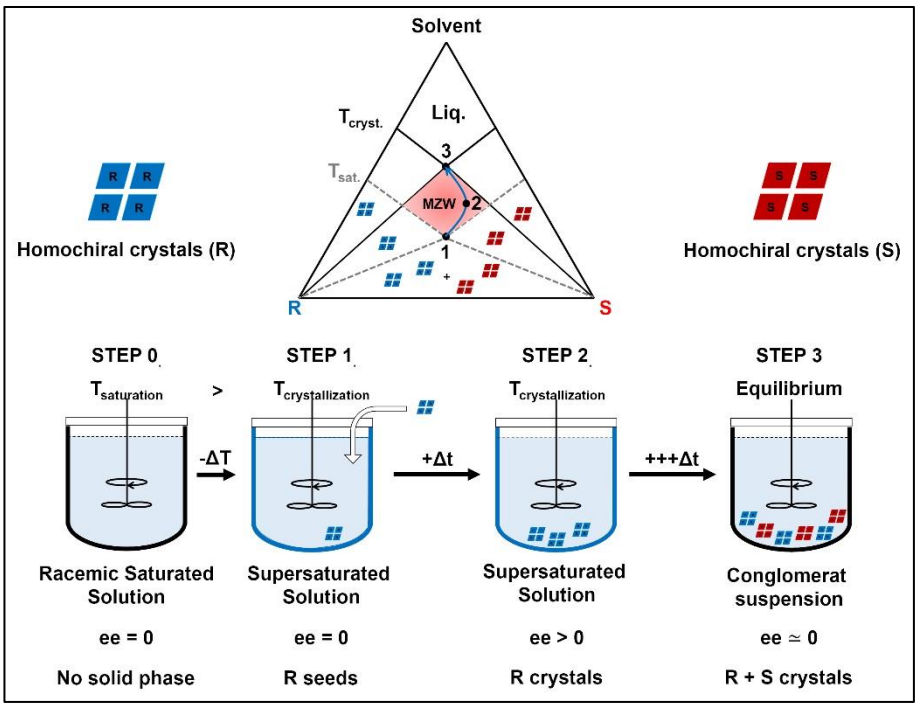

Figure 2-9. (top) Thereotical ternary phase diagram of a conglomerate (+ PC steps) and (below) the general concept of the Ideal Seeded Isothermal Preferential Crystallization (SIPC).

As mentioned in the previous section, many parameters affect the kinetics of crystallization and nucleation i.e. the supersaturation degree (ΔC), the working temperature range (T and ΔT), the stirring rate, the processing time (Δt) and the flow rate (Q) in case of coupled-reactors. To get an efficient preferential crystallization and a high-resolution index (RI, Eq. 41), purity (Pu, Eq. 42) and productivity (Pr, Eq. 43), the effect of all these parameters must be studied.[139, 151-152]

$$RI = \frac{m_{recovered} - m_{seed}}{m_{seed}} \quad \text{(Eq. 41)}$$

$$Pu^{(S)}(t) = \frac{m^{(S)}_{recovered}}{m^{(S)}_{recovered} + m^{(R)}_{recovered}} \quad \text{(Eq. 42)}$$

$$Pr^{(S)}(t) = \frac{m_{recovered} - m_{seed\,(S)}}{t \times 0.5 \times m_{racemate}} \quad \text{(Eq. 43)}$$

Where t is the processing time, $m_{recovered}$ is the total mass of enantiopure crystal recovered after the process time, m_{seed} the mass of the homochiral seed added to the supersaturation, $m_{racemate}$ the initial mass used to prepare the supersaturated solution. The absolute configuration of the solid phase is commonly followed over time by *in situ* sampling during the process and determined by chiral HPLC or optical rotation analysis. In case of a one-batch process, the enantiomeric excess (*ee*%) of the liquid phase may also be followed. Many varieties of the preferential crystallization process have been developed and are applied industrially. They all differ slightly in their set-up and operating parameters:[153]

- **I**deal **S**eeded **I**sothermal **P**referential **C**rystallization (SIPC): the supersaturation is achieved by fast cooling of a saturated solution from the saturation temperature (T_{sat}) to the crystallization one (T_{cryst}). The solution is then seeded at T_{cryst} with the homochiral crystal and the entrainment initiates.
- **I**deal **S**eeded **P**olythermic **P**referential **C**rystallization (S3PC): The saturated solution (T_{sat}) is seeded and a slow cooling rate is applied, allowing a smooth crystal growth and heterogeneous nucleation.

These two methods have been developed in the case of one single vessel. In **Figure 2-10**, a similar SIPC process may be set up with two coupled-vessels using a gear pump. Indeed, pumping of the mother liquor allows reducing the supersaturation of the counter enantiomer in each vessel (CPC2). Taking the process even further, **C**ontinuous **C**oupled **P**referential **C**rystallization with coupled-vessels (CCPC2 and CCPC3) requires a continuous feeding of a supersaturated racemic solution. These set-ups are shown in **Figure 2-10**. If a supersaturated racemic solution is continuously fed and both the vessels are coupled, a continuous entrainment may be set up and no

primary nucleation of the counter enantiomer will appear. It is the reason why renewing the mother liquor (crystal-free) in each vessel avoids at maximum the crystallization of the counter enantiomer in each vessel.[149, 153] Obviously, the flow rate has to be optimized to make the liquid phase renewal possible.

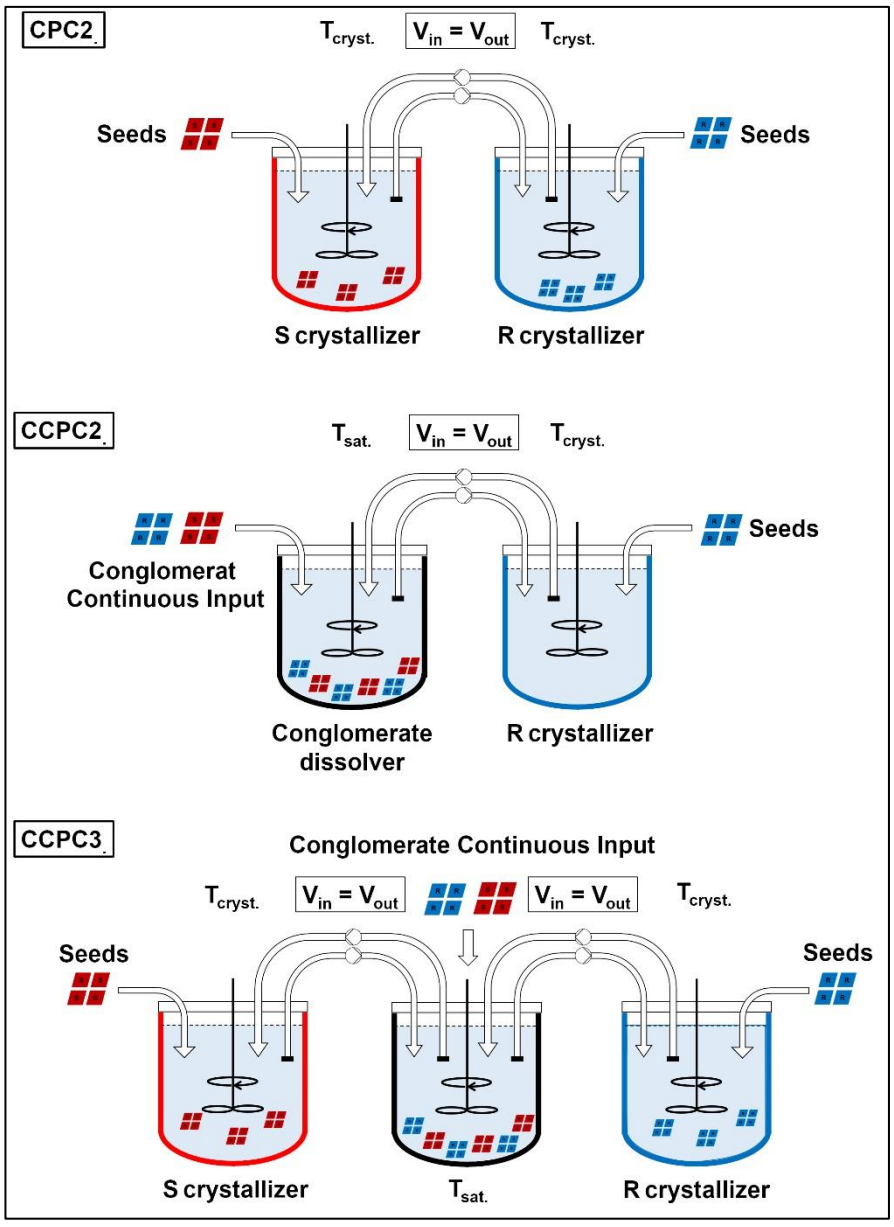

Figure 2-10. Schematic set-up of (top) a coupled-vessel PC (middle) a continuous PC with two coupled-vessels and (below) a continuous PC with three coupled-vessels.

References

This section gathers up all the bibliographic references required to draft chapters 1 and 2. It may overlap the literature references from the peer-reviewed papers (chapters 4, 5 and 6).

1. Stegemann, S.; Leveiller, F.; Franchi, D.; De Jong, H.; Lindén, H., When poor solubility becomes an issue: from early stage to proof of concept. *European journal of pharmaceutical sciences* **2007,** *31* (5), 249-261.
2. Bleicher, K. H.; Böhm, H.-J.; Müller, K.; Alanine, A. I., Hit and lead generation: beyond high-throughput screening. *Nature reviews Drug discovery* **2003,** *2* (5), 369-378.
3. Macarron, R.; Banks, M. N.; Bojanic, D.; Burns, D. J.; Cirovic, D. A.; Garyantes, T.; Green, D. V.; Hertzberg, R. P.; Janzen, W. P.; Paslay, J. W., Impact of high-throughput screening in biomedical research. *Nature reviews Drug discovery* **2011,** *10* (3), 188-195.
4. Takagi, T.; Ramachandran, C.; Bermejo, M.; Yamashita, S.; Yu, L. X.; Amidon, G. L., A provisional biopharmaceutical classification of the top 200 oral drug products in the United States, Great Britain, Spain, and Japan. *Molecular pharmaceutics* **2006,** *3* (6), 631-643.
5. Jouyban, A., *Handbook of solubility data for pharmaceuticals*. CRC Press: **2009**.
6. Mayr, L. M.; Bojanic, D., Novel trends in high-throughput screening. *Current opinion in pharmacology* **2009,** *9* (5), 580-588.
7. Pereira, D.; Williams, J., Origin and evolution of high throughput screening. *British journal of pharmacology* **2007,** *152* (1), 53-61.
8. Lipinski, C. A., Drug-like properties and the causes of poor solubility and poor permeability. *Journal of pharmacological and toxicological methods* **2000,** *44* (1), 235-249.
9. Lipinski, C. A.; Lombardo, F.; Dominy, B. W.; Feeney, P. J., Experimental and computational approaches to estimate solubility and permeability in drug discovery and development settings. *Advanced drug delivery reviews* **1997,** *23* (1-3), 3-25.
10. Amidon, G. L.; Lennernäs, H.; Shah, V. P.; Crison, J. R., A theoretical basis for a biopharmaceutic drug classification: the correlation of in vitro drug product dissolution and in vivo bioavailability. *Pharmaceutical research* **1995,** *12* (3), 413-420.

References

11. Lindenberg, M.; Kopp, S.; Dressman, J. B., Classification of orally administered drugs on the World Health Organization Model list of Essential Medicines according to the biopharmaceutics classification system. *European Journal of Pharmaceutics and Biopharmaceutics* **2004,** *58* (2), 265-278.
12. Singh, A.; Worku, Z. A.; Van den Mooter, G., Oral formulation strategies to improve solubility of poorly water-soluble drugs. *Expert opinion on drug delivery* **2011,** *8* (10), 1361-1378.
13. Pouton, C. W., Formulation of poorly water-soluble drugs for oral administration: physicochemical and physiological issues and the lipid formulation classification system. *European journal of pharmaceutical sciences* **2006,** *29* (3-4), 278-287.
14. Kawabata, Y.; Wada, K.; Nakatani, M.; Yamada, S.; Onoue, S., Formulation design for poorly water-soluble drugs based on biopharmaceutics classification system: basic approaches and practical applications. *International journal of pharmaceutics* **2011,** *420* (1), 1-10.
15. Di, L.; Fish, P. V.; Mano, T., Bridging solubility between drug discovery and development. *Drug Discovery Today* **2012,** *17* (9-10), 486-495.
16. Williams, H. D.; Trevaskis, N. L.; Charman, S. A.; Shanker, R. M.; Charman, W. N.; Pouton, C. W.; Porter, C. J., Strategies to address low drug solubility in discovery and development. *Pharmacological reviews* **2013,** *65* (1), 315-499.
17. Yalkowsky, S. H., *Solubility and solubilization in aqueous media*. American Chemical Society: **1999**.
18. Shargel, L.; Andrew, B.; Wu-Pong, S., *Applied biopharmaceutics & pharmacokinetics*. Appleton & Lange Stamford: **1999**.
19. Webster, G. K.; Bell, R. G.; Jackson, J. D., *Poorly soluble drugs: dissolution and drug release*. CRC Press: **2017**.
20. Williams III, R. O.; Watts, A. B.; Miller, D. A., *Formulating poorly water soluble drugs*. Springer: **2016**; Vol. 22.
21. Dokoumetzidis, A.; Macheras, P., A century of dissolution research: from Noyes and Whitney to the biopharmaceutics classification system. *International journal of pharmaceutics* **2006,** *321* (1-2), 1-11.
22. Anand, O.; Lawrence, X. Y.; Conner, D. P.; Davit, B. M., Dissolution testing for generic drugs: an FDA perspective. *The AAPS journal* **2011,** *13* (3), 328.
23. RS, S. A. T., 711 DISSOLUTION. **2011**.
24. Wen, H.; Park, K., *Oral controlled release formulation design and drug delivery: theory to practice*. John Wiley & Sons: **2011**.
25. Artursson, P.; Karlsson, J., Correlation between oral drug absorption in humans and apparent drug permeability coefficients in human intestinal epithelial (Caco-2) cells. *Biochemical and biophysical research communications* **1991,** *175* (3), 880-885.
26. Rubas, W.; Cromwell, M.; Shahrokh, Z.; Villagran, J.; Nguyen, T. N.; Wellton, M.; Nguyen, T. H.; Mrsny, R., Flux measurements across Caco-2

monolayers may predict transport in human large intestinal tissue. *Journal of pharmaceutical sciences* **1996,** *85* (2), 165-169.

27. Thiel-Demby, V. E.; Humphreys, J. E.; St. John Williams, L. A.; Ellens, H. M.; Shah, N.; Ayrton, A. D.; Polli, J. W., Biopharmaceutics classification system: validation and learnings of an in vitro permeability assay. *Molecular pharmaceutics* **2009,** *6* (1), 11-18.

28. Hilgers, A. R.; Conradi, R. A.; Burton, P. S., Caco-2 cell monolayers as a model for drug transport across the intestinal mucosa. *Pharmaceutical research* **1990,** *7* (9), 902-910.

29. Wouters, J.; Quéré, L., *Pharmaceutical salts and cocrystals*. Royal Society of Chemistry: **2011**.

30. Shan, N.; Perry, M. L.; Weyna, D. R.; Zaworotko, M. J., Impact of pharmaceutical cocrystals: the effects on drug pharmacokinetics. *Expert opinion on drug metabolism & toxicology* **2014,** *10* (9), 1255-1271.

31. Ishikawa, M.; Hashimoto, Y., Improvement in aqueous solubility in small molecule drug discovery programs by disruption of molecular planarity and symmetry. *Journal of medicinal chemistry* **2011,** *54* (6), 1539-1554.

32. Savjani, K. T.; Gajjar, A. K.; Savjani, J. K., Drug solubility: importance and enhancement techniques. *ISRN pharmaceutics* **2012,** *2012*.

33. Shekunov, B. Y.; York, P., Crystallization processes in pharmaceutical technology and drug delivery design. *Journal of crystal growth* **2000,** *211* (1-4), 122-136.

34. Singh, D.; Bedi, N.; Tiwary, A. K., Enhancing solubility of poorly aqueous soluble drugs: Critical appraisal of techniques. *Journal of pharmaceutical investigation* **2018,** *48* (5), 509-526.

35. Trask, A. V., An overview of pharmaceutical cocrystals as intellectual property. *Molecular pharmaceutics* **2007,** *4* (3), 301-309.

36. Bucci, R.; Magri, A.; Magri, A., Determination of diclofenac salts in pharmaceutical formulations. *Fresenius' journal of analytical chemistry* **1998,** *362* (7-8), 577-582.

37. Ip, D. P.; Brenner, G. S., Enalapril maleate. In *Analytical profiles of drug substances*, Elsevier: **1987**; Vol. 16, pp 207-243.

38. Martin, W.; Koselowske, G.; Töberich, H.; Kerkmann, T.; Mangold, B.; Augustin, J., Pharmacokinetics and absolute bioavailability of ibuprofen after oral administration of ibuprofen lysine in man. *Biopharmaceutics & drug disposition* **1990,** *11* (3), 265-278.

39. Highleyman, L., Amprenavir (Agenerase) receives FDA approval. Food and Drug Administration. *BETA: bulletin of experimental treatments for AIDS: a publication of the San Francisco AIDS Foundation* **1999,** *12* (2), 3.

40. Schouten, J., FDA approves 2 new protease inhibitors: ritonavir (Norvir) and Crixivan (Indinavir sulfate). Food and Drug Administration. *STEP perspective* **1996,** *8* (1), 7.

References

41. Shah, M. B.; Martin, J. E.; Schroeder, T. J.; First, M. R., THE EVALUATION OF THE SAFETY AND TOLERABILITY OF TWO FORMULATIONS OF CYCLOSPORINE: NEORAL AND SANDIMMUNE: A Meta-Analysis1. *Transplantation* **1999,** *67* (11), 1411-1417.

42. Solymosi, T.; Angi, R.; Basa-Dénes, O.; Ránky, S.; Ötvös, Z.; Glavinas, H.; Filipcsei, G.; Heltovics, G., Sirolimus formulation with improved pharmacokinetic properties produced by a continuous flow method. *European Journal of Pharmaceutics and Biopharmaceutics* **2015,** *94*, 135-140.

43. Dando, T. M.; Perry, C. M., Aprepitant. *Drugs* **2004,** *64* (7), 777-794.

44. Ling, H.; Luoma, J. T.; Hilleman, D., A review of currently available fenofibrate and fenofibric acid formulations. *Cardiology research* **2013,** *4* (2), 47.

45. Yoo, S. D.; Lee, S.-H.; Kang, E.; Jun, H.; Jung, J.-Y.; Park, J. W.; Lee, K.-H., Bioavailability of itraconazole in rats and rabbits after administration of tablets containing solid dispersion particles. *Drug development and industrial pharmacy* **2000,** *26* (1), 27-34.

46. Weuts, I.; Van Dycke, F.; Voorspoels, J.; De Cort, S.; Stokbroekx, S.; Leemans, R.; Brewster, M. E.; Xu, D.; Segmuller, B.; Turner, Y. T. A., Physicochemical properties of the amorphous drug, cast films, and spray dried powders to predict formulation probability of success for solid dispersions: etravirine. *Journal of pharmaceutical sciences* **2011,** *100* (1), 260-274.

47. Loftsson, T.; Brewster, M. E., Pharmaceutical applications of cyclodextrins: basic science and product development. *Journal of pharmacy and pharmacology* **2010,** *62* (11), 1607-1621.

48. Fenton, C.; Wellington, K.; Moen, M. D.; Robinson, D. M., Drospirenone/Ethinylestradiol 3mg/20µg (24/4 Day Regimen). *Drugs* **2007,** *67* (12), 1749-1765.

49. Kelly, A. L.; Gough, T.; Dhumal, R. S.; Halsey, S.; Paradkar, A., Monitoring ibuprofen–nicotinamide cocrystal formation during solvent free continuous cocrystallization (SFCC) using near infrared spectroscopy as a PAT tool. *International journal of pharmaceutics* **2012,** *426* (1-2), 15-20.

50. Alhalaweh, A.; Roy, L.; Rodriguez-Hornedo, N.; Velaga, S. P., pH-dependent solubility of indomethacin–saccharin and carbamazepine–saccharin cocrystals in aqueous media. *Molecular pharmaceutics* **2012,** *9* (9), 2605-2612.

51. Maeno, Y.; Fukami, T.; Kawahata, M.; Yamaguchi, K.; Tagami, T.; Ozeki, T.; Suzuki, T.; Tomono, K., Novel pharmaceutical cocrystal consisting of paracetamol and trimethylglycine, a new promising cocrystal former. *International journal of pharmaceutics* **2014,** *473* (1-2), 179-186.

52. Elder, D. P.; Holm, R.; de Diego, H. L., Use of pharmaceutical salts and cocrystals to address the issue of poor solubility. *International journal of pharmaceutics* **2013,** *453* (1), 88-100.

53. Sarma, B.; Chen, J.; Hsi, H.-Y.; Myerson, A. S., Solid forms of pharmaceuticals: Polymorphs, salts and cocrystals. *Korean Journal of Chemical Engineering* **2011,** *28* (2), 315-322.
54. Berge, S. M.; Bighley, L. D.; Monkhouse, D. C., Pharmaceutical salts. *Journal of pharmaceutical sciences* **1977,** *66* (1), 1-19.
55. Nie, H.; Byrn, S. R.; Zhou, Q., Stability of pharmaceutical salts in solid oral dosage forms. *Drug development and industrial pharmacy* **2017,** *43* (8), 1215-1228.
56. Serajuddin, A. T., Salt formation to improve drug solubility. *Advanced drug delivery reviews* **2007,** *59* (7), 603-616.
57. Hauss, D. J., Oral lipid-based formulations. *Advanced drug delivery reviews* **2007,** *59* (7), 667-676.
58. Pouton, C. W., Lipid formulations for oral administration of drugs: non-emulsifying, self-emulsifying and 'self-microemulsifying'drug delivery systems. *European journal of pharmaceutical sciences* **2000,** *11*, S93-S98.
59. Pouton, C. W.; Porter, C. J., Formulation of lipid-based delivery systems for oral administration: materials, methods and strategies. *Advanced drug delivery reviews* **2008,** *60* (6), 625-637.
60. Jannin, V.; Musakhanian, J.; Marchaud, D., Approaches for the development of solid and semi-solid lipid-based formulations. *Advanced drug delivery reviews* **2008,** *60* (6), 734-746.
61. Humberstone, A. J.; Charman, W. N., Lipid-based vehicles for the oral delivery of poorly water soluble drugs. *Advanced drug delivery reviews* **1997,** *25* (1), 103-128.
62. Porter, C. J.; Trevaskis, N. L.; Charman, W. N., Lipids and lipid-based formulations: optimizing the oral delivery of lipophilic drugs. *Nature reviews Drug discovery* **2007,** *6* (3), 231-248.
63. Mu, H.; Holm, R.; Müllertz, A., Lipid-based formulations for oral administration of poorly water-soluble drugs. *International journal of pharmaceutics* **2013,** *453* (1), 215-224.
64. Möschwitzer, J., Particle size reduction technologies in the pharmaceutical development process. *Am Pharm Rev* **2010,** *2010*, 54-59.
65. Möschwitzer, J.; Müller, R. H., New method for the effective production of ultrafine drug nanocrystals. *Journal of nanoscience and nanotechnology* **2006,** *6* (9-10), 3145-3153.
66. Chen, H.; Khemtong, C.; Yang, X.; Chang, X.; Gao, J., Nanonization strategies for poorly water-soluble drugs. *Drug discovery today* **2011,** *16* (7-8), 354-360.
67. Shegokar, R.; Müller, R. H., Nanocrystals: industrially feasible multifunctional formulation technology for poorly soluble actives. *International journal of pharmaceutics* **2010,** *399* (1-2), 129-139.
68. Voorhees, P. W., The theory of Ostwald ripening. *Journal of Statistical Physics* **1985,** *38* (1-2), 231-252.

References

69. Ostwald, W., Über die vermeintliche Isomerie des roten und gelben Quecksilberoxyds und die Oberflächenspannung fester Körper. *Zeitschrift für physikalische Chemie* **1900,** *34* (1), 495-503.

70. Verma, S.; Gokhale, R.; Burgess, D. J., A comparative study of top-down and bottom-up approaches for the preparation of micro/nanosuspensions. *International journal of pharmaceutics* **2009,** *380* (1-2), 216-222.

71. Sinha, B.; Müller, R. H.; Möschwitzer, J. P., Bottom-up approaches for preparing drug nanocrystals: formulations and factors affecting particle size. *International journal of pharmaceutics* **2013,** *453* (1), 126-141.

72. Paudel, A.; Worku, Z. A.; Meeus, J.; Guns, S.; Van den Mooter, G., Manufacturing of solid dispersions of poorly water soluble drugs by spray drying: formulation and process considerations. *International journal of pharmaceutics* **2013,** *453* (1), 253-284.

73. Abdelwahed, W.; Degobert, G.; Stainmesse, S.; Fessi, H., Freeze-drying of nanoparticles: formulation, process and storage considerations. *Advanced drug delivery reviews* **2006,** *58* (15), 1688-1713.

74. Van Eerdenbrugh, B.; Van den Mooter, G.; Augustijns, P., Top-down production of drug nanocrystals: nanosuspension stabilization, miniaturization and transformation into solid products. *International journal of pharmaceutics* **2008,** *364* (1), 64-75.

75. Loh, Z. H.; Samanta, A. K.; Heng, P. W. S., Overview of milling techniques for improving the solubility of poorly water-soluble drugs. *Asian journal of pharmaceutical sciences* **2015,** *10* (4), 255-274.

76. Salazar, J.; Ghanem, A.; Müller, R. H.; Möschwitzer, J. P., Nanocrystals: comparison of the size reduction effectiveness of a novel combinative method with conventional top-down approaches. *European journal of pharmaceutics and biopharmaceutics* **2012,** *81* (1), 82-90.

77. Leuner, C.; Dressman, J., Improving drug solubility for oral delivery using solid dispersions. *European journal of Pharmaceutics and Biopharmaceutics* **2000,** *50* (1), 47-60.

78. Chiou, W. L.; Riegelman, S., Pharmaceutical applications of solid dispersion systems. *Journal of pharmaceutical sciences* **1971,** *60* (9), 1281-1302.

79. Vasconcelos, T.; Sarmento, B.; Costa, P., Solid dispersions as strategy to improve oral bioavailability of poor water soluble drugs. *Drug discovery today* **2007,** *12* (23-24), 1068-1075.

80. Janssens, S.; Van den Mooter, G., Physical chemistry of solid dispersions. *Journal of Pharmacy and Pharmacology* **2009,** *61* (12), 1571-1586.

81. Van den Mooter, G., The use of amorphous solid dispersions: A formulation strategy to overcome poor solubility and dissolution rate. *Drug Discovery Today: Technologies* **2012,** *9* (2), e79-e85.

82. Vo, C. L.-N.; Park, C.; Lee, B.-J., Current trends and future perspectives of solid dispersions containing poorly water-soluble drugs. *European journal of pharmaceutics and biopharmaceutics* **2013,** *85* (3), 799-813.
83. Baghel, S.; Cathcart, H.; O'Reilly, N. J., Polymeric amorphous solid dispersions: a review of amorphization, crystallization, stabilization, solid-state characterization, and aqueous solubilization of biopharmaceutical classification system class II drugs. *Journal of pharmaceutical sciences* **2016,** *105* (9), 2527-2544.
84. Bekers, O.; Uijtendaal, E.; Beijnen, J.; Bult, A.; Underberg, W., Cyclodextrins in the pharmaceutical field. *Drug development and industrial pharmacy* **1991,** *17* (11), 1503-1549.
85. Rekharsky, M. V.; Inoue, Y., Complexation thermodynamics of cyclodextrins. *Chemical reviews* **1998,** *98* (5), 1875-1918.
86. Liu, L.; Guo, Q.-X., The driving forces in the inclusion complexation of cyclodextrins. *Journal of inclusion phenomena and macrocyclic chemistry* **2002,** *42* (1-2), 1-14.
87. Meyer, E. E.; Rosenberg, K. J.; Israelachvili, J., Recent progress in understanding hydrophobic interactions. *Proceedings of the National Academy of Sciences* **2006,** *103* (43), 15739-15746.
88. Del Valle, E. M., Cyclodextrins and their uses: a review. *Process biochemistry* **2004,** *39* (9), 1033-1046.
89. Beckmann, W., *Crystallization: basic concepts and industrial applications*. John Wiley & Sons: **2013**.
90. Mullin, J. W., *Crystallization*. Elsevier: **2001**.
91. Desiraju, G. R., Crystal engineering: a holistic view. *Angewandte Chemie International Edition* **2007,** *46* (44), 8342-8356.
92. Desiraju, G. R., Supramolecular synthons in crystal engineering—a new organic synthesis. *Angewandte Chemie International Edition in English* **1995,** *34* (21), 2311-2327.
93. Aakeröy, C. B.; Seddon, K. R., The hydrogen bond and crystal engineering. *Chemical Society Reviews* **1993,** *22* (6), 397-407.
94. Desiraju, G. R., Crystal engineering: from molecule to crystal. *Journal of the American Chemical Society* **2013,** *135* (27), 9952-9967.
95. Moulton, B.; Zaworotko, M. J., From molecules to crystal engineering: supramolecular isomerism and polymorphism in network solids. *Chemical Reviews* **2001,** *101* (6), 1629-1658.
96. Datta, S.; Grant, D. J., Crystal structures of drugs: advances in determination, prediction and engineering. *Nature Reviews Drug Discovery* **2004,** *3* (1), 42-57.
97. Blagden, N.; de Matas, M.; Gavan, P. T.; York, P., Crystal engineering of active pharmaceutical ingredients to improve solubility and dissolution rates. *Advanced drug delivery reviews* **2007,** *59* (7), 617-630.
98. Haleblian, J.; McCrone, W., Pharmaceutical applications of polymorphism. *Journal of pharmaceutical sciences* **1969,** *58* (8), 911-929.

References

99. Pudipeddi, M.; Serajuddin, A. T., Trends in solubility of polymorphs. *Journal of pharmaceutical sciences* **2005,** *94* (5), 929-939.

100. Caira, M. R., Crystalline polymorphism of organic compounds. In *Design of Organic Solids*, Springer: **1998**; pp 163-208.

101. Brittain, H. G., *Polymorphism in pharmaceutical solids*. CRC Press: **2016**.

102. Nývlt, J., The Ostwald rule of stages. *Crystal Research and Technology* **1995,** *30* (4), 443-449.

103. Bhatia, A.; Chopra, S.; Nagpal, K.; Deb, P. K.; Tekade, M.; Tekade, R. K., Polymorphism and its Implications in Pharmaceutical Product Development. In *Dosage Form Design Parameters*, Elsevier: **2018**; pp 31-65.

104. Chemburkar, S. R.; Bauer, J.; Deming, K.; Spiwek, H.; Patel, K.; Morris, J.; Henry, R.; Spanton, S.; Dziki, W.; Porter, W., Dealing with the impact of ritonavir polymorphs on the late stages of bulk drug process development. *Organic Process Research & Development* **2000,** *4* (5), 413-417.

105. Hilden, L. R.; Morris, K. R., Physics of amorphous solids. *Journal of pharmaceutical sciences* **2004,** *93* (1), 3-12.

106. Hancock, B. C.; Zografi, G., Characteristics and significance of the amorphous state in pharmaceutical systems. *Journal of pharmaceutical sciences* **1997,** *86* (1), 1-12.

107. Stillinger, F. H., Supercooled liquids, glass transitions, and the Kauzmann paradox. *The Journal of chemical physics* **1988,** *88* (12), 7818-7825.

108. Hodge, I. M., Enthalpy relaxation and recovery in amorphous materials. *Journal of Non-Crystalline Solids* **1994,** *169* (3), 211-266.

109. Babu, N. J.; Nangia, A., Solubility advantage of amorphous drugs and pharmaceutical cocrystals. *Crystal Growth & Design* **2011,** *11* (7), 2662-2679.

110. Griesser, U. J., The importance of solvates. *Polymorphism in the pharmaceutical industry* **2006**, 211-233.

111. Grothe, E.; Meekes, H.; Vlieg, E.; Ter Horst, J.; de Gelder, R. d., Solvates, salts, and cocrystals: a proposal for a feasible classification system. *Crystal Growth & Design* **2016,** *16* (6), 3237-3243.

112. Morissette, S. L.; Almarsson, Ö.; Peterson, M. L.; Remenar, J. F.; Read, M. J.; Lemmo, A. V.; Ellis, S.; Cima, M. J.; Gardner, C. R., High-throughput crystallization: polymorphs, salts, cocrystals and solvates of pharmaceutical solids. *Advanced drug delivery reviews* **2004,** *56* (3), 275-300.

113. Desiraju, G. R., Crystal and cocrystal. *CrystEngComm* **2003,** *5* (82), 466-467.

114. Dunitz, J. D., Crystal and cocrystal: a second opinion. *CrystEngComm* **2003,** *5* (91), 506-506.

115. Bond, A. D., What is a cocrystal? *CrystEngComm* **2007,** *9* (9), 833-834.

116. Etter, M. C.; MacDonald, J. C.; Bernstein, J., Graph-set analysis of hydrogen-bond patterns in organic crystals. *Acta Crystallographica Section B* **1990,** *46* (2), 256-262.

117. Schultheiss, N.; Newman, A., Pharmaceutical cocrystals and their physicochemical properties. *Crystal growth and design* **2009,** *9* (6), 2950-2967.
118. Vishweshwar, P.; McMahon, J. A.; Bis, J. A.; Zaworotko, M. J., Pharmaceutical cocrystals. *Journal of pharmaceutical sciences* **2006,** *95* (3), 499-516.
119. Bolla, G.; Nangia, A., Pharmaceutical cocrystals: walking the talk. *Chemical Communications* **2016,** *52* (54), 8342-8360.
120. Aakeröy, C. B.; Fasulo, M. E.; Desper, J., Cocrystal or salt: does it really matter? *Molecular Pharmaceutics* **2007,** *4* (3), 317-322.
121. Cruz-Cabeza, A. J., Acid–base crystalline complexes and the p K a rule. *CrystEngComm* **2012,** *14* (20), 6362-6365.
122. Childs, S. L.; Stahly, G. P.; Park, A., The salt− cocrystal continuum: the influence of crystal structure on ionization state. *Molecular pharmaceutics* **2007,** *4* (3), 323-338.
123. Duggirala, N. K.; Perry, M. L.; Almarsson, Ö.; Zaworotko, M. J., Pharmaceutical cocrystals: along the path to improved medicines. *Chemical Communications* **2016,** *52* (4), 640-655.
124. Braga, D.; Grepioni, F.; Lampronti, G. I.; Maini, L.; Turrina, A., Ionic cocrystals of organic molecules with metal halides: A new prospect in the solid formulation of active pharmaceutical ingredients. *Crystal Growth & Design* **2011,** *11* (12), 5621-5627.
125. Braga, D.; Grepioni, F.; Shemchuk, O., Organic–inorganic ionic cocrystals: a new class of multipurpose compounds. *CrystEngComm* **2018,** *20* (16), 2212-2220.
126. Buist, A. R.; Kennedy, A. R., Ionic cocrystals of pharmaceutical compounds: sodium complexes of carbamazepine. *Crystal growth & design* **2014,** *14* (12), 6508-6513.
127. Oliveira, M. A.; Peterson, M. L.; Klein, D., Continuously substituted solid solutions of organic cocrystals. *Crystal Growth and Design* **2008,** *8* (12), 4487-4493.
128. Lusi, M., Engineering crystal properties through solid solutions. *Crystal Growth & Design* **2018,** *18* (6), 3704-3712.
129. Nguyen, L. A.; He, H.; Pham-Huy, C., Chiral drugs: an overview. *International journal of biomedical science: IJBS* **2006,** *2* (2), 85.
130. Cahn, R. S.; Ingold, C.; Prelog, V., Specification of molecular chirality. *Angewandte Chemie International Edition in English* **1966,** *5* (4), 385-415.
131. Lin, G.-Q.; You, Q.-D.; Cheng, J.-F., *Chiral drugs: Chemistry and biological action*. John Wiley & Sons: **2011**.
132. Viedma, C.; Coquerel, G.; Cintas, P., Crystallization of chiral molecules. In *Handbook of Crystal Growth*, Elsevier: **2015**; pp 951-1002.
133. Blaser, H.-U., Chirality and its implications for the pharmaceutical industry. *Rendiconti Lincei* **2013,** *24* (3), 213-216.
134. Srisanga, S.; ter Horst, J. H., Racemic compound, conglomerate, or solid solution: phase diagram screening of chiral compounds. *Crystal Growth & Design* **2010,** *10* (4), 1808-1812.

References

135. Hutt, A. J.; Caldwell, J., The metabolic chiral inversion of 2-arylpropionic acids—a novel route with pharmacological consequences. *Journal of Pharmacy and Pharmacology* **1983,** *35* (11), 693-704.

136. De Camp, W. H., Chiral drugs: the FDA perspective on manufacturing and control. *Journal of pharmaceutical and biomedical analysis* **1993,** *11* (11-12), 1167-1172.

137. Sakai, K.; Hirayama, N.; Tamura, R., *Novel optical resolution technologies*. Springer: **2007**; Vol. 269.

138. Galland, A.; Dupray, V.; Berton, B.; Morin-Grognet, S.; Sanselme, M.; Atmani, H.; Coquerel, G. r., Spotting conglomerates by second harmonic generation. *Crystal Growth and Design* **2009,** *9* (6), 2713-2718.

139. Francotte, E.; Lindner, W., *Chirality in drug research*. Wiley-VCH Weinheim: **2006**; Vol. 33.

140. Guillot, M.; de Meester, J.; Huynen, S.; Collard, L.; Robeyns, K.; Riant, O.; Leyssens, T., Co-crystallization induced spontaneous deracemization: A general thermodynamic approach to deracemization. *Angewandte Chemie International Edition* **2020**.

141. Sheldon, R. A., *Chirotechnology: industrial synthesis of optically active compounds*. CRC press: **1993**.

142. Levilain, G.; Coquerel, G., Pitfalls and rewards of preferential crystallization. *CrystEngComm* **2010,** *12* (7), 1983-1992.

143. Kazakevich, Y. V.; Lobrutto, R., *HPLC for pharmaceutical scientists*. John Wiley & Sons: **2007**.

144. Kozma, D., *CRC handbook of optical resolutions via diastereomeric salt formation*. Crc Press: **2001**.

145. Myerson, A., *Handbook of industrial crystallization*. Butterworth-Heinemann: **2002**.

146. Turnbull, D.; Fisher, J. C., Rate of nucleation in condensed systems. *The Journal of chemical physics* **1949,** *17* (1), 71-73.

147. Tung, H.-H.; Paul, E. L.; Midler, M.; McCauley, J. A., *Crystallization of organic compounds: an industrial perspective*. John Wiley & Sons: **2009**.

148. Ting, H. H.; McCabe, W. L., Supersaturation and crystal formation in seeded solutions. *Industrial & Engineering Chemistry* **1934,** *26* (11), 1201-1207.

149. Rougeot, C.; Hein, J. E., Application of continuous preferential crystallization to efficiently access enantiopure chemicals. *Organic Process Research & Development* **2015,** *19* (12), 1809-1819.

150. Gonella, S.; Mahieux, J.; Sanselme, M.; Coquerel, G., Spotting a conglomerate is just halfway to achieving a preparative resolution by preferential crystallization. *Organic Process Research & Development* **2011,** *16* (2), 286-293.

151. Elsner, M. P.; Menéndez, D. F.; Muslera, E. A.; Seidel-Morgenstern, A., Experimental study and simplified mathematical description of preferential crystallization. *Chirality* **2005,** *17* (S1), S183-S195.

152. Elsner, M. P.; Ziomek, G.; Seidel-Morgenstern, A., Efficient separation of enantiomers by preferential crystallization in two coupled vessels. *AIChE journal* **2009,** *55* (3), 640-649.
153. Coquerel, G., Preferential crystallization. In *Novel optical resolution technologies*, Springer: **2006**; pp 1-51.

3. Aim of the Thesis

This thesis was performed under the supervision of Prof. Tom Leyssens, head of a Physical Chemistry laboratory in the Institute of Condensed Matter and Nanosciences (IMCN), UCLouvain. In such an environment, we focus on the crystal engineering of drugs and its application in processes as chiral resolution and/or deracemization. Indeed, crystal engineering as a tool to produce a new solid form e.g. a drug cocrystal offers many benefits like the enhanced physicochemical properties and potential patentability of the novel formulated drug. Recently, more effort has been provide combining crystal engineering and chiral resolution in particular by Preferential Cocrystallization.

In this context, this work therefore focuses on a pharmaceutical compound of interest, nefiracetam (Motiva®, Translon®). This molecule (**Figure 3-1**) is part of the racetam family of which Piracetam is likely the most known and exhibits a nootropic activity (cognitive enhancer).[1-2] Unlike Piracetam which is water-soluble, nefiracetam is fat-soluble. No significant studies on its solid-state forms and its physicochemical properties such solubility, dissolution rate or thermal stability were reported in literature.

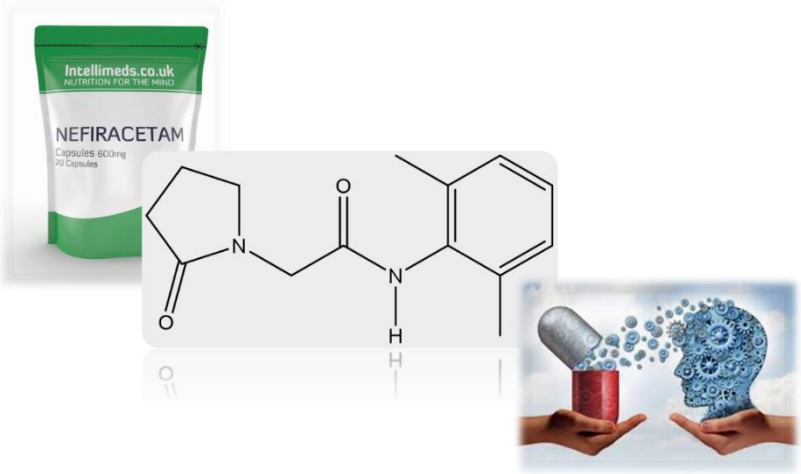

Figure 3-1. Nefiracetam (N-(2,6-dimethylphenyl)-2-(2-oxopyrrolidin-1-yl)acetamide)).

The goal of this thesis is therefore to:

- Identify and explore a large area of the new solid forms of nefiracetam through a *polymorph* and *solvate screening*. The novel forms are fully studied from a physicochemical properties point of view i.e. thermal stability and behavior in solution as the solubility and the dissolution rate. (**Chapter 4** – Published in *J.Pharm.Sci.*).

- Enhance certain physicochemical properties of nefiracetam such as solubility, dissolution rate or melting point using a *cocrystal engineering-based approach* comparing the efficiency of the novel solid forms with the parent one. (**Chapter 5** – Published in *Pharmaceutics*).

- To highlight the efficiency of the cocrystallization for the pharmaceutical field by applying the solid-state properties in the context of chiral resolution. The final chapter 6 focuses on the nefiracetam-mandelic acid system discovered during the cocrystal screening. This system is a cocrystal conglomerate forming system and is exploited to perform chiral resolution of mandelic acid through preferential cocrystallization. (**Chapter 6** – Published in *Cryst. Growth Des.*).

An overall conclusion and perspectives section (**Chapter 7**) closes this thesis and all the Supporting Materials related to the articles are given in **Chapter 8**.

References

1. Yoshii, M.; Watabe, S., Enhancement of neuronal calcium channel currents by the nootropic agent, nefiracetam (DM-9384), in NG108-15 cells. Brain research 1994, 642 (1-2), 123-131.

2. Fujimaki, Y.; Sudo, K.; Hakusui, H.; Tachizawa, H.; Murasaki, M., Single-and multiple-dose pharmacokinetics of nefiracetam, a new nootropic agent, in healthy volunteers. Journal of pharmacy and pharmacology 1992, 44 (9), 750-754.

4. Identifying, Characterizing, and Understanding Nefiracetam in Its Solid-State Forms: A Potential Antidementia Drug

Xavier Buol[a,] *, Koen Robeyns[a], Nikolay Tumanov[b], Johan Wouters[b] and Tom Leyssens[a,] *

[a]Institute of Condensed Matter and Nanosciences, UCLouvain, 1 Place Louis Pasteur, B-1348 Louvain-la-Neuve, Belgium

[b]Unité de Chimie Biologique et Structurale, Chemistry Department, UNamur, 61 rue de Bruxelles, B-5000 Namur, Belgium

4.1. Abstract

In this work, 3 hitherto unidentified solid state forms of the nootropic drug nefiracetam are identified: a monohydrate and 2 polymorphic phases of the anhydrate. These new forms were investigated from a structural and thermodynamic point of view to evaluate the possibility of using these forms in alternative formulations. Furthermore, their dissolution rate and solubility were compared.

Keywords: nefiracetam, solid state, polymorph, hydrate, dissolution, formulation.

4.2. Introduction

Hampering mental function decline is one of the pathways to battle dementia (Alzheimer or cerebrovascular dementia).[1-4] Cognitive-enhancers or nootropic agents have been developed to treat people with cerebral deficiencies (dementia or Alzheimer) that could occur due to a reduction of γ-aminobutyric acid (GABA) in the brain. GABA therefore forms the basic guide to the development of nootropic agents. Nefiracetam (N-(2,6-dimethylphenyl)-2-(2-oxopyrrolidin-1-yl)acetamide) known under the label DM-9384, Motiva or Translon is such an agent (**Figure 4-1**). Being a pyrolidone derivative, nefiracetam was produced and developed during the 90's by Daiichi Sankyo and marketed in 2002 in Japan.[5] Animal based studies suggest three main biological effects of DM-9384: a neurotransmitters release through Ca^{2+} channel

activation[6], an impact on the GABAergic, monoaminergic and cholinergic systems and an enhancement of the protein metabolism in the brain.[7-9] *In vitro* and *in vivo* toxicity studies did not show any mutagenic[10], antigenic[11], oncogenic or teratogenic[12] effects in laboratory animals. Nowadays, nefiracetam is still commercially available and administered to people with cognitive issues.

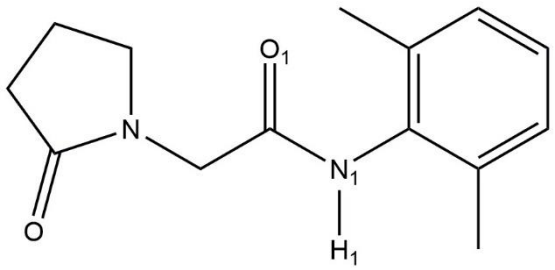

Figure 4-1. Molecular diagram of nefiracetam (N-(2,6-dimethylphenyl)-2-(2- oxopyrrolidin-1-yl)acetamide).

Owing to increasing molecular complexity, 75% of all new chemical entities show low water solubility and high permeability (BCS class II) or low water solubility and low permeability (BCS class IV).[13-14] Nefiracetam (BCS class II)[15-16] is part of the low water solubility compounds. As a consequence, the oral absorption and overall bioavailability of this molecule are low.[17] For compounds such as nefiracetam, alternative formulation tools need to be applied to increase their bioavailability.[18-19] One such solution is the use of an alternative solid phase showing a higher solubility or dissolution rate, such as the amorphous phase, metastable forms, polymorphic forms, salts (not applicable here), hydrates/solvates or cocrystals.[20-25] In this study, we set out to identify new solid-state forms of nefiracetam, and to study the potential of these forms as alternative formulation candidates. Up to now, only one single solid-state form of nefiracetam has been identified and characterized. Wang *et al.*[26] described an anhydrous form, which we will refer to as Form I (**FI**). Here, we identify two hitherto unknown polymorphs (**FII** and **FIII**) of this anhydrate as well as a hydrate form. All forms were structurally analyzed, their stability relationship studied and their dissolution profiles compared.

4.3. Material and Methods

Materials. Nefiracetam was sourced from Xiamen Top Health. All solvents used are commercially available from VWR. Solvents were used as received without any additional purification. Nefiracetam was purified by slurrying the compound overnight in ethyl acetate at room temperature after which the suspension was filtered and dried.

Evaporative Experiments were performed by dissolving 0.1 mmol of nefiracetam in a suitable amount of solvent in order to prepare undersaturated solution. Solutions were then left to evaporate (over periods ranging from 3 to 7 days) at room temperature, and solid phases retrieved.

Cooling Experiments were performed by preparing supersaturated nefiracetam solutions. An excess amount of nefiracetam was added to a given solvent at room temperature, and vials placed at 50 °C to achieve full dissolution. They were then stored at -15 °C or alternatively at 9 °C for three days. Solid phases were retrieved and analyzed.

Liquid Assisted Grinding (LAG) was performed with a Retsch MM 400 Mixer Mill, equipped with two grinding jars in which five 2 mL Eppendorf tubes can be installed. Typically, 0.2 mmol of nefiracetam is added to an Eppendorf, as well as 4 stainless steel beads and 10µl of solvent. The milling program is set for 90 minutes at 30Hz.

Slurrying Experiments were performed by preparing nefiracetam suspensions in selected solvents at 25 °C. The vials are sealed and the suspension left over 5 days at 25 °C while stirring at 700 rpm using a Cooling Thermomixer HLC. Solid phases were then retrieved and analyzed.

Single Crystal X-Ray Diffraction. Suitable crystals of nefiracetam **FI**, **FII** and **monohydrate** were analyzed using Single-Crystal X-Ray diffraction (SCXRD) with data measured on a "Rigaku Ultra X18S generator, FOX3D mirrors". The diffracted beams are detected by a "Mar345 image plate" using a MoKα (λ = 0.71 Å). Images have been integrated by "CrysalisPro". SCXRD data for nefiracetam **FIII** was collected on an Oxford Diffracton Gemini R Ultra diffractometer (Ruby CCD detector using CuKα radiation). Data reduction was carried out using the CrystAlisPro software package.[27] The resolution and the refinement by full-matrix least squares have been done using respectively SHELXT and SHELX-2014/728. Non-hydrogen atoms were refined anisotropically; H-atoms are added in calculated positions and allowed to ride on the parent atoms, with isotropic displacement factors set to 1.2 Ueq of the parent atoms (Uiso (H)= 1.5 Ueq (C) for methyl). The H-atoms of the methyl groups were allowed to undergo free rotation about the local threefold axis. Symmetry analysis and validation were carried out using PLATON.[29] Pictures were made using the molecular visualization software Mercury.[30] CCDC 1941789-1941791 contain the supplementary crystallographic data for this paper. The data can be obtained free of charge from The Cambridge Crystallographic Data Centre via www.ccdc.cam.ac.uk/structures.

Powder X-Ray Diffraction (XRPD) data were collected on a PANalytical Bragg-Brentano diffractometer, using Ni-filtered CuKα (λ = 1.54179 Å) at 45 kV and 30 mA with a X'Celerator detector. Each sample was analyzed between 4 and 40 ° in 2θ with a step size of ca. 0.0167° and a total scan time of 6min42s. Regarding the non-ambient

XRPD measurement (VT-XRPD), samples were heated using an "Anton Paar TTK-450" heating device and isotherms (15 minutes) were applied between each temperature step.

Differential Scanning Calorimetry (DSC) measurements were performed from 30 to 175 °C at a scanning rate of 5 °C.min^{-1} on a "Mettler Toledo DSC821e". Solid samples (weight of 6-7mg) were placed in an aluminum crucible with pierced sealed lids and nitrogen was used as purge gas with a flow rate of 50mL/min. Indium is used as a reference. Heats of fusion were extracted from thermograms obtained between 30 and 175 °C at a scanning rate of 2°C.min^{-1} on a "TA instrument DSC2500".

Thermogravimetric Analysis (TGA) was performed from 30 to 400 °C at a scanning rate of 10 °C.min^{-1} on a "Mettler Toledo TGA-STDA 851e". Solid samples (weight of 6-7 mg) were placed in aluminum oxide crucible and nitrogen was used as purge gas with a flow rate of 50 mL.min^{-1}.

Humidity Exposure experiments have been performed storing nefiracetam samples at 18 °C and 100% RH for different time ranges.

High Performance Liquid Chromatography (HPLC). Calibration lines were first built in order to dose the nefiracetam by correlating the area under the curve (AUC) and the concentration prepared with a linear equation. Nefiracetam samples were first diluted 1000x using an acetonitrile 1:1 water MilliQ (in volume) diluent. Nefiracetam concentrations were dosed using the following HPLC parameters: Device: Waters Alliance 2695; Column: Waters Sunfire C18, 4.6x100 mm, 3.5 µm; Detector : PDA 2998 (MaxPlot); T° = 40 °C; Injection volume: 10 µL; Flow : 1.2 mL.min^{-1}; Mobile phase A : H_2O + 0,1% H_3PO_4; Mobile Phase B : CH_3CN + 0,1% H_3PO_4; Gradient :0 min → 30 % B; 0.5 min → 30 % B; 4.5 min → 90 % B; 6.5 min → 90 % B; Stop time: 15 min.

Dissolution Experiments. FI and **monohydrate** were first ground using mortar and pestle to get approximately the same particle size range. Supersaturated nefiracetam **FI** and **monohydrate** solution in 50 mL of solvent at 0 °C and 10 °C were prepared in a 100mL flask using an "EasyMax 102 Advanced Synthesis Workstation" (manufactured by Mettler Toledo) equipped with a mechanical 150 rpm stirring and a temperature monitor. Basically, a large amount of powder is added to the solvent under constant stirring and temperature. The nefiracetam IR signature in solution is then recorded from 2800 cm^{-1} to 650 cm^{-1} every 15 seconds (50 scans) until the equilibrium using an online "React IR iC 10" by Mettler Toledo AutoChem with a 6.5 mm AgX DiComp Fiber Conduit probe as ATR crystal coupled to the crystallization reactor. ReactIR data are monitored with the iC IR software. The normalized IR intensities are then converted into molar concentration using the thermodynamic solubility determined by HPLC measurement.

4.4. Results and Discussion

4.4.1. Form Screening

A form screen (**Table 4-1**) was performed using evaporative, slurrying and cooling crystallization experiments (with 12 different solvents), grinding experiments, as well as crystallization experiments from the melt, and heating of solids. XRPD analysis was performed on each sample to identify the crystal form. Evaporation and cooling experiments in organic solvents always led to the formation of **FI** which is the form described by Wang *et al.*[26] However in water, we identified a so far unknown monohydrate of nefiracetam, both from the solvent evaporation as well as cooling crystallization experiment. Extended humidity exposure of **FI** (3-5 days at 100% RH) led also to the monohydrate formation. Once the monohydrate is formed, it remains stable over a long period of time (one week) under ambient temperature, pressure and relative humidity conditions. Traces of this form were also present when using, hygroscopic organic solvents such as alcohols. Surprisingly, when heating **FI** a transition to a second polymorph of nefiracetam (**FII**) occurred at temperatures around 135-145 °C. This solid-solid transition is clearly visible in the VT-XRPD experiments (**Figure 4-5**). Upon crystallization from the melt, a third polymorph (**FIII**) was observed. XRPD patterns clearly allow distinguishing the four solid forms of nefiracetam (**Figure 4-2**).

Table 4-1. Form screening performed on the nefiracetam and the relative solid forms.

Solvent	Crystallization method	Crystal form (XRPD)
Organic solvents[a]	Evaporation	FI
	Cooling	FI
	Grinding (LAG)	FI
	Slurrying	FI
Water	Evaporation	Monohydrate
	Cooling	Monohydrate
	Grinding (LAG)	Monohydrate
	Slurrying	Monohydrate
/	From the melt	FIII
/	Δ 135°C	FII

[a]ethyl acetate, methyl acetate, ethanol, methanol, 2-propanol, tetrahydrofuran, acetonitrile, toluene, acetone, chloroform and dichloromethane. /: no solvent used.

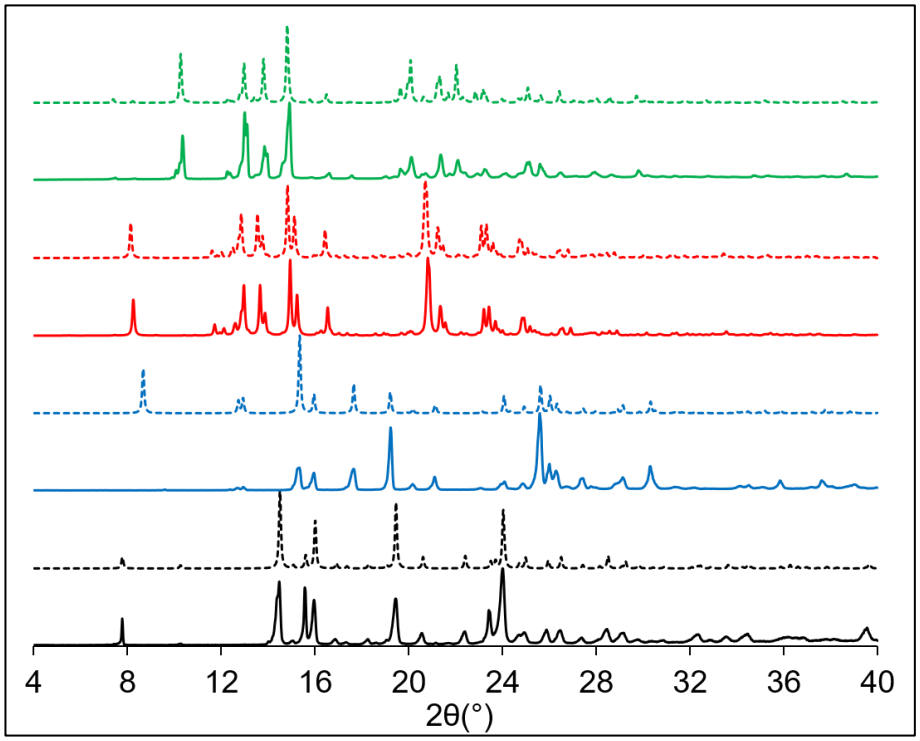

Figure 4-2. Simulated diffraction patterns from single crystals (dashed line) of all nefiracetam solid forms and comparison with the experimental ones (full line): nefiracetam **FIII** (green), nefiracetam **FII** (red), nefiracetam **FI** (black), and nefiracetam **monohydrate** (blue).

4.4.2. Structural Analysis

To investigate the structural differences between the different forms, single-crystals of each form were grown. Nefiracetam **FI** was obtained in organic solvents by evaporative and cooling crystallizations. The structure refined is identical to the one described by Wang *et al.*[26]. Single crystals of the monohydrate were grown from water. **FII** single crystals were prepared by heating a single crystal of nefiracetam **FI** to 135-145 °C and holding it there for 1h. This crystal was then quenched at room temperature and analyzed. This procedure needed to be repeated on a number of crystals to achieve a sufficient amount of diffraction data, as the single crystals of **FII** inherently reverted back to **FI** in a single crystal to single crystal transition. Concerning the third polymorphic form **FIII**, suitable single crystals were obtained from the melt, allowing this latter to cool to room temperature. As for the second polymorph, transition to **FI** ultimately occurred, so that the data set needed to be acquired over multiple samples in order to get sufficient diffraction data.

The simulated XRPD patterns overlap with the experimentally determined ones (**Figure 4-2**). **Table 4-2** and **4-3** summarize all single crystal data.

FI crystallizes in the orthorhombic $P2_12_12_1$ space group. Its crystal packing shows nefiracetam molecules in a stacked arrangement built up by intermolecular hydrogen bonds leading to a $C_1^1(4)$ pattern according to the Etter's graph notation[31-32] along the b-axis (**Figure 4-3a**). The hydrogen bond (N1-H1⋯ O1) involves the N-H group of the amide and the carbonyl group of the amide of a second molecule. In addition to this hydrogen bond, only dispersive interactions guide the molecular organization of this crystal structure and no π-stacking is observed. Nefiracetam **FII** crystallizes in the triclinic *P*-1 space group and the lattice clusters 12 molecules that display 6 non-equivalent amide-amide hydrogen bonds in the crystal structure. These hydrogen bonds form chains along the a-axis stacking the molecules in this direction as illustrated in **Figure 4-3c**. Values of distance and angle related to each intermolecular hydrogen bond are resumed in the Supporting Information. The third anhydrate **FIII** crystallizes in the monoclinic $P2_1/n$ space group and the lattice clusters 8 molecules wherein two non-equivalent hydrogen bonds lead the structural arrangement similar to the two other anhydrous forms, with parallel chains appearing along the a-axis (**Figure 4-3e**). Both **FII** and **FIII** display the same $C_2^2(8)$ hydrogen bond network, and a less dense crystalline lattice, compared to **FI**. Finally, the monohydrate is disordered around the pyrrolidone ring with only one orientation shown here for clarity. The hydrate crystallizes in the monoclinic *Pc* space group. In this structure, there are no intermolecular hydrogen bonds between two racetam molecules. Instead, water occupies sites between nefiracetam molecules and water hydrogens form an O-H⋯O hydrogen bond with the amide carbonyl group of a first nefiracetam molecule and an O-H⋯O hydrogen bond with the pyrrolidone carbonyl group of a second. Furthermore, the water oxygen atom interacts with the N-H group of the amide of a third nefiracetam molecule in a N-H⋯O bond. This leads to an extending $C_4^4(18)$ chain (**Figure 4-3g**) and reflects in a dense packing of 1.26 $g.cm^{-3}$ compared to 1.220 (**FI**), 1.205 (**FII**), 1.152 $g.cm^{-3}$ (**FIII**) for the three anhydrate forms.

Table 4-2. Main crystallographic data of all four solid forms of nefiracetam and refinement parameters (part 1).

Compound	nefiracetam **FI**[26]	nefiracetam **FII**
Empirical formula	$C_{14}H_{18}N_2O_2$	$C_{14}H_{18}N_2O_2$
Formula weight (g/mol)	246.30	246.30
Temperature (K)	293(2)	293(2)
Wavelength (Å)	0.71073	0.71073
Crystal system	Orthorhombic	Triclinic
Space group	$P2_12_12_1$	*P*-1
a, b, c (Å)	6.3390(13), 9.3130(19), 22.712(5)	9.0237(16),14.0397(13),32.872(6)
α, β, γ (°)	90, 90, 90	78.835(12),85.365(15),89.403(11)
Volume (Å³)	1340.8(5)	4072.3(11)
Z	4	12
Density calculated (Mg/m³)	1.220	1.205
Absorption coefficient (mm^{-1})	0.082	0.081
Crystal size (mm³)	/	/
F(000)	528	1584
Theta range for data collection(°)	1.79 to 25.96	2.837 to 18.845
Reflections collected	3018	9338
Independent reflections	1545 [R(int) = 0.0497]	5819 [R(int) = 0.1479]
Completeness to theta = 25.96°	100%	90.9%
Absorption correction	Psi-scan	/
Max. and min. transmission	0.9887 and 0.9657	/
Data / restraints / parameters	1545 / 0 / 170	5819 / 648 / 985
Goodness-of-fit on F^2	1.024	0.864
Final R indices [I>2sigma(I)]	R1 = 0.0459, wR2 = 0.1069	R1 = 0.0925, wR2 = 0.1138
R indices (all data)	R1 = 0.0727, wR2 = 0.1214	R1 = 0.2926, wR2 = 0.1556
Largest diff. peak and hole ($e.Å^{-3}$)	0.150 and -0.154 e.	0.136 and -0.153

Table 4-3. Main crystallographic data of all four solid forms of nefiracetam and refinement parameters (part 2).

Compound	nefiracetam **FIII**	nefiracetam **monohydrate**
Empirical formula	$C_{14}H_{18}N_2O_2$	$C_{14}H_{18}N_2O_2.H_2O$
Formula weight (g/mol)	246.30	264.32
Temperature (K)	297(2)	293(2)
Wavelength (Å)	0.71073	0.71073
Crystal system	Monoclinic	Monoclinic
Space group	$P2_1/n$	Pc
a, b, c (Å)	9.1823(10),21.497(3),14.624(2)	9.2368(7),7.3939(4),20.3969(14)
α, β, γ (°)	90,100.267(14),90	90,90.039,90
Volume (Å³)	2840.5(6)	1393.02 (17)
Z	8	4
Density calculated (Mg/m³)	1.152	1.260
Absorption coefficient (mm^{-1})	0.078	0.089
Crystal size (mm³)	/	0.35 x 0.30 x 0.20
F(000)	1056	568
Theta range for data collection(°)	2.439 to 23.292	2.930 to 25.342
Reflections collected	7989	8904
Independent reflections	3908 [R(int) = 0.0776]	4796 [R(int) = 0.0371]
Completeness to theta = 25.96°	95.3%	99.0 %
Absorption correction		Semi-empirical from equivalents
Max. and min. transmission	/	1.00000 and 0.78721
Data / restraints / parameters	3908 / 136 / 373	4796 / 198 / 476
Goodness-of-fit on F^2	1..092	1.076
Final R indices [I>2sigma(I)]	R1 = 0.0906, wR2 = 0.2227	R1 = 0.0662, wR2 = 0.1588
R indices (all data)	R1 = 0.1633, wR2 = 0.2864	R1 = 0.0836, wR2 = 0.1700
Largest diff. peak and hole ($e.Å^{-3}$)	0.370 and -0.270	0.182 and -0.197

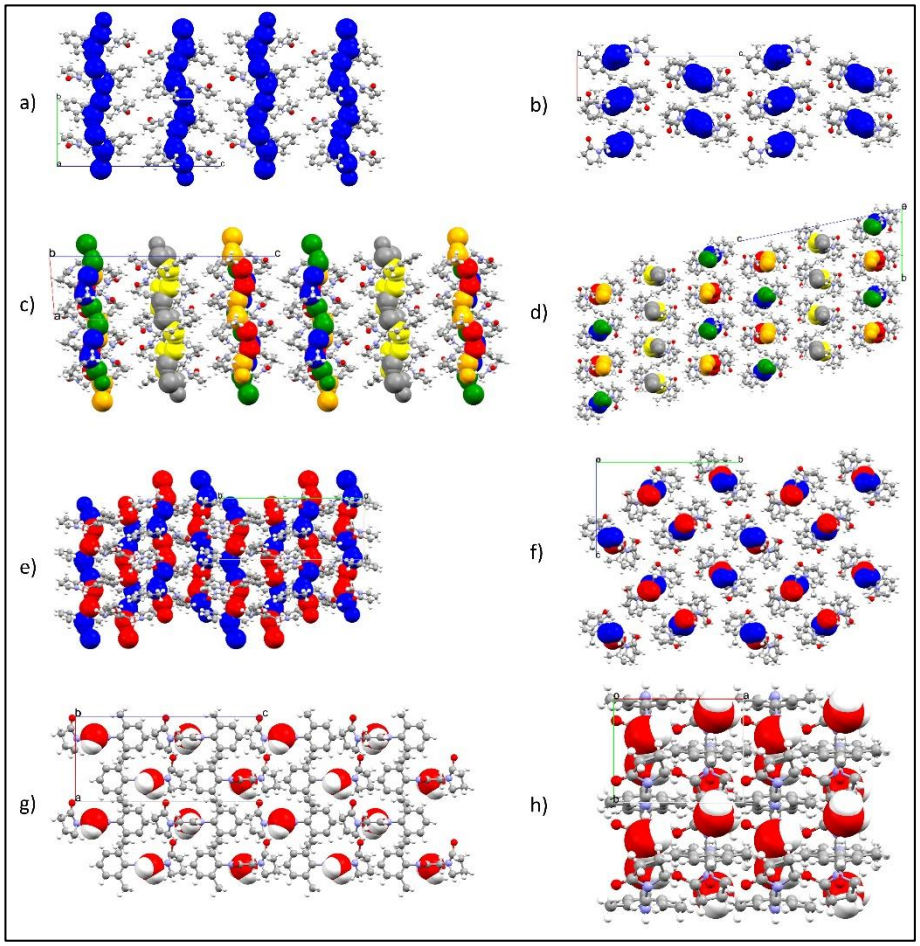

Figure 4-3. Molecular arrangements in crystalline (a) nefiracetam FI along the a-axis, (b) nefiracetam FI along the b-axis, (c) nefiracetam FII along the c-axis, (d) nefiracetam FII along the a-axis, (e) nefiracetam FIII along the b-axis, (f) nefiracetam FIII along the a-axis, (g) nefiracetam monohydrate along the b-axis, and (h) nefiracetam monohydrate along the c-axis. Regarding the anhydrous forms, hydrogen bonds (D-H⋯A) are highlighted using colored spacefill representation. Each spacefill color represents a nonequivalent amide-amide hydrogen bond. In case of the monohydrate, water is underlined using spacefill also.

4.4.3. Stability Relationship between the Different Forms

TGA data (**Figure 4-4**) shows nefiracetam to be stable up to 280 °C, temperature at which degradation occurs. The hydrate form shows a supplementary weight loss between 60 °C and 100 °C corresponding to the loss of one equivalent of water (the experimental weight loss (7%) fits the theoretical one (6.8%)).

Upon heating, FII shows a single melting endotherm at 150 °C. When heating **FI**, two successive endotherms can be observed, a first around 140 °C corresponds to the melting of **FI** combined with a recrystallization exotherm of **FII** and a second corresponding to the melting of **FII**. The VT-PXRD (**Figure 4-5**) performed on nefiracetam **FI** highlights a similar behavior with **FI** remaining stable up to 135 °C where a **FI** to **FII** transition occurs. Nefiracetam **FII** reverts back to **FI** within 2 days at room temperature. These results thus show an enantiotropic relationship between both forms.

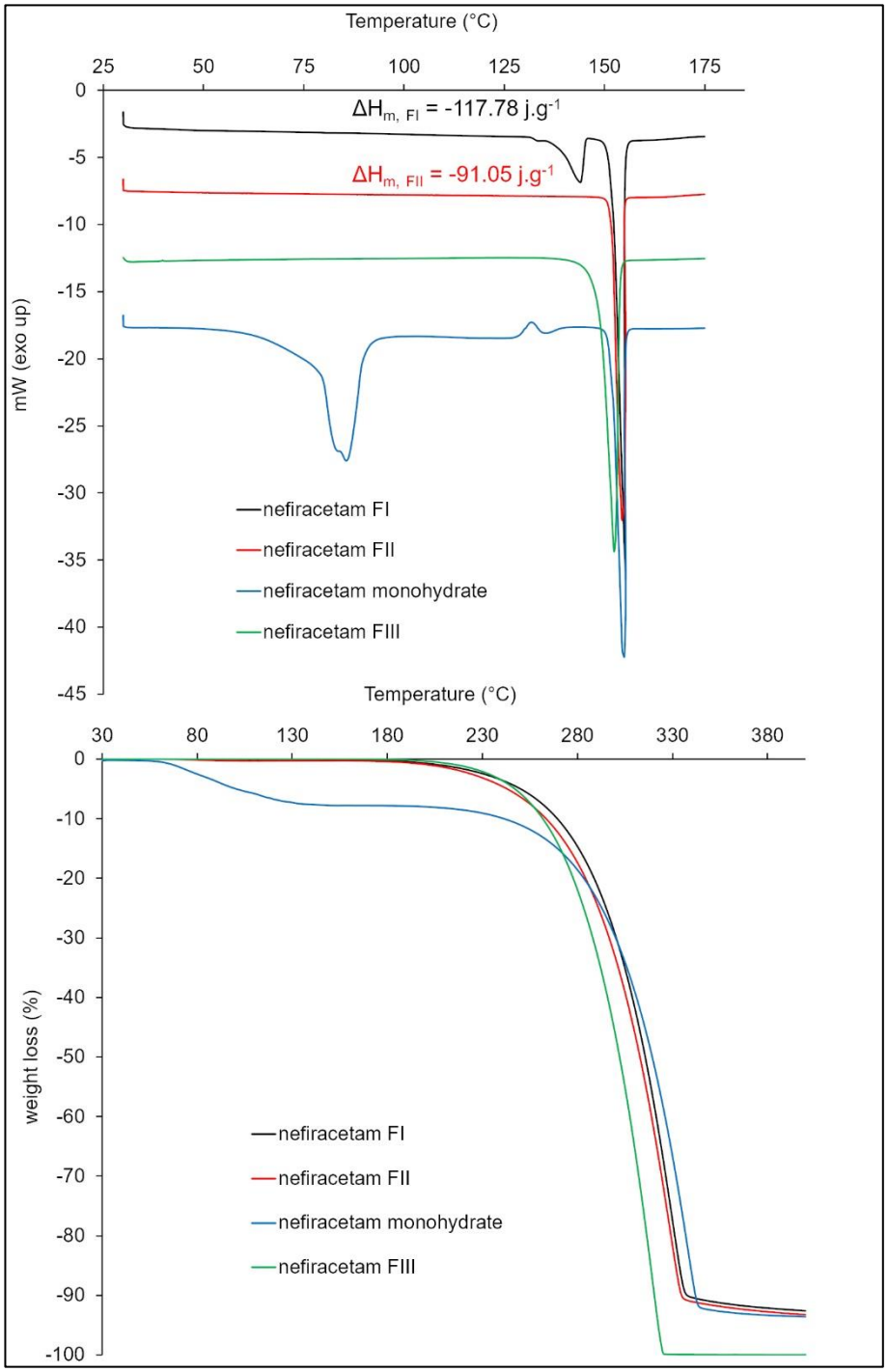

Figure 4-4. DSC (top) and TGA (bottom) curves of all four solid forms of nefiracetam.

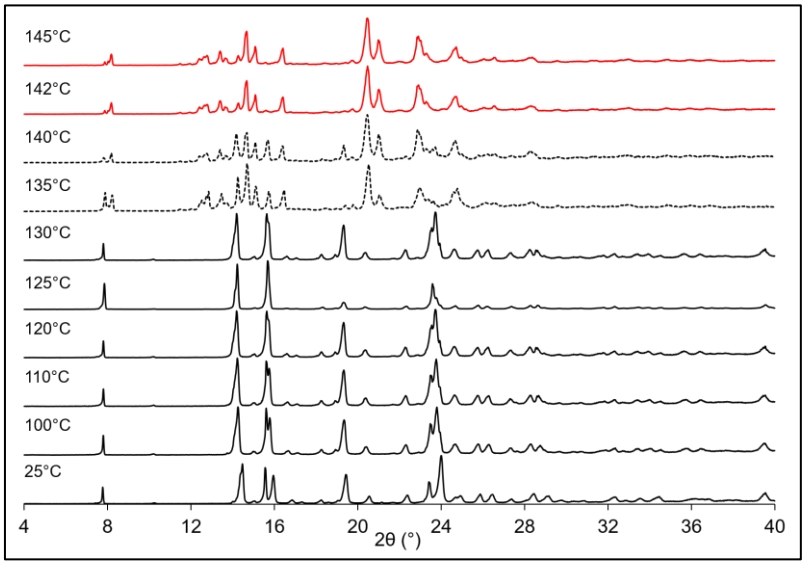

Figure 4-5. VT-XRPD pattern of nefiracetam FI. Nefiracetam FI and FII patterns are highlighted using a color code which is black (FI) and red (FII). The related dashed line highlights mixture of two forms.

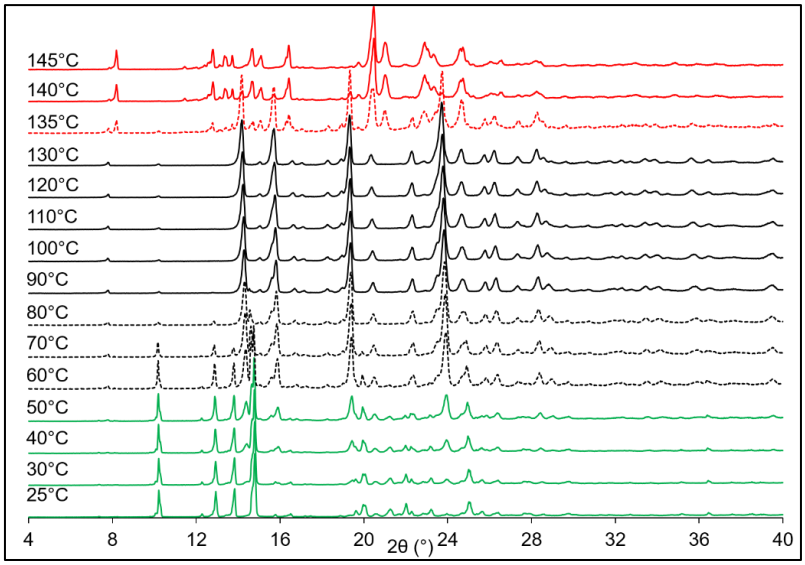

Figure 4-6. VT-XRPD pattern of nefiracetam FIII. Nefiracetam FI, FII and FIII patterns are highlighted using a color code which is black (FI), red (FII) and green (FIII). The related dashed line highlights mixture of two forms.

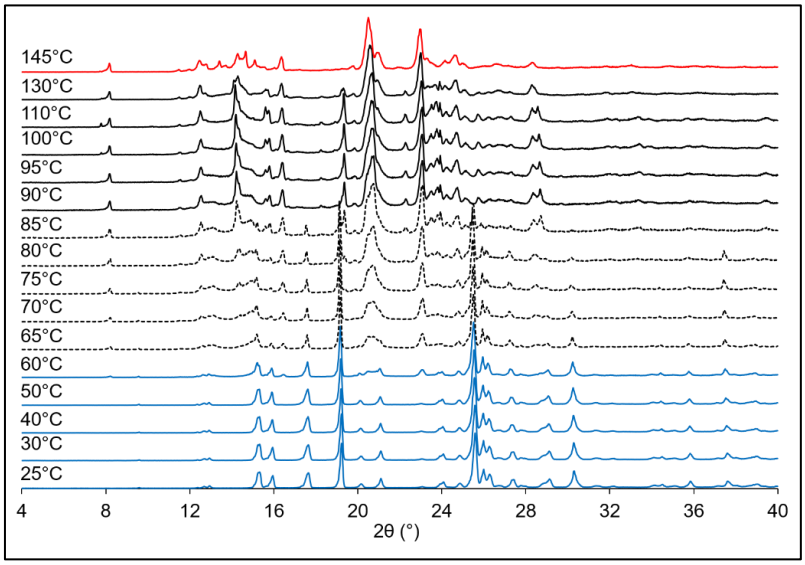

Figure 4-7. VT-XRPD pattern of nefiracetam monohydrate. Nefiracetam FI, FII and monohydrate patterns are highlighted using a color code which is black (FI), red (FII) and blue (monohydrate). The related dashed line highlights mixture of two forms.

FIII spontaneously recrystallizes from the melt if the cooling rate is low enough (2 °C.min^{-1} or less). Rapid cooling rates lead to an amorphous phase. When heating **FIII** in the DSC device, a melting endotherm overlapping the **FII** melting (150 °C) endotherm is observed. This could be due to **FII** and **FIII** having close lying melting points, or to an in situ solid-solid transformations occurring upon heating. Indeed, this form is only short living, as it completely reverts to **FI** within 16 hours at 25 °C as shown by XRPD. VT-XRPD highlights the **FIII** to **FI** conversion starting at 50-60 °C and suggests that the metastable form tends to rapidly transform at high temperature (**Figure 4-6**). DSC experiments performed on **FIII**, on the other hand, do not display such a conversion into **FI** but a direct transformation into **FII**). VT-XRPD of the hydrate (**Figure 4-7**) aligns with the DSC and TGA data, showing a dehydration at around 80 °C. After this loss of crystalline water, **FI** is observed (VT-XRPD), which aligns with the DSC measurement showing an endothermic event at around 135 °C attributed to the **FI-FII** solid-solid transition. In a summary, **Figure 4-8** highlights the transitions observed in this contribution between all solid forms of nefiracetam.

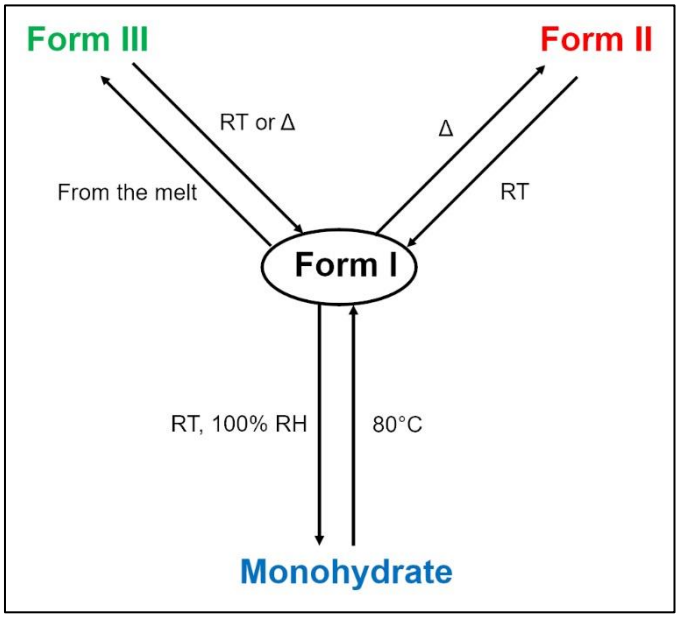

Figure 4-8. Transitions between nefiracetam crystalline forms.

FI is clearly the most stable form at ambient temperature, which is also in alignment with the more dense packing of this form. **FII** and **FI** were found to be enantiotropically[33] related. A transition point exists before the melting point of **FI** (140 °C), with **FI** being stable below this transition point and **FII** above this temperature. The enantiotropic relationship between **FI** and **FII** is also confirmed by the heat of fusion rule. The heat of melting of **FI** ($\Delta H_{m,FI}$) has been measured integrating the total heat exchanges from before the onset of melting of **FI** up to total fusion of **FII** (starting with a solid phase **FI** up to a liquid phase). Values of -117.78 $J.g^{-1}$ (-29.0 $kJ.mol^{-1}$) and -91.05 $J.g^{-1}$ (-22.43 $kJ.mol^{-1}$) are obtained respectively, for $\Delta H_{m,FI}$ and $\Delta H_{m,FII}$. Since **FII** has a higher melting point, this indeed aligns with Burger's Heat of Fusion Rule (HFR)[34-35] for an enantiotropic system, showing the system with the highest melting point to have the lowest heat of fusion. **Figure 4-9** represents it schematically in an energy diagram of **FI**, **FII** and the melt. **FIII** is identified as a meta-stable polymorph, which transforms rapidly into **FI** at room temperature or alternatively into **FII** upon heating.

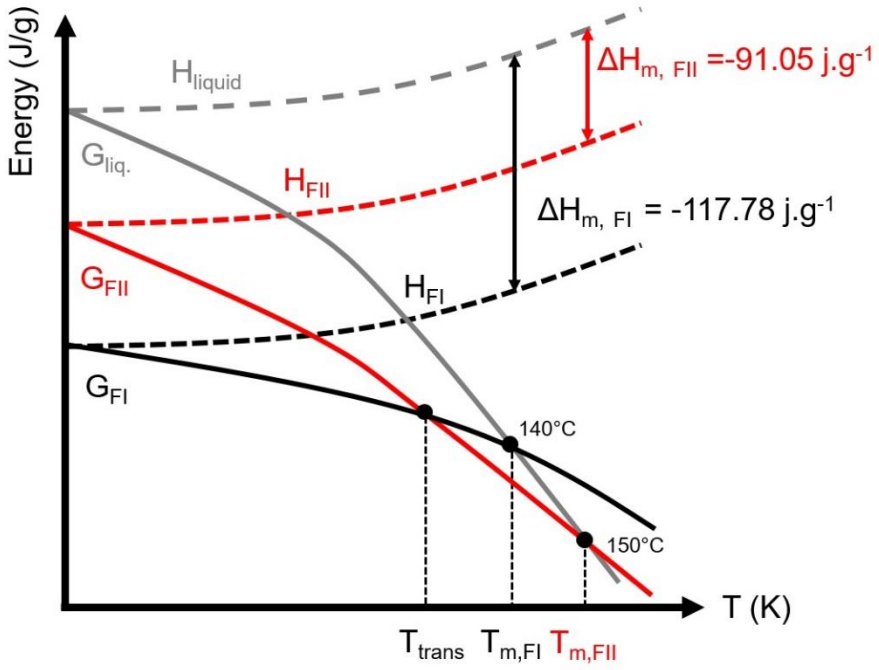

Figure 4-9. Energy diagram in case of enantiotropic system.

4.4.4. Dissolution Profile of the Nefiracetam Solid Forms in Organic Solvents

Figure 4-10 shows the dissolution curves of **FI** and monohydrate in ethanol and acetonitrile. Both solvents show a rapid dissolution of both forms, with solubility being reached in the first five minutes. In both solvents, the hydrate displays a significant solubility improvement. In ethanol, the nefiracetam **FI** solubility at the equilibrium is about 0.32 mM and about 0.40 mM using the monohydrate as solid form. However, this improvement appears to be stronger in acetonitrile where the solubility increases from 0.19 mM to 0.34 mM. Such a difference could be explained due to the difference in water activity which is solvent dependent. No solid transition between **FI** to/from the hydrate was observed in the 2h time-laps of the experiment. For the metastable form (**FIII**), it was not possible to determine the "apparent" or "kinetic" solubility[36-37], as the solvent-mediated conversion into the most stable form occurs too rapidly. As **FII** is only observable at high temperature, its dissolution behavior could not be evaluated.

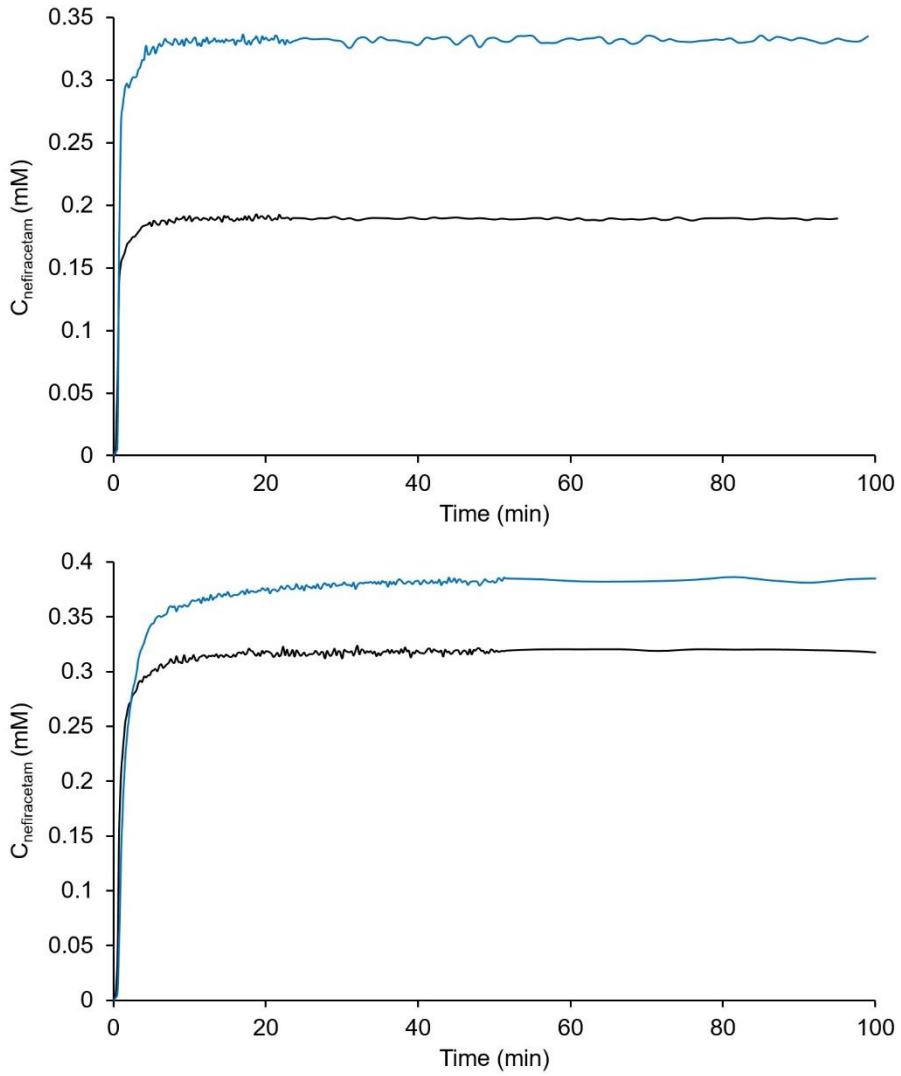

Figure 4-10. Dissolution curve of nefiracetam FI (black) and monohydrate (blue) in (above) acetonitrile at 10°C and (below) ethanol at 0°C. The nefiracetam concentration in solution is recorded over time.

4.5. Conclusion

Solid forms of the anti-dementia agent nefiracetam have been fully screened by evaporative, cooling, slurrying, grinding and melt crystallization methods. Three novel solid-state forms of nefiracetam have been discovered: a second and a third

anhydrous polymorph as well as a monohydrate. All the solid forms have been structurally and thermally analyzed and their respective stability evaluated. An enantiotropic relationship between the stable polymorph (**FI**) at room temperature and one of the other two forms (**FII**) has been highlighted. Since the solid-solid transition between the **FI** and **FII** forms occurs at high temperature and nefiracetam **FIII** only exists for a few hours after recrystallization from the melt, nefiracetam FI as well as the hydrated form appear as interesting candidates for formulation purposes. Long-term exposure (about 3 days) of **FI** at 100% RH reveals the formation of monohydrate with the monohydrate remaining stable at least for one week under ambient conditions. Dissolution experiments performed on the nefiracetam monohydrate solid form have shown that the hydrate form significantly improves the solubility in organic solvents. So given the appropriate formulation conditions this drug shows a case where two different solid forms could potentially successfully be marketed.

4.6. References

1. Watabe, S.; Yamaguchi, H.; Ashida, S.-i., DM-9384, a new cognition-enhancing agent, increases the turnover of components of the GABAergic system in the rat cerebral cortex. *European journal of pharmacology* **1993,** *238* (2-3), 303-309.
2. Otomo, E.; Takasu, Y.; Shiotani, T.; Hasegawa, K.; Honma, A., Agent for improving dementia. Google Patents: **1999**.
3. Otomo, E.; Takasu, Y., Use of nefiracetam for treating neurodegeneration. Google Patents: **2004**.
4. Hirata, K.; Katayama, S.; Yamazaki, K.; Fujikane, M.; Katayama, K., Electric field distribution of event-related potentials in stroke patients. *Brain topography* **1996,** *8* (3), 279-284.
5. Crespi, F., nefiracetam. Daiichi Seiyaku. *Current opinion in investigational drugs (London, England: 2000)* **2002,** *3* (5), 788-793.
6. Yoshii, M.; Watabe, S., Enhancement of neuronal calcium channel currents by the nootropic agent, nefiracetam (DM-9384), in NG108-15 cells. *Brain research* **1994,** *642* (1-2), 123-131.
7. Shimomura, K.; Shimada, M.; Hagiwara, M.; Harada, S.; Kato, M.; Furuhama, K., Testicular toxicity induced in dogs by nefiracetam, a neutrotransmission enhancer. *Reproductive Toxicology* **2004,** *18* (3), 423-430.
8. Nabeshima, T.; Tohyama, K.; Murase, K.; Ishihara, S.-i.; Kameyama, T.; Yamasaki, T.; Hatanaka, S.; Kojima, H.; Sakurai, T.; Takasu, Y., Effects of DM-9384, a cyclic derivative of GABA, on amnesia and decreases in GABAA and muscarinic receptors induced by cycloheximide. *Journal of Pharmacology and Experimental Therapeutics* **1991,** *257* (1), 271-275.
9. Suliman, N. A.; Taib, M.; Norma, C.; Moklas, M.; Aris, M.; Adenan, M. I.; Hidayat Baharuldin, M. T.; Basir, R., Establishing natural nootropics: recent

molecular enhancement influenced by natural nootropic. *Evidence-Based Complementary and Alternative Medicine* **2016,** *2016*.

10. Shimada, H.; Hattori, C.; Tanaka, N.; Takayama, S., Mutagenicity study of the new cognition-enhancing agent nefiracetam. *Arzneimittel-Forschung* **1994,** *44* (2A), 251-253.
11. Wagai, N.; Yamaguchi, F.; Hasegawa, T.; Takayama, S., Antigenicity study of the new cognition-enhancing agent nefiracetam. *Arzneimittel-Forschung* **1994,** *44* (2A), 247-250.
12. Watanabe, T.; Matsuhashi, K.; Shimada, M.; Harada, S.; Tawara, K.; Takayama, S., Reproductive toxicity studies of the new cognition-enhancing agent nefiracetam in rats and rabbits. *Arzneimittel-Forschung* **1994,** *44* (2A), 239-242.
13. Kawabata, Y.; Wada, K.; Nakatani, M.; Yamada, S.; Onoue, S., Formulation design for poorly water-soluble drugs based on biopharmaceutics classification system: basic approaches and practical applications. *International journal of pharmaceutics* **2011,** *420* (1), 1-10.
14. Di, L.; Fish, P. V.; Mano, T., Bridging solubility between drug discovery and development. *Drug Discovery Today* **2012,** *17* (9-10), 486-495.
15. Amidon, G. L.; Lennernäs, H.; Shah, V. P.; Crison, J. R., A theoretical basis for a biopharmaceutic drug classification: the correlation of in vitro drug product dissolution and in vivo bioavailability. *Pharmaceutical research* **1995,** *12* (3), 413-420.
16. Ku, M. S., Use of the biopharmaceutical classification system in early drug development. *The AAPS journal* **2008,** *10* (1), 208-212.
17. Savjani, K. T.; Gajjar, A. K.; Savjani, J. K., Drug solubility: importance and enhancement techniques. *ISRN pharmaceutics* **2012,** *2012*.
18. Dokoumetzidis, A.; Macheras, P., A century of dissolution research: from Noyes and Whitney to the biopharmaceutics classification system. *International journal of pharmaceutics* **2006,** *321* (1-2), 1-11.
19. Gardner, C. R.; Walsh, C. T.; Almarsson, Ö., Drugs as materials: valuing physical form in drug discovery. *Nature Reviews Drug Discovery* **2004,** *3* (11), 926.
20. Chen, J.; Sarma, B.; Evans, J. M.; Myerson, A. S., Pharmaceutical crystallization. *Crystal growth & design* **2011,** *11* (4), 887-895.
21. Elder, D. P.; Holm, R.; de Diego, H. L., Use of pharmaceutical salts and cocrystals to address the issue of poor solubility. *International journal of pharmaceutics* **2013,** *453* (1), 88-100.
22. Morissette, S. L.; Almarsson, Ö.; Peterson, M. L.; Remenar, J. F.; Read, M. J.; Lemmo, A. V.; Ellis, S.; Cima, M. J.; Gardner, C. R., High-throughput crystallization: polymorphs, salts, cocrystals and solvates of pharmaceutical solids. *Advanced drug delivery reviews* **2004,** *56* (3), 275-300.
23. Serajuddin, A. T., Salt formation to improve drug solubility. *Advanced drug delivery reviews* **2007,** *59* (7), 603-616.

24. Thipparaboina, R.; Kumar, D.; Chavan, R. B.; Shastri, N. R., Multidrug cocrystals: towards the development of effective therapeutic hybrids. *Drug Discovery Today* **2016,** *21* (3), 481-490.
25. Wouters, J.; Quéré, L., *Pharmaceutical salts and cocrystals*. Royal Society of Chemistry: **2011**.
26. Wang, P.-L.; Wang, H.-B.; Ding, W.-L.; Liu, Z.-Q.; Xing, Z.-T., N-(2, 6-Dimethylphenyl)-2-(2-oxo-1-pyrrolidin-1-yl) acetamide. *Acta Crystallographica Section E: Structure Reports Online* **2006,** *62* (9), o3838-o3839.
27. Rigaku, O. D., CrysAlisPro Software System, Version 1.171. 38.41 l, Rigaku Coorporation. Oxford, UK: **2015**.
28. Sheldrick, G. M., Crystal structure refinement with SHELXL. *Acta Crystallographica Section C: Structural Chemistry* **2015,** *71* (1), 3-8.
29. Spek, A. L., Structure validation in chemical crystallography. *Acta Crystallographica Section D: Biological Crystallography* **2009,** *65* (2), 148-155.
30. Macrae, C. F.; Bruno, I. J.; Chisholm, J. A.; Edgington, P. R.; McCabe, P.; Pidcock, E.; Rodriguez-Monge, L.; Taylor, R.; Streek, J. v. d.; Wood, P. A., Mercury CSD 2.0–new features for the visualization and investigation of crystal structures. *Journal of Applied Crystallography* **2008,** *41* (2), 466-470.
31. Etter, M. C.; MacDonald, J. C.; Bernstein, J., Graph-set analysis of hydrogen-bond patterns in organic crystals. *Acta Crystallographica Section B* **1990,** *46* (2), 256-262.
32. Bernstein, J.; Davis, R. E.; Shimoni, L.; Chang, N. L., Patterns in hydrogen bonding: functionality and graph set analysis in crystals. *Angewandte Chemie International Edition in English* **1995,** *34* (15), 1555-1573.
33. Park, K.; Evans, J. M.; Myerson, A. S., Determination of solubility of polymorphs using differential scanning calorimetry. *Crystal Growth & Design* **2003,** *3* (6), 991-995.
34. Burger, A.; Ramberger, R., On the polymorphism of pharmaceuticals and other molecular crystals. I. *Microchimica Acta* **1979,** *72* (3-4), 259-271.
35. Burger, A.; Ramberger, R., On the polymorphism of pharmaceuticals and other molecular crystals. II. *Microchimica Acta* **1979,** *72* (3-4), 273-316.
36. Nicoud, L.; Licordari, F.; Myerson, A. S., Estimation of the Solubility of Metastable Polymorphs: A Critical Review. *Crystal Growth & Design* **2018,** *18* (11), 7228-7237.
37. Nicoud, L.; Licordari, F.; Myerson, A. S., Polymorph control in batch seeded crystallizers. A case study with paracetamol. *CrystEngComm* **2019**.

5. Improving Nefiracetam Dissolution and Solubility Behavior using a Cocrystallization Approach

Xavier Buol[a, *], Koen Robeyns[a] , Camila Caro Garrido [a], Nikolay Tumanov[b], Laurent Collard [a], Johan Wouters[b] and Tom Leyssens[a, *]

[a]Institute Of Condensed Matter and Nanosciences, UCLouvain, 1 Place Louis Pasteur, B-1348 Louvain-la-Neuve, Belgium

[b]Namur Research Institute for Life Sciences (Narilis), Chemistry department, UNamur, 61 rue de Bruxelles, B-5000 Namur, Belgium

5.1. Abstract

In this work, we are the first to identify thirteen cocrystals of nefiracetam, a poor water-soluble nootropic compound. Three of which were obtained with the biocompatible cocrystallization agents citric acid, oxalic acid, and zinc chloride. These latter have been fully structurally and physically characterized and the solubility, dissolution rate, and stability were compared to that of the initial Active Pharmaceutical Ingredient (API).

Keywords: nefiracetam; solid state; cocrystals; solubility; dissolution rate; stability; formulation

5.2. Introduction

Nefiracetam, a member of the racetam family, is a nootropic compound typically administered as a cognitive enhancer. This API ((N-(2,6-dimethylphenyl)-2-(2-oxopyrrolidin-1-yl)acetamide)) known under the label DM-9384 is a pyrrolidone derivative produced and developed during the 90s by Daiichi Seiyaku and marketed in 2002 in Japan.[1-2] Recently, a polymorph screen by our group[3] revealed the existence of three anhydrous polymorphs as well as a monohydrate form with the asymmetric units illustrated in **Figure 5-1**. Different solid-state forms exhibit distinct physicochemical properties such as the melting point, hygroscopicity, solubility, dissolution rate, and bioavailability. Polymorphs **FI** and **FII** are enantiotropically related anhydrous forms with **FI** found to be the most stable form below 140 °C, whereas **FII** is stable above this temperature. Polymorph **FIII** is metastable at all

temperatures. Evaluation of the solubility/dissolution rate differences between polymorphs was challenging due to the fast solvent-mediated transformation of the meta-stable forms into the most stable one in suspension.

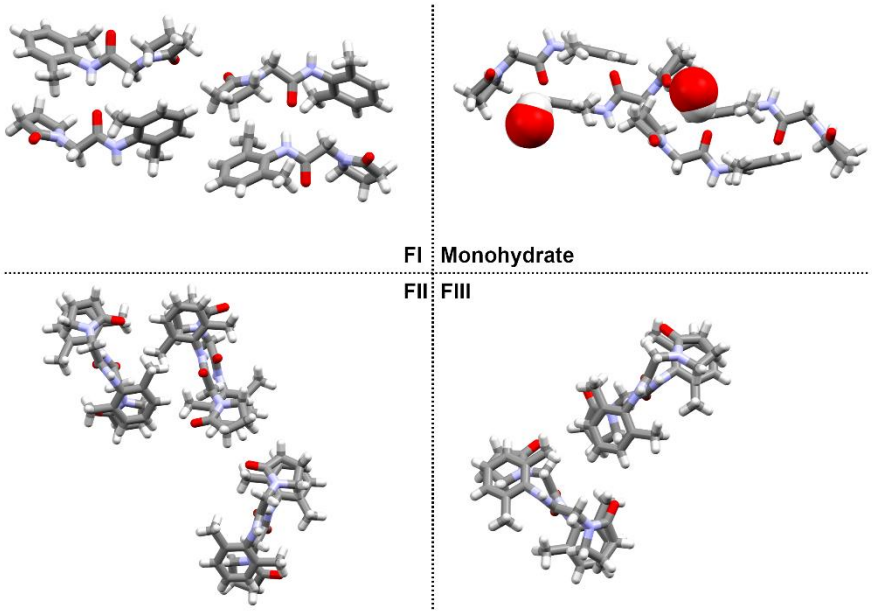

Figure 5-1. View of the crystal packing along the a-axis of each (pseudo)-polymorphic form of nefiracetam (*N*-(2,6-dimethylphenyl)-2-(2-oxopyrrolidin-1-yl)acetamide). The spacefill representation is used to highlight water molecules in the monohydrate crystal structure.

Therefore, as polymorphism does not seem a reasonable approach to modulate the dissolution/solubility properties of this drug, due to the high-energy state of its polymorphs, we here investigate an alternative approach focusing on cocrystal and ionic cocrystal formation.[4-8] Such an approach seems promising for nefiracetam as it is a non-ionizable, low-water soluble drug (Biopharmaceutical Classification System (BCS) II) displaying synthons favorable for hydrogen bonding and metal coordination, but rendering salt-formation impossible. The FDA guidance defines cocrystals as "solids that are crystalline materials composed of two or more different molecules generally held together by hydrogen bonds in the same crystal lattice".[9,10] Considering that the molecular components have to be neutral and solid under ambient conditions, salts and solvates can be excluded from this terminology.[9,11] Ionic cocrystals (ICC) can also be included in this category with the specificity that they result from cocrystallization between a neutral organic molecule and an inorganic salt through complexation.[12,13] In the last two decades, cocrystallization has been widely

used on pharmaceutical compounds to tune the solubility and/or dissolution rate[14-17], offering novel patentability opportunities in parallel.[18] Metaxalone cocrystals[19] with succinic acid, adipic acid, fumaric acid, salycilic acid, and maleic acid were patented in 2014 showing enhanced physicochemical properties. In 2006, Mc Amara *et al.*[20] showed that the use of glutaric acid as a cocrystallization agent increased the water solubility of a non-disclosed API about eighteen times and the dissolution rate about three times. Brittain *et al.*[21-23] recently reported the increasing importance of pharmaceutical cocrystals in the last decade.

5.3. Material and Methods

Starting Materials. Nefiracetam was purchased from Xiamen Top Health (Fujian, China). The solvents were sourced from VWR (Haasrode, Belgium) and directly used without any purification steps. In the cases of ethyl acetate and acetonitrile, they were dried using a dessicant as calcium hydride (CaH_2). nefiracetam was purified by a slurry crystallization in ethyl acetate (room temperature, ca. 300 rpm and overnight) and the solid phase was filtrated, washed, and dried. All coformers were commercially available from Alfa Aesar (Kandel, Germany), Acros Organics (Leuven, Belgium), TCI (Zwijndrecht, Belgium) , and Merck (Overijse, Belgium) and used as received.

Nefiracetam Cocrystal Screening. A total of 133 cocrystallization agents typically used in cocrystallization efforts were selected among carboxylic acids, amides, sugars, inorganic salts and amino acids, other racetams, and profens. The cocrystal screening was performed through liquid assisted grinding (LAG) using a MM 400 Mixer Mill grinder manufactured by Retsch (Haan, Germany). The device is equipped with two grinding cells in which five 2 mL Eppendorf tubes can be set. To do so, equimolar amounts of nefiracetam (0.2 mmol) and coformer (0.2 mmol) were weighted in an Eppendorf, and 4–5 stainless steel beads and 10 µL of solvent (methanol) were appended. Once the jars were filled, the milling ran for 90 min at 30 Hz.

For the three cocrystals studied in more detail in this work, these experiments were repeated using 12 different solvents in the LAG experiments as the nature of the solvent has been shown to impact on the outcome of such an experiment.[24,25] Using a 2:1 nefiracetam/acid ratio for oxalic and citric acid and a 1:1 ratio for $ZnCl_2$. The tested solvents were ethanol (EtOH), methanol, acetonitrile (MeCN), tetrahydrofuran, acetone, dichloromethane, chloroform, ethyl acetate, methyl acetate, diethylether, 2-propanol, and water, using approximately 10 µL of solvent.

Single Crystal Growth. Single crystals were mainly obtained from evaporative experiments. Nefiracetam and coformer were added in the molar ratio found in the cocrystal, and solids dissolved by the addition of a sufficient amount of solvent. Solutions were then left to evaporate slowly (over periods ranging from three to seven

days) at room temperature, and single crystals retrieved. A 2:1 nefiracetam-citric acid cocrystal Form I (**NCA**) and 1:1:1 nefiracetam-zinc chloride-water ionic cocrystal hydrate (**NZCW**) suitable crystals were obtained from ethyl acetate, while the 2:1 nefiracetam-oxalic acid cocrystal (**NOA**) crystals were harvested from ethyl acetate and tetrahydrofuran. Cooling experiments were performed by preparing supersaturated nefiracetam and coformer solutions. An excess of nefiracetam and coformer (equimolar) was added to a given solvent volume at room temperature, and the vials were placed at 15 °C below the related solvent boiling point until the full dissolution. Once the full dissolution was achieved, they were then stored at −15 or 9 °C in the case of water. Solid phases were then retrieved and analyzed. The 1:1 nefiracetam-zinc chloride ionic cocrystal (**NZC**) suitable crystals were obtained from a cooling crystallization in dried acetonitrile.

Nefiracetam Cocrystal Bulk Material Preparation. The bulk material for dissolution testing was prepared through crystallization from the solution. To identify an appropriate solvent, slurrying experiments were performed by placing excess amounts of nefiracetam-coformer in suspension in different solvents at 25 °C. Vials were sealed and the suspension was left over three days at 25 °C stirring at 700 rpm using a Cooling Thermomixer HLC manufactured by Ditabis (Pforzheim, Germany). Each vial was seeded with all possible solid forms (nefiracetam and cocrystal) after 2 h of stirring. After three days, solid phases were retrieved and analyzed. The 12 aforementioned solvents were used for this section. A solvent was then selected in which the system behaves congruently (meaning a full transformation to cocrystal occurred over the three days), and an upscaled solvent-mediated cocrystal formation was performed. This upscaling was performed in an EasyMax 102 (Mettler Toledo, Zaventem, Belgium) crystallizer equipped with a hermetically closed 100 mL flask, under mechanic stirring (150 rpm) at 25 °C. After three days, the solids were retrieved, washed, and dried overnight at 50 °C. The solids were then used for dissolution measurements. **NCA** was upscaled to 30 g of the bulk material in ethyl acetate while **NOA** and **NZC** were upscaled in acetonitrile.

Single-Crystal X-Ray Diffraction (SCXRD). Suitable crystals of **NZCW** to perform the SCXRD analysis have been analyzed using a Rigaku (Neu-Isenburg, Germany) Ultra X18S rotating anode, FOX3D mirrors. The diffracted beams were collected on a MAR345 image plate detector using MoKα (λ = 0.71073 Å). Single-crystal X-ray diffraction data for **NCA**, 2:1 nefiracetam-citric acid cocrystal Form II (**NCA1**), and **NZC** (100 K) were collected on an Oxford Diffraction Gemini R Ultra diffractometer (Ruby CCD detector using CuKα radiation) and crystals of **NOA** were measured at the SNBL beamline (Pilatus 2 M hybrid pixel detector), ESRF Grenoble. All the methodologies for the data reduction[26], resolution and refinement[27], and validation[28] were specified as in our previous work[3]. The images of the crystal structures were drawn using the software Mercury 4.1.3.[29] CCDC 2010261-2010276 contain the

supplementary crystallographic data for this paper. These data can be obtained free of charge from The Cambridge Crystallographic Data Centre via www.ccdc.cam.ac.uk/structures.

Powder X-Ray Diffraction (XRPD) data were collected on a diffractometer Bragg-Brentano manufactured by PANalytical (Eindhoven, Netherlands). The X-Ray source, a Ni-filtered CuKα (λ = 1.54179 Å), was used at 40 kV and 30 mA. The detection was carried out using a X'Celerator detector. All the powders were analyzed in a 2θ angle range from 4 to 40° for a total scan time of 6 min 42 s (step size = ca. 0.0167°).

Differential Scanning Calorimetry (DSC) measurements were performed from 25 to 175 °C at a scanning rate of 5 °C·min^{-1} on a TA instrument DSC2500 (Zellik, Belgium) in the cases of **NCA** and **NOA**. The temperature range was extended to 275 °C for **NZC** and **NZCW**. Solid samples (6–7 mg) were placed in an aluminum crucible (40 µL) with pierced sealed lids and nitrogen was used as purge gas with a flow rate of 50 mL.min^{-1}. Indium was used as a reference. Regarding the DSC measurements performed on the suspected and other confirmed cocrystals, the temperature range was extended to 200 and 225 °C.

Thermogravimetric Analysis (TGA). These analyses were carried out on a TGA-STDA 851e manufactured by Mettler Toledo. The samples were analyzed in a temperature range from 25 to 400 °C (600 °C for **NZC** and **NZCW**). The scanning rate applied during the analysis was 10 °C·min^{-1}. About 7–10 mg of solid materials were placed in an aluminum oxide crucible and a purge gas (nitrogen) was used with a flow rate of 50 mL.min^{-1}.

Dynamic Vapor Sorption (DVS) analyses were performed at 25 °C on a Q5000 SA from TA instruments. Solid samples (weight from 7 to 14 mg) were placed in a hanging platinum crucible and an empty crucible is used as the reference. These crucibles were placed in a chamber with controlled humidity and temperature. Nitrogen was used as flowing gas. Samples were first dried at 40 °C for 1h before being exposed to variable relative humidity within a range of 10% to 90%. The equilibrium was considered to have been reached when the weight change was less than 0.010 mg.min^{-1} or no weight change has occurred for 2 h.

Moisture Exposure. Samples (100 mg) of **NCA**, **NOA**, and **NZC** were stored for one month at room temperature in a sealed box containing an open water flask. The atmosphere was assumed to be saturated in water (100% RH). Both the XRPD and DSC analyses were performed on these powders after the exposure.

High Performance Liquid Chromatography (HPLC). The calibration line (linear equation) for the nefiracetam dosage was drawn by interrelating the area under the curve (AUC) with the concentration prepared. To do so, nefiracetam samples were

diluted 1000 times using a 1:1 acetonitrile-Milli-Q water diluent (in volume). nefiracetam chromatograms were then recorded according to the HPLC parameters: Device: Waters Alliance 2695 (Zellik, Belgium); Column: Waters Sunfire C18, 4.6 × 100 mm, 3.5 µm; Detector: PDA 2998 (MaxPlot); T° = 40 °C; injection volume: 10 µL; flow: 1.2 $mL.min^{-1}$; mobile phase A: H_2O + 0.1% H_3PO_4; mobile phase B: CH_3CN + 0.1% H_3PO_4; gradient: 0 to 0.5 min at 30% B; 0.5 to 4.5 min 30% B→90% B; 4.5 to 6.5 min at 90% B. The calibration line is reported in the Supporting Information.

UltraViolet Spectroscopy (UVS). The calibration line for UV spectroscopy was drawn in order to dose the nefiracetam by matching the absorbance at λ_{max} (= 263 nm) and the concentration prepared with a linear equation. Acetonitrile was used as a diluent and blank. Sample UV-absorption spectra were recorded from 300 to 200 nm using a UV-1700 PharmaSpec spectrophotometer manufactured by SHIMADZU (Wemmel, Belgium).

Dissolution Experiments. Nefiracetam FI, **NCA**, **NOA**, and **NZC** were first ground using a mortar and pestle to get approximately the same particle size range. An excess amount of compound was added to 50 mL of solvent at 18 °C in a 100 mL flask under magnetic 100 rpm stirring. The 10 µL sampling occurred using a syringe equipped with a micro filter (0.02 µm). Sampling was performed every 10–15 s during the first minute up to t = 1 min, every 30 s up to t = 5 min, and every minute up to t = 15 min. A final sampling (triplicate) was performed after 24 h considering the equilibrium has been reached. Samples were diluted from 2000 to 5000 times depending on the fraction considered with a MeCN-water Milli-Q (1:1 in volume) diluent. Those fractions were then injected in HPLC and dosed as mentioned above. Concerning **NZC**, the 10 µL-fractions were diluted 250 times with MeCN before being dosed using a UV-1700 PharmaSpec (SHIMADZU) spectrophotometer. HPLC data as well as the UVS data related to the dissolution experiments are presented in the Supporting Information.

5.4. Results and Discussion

5.4.1. Cocrystal Screening

A large cocrystal screen has been performed on nefiracetam using liquid-assisted grinding (LAG) and 133 different coformers. A full list is shown in the Supporting Information. Coformers have been selected based on crystal engineering principles, with all presenting synthons prone to cocrystal formation.[30,31] Seventeen cocrystals have been suspected based on XRPD data only, corresponding respectively to a success rate of 13%, which is in alignment with cocrystal success rates as reported in the literature[32]. Here, we report only those cases for which single crystals were

obtained. This was the case for the following 13 coformers: (RS)-phenylsuccinic acid (5), parahydroxybenzoic acid (6), 5-hydroxyisophthalic acid (7), 5-nitroisophthalic acid (8), 5-bromoisophthalic acid (9), (RS)-2-phenylbutyric acid (10), (RS)-3-phenyllactic acid (11), gallic acid (12), 2-benzoylbenzoic acid (13), 5-cyano-1,3-benzenedicarboxylic acid (14), citric acid (15), oxalic acid (16) and zinc chloride (17) (**Figure 5-2**). Cocrystals are also suspected by XRPD and DSC for the positional coformers β-resorcylic acid (2), gentisic acid (3) and protocatechuic acid (4) and dipiconilic acid (1) but no single crystal confirmation has been obtained so far.

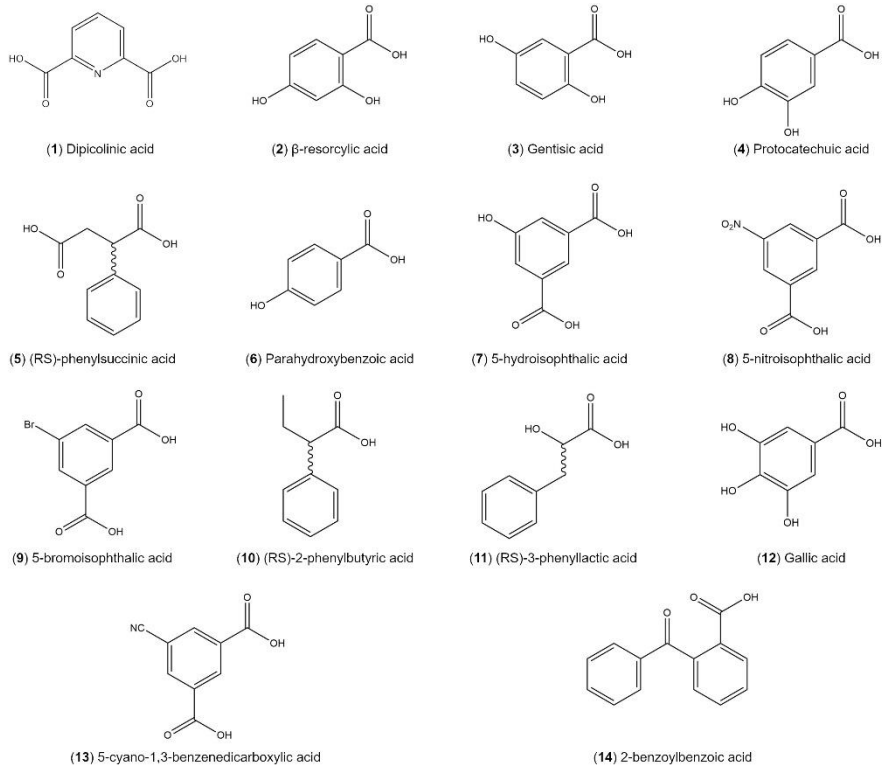

Figure 5-2. (**1**–**4**) Coformers for which a new nefiracetam cocrystal is suspected and (**5**–**17**) coformers for which a single crystal cocrystal confirmation has been achieved.

In a more general manner, successful coformers usually tend to have at least one carboxylic acid group and a phenyl ring present. A similar trend has been observed for the cocrystallization of other racetam compounds.[33,34] Recently, we have also shown inorganic salts to be good cocrystal formers for racetam compounds[35,36], which is also confirmed here. **Table 5-1** summarizes the main results for the 13 coformers leading to confirmed cocrystals. When the ground pattern does not match the simulated pattern from the single crystal, cocrystal polymorphs, solvates, or stoichiometrically diverse cocrystals are suspected.[37,38] This table also summarizes

melting/dehydration temperatures of the nefiracetam forms as well as the obtained cocrystals. Interestingly, we show that a very wide range of properties may be obtained using cocrystallization as a tool. Melting points vary from 68 to 243 °C merely by playing on the nature of the coformer. This shows the potential for variability one can achieve using cocrystallization as a crystal engineering tool. Furthermore, **Table 5-1** also highlights the importance of screening for the various solid-state forms of a given API/coformer system, as cocrystal polymorphs or cocrystal hydrates can be readily encountered.

Table 5-1. Cocrystal forms identified, together with the melting point. Pharmaceutical systems of interest are highlighted in bold. RT: Room temperature; HT: High temperature.

Coformer	Multiple Cocrystal Forms	Form	Cocrystal/Coformer Melting Point (°C)
(nefiracetam itself[3] **(N)**/**Figure 6-1**)	/	Form I	140
		Form II	150
		Form III	n/a
		Monohydrate	80 (dehydration)
5-nitroisophthalic acid	Yes	1:1 Cocrystal Form I	171/259
		1:1 Cocrystal Form II	199
5-hydroxyisopthalic acid	No	1:1 Cocrystal	196/298
5-cyano-1,3-benzenedicarboxylic acid	Yes	1:1 Cocrystal Form I (RT)	160/248
		1:1 Cocrystal Form II (HT)	180
5-bromoisophthalic acid	No	1:1 Cocrystal	199/270
(RS)-phenylsuccinic acid	No	2:1 Cocrystal (racemic)	95/166
4-hydroxybenzoic acid	No	1:1 Cocrystal	122/213
(RS)-2-phenylbutyric acid	No	Form I (solid solution)	72/39
(RS)-3-phenyllactic acid	No	1:1 Cocrystal (racemic)	68/95
2-benzoylbenzoic acid	No	1:1 Cocrystal	92/126
Gallic acid	No	4:1:1 Cocrystal hydrate	n/a/251
Citric acid (CA)	Yes	**2:1 Cocrystal Form I**	81 (phase transition)
		2:1 Cocrystal Form II	n/a
Oxalic acid (OA)	No	**2:1 Cocrystal**	162
Zinc chloride (ZC)	Yes	**Ionic cocrystal hydrate**	210 (dehydration)/290
		Ionic cocrystal	243

The cocrystals of citric acid, oxalic acid, and zinc chloride are described in more detail as these cocrystals are pharmaceutically acceptable (**Figure 5-3**). For the analysis of the others, we refer to the Supporting Information. For citric acid (**NCA**), oxalic acid (**NOA**), and zinc chloride (**NZC**), LAG experiments all yielded the same outcome, irrespective of the solvent used. For these systems, a more profound form screening was performed using evaporative, slurrying, and cooling crystallization when applicable. Twelve solvents were used for a total of 125 experiments with results shown in the Supporting Information. These results led to no additional crystalline form for the **NOA** cocrystal but did lead to the identification of a second 2:1 cocrystal form for the **NCA** system and a cocrystal hydrate for the **NZC** system, highlighting the importance of screening for multiple cocrystal forms once a positive coformer has been identified.

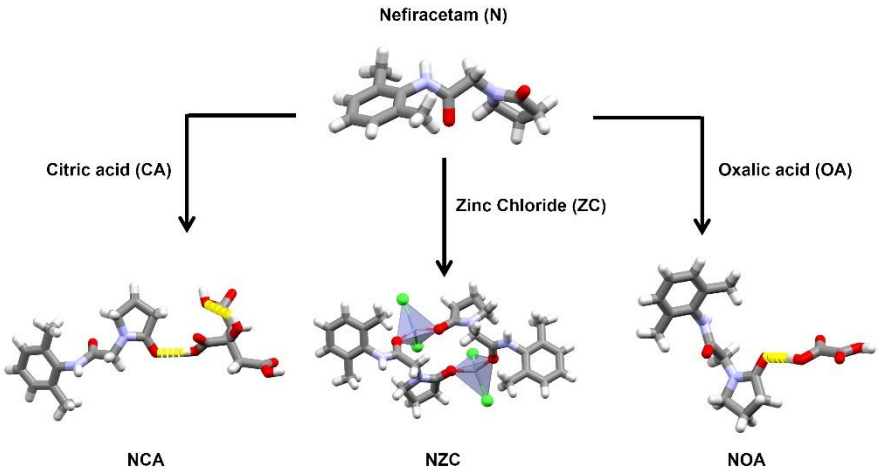

Figure 5-3. Biocompatible nefiracetam cocrystals identified and studied in detail in this work. Relevant intramolecular interactions between nefiracetam and the coformers are highlighted by yellow stick contacts.

5.4.2. The 2:1 Nefiracetam-Oxalic Acid Cocrystal (NOA)

As mentioned above, only one form of the **NOA** cocrystal has been identified, which is easily identifiable through its 2θ peaks at 11.3°, 13.6°, and 15.9°. The bulk product pattern is furthermore shown to match the one simulated from the powder resolution analysis (**Figure 5-4a**), which shows **NOA** to crystallize in the monoclinic $P2_1$ space group. **Figure 5-5a** shows a main hydrogen bond $C_1^1(4)$ chain pattern according to Etter's graph-set notation[39,40] built through N-H···O (2.86(1) Å, 152.0° as a hydrogen bond distance N···O and NHO angle) hydrogen bonds between nefiracetam amide moieties. Nefiracetam is linked to the oxalic acid through a hydrogen bonding pattern

between the hydroxyl group from both the carboxylic acid moieties and the oxygen of the γ-lactam moiety of two different nefiracetam molecules. These interactions (2.54(1) Å, 167 and 171.5°) result in a $D_1^1(2)$ hydrogen-bond pattern. This assembly creates an overall pattern with nefiracetam chains along the *a*-axis and oxalic acid acting as a linker between chains (zig-zag feature in **Figure 5-5a** represented by a full black line). The main crystallographic parameters related to each form and the refinement parameters are summarized in **Table 8-2-2** in the Supporting Information. Upon heating, **NOA** shows a sharp melting endotherm at 162 °C (**Figure 5-6c**) and right upon melting, a weight loss of about 15% is observed (**Figure 5-6a**), corresponding to oxalic acid sublimation.[41,42] Above 200 °C, degradation of nefiracetam is observed. After a prolonged (one-month) exposure under a humidity saturated atmosphere (100% RH), no transformation of **NOA** into another form or deliquescence was observed by XRPD and DSC measurements (Supporting Information).

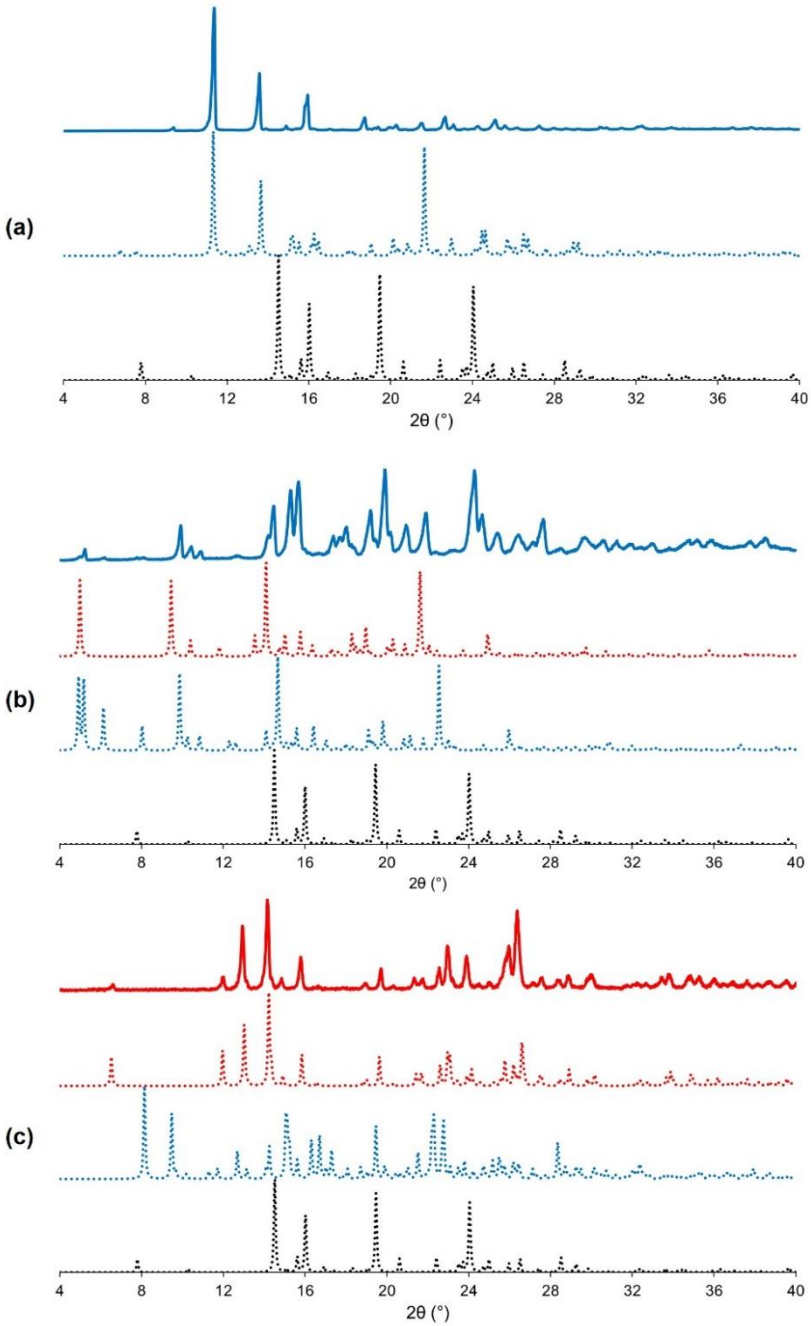

Figure 5-4. Simulated diffraction patterns (dashed line) and experimental powders (full line) of (**a**) nefiracetam-oxalic acid cocrystal (NOA) (blue), (**b**) nefiracetam-citric acid cocrystal (NCA) (blue) and NCA1 (red), and (**c**) nefiracetam-zinc chloride ionic cocrystal (NZCW) (blue) and NZC (red). Patterns are compared to the nefiracetam one (black).

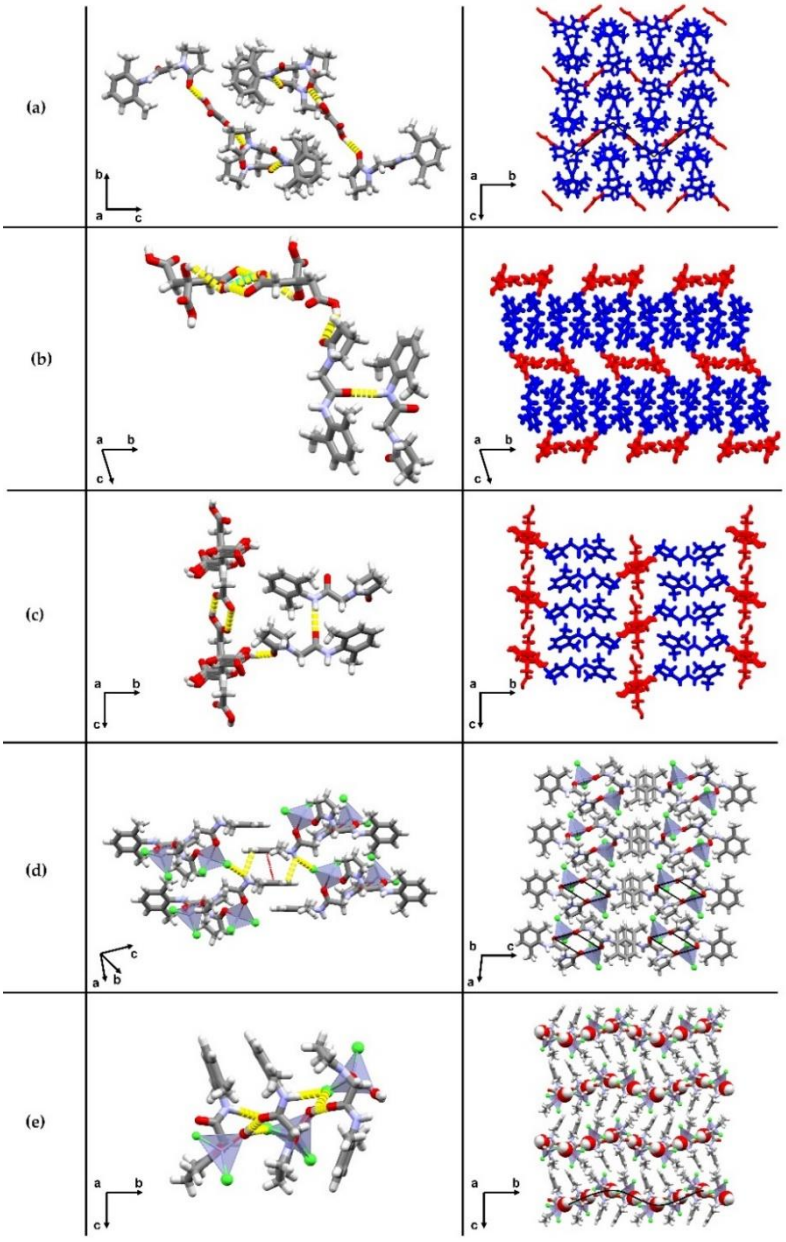

Figure 5-5. Main intermolecular interactions and crystal packing along the *a*- and *b*-axis in the crystal structure of NCA (**a**), NCA1 (**b**), NOA (**c**), NZC (**d**), and NZCW (**e**). The tetragonal geometry of the Zn^{2+} based-complex and the water molecules are respectively highlighted using the polyhedral and spacefill representation. Intermolecular contacts are shown using yellow dashed lines. The red dashed line is used to show the centroid-centroid distance in the NZC crystal structure.

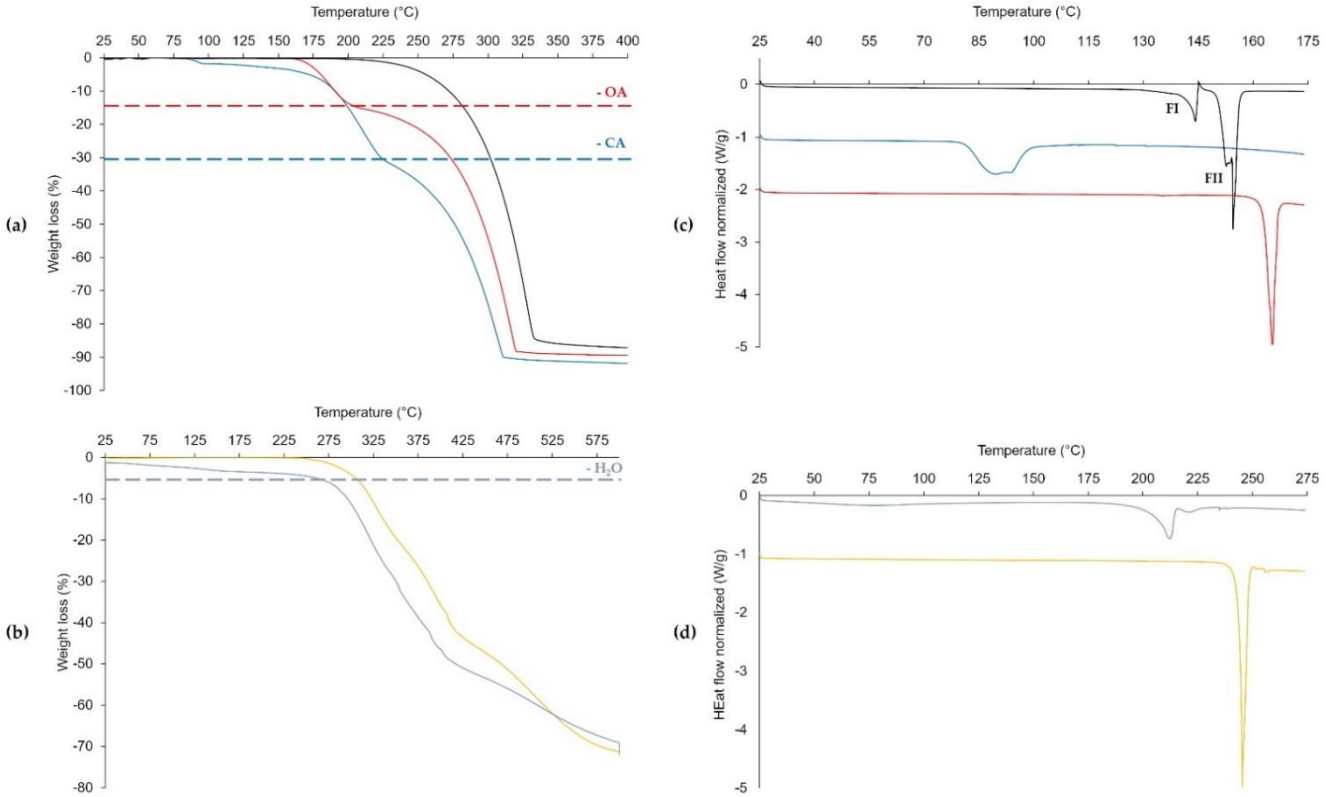

Figure 5-6. TGA curves (**a**) and (**b**) and DSC curves (**c**) and (**d**) of nefiracetam (black), NCA (blue), NOA (red), NZC (yellow), and NZCW (grey).

5.4.3. The 2:1 Nefiracetam-Citric Acid Cocrystal (NCA and NCA1)

Two different polymorphs of the 2:1 nefiracetam-citric acid cocrystal have been obtained. All screening experiments led to the same 2:1 cocrystal form (**NCA**). Single crystals of this form were obtained from a slow evaporation from ethyl acetate. Unexpectedly, the SCXRD diffraction experiment of **NCA** revealed also the presence of a second 2:1 form **NCA1**, in the same crystal. This latter is likely due to a phenomenon of cross-nucleation, i.e. the heterogeneous nucleation of Form II (**NCA1**, daughter form) on the surface of the other (**NCA**, parent form).[43,44] This Form II was never observed in sufficient quantity in any of the screening or bulk material preparation experiments, and is therefore likely a kinetic form, crystallizing under highly supersaturated conditions, which occurs at the end of the solvent evaporation process. As during upscaling, the crystallization solvent is never fully evaporated, and the material is washed, this polymorph is very likely not present in the bulk material that fits the **NCA** simulated powder pattern in **Figure 5-4b**. **NCA** crystallizes in the triclinic *P*-1 space group. As for the anhydrous forms of nefiracetam[3], the nefiracetam molecules are stacked in a chain, by intermolecular amide-amide hydrogen bonds (N-H···O, 2.773(5) Å, 168.2°) leading to a $C_1^1(4)$ hydrogen-bond pattern. In **Figure 5-5b**, the recognition between nefiracetam and citric acid is due to two extra $D_1^1(2)$ intermolecular hydrogen bonds (O-H···O, 3.18(1) Å, 146.64° and O-H···O, 2.596(5) Å, 168.01°) which link one citric acid molecule to two nefiracetam molecules through the oxygen of the γ-lactam moiety (nefiracetam) and the hydroxyl of a carboxylic acid (citric acid). Moreover, a ring feature ($R_2^2(8)$ with 2.654(6) Å and 152.45°) leading to a cyclic citric acid dimer is observable between two carboxylic acids from different citric acid molecules. Finally, an intramolecular hydrogen bond O-H···O ($S_1^1(3)$, 3.176(7) Å, 121.48°) is present in each citric acid molecule.

Polymorph **NCA1** shows disorder and crystallizes in the monoclinic $P2_1/c$ space group. Intermolecular interactions between citric acid and nefiracetam are identical to those mentioned for the first **NCA** form (**Figure 5-5c**). In **Figure 5-6a**, TGA data shows three respective weight losses in the case of **NCA**. A first weight loss occurs around 80 °C, and must likely correspond to the loss of water molecules trapped in the channel-like structure observed for this cocrystal, evidencing that **NCA** is likely a non-stoichiometric hydrate. The following waves correspond to citric acid degradation (±28%, 175 °C)[45] and nefiracetam degradation (from 225 °C), respectively. The DSC endotherm at around 80 °C corresponds to a potential dehydration of a non-stoichiometric hydrate, but could potentially also correspond to a melting point. DVS shows a deliquescent (+20% in weight) behavior at RH > 80%. When exposing **NCA** to a saturated humidity atmosphere for a long time period (one month), deliquescence is followed by nefiracetam monohydrate crystallization (Supporting Information).

5.4.4. The 1:1 Nefiracetam-Zinc Chloride Ionic Cocrystal (NZC)

The form screening with zinc chloride led to two different cocrystals. The full screening results are presented in the Supporting Information. Slurrying crystallization in a congruent and dried solvent, led to a 1:1 ionic cocrystal (**NZC**) wherein nefiracetam is coordinated with the Zn^{2+}. In addition, evaporative experiments at room temperature with water traces in the solvent (ethyl acetate) led to a 1:1:1 hydrated ionic cocrystal (so called **NZCW**) form whose structure was solved showing a zinc chloride complex with nefiracetam and one water molecule. Only **NZC** was upscaled in dried acetonitrile. We were unsuccessful at obtaining larger amounts of **NZCW** as all experimental conditions tried led to mixtures of the nefiracetam monohydrate, **NZCW,** and anhydrous **NZC**. The experimental and simulated XRPD data related to each system are presented in **Figure 5-4c**. Single crystals obtained from slowly cooling a supersaturated acetonitrile solution, yielded suitable monoclinic *C*2/*c* cube-like single crystals of the anhydrate (**NZC**) wherein nefiracetam is complexed to zinc chloride showing a tetragonal geometry around the Zn^{2+} ion. nefiracetam molecules are bound to each other by two identical (by symmetry), tetrahedral complexes as shown in **Figure 5-3** and **Figure 5-5d** (right). Complexation occurs between zinc chloride and the γ-lactam C=O moiety of a first molecule and the amide C=O from a second molecule and vice versa. The donor moiety (N-H) from the amide is involved in a hydrogen bond pattern ($C_1^1(4)$, 3.496(1) Å, 146.49°) with the chloride from the tetragonal complex along the *a*-axis. These tetrahedral complexes form a network of nefiracetam dimer molecules as shown with black diamonds in **Figure 5-5d**. The π-stacking interactions are present between the nefiracetam aromatic moieties with a centroid-centroid distance of about 3.54°. This stacking may explain the higher density (1.637 $Mg.m^{-3}$) comparing **NZC** with **NZCW**.

NZCW crystallizes in the monoclinic $P2_1$ space group. The amide-amide hydrogen bond between nefiracetam molecules as described above remains present but does not lead to a $C_1^1(4)$ chain pattern as in the previous cases. Indeed, the nefiracetam chains are interrupted by water molecules and nefiracetam amide moieties are now involved in three $D_1^1(2)$ hydrogen-bond patterns with respectively a water hydrogen (O-H···H, 2.734(2) Å, 174.33°), a second nefiracetam amide moiety (N-H···O, 3.019(3) Å, 164.80°), and with a chloride ion (N-H···Cl, 3.331(2) Å, 169.63°). An infinite chain (O-H···Cl, $C_1^1(4)$, 3.154(2) Å, 169.19°) is also observed involving the second hydrogen from the water molecule and a chloride ion. In the presence of zinc chloride, the carbonyl not belonging to the pyrrolidone group is coordinated to the Zn^{2+} cation as well as to the water oxygen atom leading to a tetrahedral complex. This complex is highlighted in **Figure 5-5e** and forms "wave" chains stacking nefiracetam densely (1.514 $Mg.m^{-3}$) along the *b*-axis. **NZC** shows a single melting endotherm at 243 °C.

On the other hand, **NZCW** shows a continuous dehydration behavior (coordinated-water loss of ±4.5% corresponds to 1 equivalent of water) up until 175 °C. The DSC analysis then shows an endothermic peak at 200 °C which potentially corresponds to the melting of another polymorphic form of the ionic cocrystal or is a mere effect of the water still being present in the DSC capsule. To observe the potential transformation of **NZC** into **NZCW**, **NZC** was stored for one month in a saturated humidity chamber at room temperature. Even though, the DSC analysis indicates traces of the hydrated form (small endotherm around 210 °C), XRPD shows no such transformation. If **NZCW** is present in the bulk, it would only be in trace amount (Supporting Information). Therefore, **NZC** could be a potentially interesting form to market.

5.4.5. Solubility and Dissolution Profile of Nefiracetam Cocrystals

Ethanol and acetonitrile were selected to study the dissolution profile at 18 °C (100 rpm) of **NCA**, **NOA**, and **NZC** in comparison to the API (nefiracetam FI). As the cocrystals considered here behave incongruently in water, with nefiracetam monohydrate crystallizing out rapidly, we were unable to determine the apparent cocrystal solubility in this solvent. Therefore, we decided to perform the dissolution studies in EtOH and MeCN as we aim at underlining the potential impact cocrystals can have on physicochemical parameters. **NCA**, **NOA**, and **NZC** are incongruent in EtOH leading to a final slurry of nefiracetam, whereas a congruent dissolution is observed in MeCN. In the case of an incongruent system in EtOH, a "spring-parachute"[46,47] behaviour (**Figure 5-7a**) is expected meaning that the concentration reaches a maximum ("apparent solubility"[48,49]) before dropping to the solubility of the drug form crystallizing out (here nefiracetam FI). The final solubility of nefiracetam might, however, still be different as solution interactions will occur. In the present case, the cocrystal dissolution kinetics combined to the crystallization kinetics of nefiracetam FI occur too rapidly for the "spring-parachute" behavior to be observable. Nevertheless, one notices a clear impact of the coformer on the solubility of nefiracetam (**Table 5-2**) with the overall solubility at 18 °C observed in both cases around 750 mM (+40%) instead of 519 mM for the parent drug (**Figure 5-7c**) in EtOH. The presence of $ZnCl_2$ on the other hand, reduces solubility to about 199 mM.

Table 5-3 also shows a true cocrystal solubility in MeCN where all cocrystals behave congruently. Here, one also clearly sees the importance of the coformer nature on the overall solubility, with citric acid slightly increasing the amount of nefiracetam dissolved, whereas oxalic acid reduces this amount by about 30% in comparison to nefiracetam FI. A striking drop in nefiracetam present in the solution of about 90% is observed using the **NZC** cocrystal.

The changes in solubility also reflect in the dissolution rate. However, they are all lower with respect to the dissolution rate of the parent compound. It should nevertheless be noticed that all solid forms dissolve very rapidly, with half of the maximum solubility reached in the first minute and full solubility reached in the first 5 min of adding powder to the reactor. Therefore, we expect the bioavailability to be impacted by the type of solid form used, not for the impact on the time required to reach solubility, but rather by the impact on the solubility value.

Table 5-2. Dissolution rates and solubility at 18 °C in EtOH in the case of nefiracetam FI, **NCA**, **NOA**, and **NZC**.

Solid Forms	Dissolution Rate* ($mM.s^{-1}$)/Time (min)	Solubility (mM, 18 °C)
nefiracetam FI	1299/0.2	519.59 (±11.88)
NCA	419/0.9	753.47 (±25.65)
NOA	246/1.5	737.53 (±8.58)
NZC	332/0.3	199.46 (±1.61)

* Dissolution rates correspond to the rate calculated when half the solubility is reached, with the corresponding time also given.

Table 5-3. Dissolution rates and solubility at 18 °C in MeCN in the case of nefiracetam FI, **NCA**, **NOA**, and **NZC**.

Solid Forms	Dissolution Rate* ($mM.s^{-1}$)/Time (min)	Solubility (mM, 18 °C)	Solubility Product (Ks, 18 °C)	pKs
nefiracetam FI	969/0.1	290.83 (±10.97)	/	/
NCA	323/0.5	322.87 (±4.32)	1.35×10^{-1}	0.87
NOA	538/0.2	215.03 (±1.03)	3.98×10^{-2}	1.40
NZC	64/0.2	25.45 (±0.63)	6.48×10^{-4}	3.19

* Dissolution rates correspond to the rate calculated when half the solubility is reached, with the corresponding time also given.

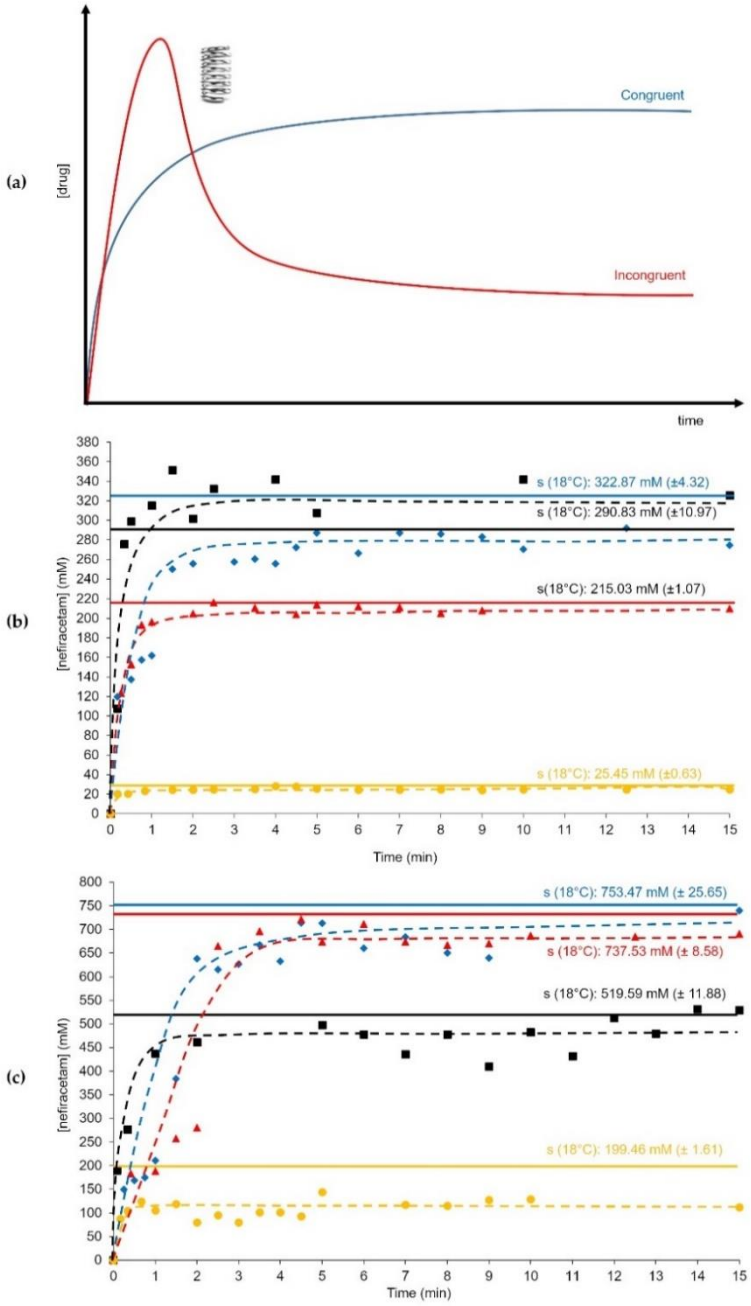

Figure 5-7. (**a**) Theoretical dissolution curve in the case of a congruent and an incongruent system (with spring-parachute behavior). Experimental dissolution curves of nefiracetam FI (black ■), NCA (blue ♦), NOA (red ▲), and NZC (yellow ●) in (**b**) MeCN at 18 °C with a 100-rpm stirring and (**c**) EtOH at 18 °C with a 100-rpm stirring.

5.5. Conclusion

Nefiracetam cocrystal screening led to the identification of 13 novel cocrystal systems. Among these, three biocompatible systems were identified (**NCA**, **NOA**, and **NZC**) and their physicochemical properties (stability, solubility, and dissolution) were evaluated and compared to those of the parent compound nefiracetam. The zinc chloride ionic cocrystal showed an impressive improvement in thermal stability, but strongly reduced the solubility by about 90% in organic solvents in comparison with the parent drug. The use of tri- and dicarboxylic acid coformers can induce a complete different behavior, with citric acid improving the solubility, while oxalic acid reduces this latter when the cocrystal behaves congruently. For non-congruent systems, the presence of the coformer always increases the overall solubility. All cocrystals, as well as the parent compound, are rapidly dissolving. Overall, this study confirms that cocrystallization can be used as an effective tool to impact the physico-chemical properties of a drug compound. A relevant choice in the coformer can either help improve formulation stability, or bioavailability of the drug. The coformer selection is of utter importance, as strong variations can occur depending on the nature of the selected coformer.

5.6. References

1. Wang, P.L.; Wang, H.B.; Ding, W.L.; Liu, Z.Q.; Xing, Z.T. N-(2, 6-Dimethylphenyl)-2-(2-oxo-1-pyrrolidin-1-yl) acetamide. *Acta Crystallogr. Sect. E* **2006**, *62*, 3838–3839.
2. Crespi, F. nefiracetam. Daiichi Seiyaku. *Curr. Opin. Investig. Drugs* **2002**, *3*, 788–793.
3. Buol, X.; Robeyns, K.; Tumanov, N.; Wouters, J.; Leyssens, T. Identifying, Characterizing, and Understanding nefiracetam in Its Solid State Forms: A Potential Antidementia Drug. *J. Pharm. Sci.* **2019**, *108*, 3616–3622.
4. Duggirala, N.K.; Perry, M.L.; Almarsson, Ö.; Zaworotko, M.J. Pharmaceutical cocrystals: Along the path to improved medicines. *Chem. Commun.* **2016**, *52*, 640–655.
5. Schultheiss, N.; Newman, A. Pharmaceutical cocrystals and their physicochemical properties. *Cryst. Growth Des.* **2009**, *9*, 2950–2967.
6. Bolla, G.; Nangia, A. Pharmaceutical cocrystals: Walking the talk. *Chem. Commun.* **2016**, *52*, 8342–8360.
7. Shan, N.; Zaworotko, M.J. The role of cocrystals in pharmaceutical science. *Drug Discov. Today* **2008**, *13*, 440–446.

8. Grepioni, F.; Wouters, J.; Braga, D.; Nanna, S.; Fours, B.; Coquerel, G.; Longfils, G.; Rome, S.; Aerts, L.; Quéré, L. Ionic cocrystals of racetams: Solid-state properties enhancement of neutral active pharmaceutical ingredients via addition of Mg^{2+} and Ca^{2+} chlorides. *CrystEngComm* **2014**, *16*, 5887–5896.
9. Aitipamula, S.; Banerjee, R.; Bansal, A.K.; Biradha, K.; Cheney, M.L.; Choudhury, A.R.; Desiraju, G.R.; Dikundwar, A.G.; Dubey, R.; Duggirala, N. Polymorphs, salts, and cocrystals: what's in a name? *Cryst. Growth Des.* **2012**, *12*, 2147–2152.
10. Thipparaboina, R.; Kumar, D.; Chavan, R.B.; Shastri, N.R. Multidrug cocrystals: Towards the development of effective therapeutic hybrids. *Drug Discov. Today* **2016**, *21*, 481–490.
11. Bond, A.D. What is a cocrystal? *CrystEngComm* **2007**, *9*, 833–834.
12. Braga, D.; Grepioni, F.; Lampronti, G.I.; Maini, L.; Turrina, A. Ionic cocrystals of organic molecules with metal halides: A new prospect in the solid formulation of active pharmaceutical ingredients. *Cryst. Growth Des.* **2011**, *11*, 5621–5627.
13. Braga, D.; Grepioni, F.; Shemchuk, O. Organic–inorganic ionic cocrystals: A new class of multipurpose compounds. *CrystEngComm* **2018**, *20*, 2212–2220.
14. Singh, D.; Bedi, N.; Tiwary, A.K. Enhancing solubility of poorly aqueous soluble drugs: Critical appraisal of techniques. *J. Pharm. Investig.* **2018**, *48*, 509–526.
15. Shevchenko, A.; Bimbo, L.M.; Miroshnyk, I.; Haarala, J.; Jelínková, K.; Syrjänen, K.; van Veen, B.; Kiesvaara, J.; Santos, H.A.; Yliruusi, J. A new cocrystal and salts of itraconazole: Comparison of solid-state properties, stability and dissolution behavior. *Int. J. Pharm.* **2012**, *436*, 403–409.
16. Shan, N.; Perry, M.L.; Weyna, D.R.; Zaworotko, M.J. Impact of pharmaceutical cocrystals: The effects on drug pharmacokinetics. *Expert Opin. Drug Metab. Toxicol.* **2014**, *10*, 1255–1271.
17. Thakuria, R.; Delori, A.; Jones, W.; Lipert, M.P.; Roy, L.; Rodríguez-Hornedo, N. Pharmaceutical cocrystals and poorly soluble drugs. *Int. J. Pharm.* **2013**, *453*, 101–125.
18. Leyssens, T.; Harmsen, B. WO2019143829-Fasoracetam Crystalline Forms. **2019**. Available online : https://patentscope.wipo.int/search/en/detail.jsf?docId=WO2019143829 (accessed on 26 May 2020).
19. Holland, J.; Frampton, C.; Chorlton, A.; Gooding, D. Metaxalone Cocrystals. U.S. Patent No. 8,871,793, 28 October 2014.
20. McNamara, D.P.; Childs, S.L.; Giordano, J.; Iarriccio, A.; Cassidy, J.; Shet, M.S.; Mannion, R.; O'Donnell, E.; Park, A. Use of a glutaric acid cocrystal to improve oral bioavailability of a low solubility API. *Pharm. Res.* **2006**, *23*, 1888–1897.
21. Brittain, H.G. Cocrystal Systems of Pharmaceutical Interest: 2012–2014. *Profiles Drug Subst. Excip. Relat. Methodol.* **2019**, *44*, 415–443.

22. Brittain, H.G. Cocrystal systems of pharmaceutical interest: 2010. *Cryst. Growth Des.* **2012**, *12*, 1046–1054.
23. Brittain, H.G. Cocrystal systems of pharmaceutical interest: 2011. *Cryst. Growth Des.* **2012**, *12*, 5823–5832.
24. Friščić, T.; Childs, S.L.; Rizvi, S.A.; Jones, W. The role of solvent in mechanochemical and sonochemical cocrystal formation: A solubility-based approach for predicting cocrystallisation outcome. *CrystEngComm* **2009**, *11*, 418–426.
25. Fischer, F.; Heidrich, A.; Greiser, S.; Benemann, S.; Rademann, K.; Emmerling, F. Polymorphism of mechanochemically synthesized cocrystals: A case study. *Cryst. Growth Des.* **2016**, *16*, 1701–1707.
26. Rigaku, O.D. *CrysAlisPro Software System, Version 1.171. 38.41 l, Rigaku Coorporation*; Oxford, UK: **2015**.
27. Sheldrick, G.M. Crystal structure refinement with SHELXL. *Acta Crystallogr. Sect. C* **2015**, *71*, 3–8.
28. Spek, A.L. Structure validation in chemical crystallography. *Acta Crystallogr. Sect. D* **2009**, *65*, 148–155.
29. Macrae, C.F.; Bruno, I.J.; Chisholm, J.A.; Edgington, P.R.; McCabe, P.; Pidcock, E.; Rodriguez-Monge, L.; Taylor, R.; Streek, J.V.D.; Wood, P.A. Mercury CSD 2.0–new features for the visualization and investigation of crystal structures. *J. Appl. Crystallogr.* **2008**, *41*, 466–470.
30. Blagden, N.; De Matas, M.; Gavan, P.T.; York, P. Crystal engineering of active pharmaceutical ingredients to improve solubility and dissolution rates. *Adv. Drug Deliv. Rev.* **2007**, *59*, 617–630.
31. Desiraju, G.R. Supramolecular synthons in crystal engineering—a new organic synthesis. *Angew. Chem. Int. Ed. Engl.* **1995**, *34*, 2311–2327.
32. James, S.L.; Adams, C.J.; Bolm, C.; Braga, D.; Collier, P.; Friščić, T.; Grepioni, F.; Harris, K.D.; Hyett, G.; Jones, W. Mechanochemistry: Opportunities for new and cleaner synthesis. *Chem. Soc. Rev.* **2012**, *41*, 413–447.
33. Springuel, G.R.; Robeyns, K.; Norberg, B.; Wouters, J.; Leyssens, T. Cocrystal formation between chiral compounds: How cocrystals differ from salts. *Cryst. Growth Des.* **2014**, *14*, 3996–4004.
34. Springuel, G.R.; Norberg, B.; Robeyns, K.; Wouters, J.; Leyssens, T. Advances in pharmaceutical cocrystal screening: Effective cocrystal screening through structural resemblance. *Cryst. Growth Des.* **2012**, *12*, 475–484.
35. Song, L.; Shemchuk, O.; Robeyns, K.; Braga, D.; Grepioni, F.; Leyssens, T. Ionic cocrystals of etiracetam and levetiracetam: The importance of chirality for ionic cocrystals. *Cryst. Growth Des.* **2019**, *19*, 2446–2454.
36. Shemchuk, O.; Song, L.; Tumanov, N.; Wouters, J.; Braga, D.; Grepioni, F.; Leyssens, T. Chiral resolution of RS-oxiracetam upon cocrystallization with pharmaceutically acceptable inorganic salts. *Cryst. Growth Des.* **2020**.

37. Porter Iii, W.W.; Elie, S.C.; Matzger, A.J. Polymorphism in carbamazepine cocrystals. *Cryst. Growth Des.* **2008**, *8*, 14–16.
38. Leyssens, T.; Springuel, G.; Montis, R.; Candoni, N.; Veesler, S.P. Importance of solvent selection for stoichiometrically diverse cocrystal systems: Caffeine/maleic acid 1: 1 and 2: 1 cocrystals. *Cryst. Growth Des.* **2012**, *12*, 1520–1530.
39. Etter, M.C.; MacDonald, J.C.; Bernstein, J. Graph-set analysis of hydrogen-bond patterns in organic crystals. *Acta Crystallogr. Sect. B* **1990**, *46*, 256–262.
40. Bernstein, J.; Davis, R.E.; Shimoni, L.; Chang, N.L. Patterns in hydrogen bonding: Functionality and graph set analysis in crystals. *Angew. Chem. Int. Ed. Engl.* **1995**, *34*, 1555–1573.
41. Oxalic acid-Registration Dossier- ECHA: https://echa.europa.eu/registration-dossier/-/registered-dossier/14786/4/3 (accessed on 26 May 2020).
42. United States Department of Labor- Occupational Safety and Health Administration-Oxalic acid: https://www.osha.gov/chemicaldata/chemResult.html?RecNo=270 (accessed on 26 May 2020).
43. Yu, L. Survival of the fittest polymorph: How fast nucleater can lose to fast grower. *CrystEngComm* **2007**, *9*, 847–851.
44. Looijmans, S.F.; Cavallo, D.; Yu, L.; Peters, G.W. Cross-nucleation between polymorphs: Quantitative modeling of kinetics and morphology. *Cryst. Growth Des.* **2018**, *18*, 3921–3926.
45. Barbooti, M.M.; Al-Sammerrai, D.A. Thermal decomposition of citric acid. *Thermochim. Acta* **1986**, *98*, 119–126.
46. Bavishi, D.D.; Borkhataria, C.H. Spring and parachute: How cocrystals enhance solubility. *Prog. Cryst. Growth Charact. Mater.* **2016**, *62*, 1–8.
47. Guzmán, H.R.; Tawa, M.; Zhang, Z.; Ratanabanangkoon, P.; Shaw, P.; Gardner, C.R.; Chen, H.; Moreau, J.P.; Almarsson, Ö.; Remenar, J.F. Combined use of crystalline salt forms and precipitation inhibitors to improve oral absorption of celecoxib from solid oral formulations. *J. Pharm. Sci.* **2007**, *96*, 2686–2702.
48. Nicoud, L.; Licordari, F.; Myerson, A.S. Estimation of the Solubility of Metastable Polymorphs: A Critical Review. *Cryst. Growth Des.* **2018**, *18*, 7228–7237.
49. Nicoud, L.; Licordari, F.; Myerson, A.S. Polymorph control in batch seeded crystallizers. A case study with paracetamol. *CrystEngComm* **2019**, *21*, 2105–2118.

6. Chiral Resolution of Mandelic acid through Preferential Cocrystallization with Nefiracetam

Xavier Buol[a, *], Camila Caro Garrido[a], Koen Robeyns[a], Nikolay Tumanov[b], Laurent Collard[a], Johan Wouters[b] and Tom Leyssens[a, *]

[a]Institute Of Condensed Matter and Nanosciences, UCLouvain, 1 Place Louis Pasteur, B-1348 Louvain-la-Neuve, Belgium.

[b]Namur Research Institute for Life Sciences (Narilis), Chemistry department, UNamur, 61 rue de Bruxelles, B-5000 Namur, Belgium.

6.1. Abstract

In this paper, we identify a cocrystal conglomerate of mandelic acid using a drug compound as coformer. We then developed a chiral resolution process based on preferential cocrystallization. Several versions of such a process were explored, optimized and led to a successful resolution of mandelic acid, evidencing the efficiency of our system. Excellent enantiopurity (98-99%) was obtained with a process that can run for multiple cycles.

Keywords: Chiral resolution, preferential crystallization, cocrystal conglomerate, nefiracetam, mandelic acid.

6.2. Introduction

A chiral molecule exists in two non-superimposable configuration images called enantiomers. These enantiomers exhibit identical physicochemical properties in an achiral environment[1-2]. When placed in a chiral surrounding, differences in behavior of enantiomers can occur[3]. The human body typically shows such a chiral setting, often reflecting in differences in therapeutic effect between two enantiomers of pharmaceutically active compounds. Whereas one enantiomer shows a desired effect (eutomer), the other enantiomer (distomer) either shows a similar, no, or a negative effect. To avoid issues such as those observed in the case of Thalidomide[4], new chiral drugs are marketed containing only the desired enantiomer.[5] It is therefore important

during drug development to develop a production process that eventually leads to the eutomer.[3, 6-7] Two approaches are common. A first approach is to develop a synthetic pathway for a single enantiomer through asymmetric synthesis. Asymmetric synthesis groups different approaches such as enantioselective synthesis, the chiral pool[8], the use of chiral auxiliaries[9] and asymmetric catalysis.[10-11] This pathway is however not always feasible or cost-effective. An alternative, common approach is to resolve both enantiomers from a racemic mixture. Common resolution methods are kinetic resolution[12], chiral chromatography,[13] diastereoisomeric salt formation,[14] resolution by enantiospecific[15] or diastereomeric cocrystallization[16] and *Preferential Crystallization (PC).*[17-18] The latter three methods are crystallization-based processes, with the advantage of preferential crystallization that no external resolution agent needs to be added (and separated from the mixture in a further process). Preferential Crystallization or resolution by entrainment, however, can only be performed when the compound crystallizes as a conglomerate (defined as *a physical mixture of mirror-image crystalline phases exhibiting symmetrical enantiomeric excesses[17])* which only occurs in less than 10% of cases.[19-20] To increase the potential of PC, a recent tactics focuses on converting a racemic compound into a conglomerate using a crystal engineering approach.[21] Typically, salt[22] formation or the use of solvates[23] are commonly encountered for this transformation. Recently cocrystallization[24-27] has also been explored as an interesting alternative. Harfouche *et al.*[28] then went beyond mere identification of a cocrystal conglomerate, showing the first application of PC to the racemic pharmaceutical substance proxyphylline through the conversion of the racemic compound into a monohydrate conglomerate cocrystal. A purity of 91.6 % in favor of the desired enantiomer was achieved in a single entrainment step.

In this work, we also use preferential cocrystallization, being the first to propose resolution of racemic mandelic acid through preferential crystallization. To do so, the racemic compound of mandelic acid is transformed into a conglomerate, cocrystallizing this latter with nefiracetam[29-32] an achiral nootropic drug molecule (**Figure 6-1**). Mandelic acid, which is resolved by diastereoisomeric salt formation,[33] is commonly used in the pharmaceutical industry due to its analgesic, antirheumatic and spasmolytic effects and its enantiopure forms are widely used as resolving agent.[34-35] We here present detailed evidence of this dual-drug conglomerate formation, and then subsequently develop a preferential crystallization for the resolution of mandelic acid using different approaches such as a **S**eeded **I**sothermal **P**referential **C**rystallization (SIPC) and a **S**eeded **Poly**thermal **P**referential **C**rystallization (S3PC).[36-38] We were able to develop a cyclic process in which we resolved at least up to 2.4 g of mandelic acid, with an enantiopurity of 98-99%, being the first to report mandelic acid resolution using preferential cocrystallization.

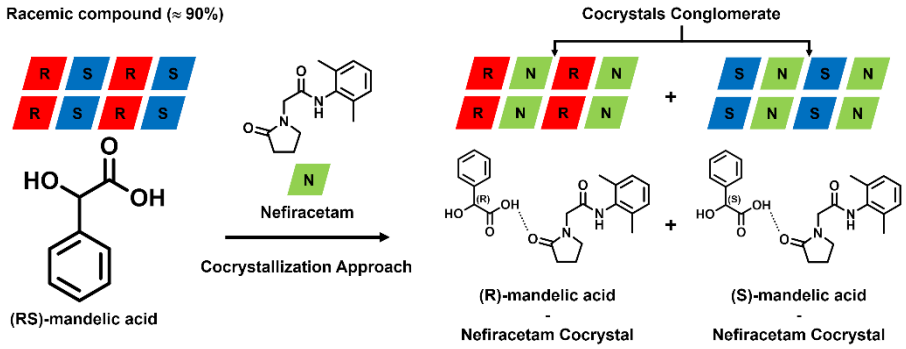

Figure 6-1. Cocrystallization approach to convert the racemic compound of mandelic acid into a nefiracetam cocrystal conglomerate.

6.3. Material and Methods

Materials. Nefiracetam (N) was sourced from Xiamen Top Health. All solvents used are commercially available from VWR. Solvents were used as received without any additional purification. nefiracetam was purified by slurrying the compound overnight in ethyl acetate at room temperature after which the suspension was filtered and dried. (RS)-mandelic acid (RSMA, >99%), (S)-mandelic acid (SMA, >99%) and (R)-mandelic acid (RMA, >99%) were purchased respectively from ACROS, TCI and Sigma-Aldrich and used as received.

Cocrystal Conglomerate Screening was performed by liquid-assisted grinding (LAG), using a "Retsch Mixer Mill MM 400" equipped with two grinding jars each able to contain five Eppendorf tubes of 2 mL. Each tube was filled with an equimolar amount (+/-0.3 mmol) of nefiracetam and mandelic acid (RSMA, RMA or SMA), four small stainless-steel beads and 10 µL of methanol. Grinding was then performed at 30 Hz for 90 minutes.

Single Crystal Growth was achieved through evaporative crystallization experiments, performed by preparing undersaturated solutions of an equimolar amount (0.1 mmol) of nefiracetam and mandelic acid (RSMA and RMA) in a suitable amount of solvent. The solutions were then left to evaporate slowly (from three to seven days) at room temperature and the crystals retrieved once they appeared. Solvents tried include ethanol, methanol, acetonitrile (MeCN), tetrahydrofuran (THF), acetone, dichloromethane, chloroform, ethyl acetate (EtOAc), methyl acetate, diethyl ether, 2-propanol and water. Crystals of **NRMA** (1:1 nefiracetam-(R)-mandelic acid cocrystal) suitable for SCXRD were obtained from ethyl acetate.

Congruency Experiments were achieved through slurry crystallization. Slurrying experiments were performed by preparing equimolar suspensions (0.3 mmol) of nefiracetam and mandelic acid (RSMA, RMA or SMA) in the aforementioned solvents. The suspensions were stirred at 700 rpm during 3 days at 25°C in sealed vials using a Cooling Thermomixer HLC. After 2h of stirring, each vial is seeded with all possible solid forms (parent compounds and the enantiopure cocrystal or cocrystal conglomerate). Once the equilibrium reached, the powders were filtered, washed, dried, and analyzed using XRPD.

Enantiopure seeds (**NRMA** and **NSMA**) production was upscaled to ±16 g in ethyl acetate. To do so, equimolar amounts of nefiracetam (12.00 g) and RMA or alternatively SMA (7.41 g) were added to a reactor vessel filled with ethyl acetate (100 mL). The suspension was left to stir (ca. 300 rpm) for 48h at 23 °C, after which the suspension was filtered and the solids washed with ethyl acetate and dried. This material was used as seeding material. **NRSMA** (1:1 nefiracetam-(RS)-mandelic acid cocrystal conglomerate) was upscaled to ±65 g in ethyl acetate as well using a 1L-Reactor-Ready™ Lab Reactor from radleys and the material used for the PC process. Nefiracetam (50.00 g) and (RS)-mandelic acid (30.89 g) were added to 750 mL of ethyl acetate and left to stir at 23 °C. After a two-day time period, the suspension was filtered and the solid recovered as aforementioned.

Powder X-Ray Diffraction (XRPD) data were collected on a PANalytical Bragg-Brentano diffractometer, using Ni-filtered CuKα ($\lambda = 1.54179$ Å) at 45 kV and 30 mA with a X'Celerator detector. Each sample was analyzed between 4 and 40° in 2θ with a step size of ca. 0.0167° and a total scan time of 6min42s.

Single Crystal X-Ray Diffraction (SCXRD) was performed on a suitable single crystal of **NRMA** and analyzed using an Oxford Diffracton Gemini R Ultra diffractometer (Ruby CCD detector using CuKα radiation). Data reduction was carried out using the CrystAlisPRO software package.[39] The resolution and the refinement by full-matrix least squares have been done using respectively SHELXT and SHELX-2018/3.[40] Non-hydrogen atoms were refined anisotropically; H-atoms are added in calculated positions and allowed to ride on the parent atoms, with isotropic displacement factors set to 1.2 Ueq of the parent atoms (Uiso (H)= 1.5 Ueq (C) for methyl). The H-atoms of the methyl groups were allowed to undergo free rotation about the local threefold axis. Symmetry analysis and validation were carried out using PLATON.[41] Figures were made using the molecular visualization software Mercury v4.1.3.[42] CCDC 2023975 and 2032987 include the supplementary crystallographic data and can be downloaded free of charge from The Cambridge Crystallographic Data Centre via www.ccdc.cam.ac.uk/structures

Differential Scanning Calorimetry (DSC) experiments were performed from 25 to 175 °C, with a scanning rate of 5 °C.min^{-1} on a "TA instrument DSC2500". The heating rate was increased to 10 °C.min^{-1} for some of the routine analyses. The solid phases were weighed (6-7 mg) in aluminum pans with perforated lids. The purge gas was nitrogen, with a flow rate of 50 mL.min^{-1}. Indium was used as a reference prior to the analyses. The data were treated using "TA instrument TRIOS v5.1.0.46403" software.

Thermogravimetric Analysis (TGA) was performed on a "Mettler Toledo TGA-STDA 851e", varying the temperature from 25 to 400 °C, at a scanning rate of 10 °C.min^{-1}. Solid samples (7-10 mg) were placed in aluminium oxide crucibles and nitrogen was used as purge gas with a flow rate of 50 mL/min. Data were treated with the "STARe 12.12" software.

Solubility Curves of **NRSMA** and **NRMA** were obtained weighing the solids in increasing amounts in vials of 1.5 mL, topped with 1 mL of acetonitrile and then sealed. Each vial was equipped with a stirring magnet. A heating-cooling cycle was then applied on the vials from 0 to 60 °C with a heating/cooling rate of 0.1 °C.min^{-1} and under a continuous stirring of ca. 700 rpm. Using a "Crystal 16" crystallization system (Technobis), turbidity was continuously monitored, allowing to identify clear (solubility) and cloud (nucleation) points. The software "Crystal Clear 1.0.1.614" was used to process the data and to construct solubility and crystallization curves.

A Binary Phase Diagram (BPD**)** was built by plotting onset and endset of melting obtained from the DSC data performed on a set of 11 samples. Samples were prepared by weighing RMA and SMA in different molar fractions (with n_{tot} = 0.244 mmol) and a constant amount of nefiracetam (n = 0.244 mmol) in Eppendorf tubes of 2 mL. A classical LAG method as described previously is applied on the samples.

Chiral High Performance Liquid Chromatography (cHPLC). Calibration lines for HPLC were constructed to dose RMA by correlating the concentration and the area under the curve (AUC) with a linear equation. The samples were first diluted using a mixture of ethanol and isohexane (1:1) as diluent (dilution factor from 1 to 0.25). The concentrations were dosed using the following HPLC parameters: Device: Waters Alliance 2695; Column: Chiralpak® IC, 4.6x250 mm, 5 µm; Detector : Waters 996 Photodiode Array Detector (PDA) (Max Plot); T° = 25 °C; Injection volume: 10 µL; Flow : 1 mL.min^{-1}; Mobile Phase : 95 % isohexane (iHex), 5 % 2-propanol (IPA), 0.1 % trifluoroacetic acid (TFA); Equilibrate time of 30 min. and wash of the column with isohexane/ethanol (80:20) after 3 sample runs; Stop time: 30 min. The calibration line is reported in the Supporting Information. Slight changes in the mobile phase (iHex, IPA and TFA) composition strongly impact the elution and therefore retention times may vary from one experiment to another.

Reverse High Performance Liquid Chromatography (rHPLC). Calibration lines for High Performance Liquid Chromatography (HPLC) were first built to dose nefiracetam by correlating the area under the curve (AUC) and the concentration prepared with a linear equation. The filtered liquid phase from the **NRSMA** suspensions in MeCN were first diluted 4000x using an acetonitrile 1:1 water MilliQ (in volume) diluent. nefiracetam concentrations were dosed using the following HPLC parameters: Device: Waters Alliance 2695; Column: Waters Sunfire C_{18}, 4.6x100 mm, 3.5 µm; Detector: PDA 2998 (MaxPlot); T° = 40 °C; Injection volume: 10 µL; Flow: 1.2 $mL.min^{-1}$; Mobile phase A : H_2O + 0.1% H_3PO_4; Mobile Phase B : CH_3CN + 0.1% H_3PO4; Gradient: 0 min → 30 % B; 0.5 min → 30 % B; 4.5 min → 90 % B; 6.5 min → 90 % B; Stop time: 15 min. The **NRSMA** solubility is extrapolated from the nefiracetam concentration. The calibration line is reported in the Supporting Information (**Figures 8-3-14** to **16**).

An isothermal section of the **Ternary Phase Diagram** (TPD) at 23 °C in MeCN of the NRSMA conglomerate was represented using the software "ProSim Ternary Diagram". To do so, 11 slurry samples were prepared by weighing RMA and SMA in different molar fractions (with n_{tot} = 0.5 mmol) and an equimolar and constant amount of nefiracetam (n = 0.5 mmol) in a constant volume of 0.5 mL of acetonitrile. The vials were then sealed and stirred at 700 rpm for 3 days at 23 °C. Once the equilibrium reached, the saturated mother liquors were recovered by filtration and 20 µL of each liquid phase weighed (m_{tot}) and diluted 250-fold, using a (1:1) ratio mixture of isohexane and ethanol. 20 µL from each dilution is injected in the chiral HPLC. The aforementioned calibration line, yield the concentration and so, the molar fraction of **NRMA** and/or **NSMA**. The molar amount of nefiracetam is equivalent to the total amount of mandelic acid in solution and the molar fraction of the solvent is deduced by mass balance.

Preferential Crystallization Process. The preferential crystallization experiments in single (SIPC and S3PC) vessel have been performed in an "EasyMax 102 Advanced Workstation (Mettler Toledo)", equipped with two jacket flasks of 100 mL, stirring and temperature control (resolution 0.1 °C). To create a saturated solution for the SIPC mode, a **NRSMA** conglomerate suspension was prepared at temperature T1. Once the equilibrium (24h is considered here) reached, the suspension was filtered, and the filtrate saturated at temperature T1, rapidly cooled down to the crystallization temperature T2 (without any spontaneous nucleation observable). Homochiral seeds of **NRMA** were then added to the crystallizer reducing stirring to 150 rpm allowing the preferential crystallization to set in. The batch crystallization process was stopped after a given time t_{end}. The solid phase was recovered through filtration and washed with cold ethyl acetate. In case of a S3PC mode, the saturated solution is seeded at T1 and a slow cooling ramp (cfr **Table 6-2**) is applied until T2.

Liquid Phase Sampling. For the kinetic follow-up of the process a volume of 250 µL of the liquid phase was sampled every 10 min, using a 1 mL syringe with a microfilter (porosity 0.2 µm) to follow the *ee* over time.

Solid Phase Sampling. For the kinetic follow-up of the process a volume of 2 mL of the liquid phase containing solid particles was sampled every 10 min, using a 2 mL syringe. The liquid phase is then filtered and the solid recovered. No washing is applied.

6.4. Results and Discussion

6.4.1. Nefiracetam-(RS)-Mandelic Acid Cocrystal Conglomerate

In our previous work[31], we set out to enhance nefiracetam solubility through cocrystallization. A cocrystal screen was performed, choosing potential coformers based on supramolecular synthons. As nefiracetam exhibits an amide group, carboxylic acids were the obvious choice, as the acid-amide heterosynthon is often encountered in cocrystals. Grinding a 1:1 mixture of (RS)-mandelic acid with nefiracetam led to the formation of a new solid phase as shown in **Figure 6-2**, with the ground product exhibiting easily observable peaks (at 2θ = 4.71°, 9.43°, 9.93°, 14.09°, 14.96° and 17.46°) not belonging to the parent compounds. Furthermore, the characteristic peaks of nefiracetam and (RS)-mandelic acid were no longer present in the ground material.

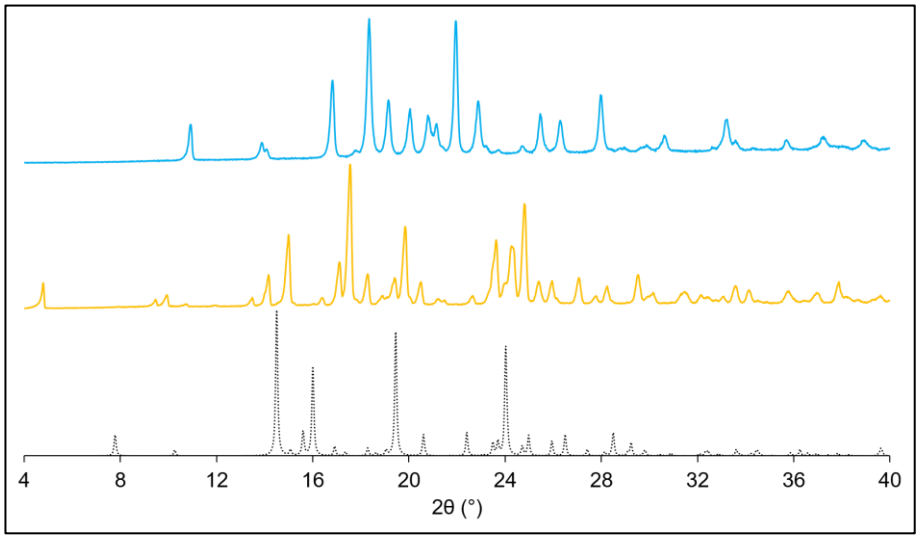

Figure 6-2. Simulated diffraction patterns (dashed line) and experimental powders (full line) of nefiracetam FI (black), 1:1 nefiracetam-(RS)-mandelic acid ground product (orange) and (RS)-mandelic acid (light blue).

Single crystals were then grown to confirm cocrystal formation starting from a nefiracetam/mandelic acid racemate (1:1) undersaturated solution in ethyl acetate through evaporative crystallization. Single crystal X-ray diffraction (SCXRD) measurements were carried out using a Cu-radiation allowing ful characterization of the crystal and determination of its absolute configuration of the crystal. The crystal presented a cube-like shape (**Figure 6-5B**) and was shown to be a 1:1 cocrystal of nefiracetam and (R)-mandelic acid in the chiral orthorhombic $P2_12_12_1$ space group. The crystal was harvested from a mixture containing both R and S mandelic acid and the absolute configuration was unambiguously assigned by analysis of the anomalous difference, the refined Flack parameter was -0.03(10). Further SCXRD experiments on a single crystal grown by evaporation from a nefiracetam-(R)-mandelic acid solution resulted in a similar Flack parameter (-0.07(6)). The main crystallographic and refinement parameters are summarized in **Table 8-3-1** in the Supporting Information. The molecules of nefiracetam are linked together via strong intermolecular amide-amide hydrogen bonds (O2⋯H2-N2, 2.834(2) Å, 171(2) °), between the -NH moiety of the amide group and the carbonyl moiety of the amide group of a neighbouring molecule (**Figure 6-3A)**. This arrangement leads to a $C_1^1(4)$ hydrogen bonding pattern according to the Etter's graph notation.[43] Each mandelic acid molecule is shown to share two hydrogen bonds (**Figure 6-3B**). A first hydrogen bond is formed with another mandelic acid molecule, between the carbonyl moiety of the carboxylic acid group of one molecule and the hydroxyl group of the other (O4⋯H5-O5, 2.762(3) Å, 16 (4)°). The second hydrogen bond is found between mandelic acid and a nefiracetam molecule, with the -OH moiety of the carboxylic acid

group of mandelic acid linking to the carbonyl moiety of the γ-lactam ring (O1···H3-O3, 2.601(3) Å, 162(3) °). These hydrogen bonding patterns can be described by a $C_1^1(4)$ infinite chain pattern for the intermolecular hydrogen bond O4···H5-O5 and a $D_1^1(2)$ finite pattern for the hydrogen bond O1···H3-O3 between mandelic acid and nefiracetam molecules. To allow for both hydrogen bonding patterns, all mandelic acid molecules must have the same absolute configuration. Overall (**Figure 6-3C)** sheets of nefiracetam molecules are present thanks to the amide-amide interactions. These sheets are linked together by dimeric layers of mandelic acid molecules. The orientation of the hydrogen atom on the asymmetric carbon alternates from one layer to the other. Such an orientation does not allow for mandelic acid molecules of opposite handedness.

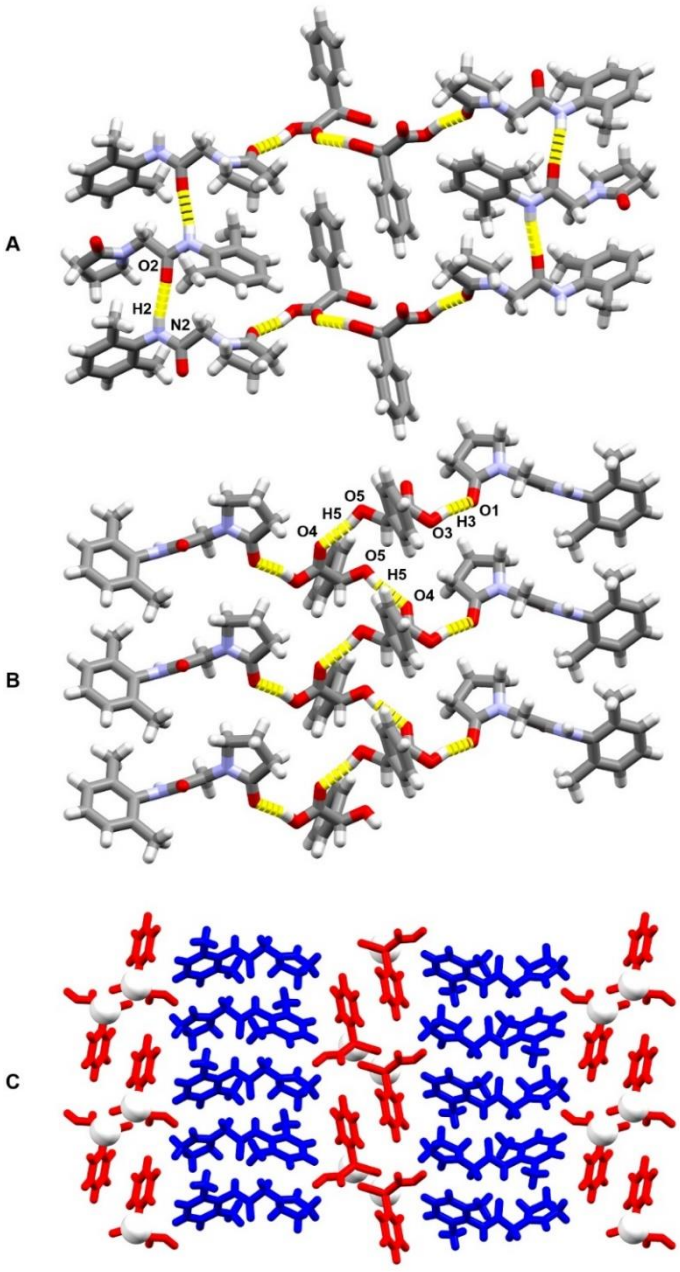

Figure 6-3. View along the (**A**) a-axis and (**B**) b-axis showing the hydrogen bond network in the NRMA cocrystal. Atoms involved in the hydrogen bond pattern description are labelled. Wide view along the a-axis (**C**) of the NRMA cocrystal. Nefiracetam and (R)-mandelic acid are respectively colored in blue and red. The hydrogens on the asymmetric carbon of (R)-mandelic acid are highlighted using spacefill representation.

As the initial enantiopure nefiracetam-(R)-mandelic acid single crystal was grown from a racemic solution, conglomerate formation was suspected. Furthermore, the simulated XRPD pattern from this structure fits with that obtained by grinding of racemic mandelic acid with nefiracetam. To confirm conglomerate formation, slurry crystallization experiments were performed in ethyl acetate using racemic as well as enantiopure mandelic acid and an equimolar amount of nefiracetam. The obtained patterns are shown in **Figure 6-4**. XRPD does not indicate parent compounds to be present in the isolated solids, indicating a congruent behaviour of the cocrystal in this solvent. Furthermore, XRPD patterns of the racemic and enantiopure slurry products perfectly overlap, and correspondence more to the simulated pattern of the enantiopure single crystal.

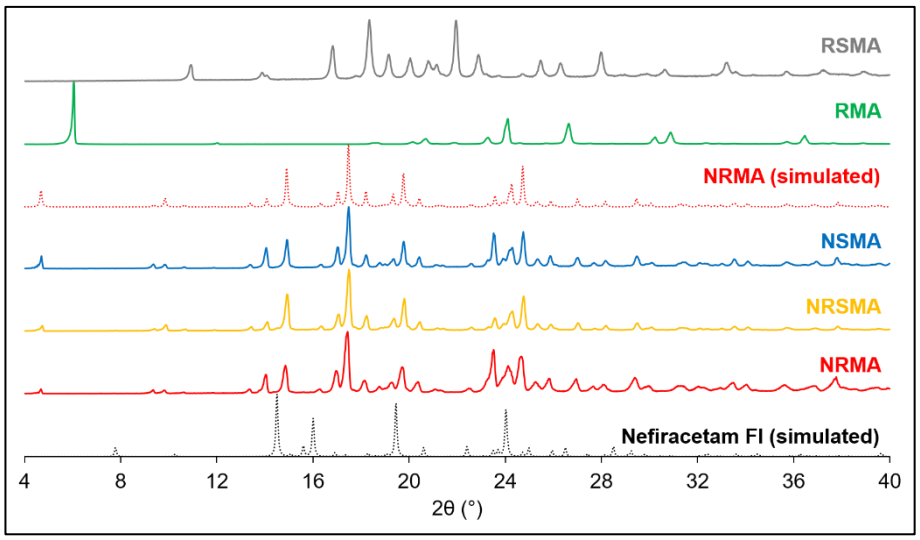

Figure 6-4. Simulated diffraction patterns from single crystal (dashed line) and experimental powders (full line) of nefiracetam simulated (black), 1:1-nefiracetam-(R)-mandelic acid (NRMA, red), 1:1-nefiracetam-(RS)-mandelic acid (NRSMA, orange), 1:1-nefiracetam-(S)-mandelic acid (NSMA, blue), 1:1-nefiracetam-(R)-mandelic acid simulated (NRMA, red), (R)-mandelic acid (RMA, green) and (RS)-mandelic acid (RSMA, grey) from slurry experiments in ethylacetate.

Further proof of conglomerate formation was given by hand-picking a single cube-like cocrystal obtained from a nefiracetam-(RS)-mandelic acid cooling experiment and analyzing this latter by chiral HPLC. In parallel, the overall powder obtained upon full evaporation of an undersaturated nefiracetam-(RS)-mandelic acid solution was also tested as a reference. As expected this latter shows two distinct peaks, at retention times of 9.403 min (RMA) and 10.189 min (SMA) (**Figure 6-5A**), with a 50:50 R/S

composition. For the former however, a single retention peak is observed (**Figure 6-5B**), confirming the enantiopurity of the crystals obtained.[a]

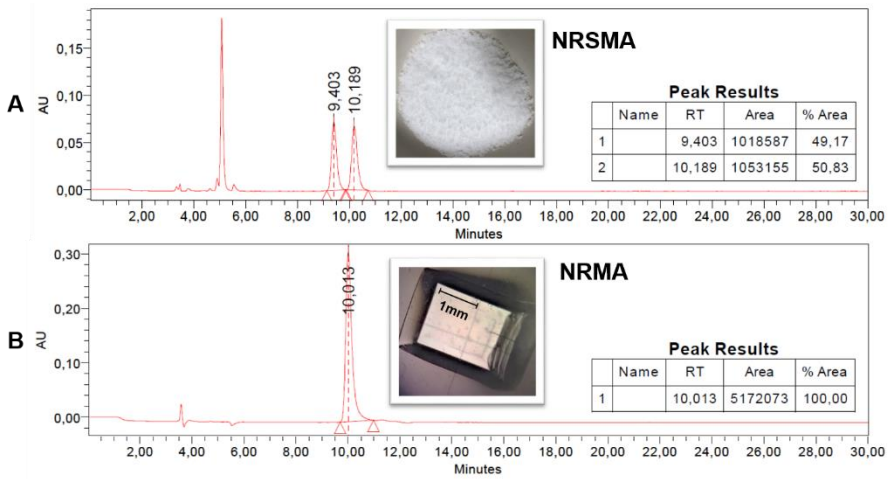

Figure 6-5. cHPLC chromatograms of (A) NRSMA bulk material and (B) a single crystal from a cooling experiment of NRSMA in ethyl acetate. Pictures of the NRSMA bulk material as well as the NRMA single crystal are provided as well. The full chromatograms are presented in the Supporting Information (**Figure 8-3-4**).

As final proof of conglomerate formation, a binary melting diagram was constructed. **Figure 6-7** shows a diagram typical of a conglomerate with a single eutectic melt at the racemic composition. **NRMA** (and **NSMA**) shows a melting temperature at 114.9 °C, whereas the eutectic melt is located at 98.4 °C (**Figure 6-6**)[b]. DSC data required for the diagram construction are presented in the Supporting Information (**Table 8-3-2** and **Figure 8-3-1**). Integration of both peaks shows an enthalpy of fusion ΔHf of about 40.3 kJ.mol^{-1} for **NRSMA** and 48.6 kJ.mol^{-1} for **NRMA**. The negative value of the difference in enthalpy of fusion ($\Delta\Delta H_f$ is -8.3 kJ.mol^{-1}), is typical for a conglomerate forming system.[44] The theoretical melting point in case of a conglomerate may be also extrapolated by the Schröder-van Laar equation using the melting point and the enthalpy of fusion of the enantiopure form. The value calculated is about 97.8 °C and matches the one determined by DSC (98.4 °C).[45-47] A ternary phase diagram in MeCN at 23 °C is also presented in the Supporting Information

[a] Retention times vary from sample to sample as they significantly depend on the composition of the mobile phase.
[b] TGA analysis (**Figure 8-3-2**) of **NRMA** does not show any degradation prior to 175 °C, implying degradation was overlapping with the calorimetric measurements needed to construct the phase diagram.

(**Table 8-3-3** and **Figures 8-3-5** to **9**), once more evidencing the conglomerate behavior of the system.

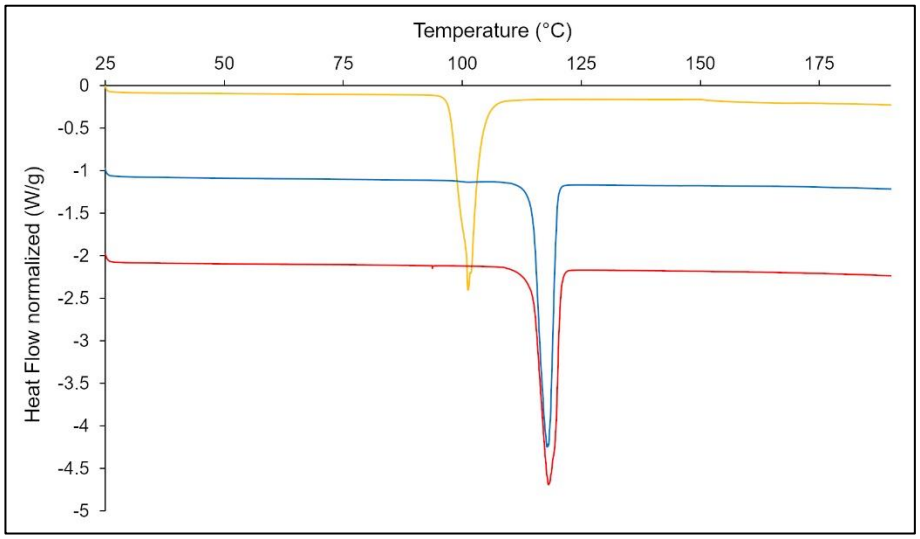

Figure 6-6. DSC curves of NRSMA bulk material (orange), NSMA (blue) and NRMA (red).

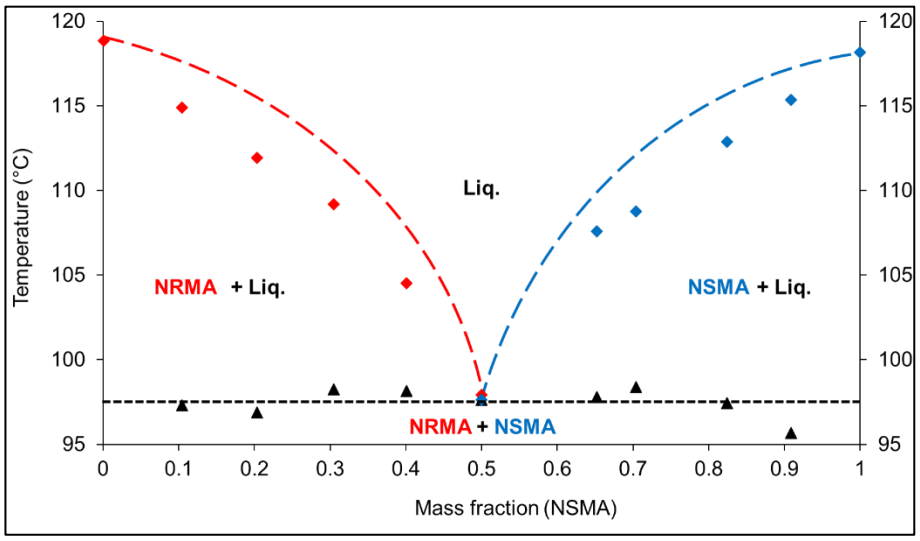

Figure 6-7. Binary Melting Phase diagram of the nefiracetam-(RS)-mandelic acid system. The diagram is typical of a conglomerate forming system.

6.4.2. Chiral Resolution of Mandelic Acid by Preferential Cocrystallization

We then set out to resolve mandelic acid through a preferential cocrystallization process, which up to now has only been developed in one specific case.[28] Compared to classical preferential crystallization, preferential cocrystallization is faced not only with the risk of having both enantiomers crystallizing out, but also with that of a parent compound crystallizing out instead of the cocrystal. An ideal solvent, therefore not only needs to show a wide meta-stable zone, but also needs to lead to a congruent system. Congruency experiments were performed in acetonitrile, chloroform, dichloromethane, diethyl ether, ethanol, water, 2-propanol, tetrahydrofuran and ethyl acetate. Results are presented in the Supporting Information and reveal that the system is congruent in most of the solvents with exception of THF, 2-propanol and water. Preferential crystallization trials in ethyl acetate led to spontaneous nucleation of nefiracetam upon seeding (Supporting information), and this solvent could therefore not be used for further development. Out of the remaining solvents, acetonitrile was selected for further development. Solubility curves (**Figure 6-8**) of both nefiracetam-mandelic acid conglomerate (**NRSMA**) and the enantiopure cocrystal (**NRMA** or **NSMA**) were established. The cocrystal responds to Meyerhoffer's double solubility rule[46], e.g. at 23 °C the solubility of the **NRSMA** conglomerate is 180.15 $mg.mL^{-1}$ whereas that of the enantiopure cocrystal is 88.53 $mg.mL^{-1}$. Furthermore, the rapid increase in solubility from 20 °C onwards, already highlights the fact that any crystallization process is ideally performed with filtration below this temperature to avoid important losses in the mother liquor. Using a Van't Hoff plot (**Figure 8-3-3**) the enthalpy ΔH_{diss} and entropy ΔS_{diss} of dissolution of **NRMA** at 25 °C are determined as 81.8 $kJ.mol^{-1}$ and 251.2 $J.mol^{-1}.K^{-1}$ respectively. The values for the conglomerate mount up to 94.5 $kJ.mol^{-1}$ and 305.9 $J.mol^{-1}.K^{-1}$.

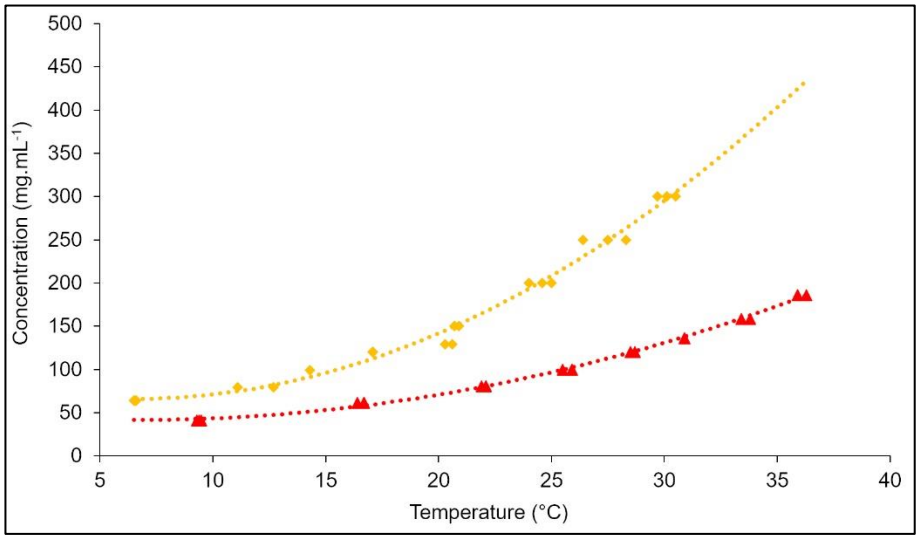

Figure 6-8. Solubility curves of **NRSMA** (orange) and **NRMA** (red) in MeCN.

We then attempted to resolve the racemate using a conventional single batch preferential crystallization (see Material and Methods), more precisely in a Seeded Isothermal Preferential Crystallization (SIPC) mode. A series of 15 experiments were performed with the most representative ones shown in **Table 6-2**, and the remaining ones placed in the Supporting Information (**Tables 8-3-4** to **5**).

Table 6-2. Process parameters and results of the 8 most representative SIPC trials (7 more experiments were performed and results shown in the Supporting information).

N°	PC Mode	V (mL)	T1 (°C)	T2 (°C)	Cooling rate (°C.min^{-1})	t_{end} (min)	Starting mass NRSMA (g)	m_{seed} (mg)	m_{end} (mg)
1	SIPC	100	23	17	1.7	120	21.06	50.43	2317.71
2	SIPC	100	23	17	1.7	60	17.34	50.20	864.42
3	SIPC	100	23	17	1.7	60	14.79	100.19	1085.41
4	SIPC	100	23	17	1.7	60	14.21	200.85	948.45
5	SIPC	750	23	17.5	0.1	180	120.36	375.47	34096.23
6	SIPC	750	23	17.5	0.1	60	133.13	376.80	2871.75
7	S3PC	100	23	17	0.07	90	18.29	51.42	243.77
8	S3PC	100	23	17	0.03	180	17.63	51.30	308.46

DSC (**Figure 6-9)** and chiral HPLC (**Figure 6-10**) analyses were performed on all solids recovered. The Resolution Index (RI) allows evaluating the efficiency of the separation according to Eq. 1 with $m_{recovered}^{(NRMA)}$ the total mass of material recovered corrected using the enantiopurity[3] to determine the amount of R-enantiomer. The enantiopurity is given by chiral HPLC (%Area). An efficient resolution ideally has a RI superior to 2[3]. The yield (γ, Eq. 3) reflects the amount of enantiopure cocrystal coming out vs. the maximum amount that can be crystallized according to the solubility data (**Figure 6-8**). The productivity ($Pr^{(NRMA)}(t)$, Eq. 2) of the process is then defined as the amount of **NRMA** that crystallized out per unit time[38], compared to the maximum amount of **NRMA** that can potentially crystallize out. The productivity is only estimated when the purity is over 90%. The supersaturation ratio β_{mass} (Eq. 4) is obtained by considering the solubility at T1 - m_{NRSMA} (T1) - and (T2) - m_{NRSMA} (T2), respectively being the mass required to saturate the solution at T1 and T2.

$$RI = \frac{m_{recovered}^{NRMA} - m_{seed}}{m_{seed}} \quad \text{(Eq. 1)}$$

$$Pr^{(NRMA)}(t) = \frac{m_{recovered}^{(NRMA)} - m_{seed}}{t \times 0.5 \times m^{NRSMA}} \quad \text{(Eq. 2)}$$

$$\gamma = \frac{m_{recovered}^{(NRMA)} - m_{seed}}{0.5 \times (m^{NRSMA}\,(23°C) - m^{NRSMA}\,(17°C))} \quad \text{(Eq. 3)}$$

$$\beta_{mass} = \frac{m_{NRSMA\,(T1)}}{m_{NRSMA\,(T2)}} \quad \text{(Eq. 4)}$$

Results are reported in **Table 7-3**.

Table 6-3. Values of purity (Pu), resolution index (RI), supersaturation degree (β_{mass}) productivity (Pr) and yield (γ) for the experiments of Table 2. Parameters are only calculated for NRMA with purity >90%.

N°	Pu NRMA (%)	β_{mass}	RI	Pr NRMA (10^{-3} g.g^{-1}.min^{-1})	γ yield (%)
1	49.78	1.74	n/a	n/a	n/a
2	98.21	1.43	15.91	1.54	27.05
3	96.36	1.22	9.44	2.13	32.04
4	99.20	1.17	4.19	1.74	25.07
5	50.51	1.32	n/a	n/a	n/a
6	96.79	1.47	6.38	0.60	11.70
7	98.73	1.51	3.68	0.23	8.55
8	95.63	1.45	4.75	0.15	11.01

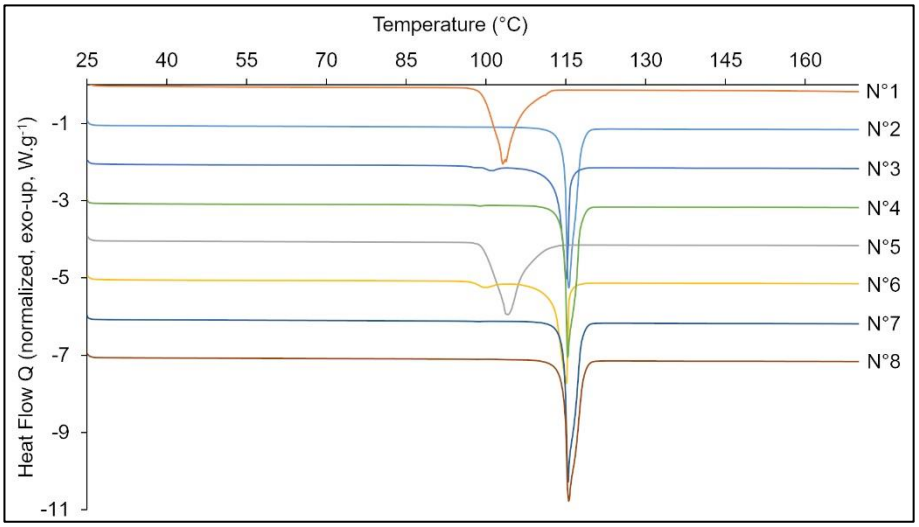

Figure 6-9. DSC analyses performed on the solid outcomes of trials 1 to 8.

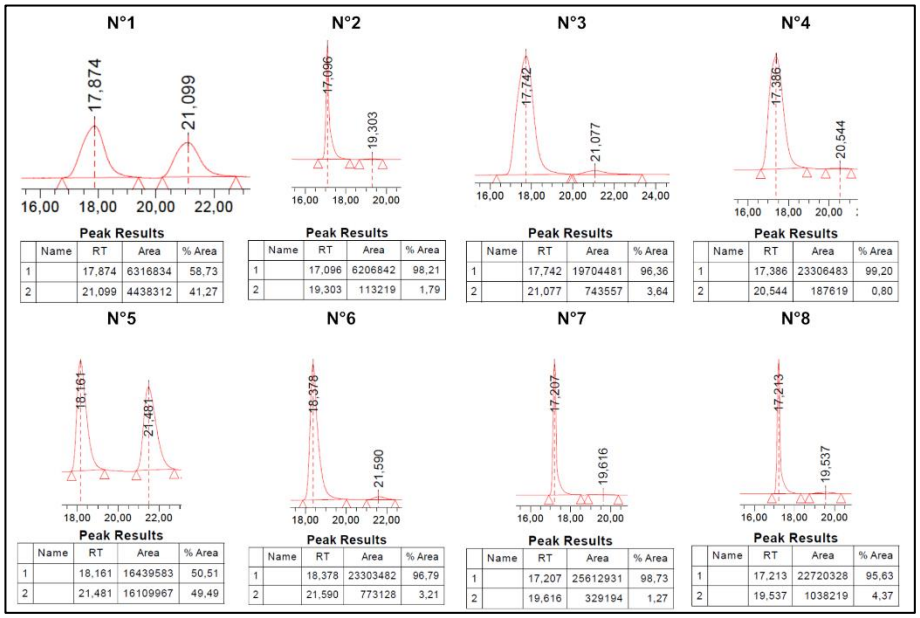

Figure 6-10. View of HPLC data related to each trial. The full chromatograms are presented in the Supporting Information (**Figures 8-3-17** to **19**).

Preliminary trials revealed a working supersaturation of 6 °C (23-17 °C) and associated β_{mass} of 1.2-1.5 to be suitable conditions for the PC process To have an approximate idea of when to expect the heterogeneous nucleation of the S-enantiomer at a 100 mL scale, a 120 min trial (**N°1**) was performed sampling the liquid phase. **Figure 6-11A** (HPLC data in Supporting Information) shows the solution *ee* over time, with t = 0 min corresponding to the addition of **NRMA** seed. The solution *ee* is shown to increase over time until approximatively 70 min, implying a depletion of the solution in R-enantiomer. After this the *ee* no longer increases, and a decrease clearly sets in after 90 min. A racemic composition of the supernatant solution is obtained once again after 110 min. We expect the heterogeneous nucleation of **NSMA** therefore to occur about 70 min into the process. In ideal circumstances, the process needs to be interrupted prior to this nucleation event. As nucleation is stochastic, we decided for the next series of experiments, to work with an end-time of 60 min which should allow sufficient crystallization of **NRMA**, while avoiding heterogeneous nucleation of the counter enantiomer.

Three experiments were then repeated under almost identical conditions, with exception of the amount of seed (**N°2**, **N°3** and **N°4**). These confirm obtention of enantiopure material after 60 min of process time (**Table 6-3**), which is also highlighted by a single melting endotherm at 115 °C corresponding to the **NRMA** cocrystal (**Figure 6-9**). The presence of traces of the S-enantiomer is due to the fact

that the small amounts recovered did not allow washing the solid. Increasing the amount of seed (comparing experiments **N°2** to **N°4**) leads to a similar yield (+/- 30%) and associated productivity (1-2 $\times 10^{-3}$ $g.g^{-1}.min^{-1}$). The Pr values calculated of 10^{-4}-10^{-3} $g.g^{-1}.min^{-1}$ (**Table 6-3**) are in the average order of magnitude in comparison with the literature.[38, 49] Inherently increasing the amount of seed, initially brings more crystals to the process, and hence an increase rate at which the solution is depleted in R-enantiomer. Based on these results and, as small amounts of seed lead to higher RI-values, 50 mg of seed was kept as parameter for further development.

Upscaling the process to 750 mL, we again carried out a time-analysis of the process, this time focusing on the solid phase crystallizing out, as sufficient material can now be recovered for analysis. **Figure 6-11B** clearly pinpoints the nucleation of the counter-enantiomer after 60 minutes of process time and a conglomerate to be obtained after about 100 min. One however has to be careful comparing this result with that obtained at the 100 mL scale, as for this latter, cooling from 23 °C to 17 °C occurs in a couple of minutes, where this takes up to 60 min for the 1 L scale. During this one hour period (prior to t = 0 of seeding), the solution is in a meta-stable state.

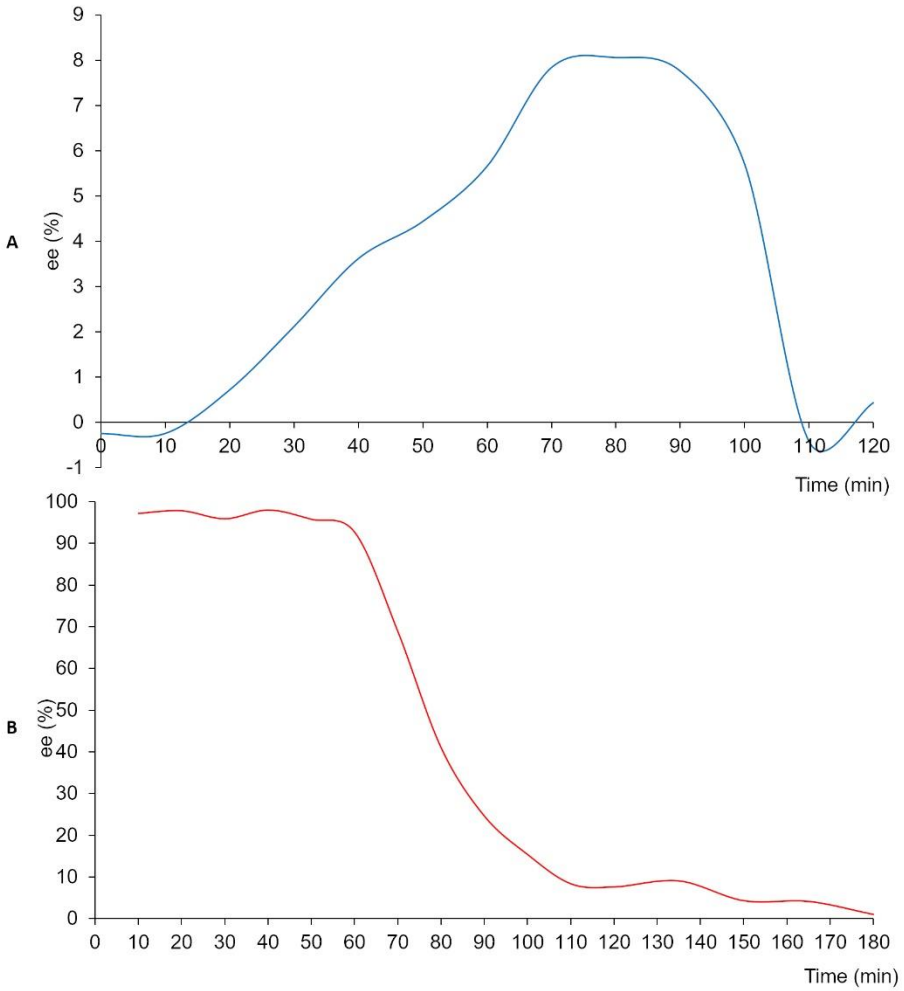

Figure 6-11. (A) **NSMA** enantiomeric excess in the liquid phase for the 100 mL resolution process and (B) **NRMA** enantiomeric excess in the solid phase for the 750 mL resolution process. t = 0 min is the addition of the seeds. The HPLC data used to build the diagram are presented in the Supporting Information (**Figures 8-3-27** to **32**).

Interrupting the upscaled experiment after 60 min (**N°6)** leads to a yield of 2.87 g (γ =11.7%) and material of high enantiopurity (96.79%) with values of RI comparable to those of the small-scale experiments albeit showing somewhat lower productivity (**Table 6-3**). The 3% counter enantiomer present in the solid phase (small eutectic endotherm in **Figure 6-9**), can once more be explained by poor washing or potential onset of nucleation of the unseeded enantiomer prior to filtration.

We then set out, to verify the resolution using a S3PC mode. In this mode, seeding is performed at the dissolution temperature T1, so the highest temperature possible for

crystals of **NRMA** and **NSMA** to be in equilibrium with a saturated solution. Using a slow cooling ramp, the S3PC mode allows for continuous crystallization of the seed material. Two trials, **N°7** and **N°8**, were performed in this mode using a cooling rate of 0.067 °C.min^{-1} (90 min) and 0.05 °C.min^{-1} (180 min) respectively. Upon reaching T2 the suspension is filtered. Enantiopure product (98.73%; **Figure 6-10**) is observed for the 90 min process (**N°7**), whereas the 180 min process (**N°8**) shows a slightly more important amount of **NSMA** present (4.4%) attributed to potential onset of crystallization of the counter-enantiomer or to insufficient washing. Calorimetric measurements once again show a single melting endotherm at 115 °C corresponding to **NRMA** (**Figure 6-9)**. The S3PC mode leads to lower yield and productivity compared to the SIPC mode. This can be attributed to the lower crystallization kinetics, as supersaturation is kept low during all along the process. As an advantage, this leads to the nucleation of the counter-enantiomer to be less likely, shown by the longer process times accessible without nucleation of this latter.

Finally, we focused on the feasibility of having a cyclic preferential crystallization, allowing recovering both enantiomers and highlighting a potential towards industrialization of this process. To do so, a 6-cycle experiment was performed, starting, with a classical SIPC set-up described previously[a]. Reaching the end of the first step, the suspension is filtered, and the mother liquor recovered for a second cycle. The recovered mother liquor is fed with an amount of **NRSMA** conglomerate equivalent to the amount of solid that crystallized out during the previous step, keeping an overall constant concentration. To dissolve the added material, the suspension was slightly heated above T1 until complete dissolution, and the solution cooled once again to a temperature of 17 °C (T2). The solution is then seeded at T2 with the desired homochiral seeds. This procedure was then repeated for all following steps. First of all, **Table 6-4** shows that each step leads to enantiopure material, alternating as expected from one enantiomer to the other. In no instance, did we encounter nucleation of the counter-enantiomer. Furthermore, addition of racemate at the onset of steps 2 to 5 leads to solution material which shows a slight excess in one of the two enantiomers, as could be expected. Overall, the six steps of the cycle, allowed resolving about 2.36 g of **NRSMA**. This cycled experiment shows the feasibility of multiple successive entrainment experiments using a racemic feed between each step.

[a] In a 100 mL vessel – T1 = 23 °C – cooling rate of 1.7 °C.min^{-1} – seeding at 17 °C (T2) – 50 mg of seeds – a process time of 60 min.

Table 6-4. Cyclic experiment outcome. Values are given for each step. Solution ratio of R/S prior to entrainment, mass of NRSMA cocrystal present in solution, mass of seed added, mass of feed added at the onset of each step, mass recovered in enantiopure material, and purity of this latter. HPLC and DSC results are shown in the Supporting Information (Figures 9-3-37 to 39). Results for the R-enantiomer are given in red, and the S-enantiomer in blue.

Cycle	Ratio R/S	m_{NRSMA} (mg)	m_{seed} (mg)	m_{feed} (mg)	$m_{recov.}$ (mg)	Pu (%)
1	50.45:49.55	17338	50.18	/	368.22	98.66
2	48.62:51.38	15652	51.65	371.5	685.03	97.87
3	51.23:48.77	16371	50.28	685.96	488.14	97.99
4	48.96:51.04	16890	51.15	490.85	310.98	98.17
5	50.49:49.51	16941	50.20	311.36	139.68	98.99
6	49.47:50.53	15882	51.69	141.15	363.24	98.14

6.5. Conclusion

We report a first complete chiral resolution of mandelic acid preferential cocrystallization. Complementary techniques confirm the existence of a stable mandelic acid nefiracetam dual-drug cocrystal conglomerate. Starting from this conglomerate, a preferential cocrystallization procedure is developed in a seeded isothermal SIPC mode, leading to enantiopure material (up to 98-99%) recovered by the entrainment process with a maximum productivity of 1.74×10^{-3} $g.g^{-1}.min^{-1}$. Follow-up of the solution and solid composition over time, show spontaneous nucleation of the counter-enantiomer to occur only after 70 to 80 min. The process was not only shown to be easily upscalable, but also to lend itself to a cyclic procedure, resolving both enantiomers. Doing so we were able to resolve 2.4 g of racemic mandelic acid leading to enantiopure material. We believe this process to not only have relevant applications at a larger scale (e.g. continuous preferential crystallization), but also to pave the way for other systems which form a conglomerate through cocrystallization.

6.6. References

1. Nguyen, L. A.; He, H.; Pham-Huy, C., Chiral drugs: an overview. *Int. J. Biomed. Sci.* **2006,** *2* (2), 85.
2. Cahn, R. S.; Ingold, C.; Prelog, V., Specification of molecular chirality. *Angew. Chem., Int. Ed. Engl.* **1966,** *5* (4), 385-415.
3. Lin, G.-Q.; You, Q.-D.; Cheng, J.-F., *Chiral drugs: Chemistry and biological action*. John Wiley & Sons: Hoboken, New Jersey, 2011.

4. Blaser, H.-U., Chirality and its implications for the pharmaceutical industry. *Rend. Accad. Naz. Lincei*. **2013,** *24* (3), 213-216.
5. Francotte, E.; Lindner, W., *Chirality in drug research*. Wiley-VCH Weinheim: Weinheim, Germany, **2006**; Vol. 33.
6. Maier, N. M.; Franco, P.; Lindner, W., Separation of enantiomers: needs, challenges, perspectives. *J. Chromatogr. A* **2001,** *906* (1-2), 3-33.
7. H Brooks, W.; C Guida, W.; G Daniel, K., The significance of chirality in drug design and development. *Curr. Trends Med. Chem.* **2011,** *11* (7), 760-770.
8. Blaser, H. U., The chiral pool as a source of enantioselective catalysts and auxiliaries. *Chem. Rev.* **1992,** *92* (5), 935-952.
9. Ager, D. J.; Prakash, I.; Schaad, D. R., 1, 2-Amino alcohols and their heterocyclic derivatives as chiral auxiliaries in asymmetric synthesis. *Chem. Rev.* **1996,** *96* (2), 835-876.
10. Noyori, R., Asymmetric catalysis: science and opportunities (Nobel Lecture). *Angew. Chem., Int. Ed.* **2002,** *41* (12), 2008-2022.
11. Jacobsen, E. N.; Pfaltz, A.; Yamamoto, H., *Comprehensive asymmetric catalysis: Supplement 1*. Springer Science & Business Media: Berlin, Germany, **2003**; Vol. 1.
12. Chen, C. S.; Fujimoto, Y.; Girdaukas, G.; Sih, C. J., Quantitative analyses of biochemical kinetic resolutions of enantiomers. *J. Am. Chem. Soc.* **1982,** *104* (25), 7294-7299.
13. Beesley, T. E.; Scott, R. P., *Chiral chromatography*. John Wiley & Sons: Chichester, England, **1999**.
14. Kozma, D., *CRC handbook of optical resolutions via diastereomeric salt formation*. CRC Press: New York, United-States of America, **2001**.
15. Harmsen, B.; Leyssens, T., Dual-Drug Chiral Resolution: Enantiospecific Cocrystallization of (S)-Ibuprofen Using Levetiracetam. *Cryst. Growth Des.* **2017,** *18* (1), 441-448.
16. Springuel, G.; Leyssens, T., Innovative chiral resolution using enantiospecific co-crystallization in solution. *Cryst. Growth Des.* **2012,** *12* (7), 3374-3378.
17. Coquerel, G., Preferential crystallization. In *Novel optical resolution technologies*, Springer: Berlin, Germany, **2006**; pp 1-51.
18. Levilain, G.; Coquerel, G., Pitfalls and rewards of preferential crystallization. *CrystEngComm* **2010,** *12* (7), 1983-1992.
19. Srisanga, S.; ter Horst, J. H., Racemic compound, conglomerate, or solid solution: phase diagram screening of chiral compounds. *Cryst. Growth Des.* **2010,** *10* (4), 1808-1812.
20. Sakai, K.; Hirayama, N.; Tamura, R., *Novel optical resolution technologies*. Springer: Berlin, Germany, **2007**; Vol. 269.

21. Galland, A.; Dupray, V.; Berton, B.; Morin-Grognet, S.; Sanselme, M.; Atmani, H.; Coquerel, G. r., Spotting conglomerates by second harmonic generation. *Cryst. Growth Des.* **2009,** *9* (6), 2713-2718.
22. Li, W. W.; Spix, L.; De Reus, S. C.; Meekes, H.; Kramer, H. J.; Vlieg, E.; ter Horst, J. H., Deracemization of a racemic compound via its conglomerate-forming salt using temperature cycling. *Cryst. Growth Des.* **2016,** *16* (9), 5563-5570.
23. Wacharine-Antar, S.; Levilain, G.; Dupray, V.; Coquerel, G., Resolution of (±)-imeglimin-2, 4-dichlorophenylacetate methanol solvate by preferential crystallization. *Org. Process Res. Dev.* **2010,** *14* (6), 1358-1363.
24. Guillot, M.; de Meester, J.; Huynen, S.; Collard, L.; Robeyns, K.; Riant, O.; Leyssens, T., Co-crystallization induced spontaneous deracemization: A general thermodynamic approach to deracemization. *Angew. Chem., Int. Ed.* **2020**, *132* (28), 11399-11402.
25. Blagden, N.; de Matas, M.; Gavan, P. T.; York, P., Crystal engineering of active pharmaceutical ingredients to improve solubility and dissolution rates. *Adv. Drug Delivery Rev.* **2007,** *59* (7), 617-630.
26. Friščić, T.; Jones, W., Benefits of cocrystallisation in pharmaceutical materials science: an update. *J. Pharm. Pharmacol.* **2010,** *62* (11), 1547-1559.
27. Sun, C. C., Cocrystallization for successful drug delivery. *Expert Opin. Drug Delivery* **2013,** *10* (2), 201-213.
28. Harfouche, L. C.; Brandel, C.; Cartigny, Y.; Petit, S.; Coquerel, G., Resolution by Preferential Crystallization of Proxyphylline by Using Its Salicylic Acid Monohydrate Co-Crystal. *Chem. Eng. Technol.* **2020**.
29. Wang, P.-L.; Wang, H.-B.; Ding, W.-L.; Liu, Z.-Q.; Xing, Z.-T., N-(2, 6-Dimethylphenyl)-2-(2-oxo-1-pyrrolidin-1-yl) acetamide. *Acta Crystallogr., Sect. E: Struct. Rep. Online* **2006,** *62* (9), o3838-o3839.
30. Crespi, F., Nefiracetam. Daiichi Seiyaku. *Curr. Opin. Invest. Drugs* **2002,** *3* (5), 788-793.
31. Buol, X.; Robeyns, K.; Caro Garrido, C.; Tumanov, N.; Collard, L.; Wouters, J.; Leyssens, T., Improving Nefiracetam Dissolution and Solubility Behavior Using a Cocrystallization Approach. *Pharmaceutics* **2020,** *12* (7), 653.
32. Buol, X.; Robeyns, K.; Tumanov, N.; Wouters, J.; Leyssens, T., Identifying, Characterizing, and Understanding Nefiracetam in Its Solid State Forms: A Potential Antidementia Drug. *J. Pharm. Sci.* **2019,** *108* (11), 3616-3622.
33. Kesslin, G.; Kelly, K. W., Resolution of racemic mandelic acid. Google Patents: **1982**.
34. Lorenz, H.; Sapoundjiev, D.; Seidel-Morgenstern, A., Enantiomeric mandelic acid system melting point phase diagram and solubility in water. *J. Chem. Eng. Data* **2002,** *47* (5), 1280-1284.
35. Sakai, K.; Sakurai, R.; Yuzawa, A.; Kobayashi, Y.; Saigo, K., Resolution of 3-(methylamino)-1-(2-thienyl) propan-1-ol, a new key intermediate for duloxetine, with (S)-mandelic acid. *Tetrahedron: Asymmetry* **2003,** *14* (12), 1631-1636.

36. Rougeot, C.; Hein, J. E., Application of continuous preferential crystallization to efficiently access enantiopure chemicals. *Org. Process Res. Dev.* **2015,** *19* (12), 1809-1819.
37. Elsner, M. P.; Menéndez, D. F.; Muslera, E. A.; Seidel-Morgenstern, A., Experimental study and simplified mathematical description of preferential crystallization. *Chirality* **2005,** *17* (S1), S183-S195.
38. Elsner, M. P.; Ziomek, G.; Seidel-Morgenstern, A., Efficient separation of enantiomers by preferential crystallization in two coupled vessels. *AIChE J.* **2009,** *55* (3), 640-649.
39. Rigaku, O. D., CrysAlisPro Software System, Version 1.171. 38.41 l, Rigaku Coorporation. Oxford, UK: **2015**.
40. Sheldrick, G. M., Crystal structure refinement with SHELXL. *Acta Crystallogr., Sect. C: Struct. Chem.* **2015,** *71* (1), 3-8.
41. Spek, A. L., Structure validation in chemical crystallography. *Acta Crystallogr., Sect. D: Biol. Crystallogr.* **2009,** *65* (2), 148-155.
42. Macrae, C. F.; Bruno, I. J.; Chisholm, J. A.; Edgington, P. R.; McCabe, P.; Pidcock, E.; Rodriguez-Monge, L.; Taylor, R.; Streek, J. v. d.; Wood, P. A., Mercury CSD 2.0–new features for the visualization and investigation of crystal structures. *J. Appl. Crystallogr.* **2008,** *41* (2), 466-470.
43. Etter, M. C.; MacDonald, J. C.; Bernstein, J., Graph-set analysis of hydrogen-bond patterns in organic crystals. *Acta Crystallogr., Sect. B* **1990,** *46* (2), 256-262.
44. Zhang, G. G.; Paspal, S. Y.; Suryanarayanan, R.; Grant, D. J., Racemic species of sodium ibuprofen: Characterization and polymorphic relationships. *J. Pharm. Sci.* **2003,** *92* (7), 1356-1366.
45. Ianno, V.; Clevers, S.; Négrier, P.; Dupray, V.; Coquerel, G.; Espeau, P., p-Synephrine enantiomers: binary phase diagram, crystal structure and kinetic stability of a metastable conglomerate monitored by nonlinear optics. *CrystEngComm* **2020**.
46. Schröder, I., Dependence of the solubility of a solid on its melting point. *Z. Phys. Chem.* **1893,** *11*, 449-465.
47. Van Laar, J., Process of the fusion curves of firm alloys and amalgams. *Arch. Neerl.* **1903,** *8*, 264-284.
48. Klussmann, M.; White, A. J.; Armstrong, A.; Blackmond, D. G., Rationalization and prediction of solution enantiomeric excess in ternary phase systems. *Angew. Chem., Int. Ed.* **2006,** *45* (47), 7985-7989.
49. Gendron, F.-X.; Mahieux, J.; Sanselme, M.; Coquerel, G., Resolution of Baclofenium Hydrogenomaleate By Using Preferential Crystallization. A First Case of Complete Solid Solution at High Temperature and a Large Miscibility Gap in the Solid State. *Cryst. Growth Des.* **2019,** *19* (8), 4793-4801.

7. Conclusions and Perspectives

The initial aim of this work was to tune the physicochemical properties of nefiracetam, a lipophilic and low water-soluble nootropic compound, using a cocrystallization approach. Prior, a polymorph screening of the target compound was performed as this information was not available for this compound. Surprisingly, we identified three novel solid forms of this API i.e. a monohydrate, a polymorph FII stable at higher temperatures and a metastable polymorph FIII in addition to the known form FI (**Chapter 4**). An exotic stability relationship was established between the polymorphs FI and FII since they were found to be enantiotropically related. The performance in solution was evaluated only in case of the monohydrate since the fast solvent-mediated conversion of FII and FIII into FI, leading us to conclude that the monohydrate was likely the most interesting candidate for formulation considering its higher solubility in polar organic solvents.

To further increase the solubility of this target compound, a cocrystallization approach was investigated. A wide cocrystal screen using over 133 cocrystallization agents was performed, ultimately coming to a satisfying success rate of about 13%. Indeed, 17 different coformers i.e. (RS)-phenylsuccinic acid, parahydroxybenzoic acid, 5-hydroxyisophthalic acid, 5-nitroisophthalic acid, 5-bromoisophthalic acid, (RS)-2-phenylbutyric acid, (RS)-3-phenyllactic acid, gallic acid, 2-benzoylbenzoic acid, 5-cyano-1,3-benzenedicarboxylic acid, citric acid, oxalic acid, zinc chloride, β-resorcylic acid, gentisic acid, protocatechuic acid and dipiconilic acid led to positive hits resulting in a variety of solid forms (including ionic cocrystals, stoichiometrically diverse cocrystals, cocrystal polymorphs, and solid solutions). The cocrystals obtained with biocompatible coformers (citric acid, oxalic acid and zinc chloride) were further valorized in a peer-reviewed article (**Chapter 5**), focusing on their structural as well as physicochemical properties such as thermal stability, hygroscopicity, dissolution rate and solubility. Based on these results, the cocrystal with citric acid appears as a valid candidate (enhanced solubility in organic solvents) for a potential formulation of nefiracetam while the use of inorganic salt (zinc chloride) is a wiser choice when thermal stability is required.

During the cocrystal screen, a remarkable result emerged. Using mandelic acid, a frequently used resolving agent with analgesic, antirheumatic and spasmolytic effects, a conglomerate was induced when cocrystallizing the racemic compound with nefiracetam. In **Chapter 6**, we fully evidenced this system to be a true conglomerate using various approaches (Single crystal XRD, slurry experiments, chiral analysis of a single crystal and phase diagram construction). Based on this finding, we enabled the chiral resolution of racemic mandelic acid by preferential cocrystallization. Once

a suitable solvent identified (MeCN), various preferential crystallization modes were explored (S3PC, SIPC and cyclic SIPC) and we ultimately developed a process allowing us to resolve up to 2.4 g of mandelic acid in a cost-effective approach with an enantiopurity of 98-99%.

The outcomes of this thesis show the potency of the crystal engineering for the pharmaceutical field to generate new solid forms with completely different physicochemical properties without any chemical alteration. Besides, such an approach as the cocrystallization one allows combining physicochemical properties enhancement and separation of enantiomers in the case of chiral drugs.

To highlight the importance of the results in this thesis, an overall sketch linking the different chapters and results is given below (**Figure 7-1**).

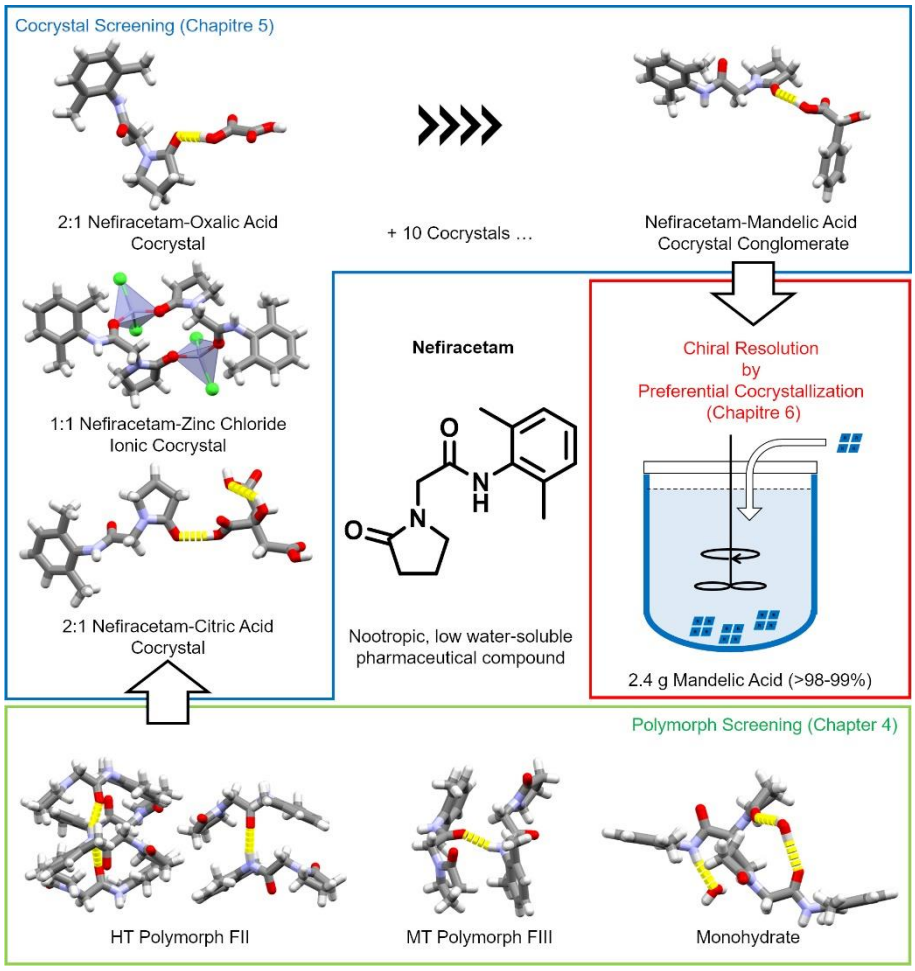

Figure 7-1. Overall sketch of the results presented in this thesis.

From a future perspective, it would be interesting to extend the preferential cocrystallization to a coupled-vessel set-up, which can be used in a continuous manner, hence being more industrially attractive. Preliminary trials were performed, but showed challenges related to the exchange of the highly viscous concentrated solution and the constraints brought by the solid in suspension. Initial results were promising but further work is needed, working e.g. with larger tube diameter or more suitable filtration units to solve technical issues occurring. As further perspective, it would be interesting to extend the process developed in this work to other systems. Recently, our group identified a cocrystal conglomerate of etiracetam by ionic cocrystallization, the use of which poses further challenges due to the use of an inorganic salt together with an organic compound. Finally, one should always keep in

mind that if the target compound is racemizable, these systems are ideal candidates for deracemization through abrasive grinding (Viedma Ripening).

8. Appendices

8.1. Supporting Information to Chapter 4

8.1.1. XRPD Patterns

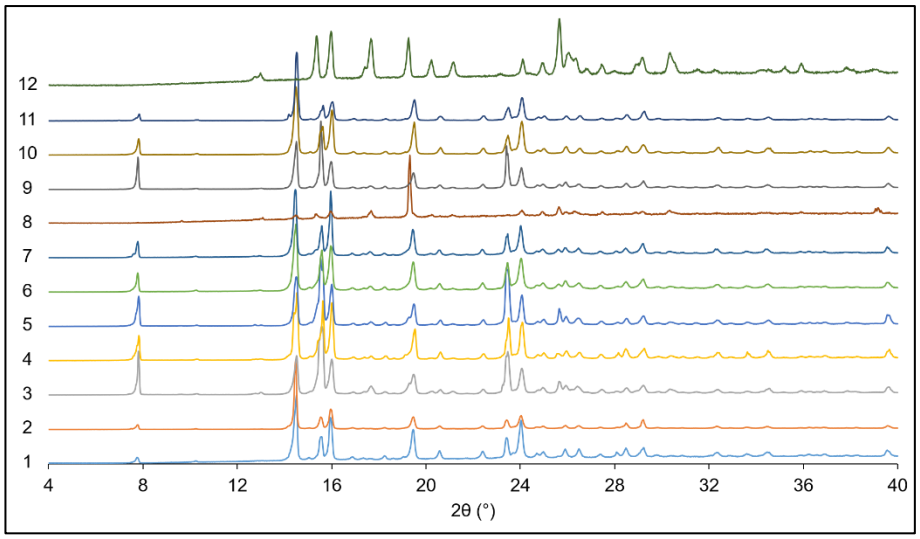

Figure 8-1-1. XRPD pattern on powders retrieved from the nefiracetam form screening through **cooling** crystallization in different solvents. **1**: ethyl acetate; **2**: methyl acetate; **3**: ethanol; **4**: methanol; **5**: 2-propanol; **6**: acetone; **7**: tetrahydrofuran; **8**: toluene; **9**: acetonitrile; **10**: dichloromethane; **11**: chloroform; **12**: water.

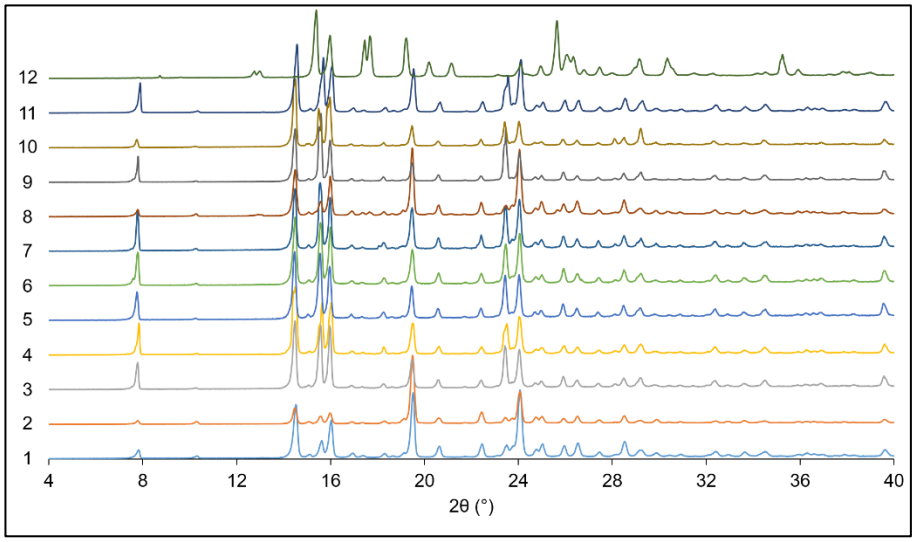

Figure 8-1-2. XRPD pattern on powders retrieved from the nefiracetam form screening through **slurrying** crystallization in different solvents. **1**: ethyl acetate; **2**: methyl acetate; **3**: ethanol; **4**: Methanol; **5**: 2-propanol; **6**: acetone; **7**: tetrahydrofuran; **8**: toluene; **9**: acetonitrile; **10**: dichloromethane; **11**: chloroform; **12**: water.

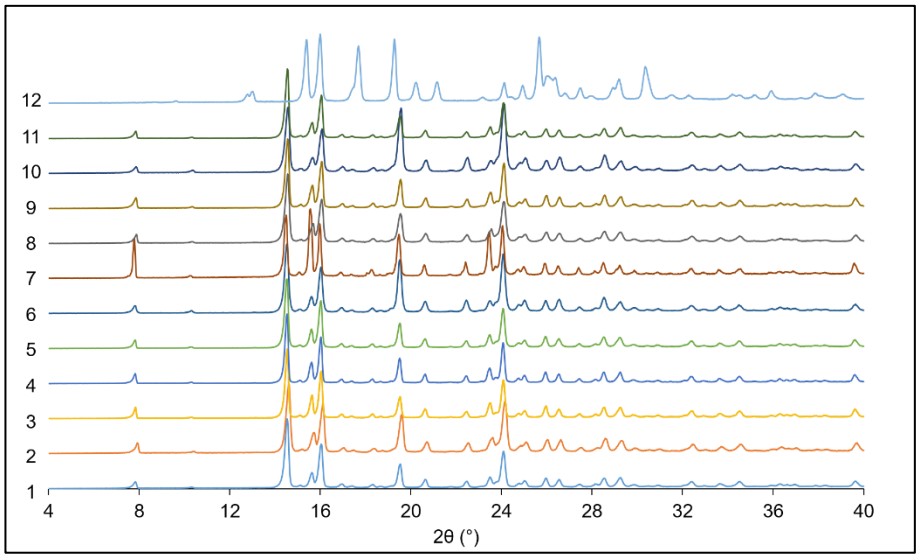

Figure 8-1-3. XRPD pattern on powders retrieved from the nefiracetam form screening through **grinding** crystallization (LAG) in different solvents. **1**: ethyl acetate; **2**: methyl acetate; **3**: ethanol; **4**: methanol; **5**: 2-propanol; **6**: acetone; **7**: tetrahydrofuran; **8**: toluene; **9**: acetonitrile; **10**: dichloromethane; **11**: chloroform; **12**: water.

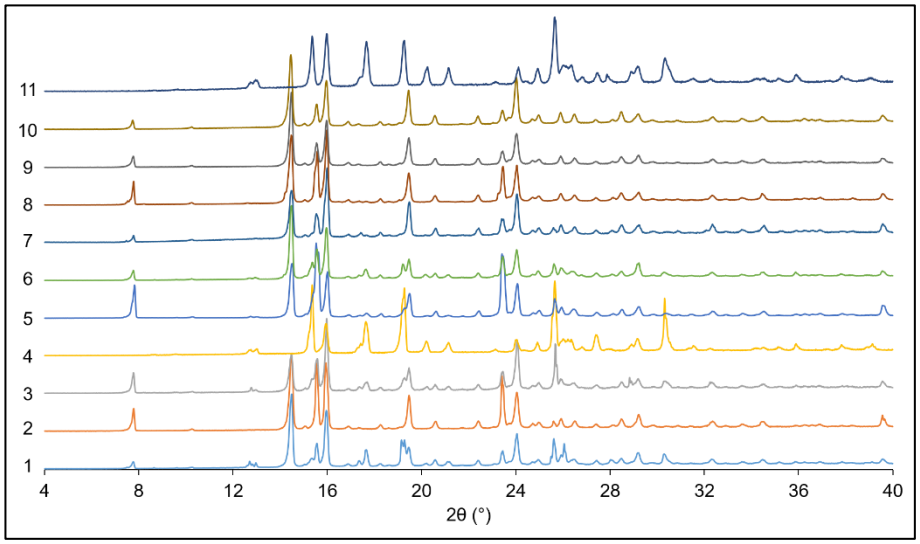

Figure 8-1-4. XRPD pattern on powders retrieved from the nefiracetam form screening through **evaporative** crystallization in different solvents. **1**: ethyl acetate; **2**: methyl acetate; **3**: ethanol; **4**: methanol; **5**: 2-propanol; **6**: acetone; **7**: tetrahydrofuran; **8**: acetonitrile; **9**: dichloromethane; **10**: chloroform; **11**: water.

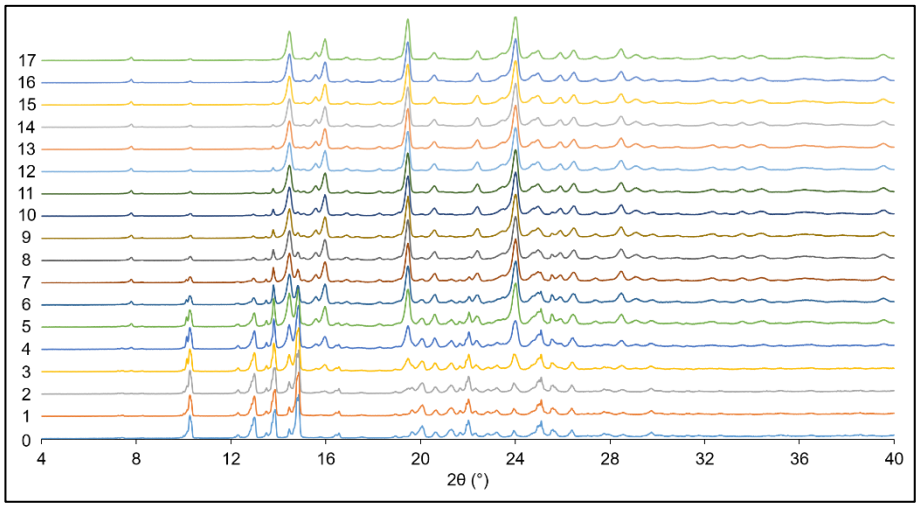

Figure 8-1-5. Overtime XRPD pattern observed from the recrystallization from the melt (0) to 17 hours (17) with a one-hour increment.

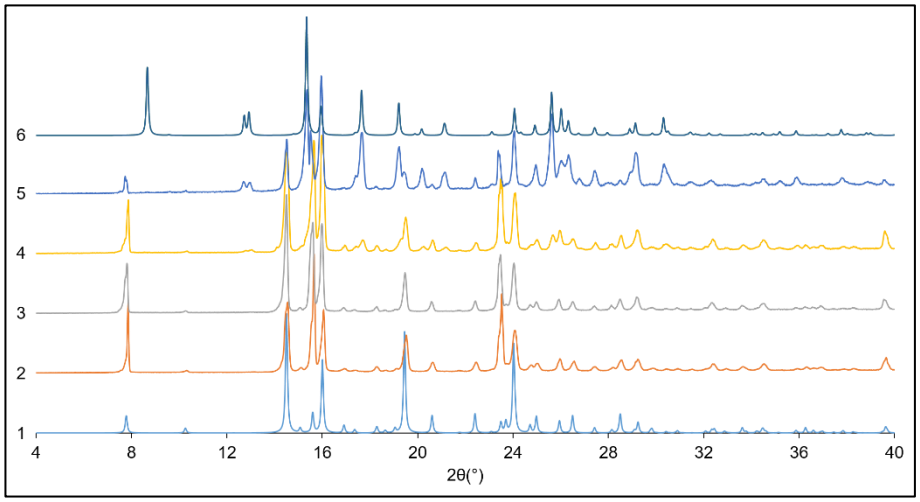

Figure 8-1-6. XRPD pattern of **1**: nefiracetam FI (simulated diffractogram), **2**: nefiracetam FI after one day exposure at 100% Relative Humidity, **3**: nefiracetam FI after 3 days exposure at 100% RH, **4**: nefiracetam FI after 4 days exposure at 100% RH, **5**: nefiracetam after 5 days exposure at 100% RH and **6**: nefiracetam monohydrate (simulated diffractogram).

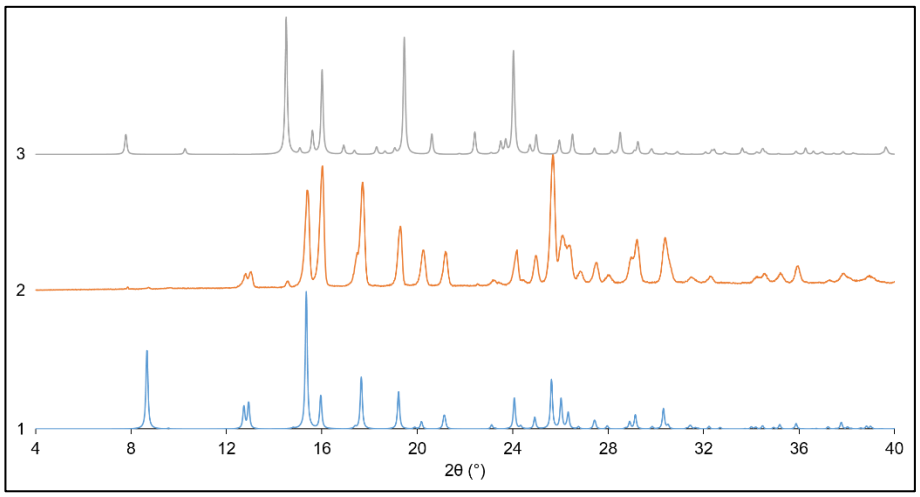

Figure 8-1-7. PXRD pattern of **1**: nefiracetam monohydrate (simulated diffractogram), **2**: nefiracetam monohydrate after one-week exposure under ambient temperature, pressure and relative humidity conditions and **3**: nefiracetam FI (simulated diffractogram).

8.1.2. Crystal Structure

Table 8-1-1. Distance, angle and color code related to the intermolecular hydrogen bonds displayed in each crystal structure.

Crystal Form	Distance (D-H···A) (Å)	Angle (D-H···A) (°)	Color code
FI	2.846(3)	165(3)	blue
FII	2.82(1)	161.7	orange
	2.75(1)	157.4	blue
	2.79(1)	169.2	yellow
	2.76(2)	170.3	grey
	2.84(2)	159.3	green
	2.84(1)	165.5	red
FIII	2.762(4)	163.22	blue
	2.772(4)	159.48	red
monohydrate	2.887	168.07	/
	2.778	147.3	/
	2.865	163.97	/

8.1.3. Dissolution Experiments

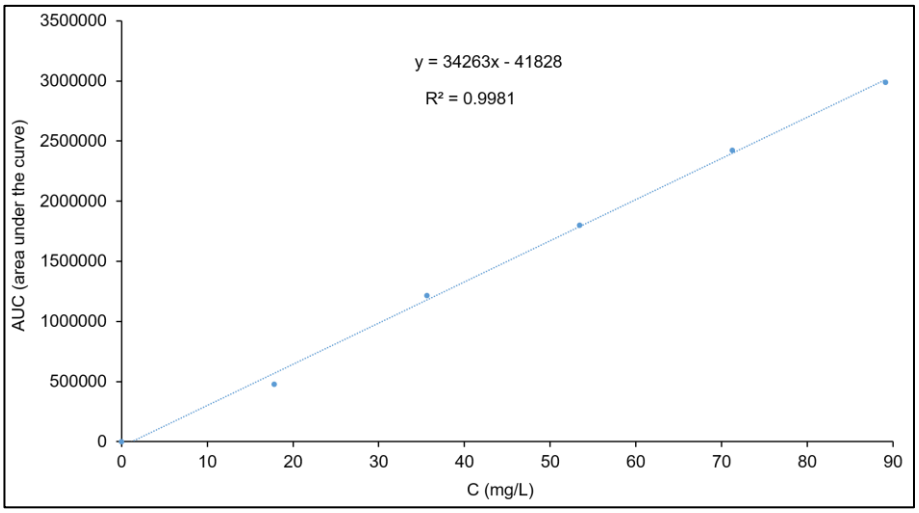

Figure 8-1-8. Nefiracetam calibration line built up for the purpose to dose the nefiracetam in solution.

8.2. Supporting Information to Chapter 5

8.2.1. Coformer List

Chapter 8

Table 8-2-1. List of the coformers screened during the cocrystal screening. Suspected

COFORMERS SCREENED		
(L)-3-phenyllactic acid	(DL)-3-phenyllactic acid	(L)-ascorbic acid
(S)-2-phenylbutyric acid	(RS)-2-phenylbutyric acid	(RS)-2-phenoxypropionic acid
(RS)-2-phenoxypropionic acid	(RS)-2-phenoxypropionic acid	(RS)-oxiracetam
(S)-oxiracetam	(RS)-phenylsuccinic acid	(RS)-tropic acid
1H-pyrazole-3,5-dicarboxylic acid monohydrate	1-hydroxy-2-napthoic acid	2,2-dimethylsuccinic acid
2,3-dihydroxybenzoic acid	2,4-dihydroxy benzoic acid	2,5-dihydroxybenzoic acid
2-aminobenzoic acid	2-benzoylbenzoic acid	2-hydroxy-1-napthoic acid
2-ketoglutaric acid	2-pyrrolidone-5-carboxylic acid	3,4-dihydroxybenzoic acid
3,5-dihydroxybenzoic acid	3-aminobenzamide	3-hydroxy-2-napthoic acid
3-hydroxybenzoic acid	3-methylbutanamide	3-nitrobenzoic acid
(RS)-3-phenylbutyric acid	4,4-bipyridine	4-aminobenzamide
4-aminobenzoic acid	4-aminomethylbenzoic acid	4-dimethylbenzoic acid
4-hydroxybenzoic acid	4-nitrobenzoic acid	5-aminoisophthalic acid
5-bromoisophthalic acid	5-cyano-1,3-benzenedicarboxylic acid	5-hydroxisophtalic acid
5-methoxyisophthalic acid	5-methylisophthalic acid	5-nitroisophtalic acid
6-hydroxy-2-napthoic acid	7-(2-hydroxyethyl)theophylline	7-(2-hydroxypropyll)theophylline
acetaminophen	acetoacetamide	acetylsalicylic acid
adipic acid	alanine (DL)	alanine (L)
aniracetam	anthranilamide	arginine (L)
asparagine (L)	aspartame	aspartic acid (DL)
aspartic acid (L)	benzenesulfonic acid	benzoic acid
calcium chloride	Caffeine	camphoric acid (D)
carphedon	carbamazepine	cholic acid
citraconic acid	citric acid	cysteine (L)
diphylline	(D)-mannitol	(D)-sorbitol
erythorbic acid	ethyl gallate	etiracetam
ferulic acid	flurbiprofen (RS)	fructose
fumaric acid	gallic acid	glucose
glutamine (L)	glutaric acid	glycine
lycolic acid	histidine (DL)	ibuprofen (RS)
isoleucine (DL)	isonicotinamide	isophtalic acid
ketoprofen (RS)	leucine (L)	leviteracetam
lysine (L)	maleic acid	malic acid
malonic acid	Maltol	mesaconic acid
methionine (L)	methyl-3,4,5-trihydroxybenzoate	magnesium chloride
myo-inositol	naproxen (RS)	nicotinamide
nicotinic acid	oxalic acid	pamoic acid
p-coumaric acid	phenylalanine (DL)	phenylsulfoxide
phtalic acid	piracetam	pramiracetam
proline (DL)	proline (L)	pyridine-2,6-dicarboxylic acid
saccharin	salicylic acid	salicylic acid
serine (DL)	serine (L)	sorbic acid
stearic acid	succinic acid	sucrose
tartaric acid	theophylline	thiomalic acid
threonine (L)	trimellitic acid	trimesic acid
tryptophane (DL)	tryptophane (L)	tyrosine (L)
urea	valine (L)	xanthine
zinc chloride		

Suspected cocrystals (orange), Confirmed cocrystals (green) and no cocrystal (black).

8.2.2. PXRD Patterns

Suspected Cocrystals

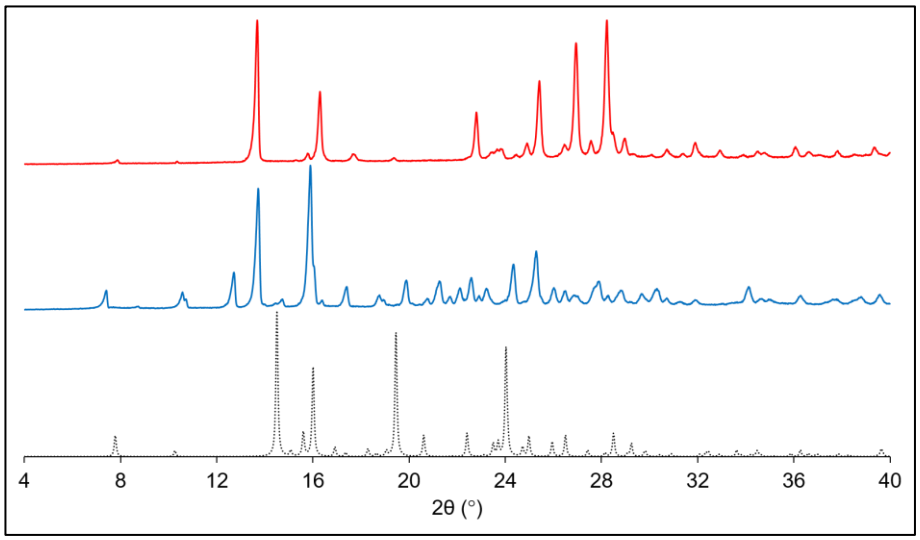

Figure 8-2-1. Experimental diffraction patterns of the 1:1 nefiracetam-**β-resorcylic acid** ground product (blue), the β-resorcylic acid coformer (red) and nefiracetam simulated diffraction pattern (dashed black).

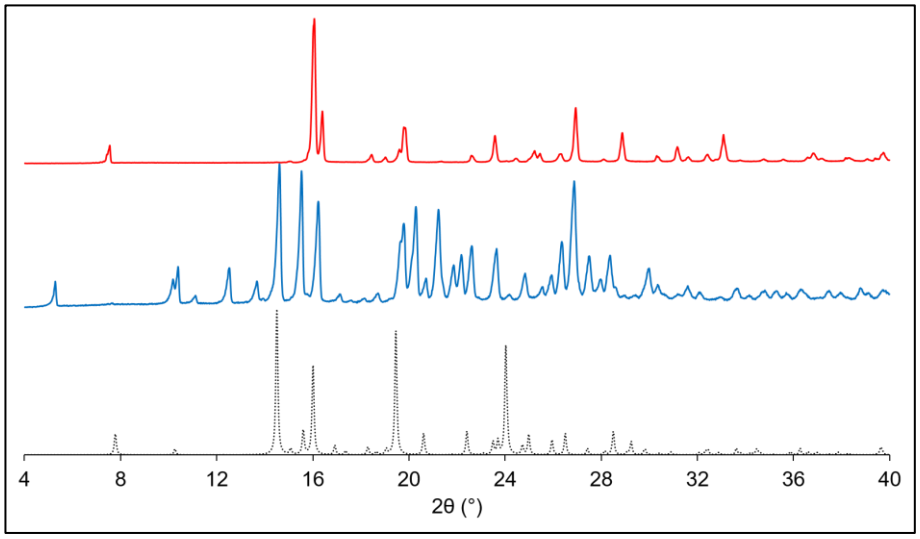

Figure 8-2-2. Experimental diffraction patterns of the 1:1 nefiracetam-**gentisic acid** ground product (blue), the gentisic acid coformer (red) and nefiracetam simulated diffraction pattern (dashed black).

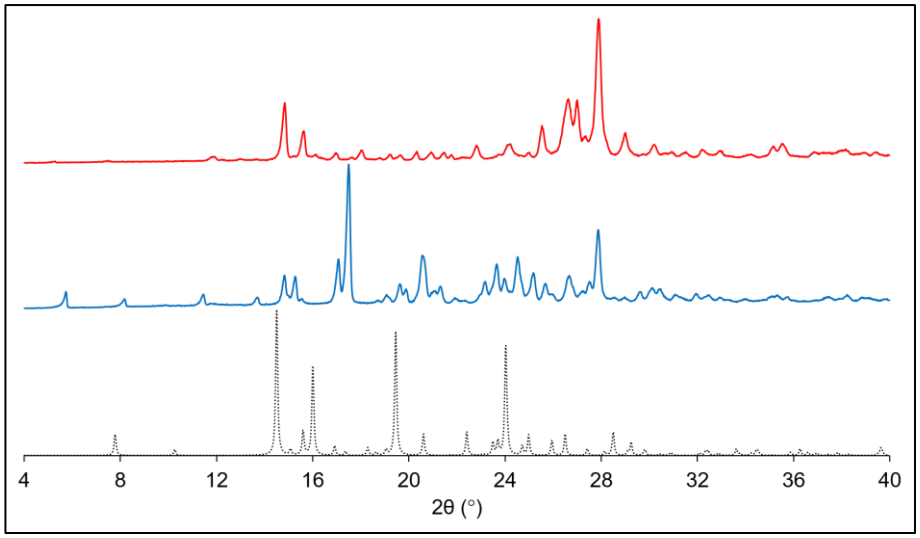

Figure 8-2-3. Experimental diffraction patterns of the 1:1 nefiracetam-**protocatechuic acid** ground product (blue), the protocatechuic acid coformer (red) and nefiracetam simulated diffraction pattern (dashed black).

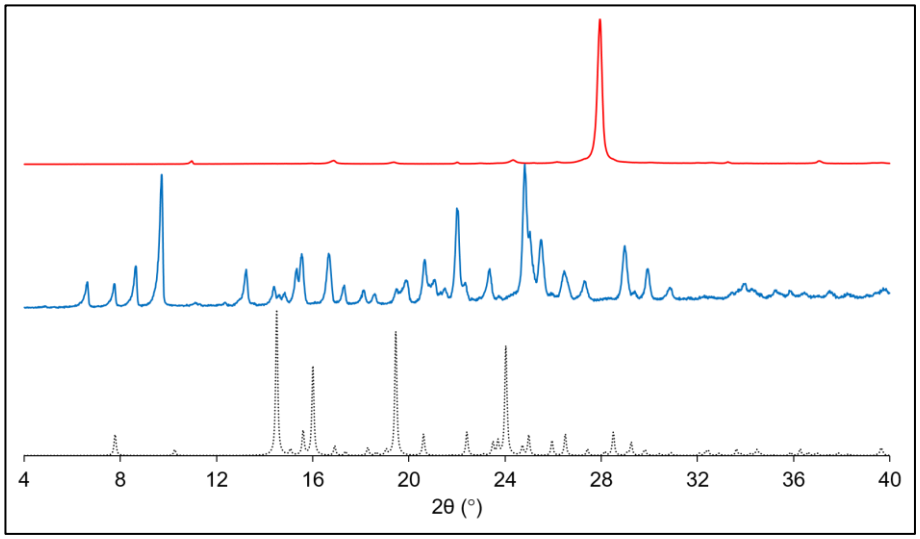

Figure 8-2-4. Experimental diffraction patterns of the 1:1 nefiracetam-**dipiconilic acid** ground product (blue), the dipiconilic acid coformer (red) and nefiracetam simulated diffraction pattern (dashed black).

Confirmed Cocrystals

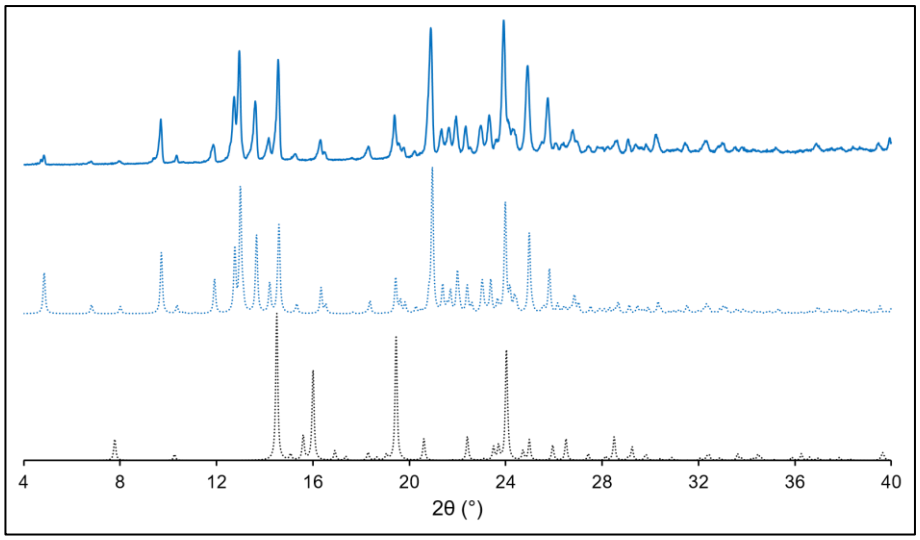

Figure 8-2-5. Simulated diffraction patterns (dashed line) of 1:1 nefiracetam-**5-hydroxyisophthalic acid** cocrystal (blue) and comparison with the experimental one (full line) and the simulated diffractogram of nefiracetam FI (black).

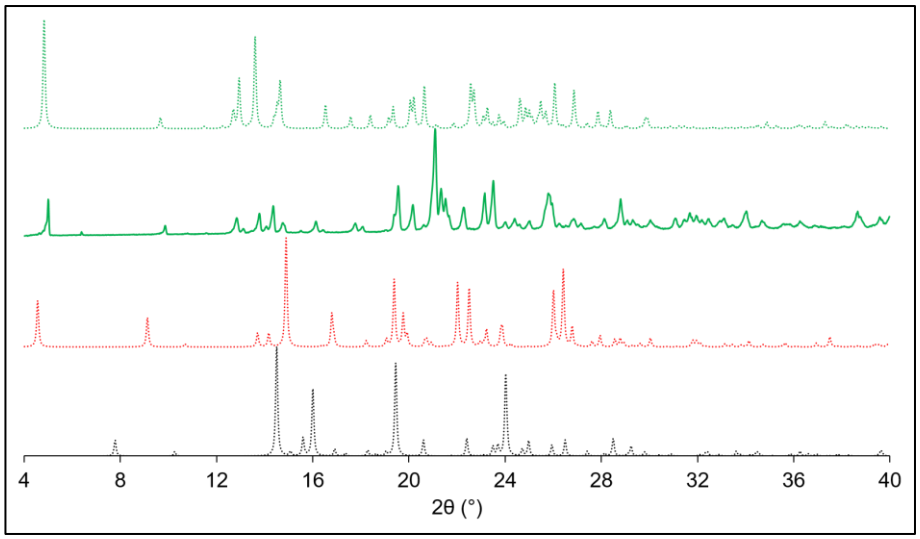

Figure 8-2-6. Simulated diffraction patterns (dashed line) of 1:1 nefiracetam-**5-nitroisophthalic acid FI** cocrystal (green) and **FII** (red) and comparison with the experimental one (full line) and the simulated diffractogram of nefiracetam FI (black).

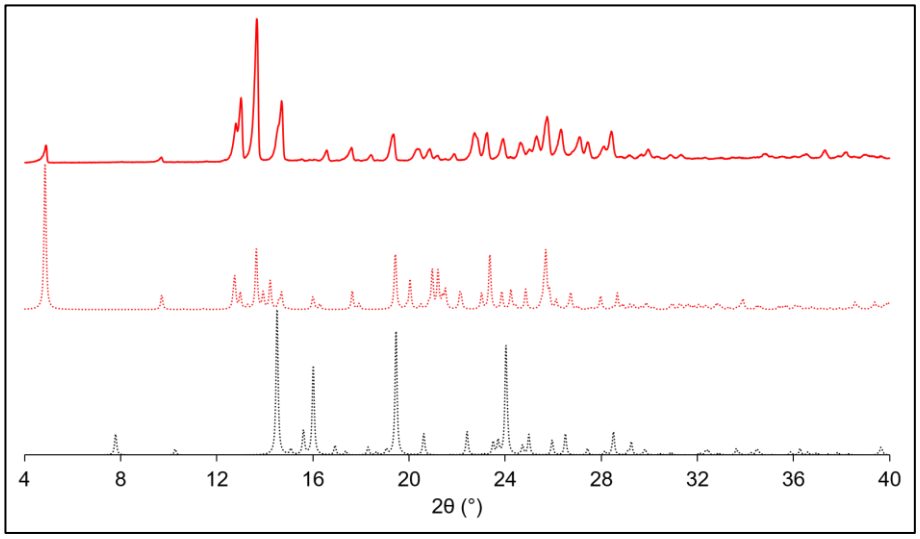

Figure 8-2-7. Simulated diffraction patterns (dashed line) of nefiracetam-**5-bromoisophthalic acid** (red) and comparison with the experimental one (red full line) and the simulated diffractogram of nefiracetam FI (black).

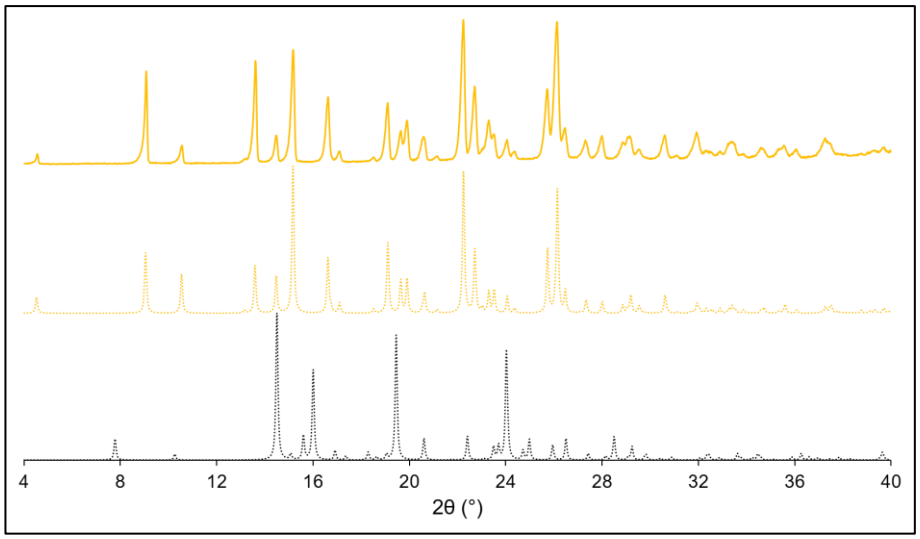

Figure 8-2-8. Simulated diffraction patterns (dashed line) of nefiracetam-**5-cyano-1,3-benzenedicarboxylic acid** (orange) and comparison with the experimental one (full line) and the simulated diffractogram of nefiracetam FI (black).

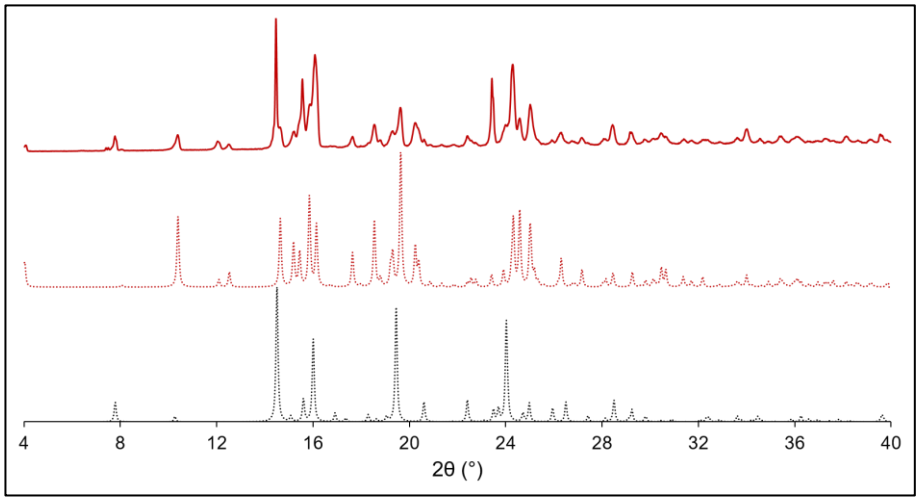

Figure 8-2-9. Simulated diffraction patterns (dashed line) of nefiracetam-**2-benzylbenzoic acid** (dark red) and comparison with the experimental one (full line) and the simulated diffractogram of nefiracetam FI (black).

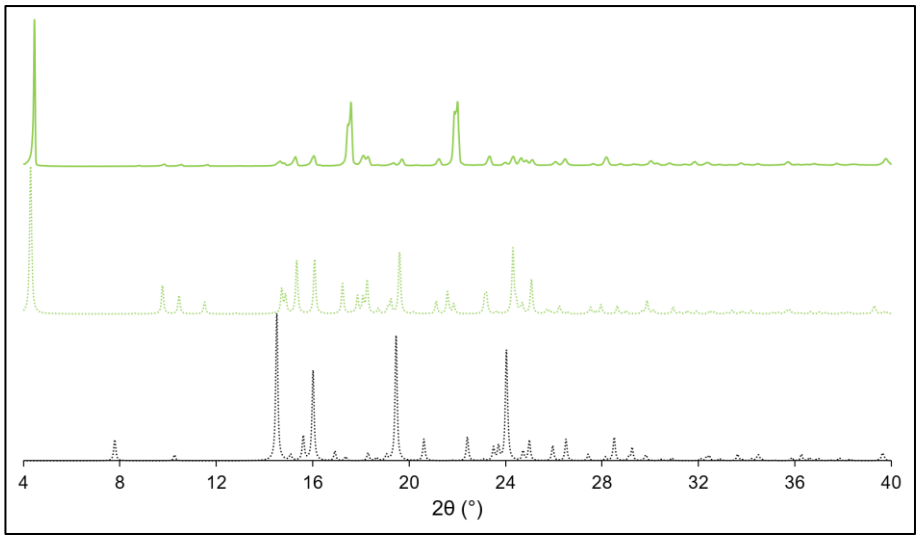

Figure 8-2-10. Simulated diffraction patterns (dashed line) of nefiracetam-**(RS)-2-phenylbutyric acid** cocrystal solid solution (light green) and comparison with the experimental one (full line) and the simulated diffractogram of nefiracetam FI (black).

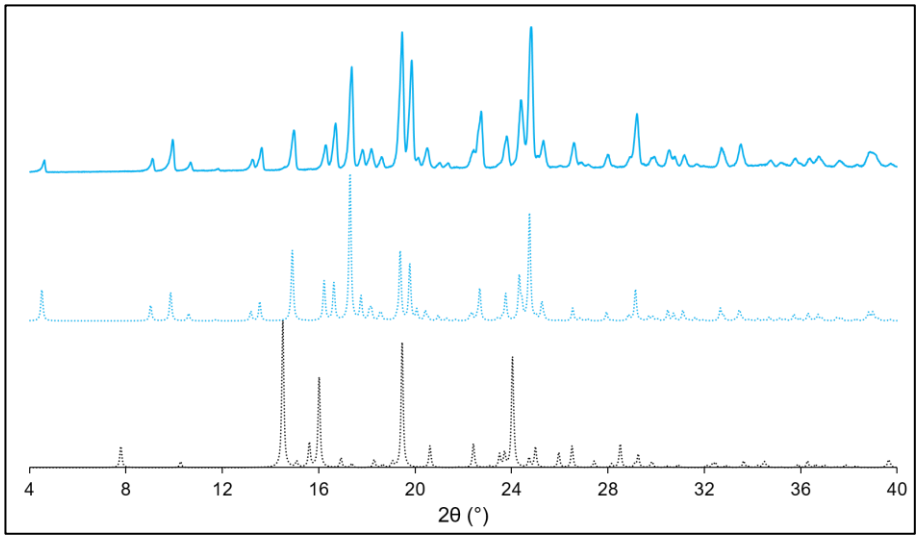

Figure 8-2-11. Simulated diffraction patterns (dashed line) of nefiracetam-**(DL)-3-phenyllactic acid** racemic cocrystal (light blue) and comparison with the experimental one (full line) and the simulated diffractogram of nefiracetam FI (black).

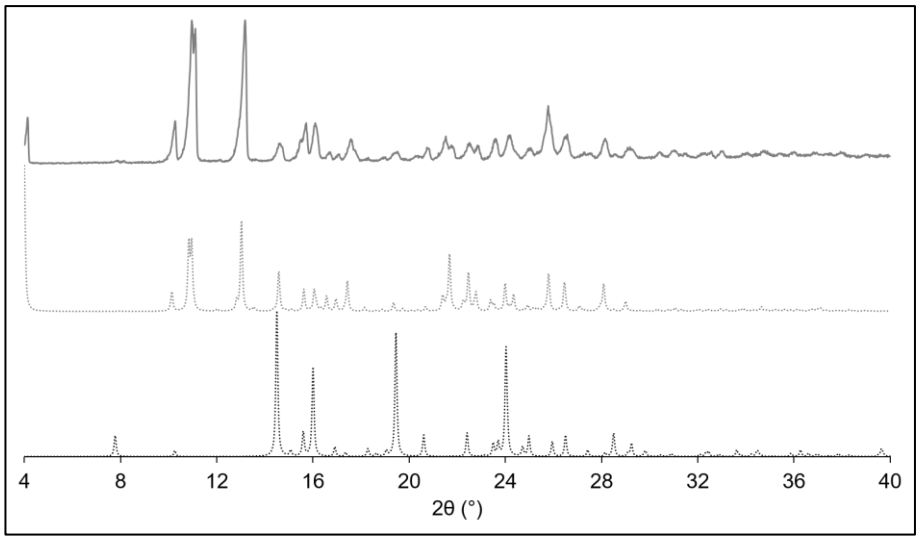

Figure 8-2-12. Simulated diffraction patterns (dashed line) of 4:1:1 nefiracetam-**3,4,5-trihydroxybenzoic acid** (gallic acid) cocrystal hydrate (grey) and comparison with the experimental one (full line) and the simulated diffractogram of nefiracetam FI (black).

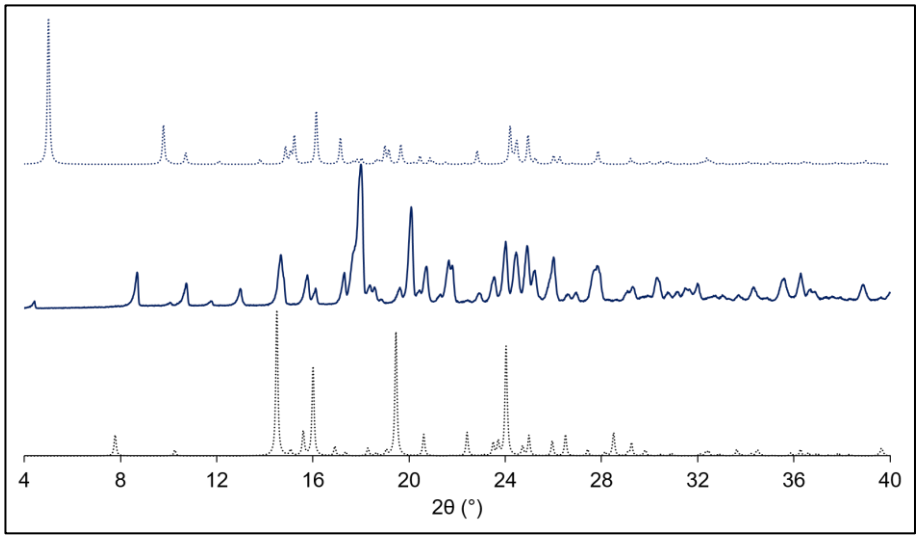

Figure 8-2-13. Simulated diffraction patterns (dashed line) of 2:1 nefiracetam-**(RS)-phenylsuccinic acid** racemic cocrystal (dark blue) and comparison with the ground product (full line) and the simulated diffractogram of nefiracetam FI (black).

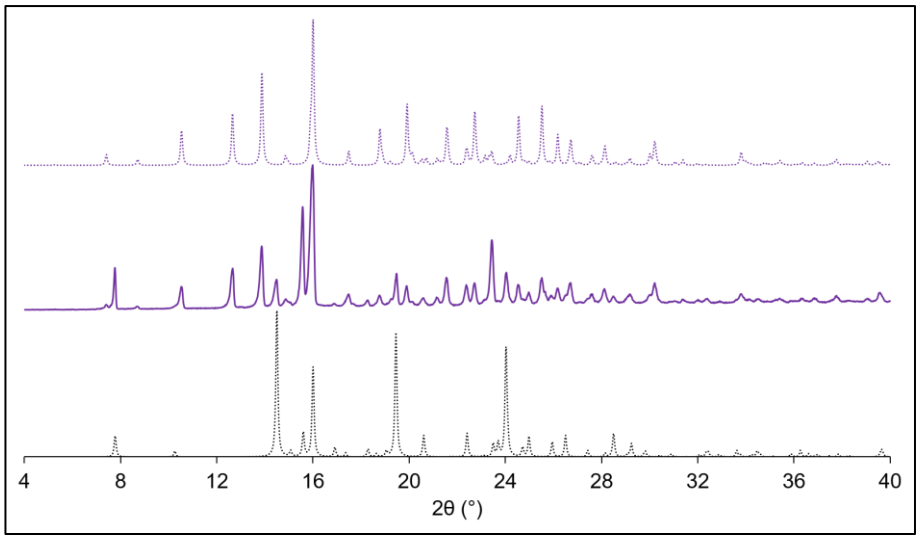

Figure 8-2-14. Simulated diffraction patterns (dashed line) of 1:1 nefiracetam-**4-hydrobenzoic acid** cocrystal (purple) and comparison with the ground product (full line) and the simulated diffractogram of nefiracetam FI (black).

8.2.3. DSC Curves

Suspected Cocrystals

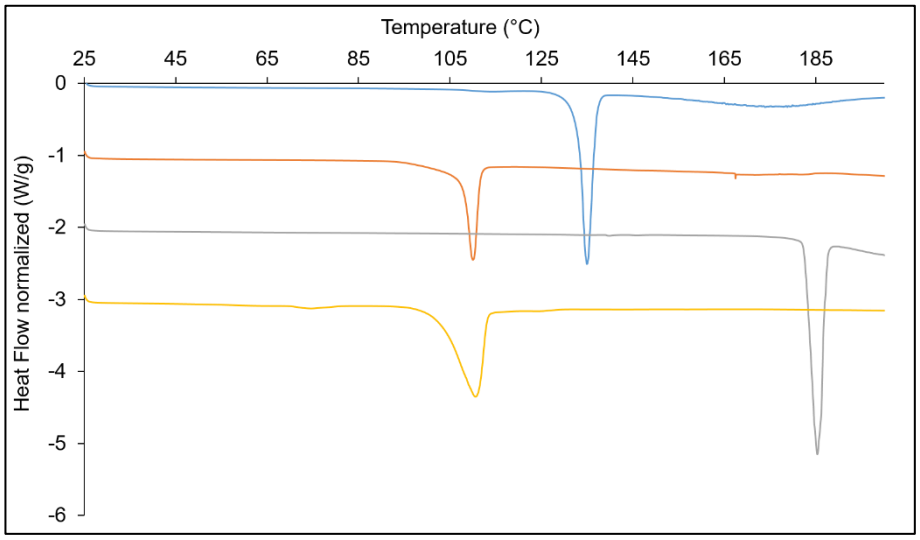

Figure 8-2-15. DSC curves of 1:1 nefiracetam-**2,4-dihydroxybenzoic acid** (bleu), 1:1 nefiracetam-**2,5-dihydroxybenzoic acid** (orange), 1:1 nefiracetam-**pyridine-2,6-dicarboxylic acid** (grey) and 1:1 nefiracetam-**3,4-dihydroxybenzoic acid** (gold) ground products.

Confirmed Cocrystals

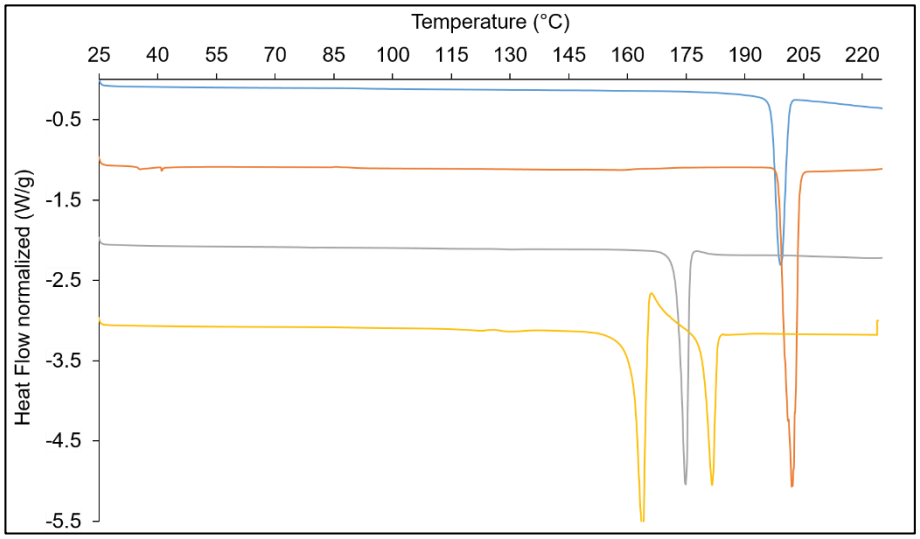

Figure 8-2-16. DSC curves of 1:1 nefiracetam-**5-hydroxyisophthalic acid** (blue), 1:1 nefiracetam-**5-bromoisophthalic acid** (orange), 1:1 nefiracetam-**5-nitroisophthalic acid FI** (grey) and 1:1 nefiracetam-**5-cyano-1,3-benzendicarboxylic acid** (gold) cocrystals.

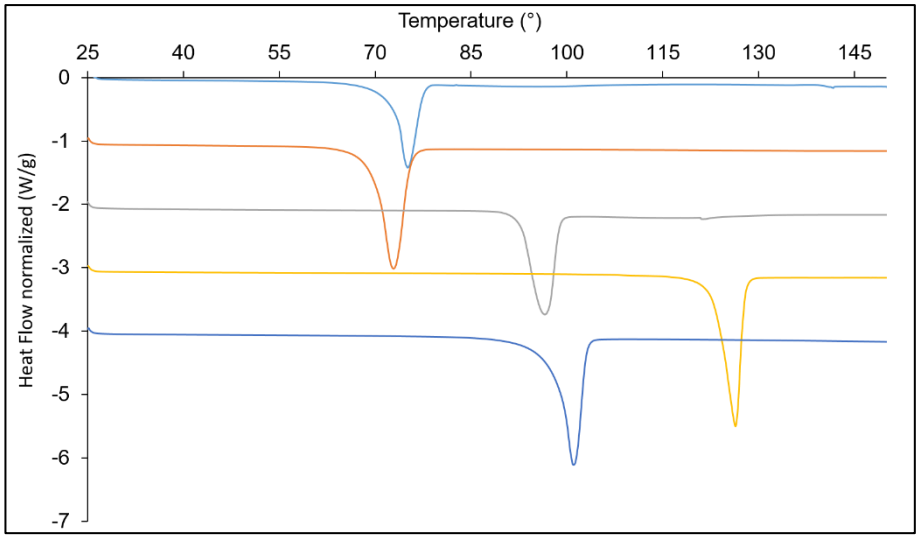

Figure 8-2-17. DSC curves of 1:1 nefiracetam-**(RS)-2-phenylbutyric acid** (blue), 1:1 nefiracetam-(DL)-**3-phenyllactic acid** (orange), and 1:1 nefiracetam-**2-benzoylbenzoic acid** (grey**),** 1:1-nefiracetam-**4-hydroxybenzoic acid** (gold) and 2:1 nefiracetam-**(RS)-phenylsuccinic acid** (darker blue) cocrystals.

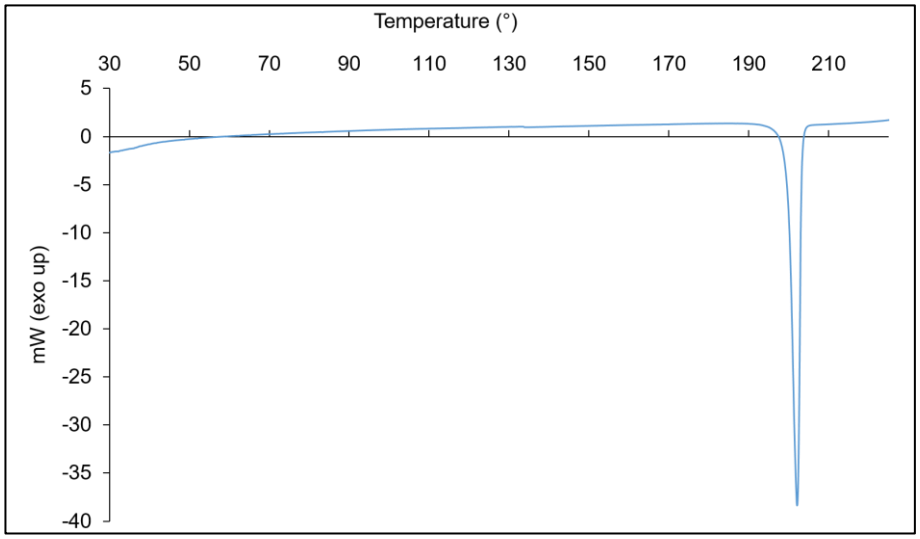

Figure 8-2-18. DSC curve of the 1:1 nefiracetam-**5-nitroisophthalic acid** FII cocrystal. The measurement was occasionally performed on measurements were performed from 30°C to 225°C at a scanning rate of 5°C.min^{-1} on a "Mettler Toledo DSC821e".

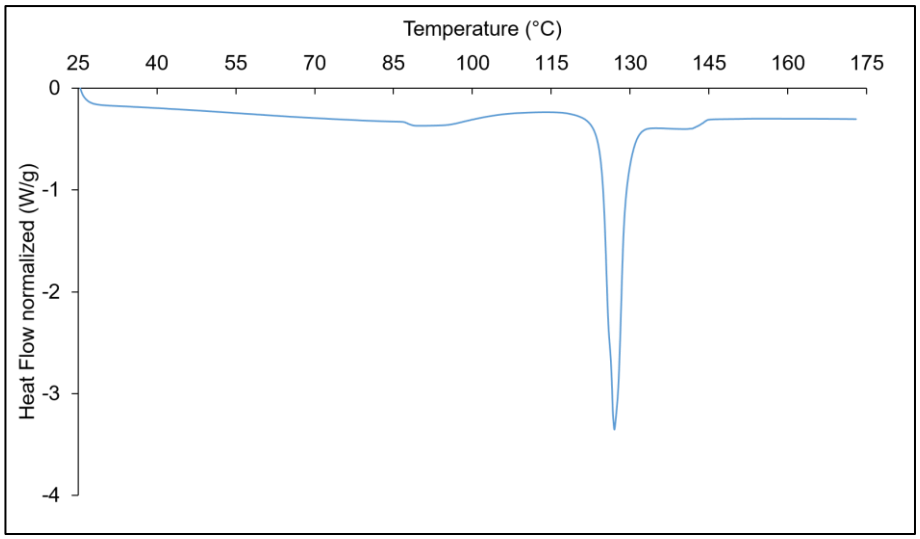

Figure 8-2-19. DSC curve of 4:1:1 nefiracetam-**gallic acid**-water cocrystal hydrate. Upon heating, the cocrystal decomposes into a mixture nefiracetam and amorphous phase.

8.2.4. Nefiracetam-Citric Acid Cocrystal (NCA)

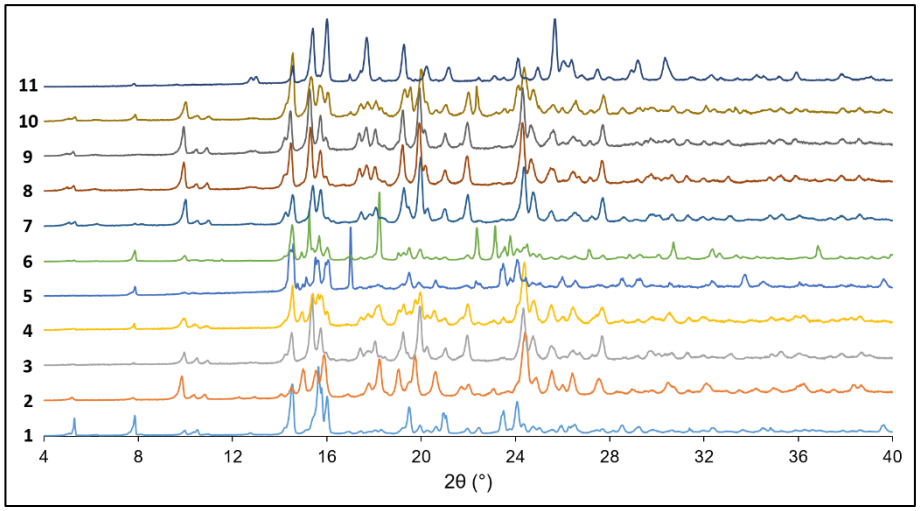

Figure 8-2-20. XRPD pattern on powders retrieved from the **NCA** form screening through **LAG** with different solvents. **1**: acetone; **2**: acetonitrile; **3**: chloroform; **4**: dichloromethane; **5**: ethyl acetate; **6**: ethanol; **7**: 2-propanol; **8**: methyl acetate; **9**: methanol; **10**: tetrahydrofuran; **11**: water.

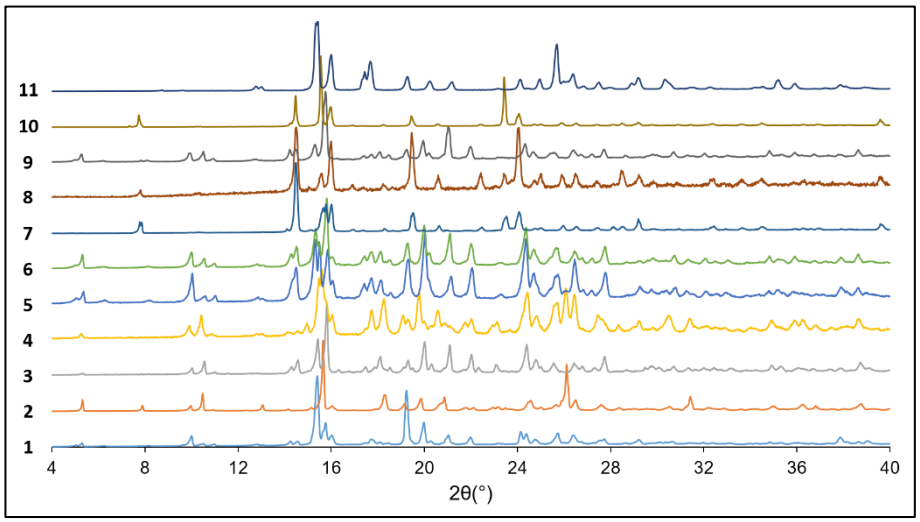

Figure 8-2-21. XRPD pattern on powders retrieved from the **NCA** form screening through **slurry** crystallization in different solvents. **1**: acetone; **2**: acetonitrile; **3**: chloroform; **4**: dichloromethane; **5**: diethyl ether; **6**: ethyl acetate; **7**: ethanol; **8**: 2-propanol; **9**: methyl acetate; **10**: tetrahydrofuran; **11**: water.

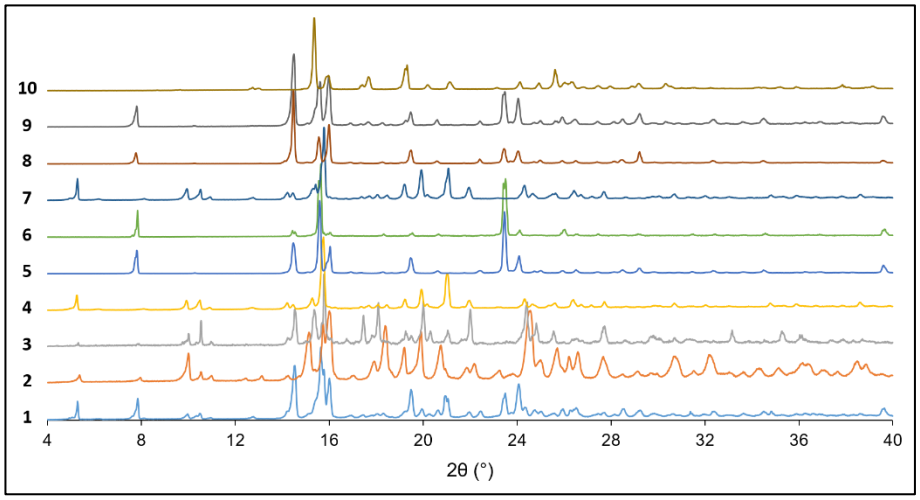

Figure 8-2-22. XRPD pattern on powders retrieved from the **NCA** form screening through **cooling** crystallization in different solvents. **1**: acetone; **2**: acetonitrile; **3**: chloroform; **4**: ethyl acetate; **5**: ethanol; **6**: 2-propanol; **7**: methyl acetate; **8**: methanol; **9**: tetrahydrofuran; **10**: water.

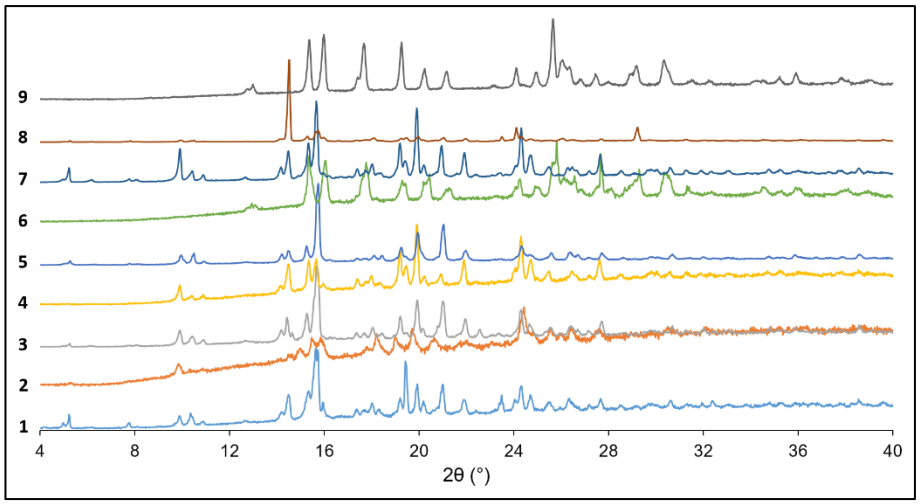

Figure 8-2-23. XRPD pattern on powders retrieved from the **NCA** form screening through **evaporative** crystallization in different solvents at room temperature. **1**: acetone; **2**: acetonitrile; **3**: ethyl acetate; **3**: ethanol; **5**: methyl acetate; **6**: methanol; **7**: 2-propanol; **8**: tetrahydrofuran; **9**: water.

8.2.5. Nefiracetam-Oxalic Acid Cocrystal (NOA)

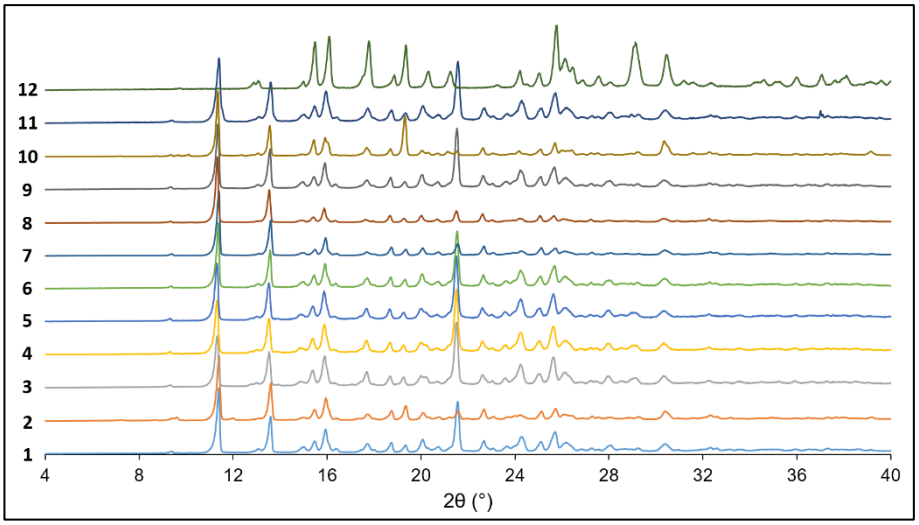

Figure 8-2-24. XRPD pattern on powders retrieved from the **NOA** form screening through **LAG** with different solvents. **1**: acetone; **2**: acetonitrile; **3**: chloroform; **4**: dichloromethane; **5**: diethyl ether; **6**: ethyl acetate; **7**: ethanol; **8**: 2-propanol; **9**: methyl acetate; **10**: methanol; **11**: tetrahydrofuran; **12**: water.

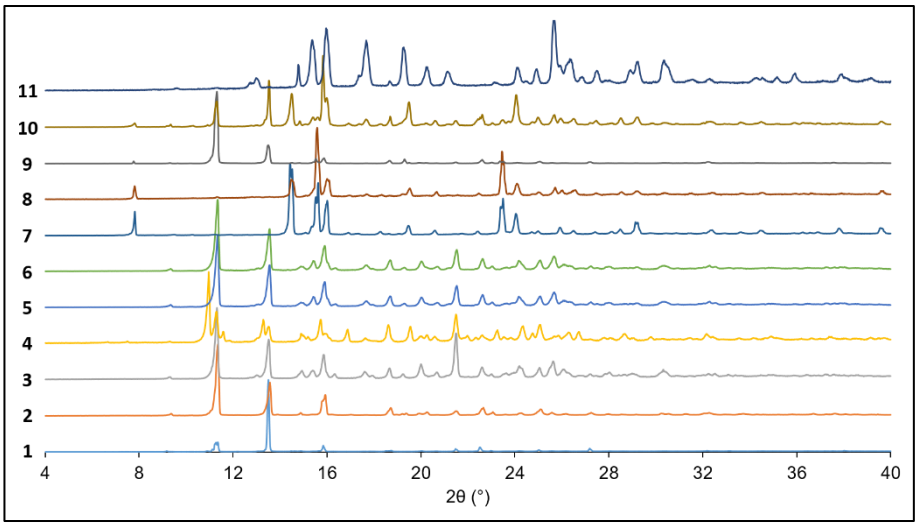

Figure 8-2-25. XRPD pattern on powders retrieved from the **NOA** form screening through **slurry** crystallization in different solvents at 25°C. **1**: acetone; **2**: acetonitrile; **3**: chloroform; **4**: dichloromethane; **5**: diethyl ether; **6**: ethyl acetate; **7**: ethanol; **8**: 2-propanol; **9**: methyl acetate; **10**: tetrahydrofuran; **11**: water.

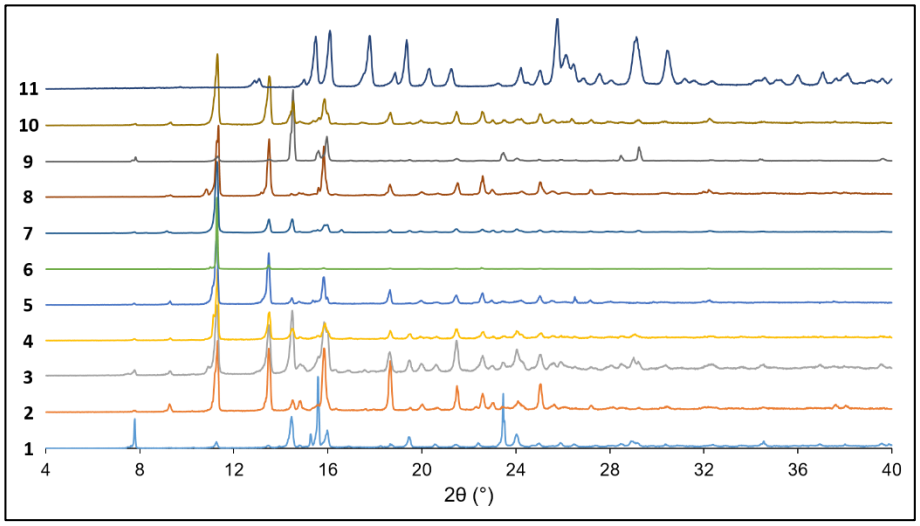

Figure 8-2-26. XRPD pattern on powders retrieved from the **NOA** form screening through **evaporative** crystallization in different solvents at room temperature. **1**: acetone; **2**: acetonitrile; **3**: chloroform; **4**: dichloromethane; **5**: ethyl acetate; **6**: ethanol; **7**: 2-propanol; **8**: methyl acetate; **9**: methanol; **10**: tetrahydrofuran; **11**: water.

8.2.6. Nefiracetam-Zinc Chloride Ionic Cocrystal (NZC)

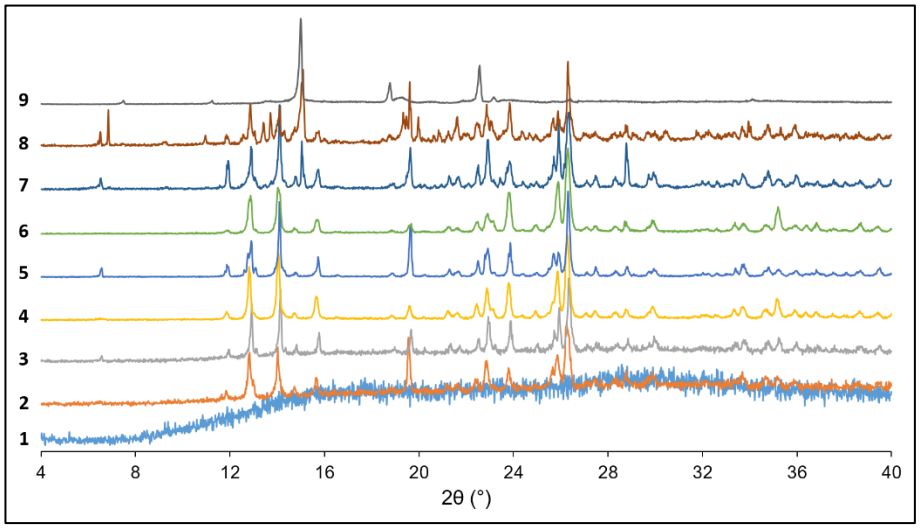

Figure 8-2-27. XRPD pattern on powders retrieved from the **NZC** stoichiometry screening through **slurry** crystallization in acetonitrile at 25°C. **1**: 100% ZC; **2**: ZC 89%-11% N; **3**: ZC 81%-19% N; **4**: ZC 70%-30% N; **5**: ZC 57%-43% N; **6**: ZC 48%-52% N; **7**: ZC 46%-54% N; **8**: ZC 30%-70% N; **9**: ZC 19%-81% N. Percent are given in molar ratio with N = nefiracetam and ZC = zinc chloride.

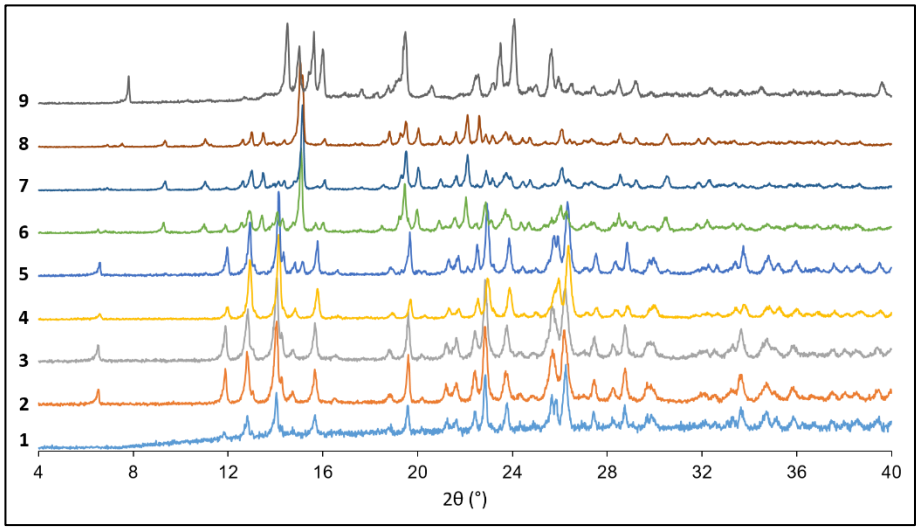

Figure 8-2-28. XRPD pattern on powders retrieved from the **NZC** stoichiometry screening through slurry crystallization in ethyl acetate at 25°C. **1**: ZC 89%-11% N; **2**: ZC 80%-20% N; **3**: ZC 68%-32% N; **4**: ZC 59%-41% N; **5**: ZC 50%-50% N; **6**: ZC 39%-61% N; **7**: ZC 37%-63% N; **8**: ZC 31%-69% N; **9**: ZC 10%-90% N. Percent are given in molar ratio with N = nefiracetam and ZC = zinc chloride.

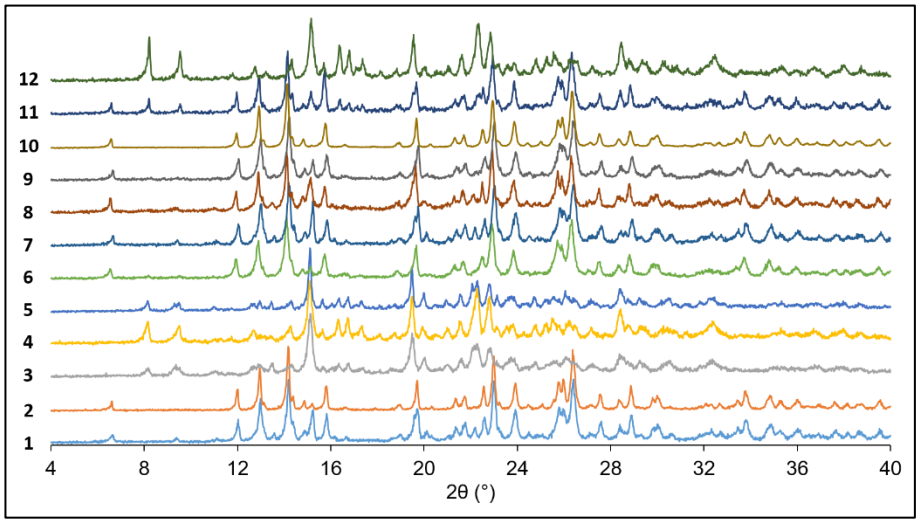

Figure 8-2-29. XRPD pattern on powders retrieved from the **NZC** form screening through **LAG** with different solvents. **1**: acetone; **2**: acetonitrile; **3**: chloroform; **4**: dichloromethane; **5**: diethyl ether; **6**: ethyl acetate; **7**: ethanol; **8**: methyl acetate; **9**: 2-propanol; **10**: methanol; **11**: tetrahydrofuran ; **12**: water.

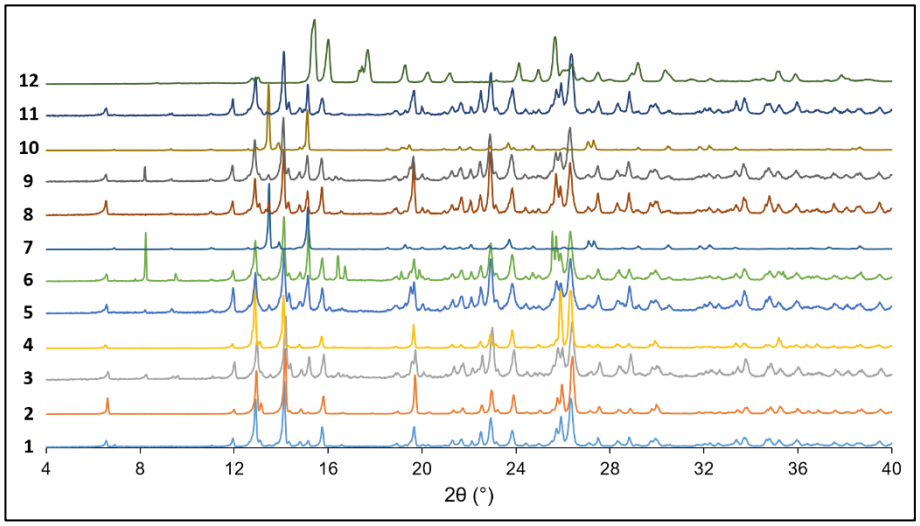

Figure 8-2-30. XRPD pattern on powders retrieved from the **NZC** form screening through **slurry** crystallization with different solvents at 25°C. **1**: acetone; **2**: acetonitrile; **3**: chloroform; **4**: dichloromethane; **5**: diethyl ether; **6**: ethyl acetate; **7**: ethanol; **8**: 2-propanol; **9**: methyl acetate; **10**: methanol; **11**: tetrahydrofuran; **12**: water.

8.2.7. Crystal Packing and Crystallographic Tables

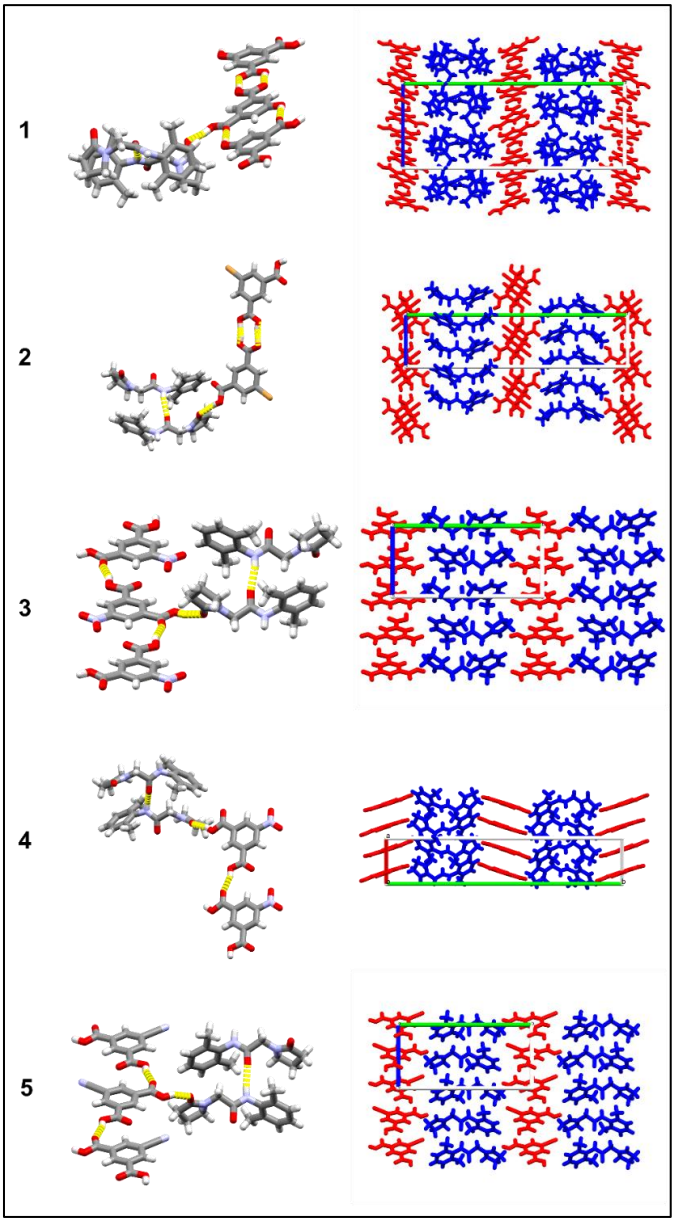

Figure 8-2-31. (left) Main intermolecular interactions and (right) crystal packing of **1**: 1:1 nefiracetam-5-hydroxyisophthalic acid, **2**: 1:1 nefiracetam-5-bromoisophthalic acid, **3**: 1:1 nefiracetam-5-nitroisophthalic acid FII, **4**: 1:1 nefiracetam-5-nitroisophthalic acid FI and **5**: 1:1 nefiracetam-5-cyano-1,3-benzenedicarboxylic acid cocrystals. The nefiracetam molecules and coformers are respectively colored in blue and red in the crystal lattices. Yellow contact sticks are used to highlight the intermolecular hydrogen bonds

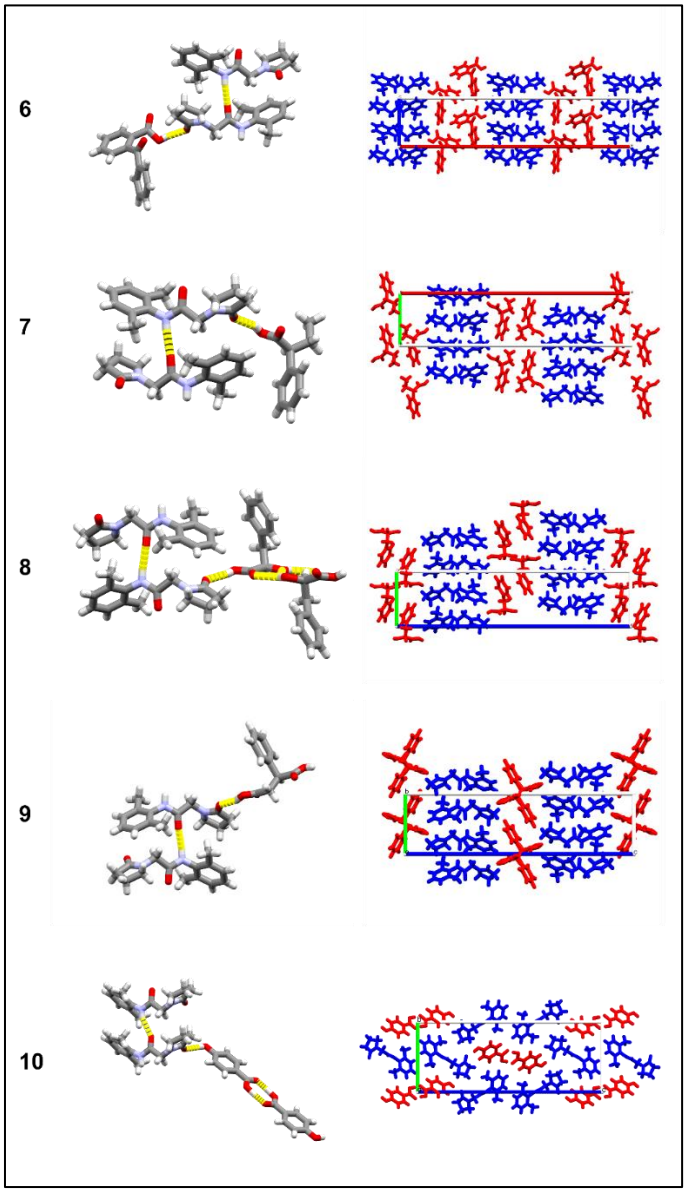

Figure 8-2-32. (left) Main intermolecular interactions and (right) crystal packing of **6**: 1:1 nefiracetam-2-benzoyl benzoic acid, **7**: nefiracetam-(RS)-2-phenylbutyric acid and **8**: nefiracetam-(DL)-3-phenyllactic acid (solid solution), **9**: 2:1 nefiracetam-(RS)-phenylsuccinic acid (racemic) and **10**: 1:1 nefiracetam-4-hydroxybenzoic acid cocrystals. The nefiracetam molecules and coformers are respectively colored in blue and red in the crystal lattices. Yellow contact sticks are used to highlight the intermolecular hydrogen bonds. The cocrystal structure of 2:1 nefiracetam-(RS)-phenylsuccinic acid exhibits an inversion centre on each phenylsuccinic acid molecule.

Table 8-2-2a. Main crystallographic data of **NCA**, **NCA1**, **NOA**, **NZC** and **NZCW** and refinement parameters (in the manuscript).

Compound	**NCA**	**NCA1**	**NOA**
Empirical formula	$C_{68}H_{87}N_8O_{22}$	$C_{34}H_{43}N_{24}O_{11}$	$C_{30}H_{38}N_4O_8$
Formula weight ($g.mol^{-1}$)	1368.45	683.72	582.84
Temperature (K)	297(2)	297(2)	100(2)
Wavelength (Å)	1.54184	1.54184	0.798
Crystal system	Triclinic	Monoclinic	Monoclinic
Space group	*P*-1	*P*21/*c*	$P2_1$
a, b, c (Å)	6.1877(2),18.7399(4),35.3540(11)	6.439(3),35.361(9),9.782(3)	88.4663(5),15.4852(9),23.4755(11)
α, β, γ (°)	74.626(3), 87.939(3), 82.248(2)	90, 97.68(3). 90	90, 99.903(6), 90
Volume ($Å^3$)	3916.7(2)	2207.3(13)	3031.8(3)
Z	2	2	4
Density ($g.cm^{-3}$)	1.160	1.029	1.276
Absorption coefficient (mm^{-1})	0.727	0.645	0.120
F(000)	1454	726	1240
Crystal size (mm^3)	0.500 x 0.385 x 0.039	Crystallized on **NCA**	0.50 x 0.04 x 0.02
Theta range for data collection (°)	6.493 to 66.601	8.182 to 58.930	1.777 to 28.729
Reflections collected	13586	14428	24245
Completeness to θ = 25.242°	98.8 % (to theta = 66.601°)	99%	98.1 % (to 28.607°)
Max. and min. transmission	1.000 and 0.836	1.000 and 0.836	1.000 and 0.747
Refinement method	Full-matrix least-squares on F^2	Full-matrix least-squares on F^2	Full-matrix least-squares on F^2
Data / restraints / parameters	13586 / 451 / 972	3125 / 30 / 282	24245 / 1 / 767
Goodness-of-fit on F^2	1.086	1.087	1.091
Final R indices [I>2sigma(I)]	R1 = 0.0747, wR2 = 0.1703	R1 = 0.0969, wR2 = 0.1878	R1 = 0.0806, wR2 = 0.2053
R indices (all data)	R1 = 0.0849, wR2 = 0.1777	R1 = 0.1688, wR2 = 0.2275	R1 = 0.0976, wR2 = 0.2213
Δρ (max, min) ($e.Å^{-3}$)	0.498 and -0.274	0.238 and -0.201	0.312 and -0.2451

Table 8-2-2b. Main crystallographic data of **NCA**, **NCA1**, **NOA**, **NZC** and **NZCW** and refinement parameters (in the manuscript).

Compound	**NZC**	**NZCW**
Empirical formula	$C_{14}H_{18}Cl_2N_2O_2Zn$	$C_{14}H_{20}Cl_2N_2O_3Zn$
Formula weight ($g.mol^{-1}$)	382.57	400.59
Temperature (K)	100(2)	297(2)
Wavelength (Å)	0.71073	0.71073
Crystal system	Monoclinic	Monoclinic
Space group	*C2/c*	$P2_1/c$
a, b, c (Å)	14.9275(3),7.66202(16),27.3619(6)	8.8632(3),18.2415(8),22.1746(12)
α, β, γ (°)	90, 97.3147(19), 90	90, 101.353(5), 90
Volume ($Å^3$)	3104.06(11)	3515.0(3)
Z	8	8
Density ($g.cm^{-3}$)	1.637	1.514
Absorption coefficient (mm^{-1})	1.931	1.713
F(000)	1568	1648
Crystal size (mm^3)	0.490 x 0.280 x 0.280	0.45 x 0.30 x 0.07
Theta range for data collection (°)	2.751 to 32.666	3.025 to 25.688
Reflections collected	10307	31528
Completeness to θ = 25.242°	100.0 %	99.7 %
Max. and min. transmission	0.701 and 0.582	1.000 and 0.428
Refinement method	Full-matrix least-squares on F^2	Full-matrix least-squares on F^2
Data / restraints / parameters	5151 / 0 / 196	6638 / 0 / 407
Goodness-of-fit on F^2	1.105	1.037
Final R indices [I>2sigma(I)]	R1 = 0.0258, wR2 = 0.0577	R1 = 0.0351, wR2 = 0.0846
R indices (all data)	R1 = 0.0295, wR2 = 0.0590	R1 = 0.0447, wR2 = 0.0891
Δρ (max, min) ($e.Å^{-3}$)	0.427 and -0.395	0.541 and -0.411

Table 8-2-3. Main crystallographic data and refinement parameters of all cocrystal structures (part 1) not presented in the main manuscript.

Compound	1:1 nefiracetam-5-nitroisophthalic acid FI	1:1 nefiracetam-5-nitroisophthalic acid FII	1:1 nefiracetam-5-bromoisophthalic acid	1:1 nefiracetam-5-hydroxyisophthalic acid
Empirical formula	C_{22} H_{23} N_3 O_8	C_{22} H_{23} N_3 O_8	C_{22} H_{23} Br N_2 O_6	C_{22} H_{24} N_2 O_7
Formula weight ($g.mol^{-1}$)	457.43	457.43	491.33	428.43
Temperature (K)	297(2)	295(2)	297(2)	297(2)
Wavelength (Å)	1.54184	1.54184	0.71073	0.71073
Crystal system	Monoclinic	Monoclinic	Monoclinic	Monoclinic
Space group	$P2_1/n$	Pc	$P2_1/c$	$P2_1/c$
a, b, c (Å)	7.87163(18),36.5803(6),8.70817(18)	6.33727(5),19.36454(12), 9.28378(8)	7.5009(5), 6.4477(18), 9.2134(5)	8.7567(4), 36.4005(17), 14.2304(6)
α, β, γ (°)	90, 115.254(3), 90	90, 99.8062(8), 90	90, 112.191 (8), 90	90, 102.985(4), 90
Volume ($Å^3$)	2267.84(9)	1122.644(14)	2332.3(3)	4419.9(3)
Z	4	2	4	8
Density ($g.cm^{-3}$)	1.340	1.353	1.399	1.288
Absorption coefficient (mm^{-1})	0.872	0.881	1.801	0.0997
F(000)	960	480	1008	1808
Crystal size (mm^3)	0.572 x 0.423 x 0.239	0.450 x 0.330 x 0.047	0.45 x 0.30 x 0.10	0.50 x 0.50 x 0.40
θ range for data collection (°)	4.836 to 67.118	2.282 to 67.115	3.439 to 25.790	2.918 to 26.267
Reflections collected	11946	24140	10325	31147
Completeness (%)	98.6 % (to theta = 67.118°)	99.5 (to theta = 67.115°)	96.8 (to theta = 25.242°)	99.0 (to theta = 25.242°)
Max. and min. transmission	1.000 and 0.918	0.960 and 0.763	1.000 and 0.705	1.000 and 0.873
Refinement method	Full-matrix least-squares on F^2	Full-matrix least-squares on F^2	Full-matrix least-squares on F^2	Full-matrix least-squares on F^2
Data / restraints / parameters	4012 / 147 / 441	3871 / 2 / 306	4295 / 5 / 320	8765 / 0 / 571
Goodness-of-fit on F^2	1.088	0.950	1.082	1.056
Final R indices [I>2sigma(I)]	R1 = 0.0465, wR2 = 0.1153	R1 = 0.0295, wR2 = 0.0885	R1 = 0.0515, wR2 = 0.1367	R1 = 0.0516, wR2 = 0.1404
R indices (all data)	R1 = 0.0510, wR2 = 0.1191	R1 = 0.0298, wR2 = 0.0892	R1 = 0.0767, wR2 = 0.1536	R1 = 0.0613, wR2 = 0.1477
Δρ (max, min) ($e.Å^{-3}$)	0.216 and -0.172	0.149 and -0.146	0.354 and -0.426	0.262 and -0.187

Table 8-2-4. Main crystallographic data and refinement parameters of all cocrystal structures (part 2) not presented in the main manuscript.

Compound	1:1 nefiracetam-5-cyano-1,3-benzenedicarboxylic	nefiracetam-(RS)-2-phenylbutyric acid	1:1 nefiracetam-2-benzoylbenzoic acid	1:1 nefiracetam-(RS)-3-phenyllactic acid
Empirical formula	C_{23} H_{23} N_3 O_6	C_{24} H_{30} N_2 O_4	C_{28} H_{28} N_2 O_5	C_{23} H_{28} N_2 O_5
Formula weight ($g.mol^{-1}$)	437.44	410.50	472.52	412.47
Temperature (K)	297(2)	297(2) K	297(2)	297(2) K
Wavelength (Å)	0.71073	0.71073 Å	0.71073	0.71073 Å
Crystal system	Monoclinic	Orthorhombic	Orthorhombic	Orthorhombic
Space group	*Pc*	$P2_12_12$	*Pca*21	$P2_12_12_1$
a, b, c (Å)	6.1863(3), 19.5370(8), 9.3910(4)	41.158(2), 9.2846(6), 6.0202(4)	43.8966(14),6.04575(19),9.2293(3)	6.0151(5), 9.2249(6), 39.209(2)
α, β, γ (°)	90, 98.507, 90	90, 90, 90	90, 90, 90	90, 90, 90
Volume ($Å^3$)	1122.52(8)	2300.5(3)	2449.33(13)	2175.6(3)
Z	2	4	4	4
Density ($g.cm^{-3}$)	1.294	1.185 Mg/m	1.281	1.259 Mg/m
Absorption coefficient (mm^{-1})	0.095	0.081	0.088	0.089
F(000)	460	880	1000	880
Crystal size (mm^3)	0.35 x 0.28 x 0.09	0.490 x 0.301 x 0.148	0.28 x 0.19 x 0.02	0.410 x 0.270 x 0.085
Theta range for data collection (°)	3.026 to 25.243	2.249 to 25.679°	3.402 to 25.265	2.268 to 25.247°.
Reflections collected	7577	6688	19309	5814
Completeness (%)	94.9 (to theta = 25.242°)	99.5 %	99.2 (to theta = 25.242°)	99.0 %
Max. and min. transmission	1.00000 and 0.85329	0.959 and 0.871	1.00000 and 0.88720	0.975 and 0.923
Refinement method	Full-matrix least-squares on F^2	Full-matrix least-squares on F^2	Full-matrix least-squares on F^2	Full-matrix least-squares on F^2
Data / restraints / parameters	7577 / 2 / 294	4063 / 81 / 360	4399 / 1 / 318	3606 / 0 / 275
Goodness-of-fit on F^2	1.040	1.082	1.077	1.057
Final R indices [I>2sigma(I)]	R1 = 0.0404, wR2 = 0.1028	R1 = 0.0667, wR2 = 0.1123	R1 = 0.0442, wR2 = 0.1051	R1 = 0.0619, wR2 = 0.1027
R indices (all data)	R1 = 0.0589, wR2 = 0.1084	R1 = 0.1118, wR2 = 0.1320	R1 = 0.0514, wR2 = 0.1093	R1 = 0.0915, wR2 = 0.1211
Δρ (max, min) ($e.Å^{-3}$)	0.135 and -0.110	0.148 and -0.148	0.188 and -0.161	0.164 and -0.166

Table 8-2-5. Main crystallographic data and refinement parameters of all cocrystal structures (part 3) not presented in the main manuscript.

Compound	2:1 nefiracetam-(RS)-phenylsuccinic acid	1:1 nefiracetam-4-hydroxybenzoic acid	4:1:1 nefiracetam-gallic acid-water
Empirical formula	$C_{76}H_{92}N_8O_{16}$	$C_{21}H_{24}N_2O_5$	$C_{64}H_{80}N_8O_{14}$
Formula weight ($g.mol^{-1}$)	1373.57	384.42	1185.36
Temperature (K)	293(2)	295(2)	293(2)
Wavelength (Å)	1.54184	1.54184	0.71073
Crystal system	Monoclinic	Monoclinic	Triclinic
Space group	$P2_1/n$	$P2_1/n$	P-1
a, b, c (Å)	5.98623(16), 9.3427(2), 35.3554(9)	4.7571(2), 12.7544(5), 33.4306(15)	8.3372(5), 8.8647(12), 22.302(2)
α, β, γ (°)	90, 94.247(3), 90	90, 91.108(4), 90	87.663(10), 81.860 (7), 79.777(8)
Volume ($Å^3$)	1971.91(9)	2027.99(15)	1605.5(3)
Z	1	4	1
Density ($g.cm^3$)	1.157	1.259	1.226
Absorption coefficient (mm^{-1})	0.666	0.744	0.087
F(000)	732	816	632
Crystal size (mm^3)	0.533 x 0.333 x 0.270	0.480 x 0.350 x 0.240	0.55 x 0.10 x 0.06
θ range for data collection (°)	5.017 to 66.872°	2.644 to 67.194	2.902 to 25.090°
Reflections collected	11005	5363	16276
Completeness (%)	98.0 % (to theta = 66.872°)	98.4 % (to theta = 67.194°)	98.9% (to theta = 25.090°)
Max. and min. transmission	1.000 and 0.918	1.000 and 0.938	1.000 and 0.765
Refinement method	Full-matrix least-squares on F^2	Full-matrix least-squares on F^2	Full-matrix least-squares on F^2
Data / restraints / parameters	3431 / 62 / 273	5363 / 0 / 264	5650 / 75 / 437
Goodness-of-fit on F^2	1.088	1.093	1.096
Final R indices [I>2sigma(I)]	R1 = 0.0799, wR2 = 0.1873	R1 = 0.0439, wR2 = 0.1385	R1 = 0.0666, wR2 = 0.1601
R indices (all data)	R1 = 0.0830, wR2 = 0.1889	R1 = 0.0547, wR2 = 0.1423	R1 = 0.0985, wR2 = 0.1765
Largest diff. peak and hole ($e.Å^{-3}$)	0.623 and -0.351	0.176 and -0.152	0.261 and -0.330

8.2.8. DVS and Moisture Exposure

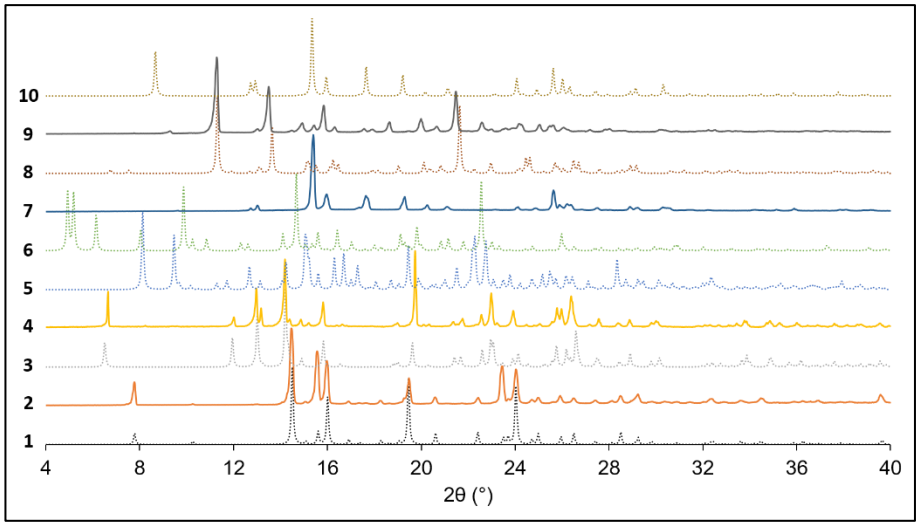

Figure 8-2-33. XRPD pattern of **1**: nefiracetam FI (simulated), **2**: nefiracetam after 7 days at 100%RH exposure, **3**: NZC (simulated), **4**: NZC (30 days at 100%RH), **5**: NZCW (simulated), **6**: NCA (simulated), **7**: NCA (30 days at 100%RH), **8**: NOA (simulated), **9**: NOA (30 days at 100%RH) and **10**: nefiracetam monohydrate (simulated).

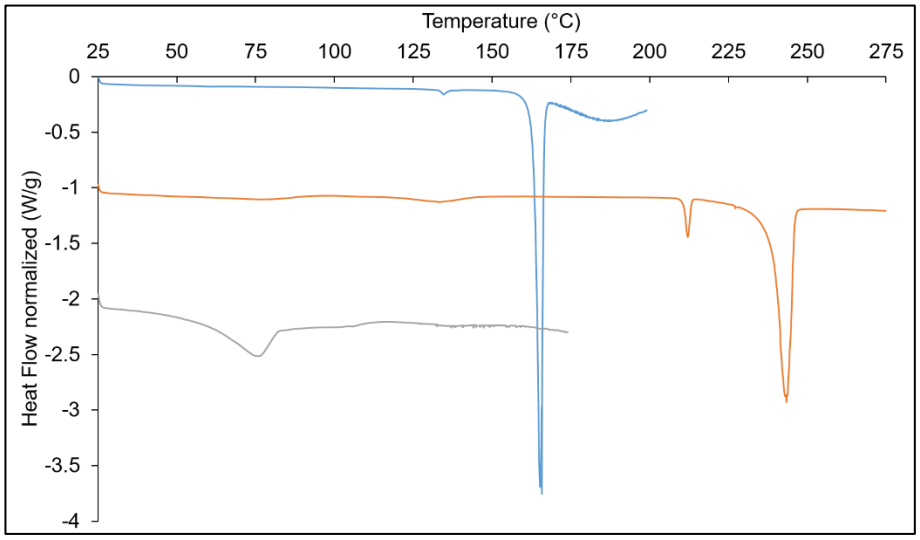

Figure 8-2-34. DSC curve of NOA (blue), NZC (orange) and NCA (grey) after 30 days under 100% RH exposure.

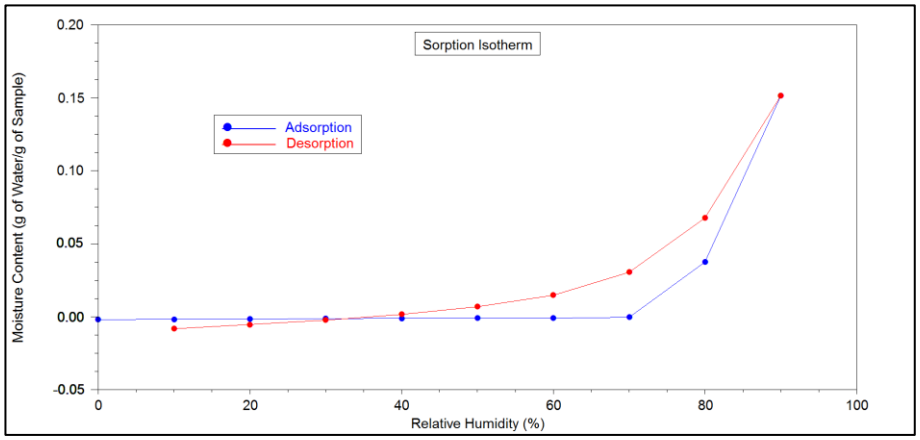

Figure 8-2-35. Sorption Isotherm (adsorption and desorption) of NCA at 25°C.

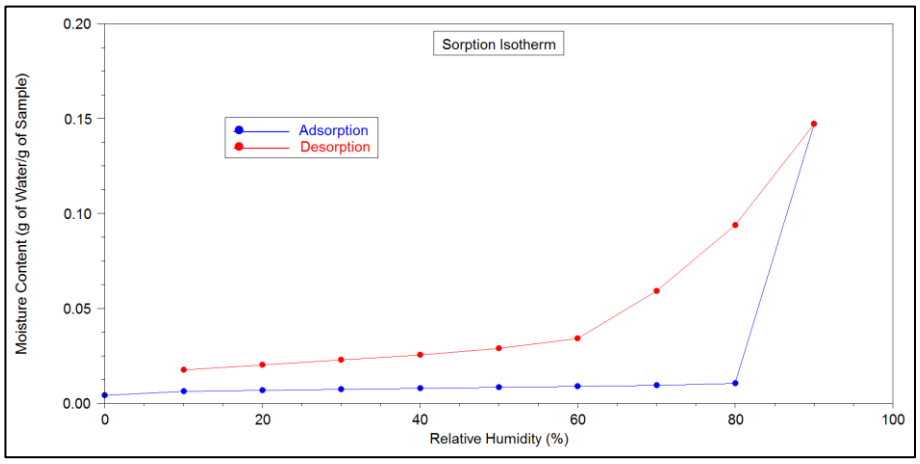

Figure 8-2-36. Sorption Isotherm (adsorption and desorption) of NZC at 25°C.

8.2.9. Calibration Lines

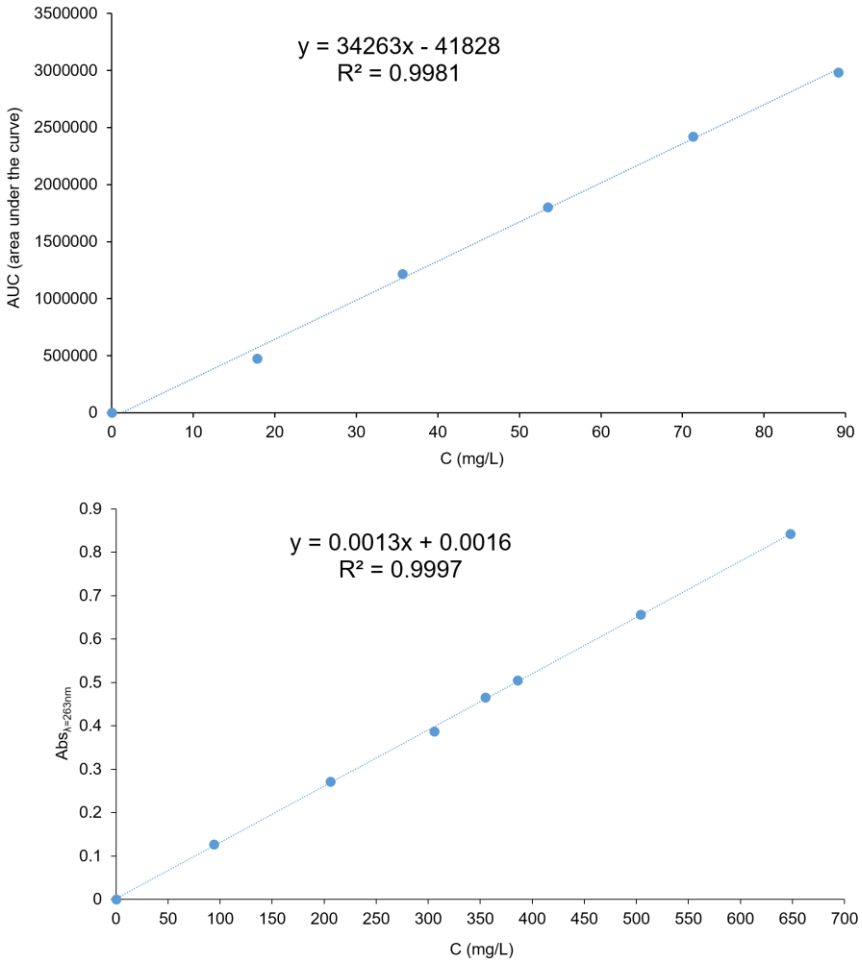

Figure 8-2-37. Calibration line used to dose nefiracetam in solution via HPLC during the dissolution experiments of NCA and NOA in EtOH and MeCN at 18°C (top). Calibration line used to dose nefiracetam in solution via UV spectroscopy during the dissolution experiments of NZC in EtOH and MeCN at 18°C (below).

8.2.10. HPLC Data

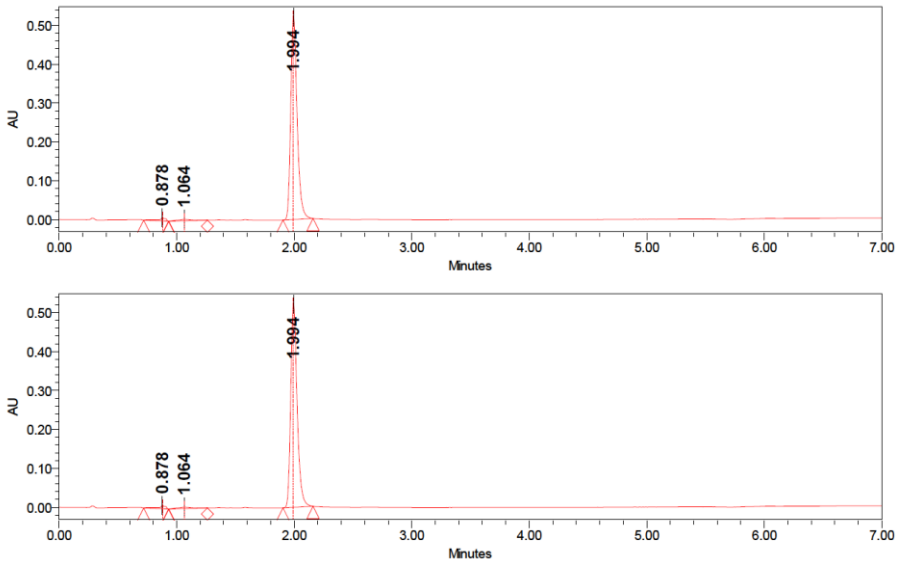

Figure 8-2-38. Typical HPLC chromatogram obtained during the quantitative analysis of nefiracetam from the dissolution experiments.

Table 8-2-6. Summary of the data used to build the dissolution curves of nefiracetam in EtOH and MeCN at 18°C under 100 rpm.

NEFIRACETAM	**ACETONITRILE**			**ETHANOL**		
Sampling time (min)	Dilution factor	Retention time (min)	AUC	Dilution factor	Retention time (min)	AUC
0	0	0	0	0	0	0
0.08333333	2000	2.014	412097	2500	2.022	599373
0.16666667						
0.25						
0.33333333	2000	1.994	1123353	2500	2.003	891775
0.41666667						
0.5	2000	1.994	1221140			
0.58333333				2500	2.001	1430751
0.66666667	2000	1.993	1360187			
0.75						
0.83333333				2500	2.001	1660412
1	2000	1.998	1290697		2.030	1803989
1.5	2000	1.999	1443300			
2	2000	1.998	1233092	2000	1.994	1903925

2.5	2000	1.998	1361664			
3	2000	2.000	1021522			
3.5						
4	2000	1.998	1401631	2000	1.996	1810678
4.5						
5	2000	1.998	1258620	2000	1.994	2058476
6				2000	1.994	1975186
7				2000	1.992	1797448
8				2000	1.994	1975222
9				2000	1.996	1688667
10	2000	1.996	1402725	2000	1.994	1994076
11				2000	1.994	1781480
12				2000	1.995	2119195
12.5				2000	1.994	1980331
13						
14				2000	1.995	2200488
15	2000	1.998	1333962	2000	1.995	2191115
30	2000	1.997	1364834	2000	1.992	1746601
45						
60	2000	2.001	1438496	2000	1.995	1775440
120				2000	1.994	1653944
180	2000	2.000	1257201			
240						
1440	2500	1.998	1141196	4000	2.039	1030530
1440	2500	2.027	1233540	4000	2.007	1052120
1440	2500	2.000	1181260	4000	2.007	1052120

Table 8-2-7. Summary of the data used to build the dissolution curves of **NCA** in EtOH and MeCN at 18°C under 100 rpm.

NCA	**ACETONITRILE**			**ETHANOL**		
Sampling time (min)	Dilution factor	Retention time (min)	AUC	Dilution factor	Retention time (min)	AUC
0	0	0	0	0	0	0
0.08333333						
0.16666667	2000	2.024	463252			
0.25				4000	2.063	273133
0.33333333						
0.41666667						
0.5	2000	1.991	537961	4000	2.030	314596
0.58333333						
0.66666667						

0.75	2000	1.991	621607	4000	2.025	327294
0.83333333	2000	1.991	640564			
1				4000	2.028	402443
1.5	2000	1.990	1016079	4000	2.030	767192
2	2000	1.990	1038334	4000	2.030	1303657
2.5	2000	1.990	864520	4000	2.029	1256000
3	2000	1.991	1046076	4000	2.031	1279776
3.5	2000	1.989	1059647	4000	2.029	1366063
4	2000	1.991	1038926	4000	2.040	1292413
4.5	2000	1.991	1109477	4000	2.030	1463559
5	2000	1.991	1171218	4000	2.031	1462498
6	2000	1.990	1083436			
7	2000	1.991	1170866	4000	2.031	1351450
8	2000	1.989	1166090	4000	2.031	1400703
9	2500	1.993	914513	4000	2.029	1330640
10	2500	1.992	873151	4000	2.033	1038031
11						
12						
12.5	2500	1.991	945260			
13						
14						
15	2500	1.994	886622	5000	2.032	1207073
30	2500	1.997			2.028	1134123
45						
60	2500	1.996	1002506	5000	2.029	1198447
120	2500	1.998	1003643	5000	2.031	1293977
180						
240				5000	2.030	1247780
1440	2500	1.998	1063223	4000	2.040	1596102
1440	2500	1.997	1046565	4000	2.008	1558081
1440	2500	1.999	1034129	4000	2.008	1664379

Table 8-2-8. Summary of the data used to build the dissolution curves of **NOA** in EtOH and MeCN at 18°C under 100 rpm.

NOA	**ACETONITRILE**			**ETHANOL**		
Sampling time (min)	Dilution factor	Retention time (min)	AUC	Dilution factor	Retention time (min)	AUC
0	0	0	0	0	0	0
0.08333333						
0.16666667				2500	2.035	695955
0.25	2000	2.147	479717			

0.33333333						
0.41666667				2500	2.003	577502
0.5	2000	2.111	603500			
0.58333333						
0.66666667						
0.75	2000	2.108	773451	2500	2.006	2140568
0.83333333						
1	2000	2.106	785345	2500	2.003	596136
1.5	2000	2.107	692512	2500	2.004	826694
2	2000	2.105	822251	2500	2.005	905026
2.5	2000	2.104	872370	2500	2.004	2202520
3	2000	2.102	708751	2500	2.003	533911
3.5	2000	2.103	848988	2500	1.999	2307427
4	2000	2.099	796181			
4.5	2000	2.098	818237	2500	1.994	2394271
5	2000	2.096	861858	2500	2.000	2233971
6	2000	2.097	853860	2500	1.998	2359543
7	2000	2.095	851519	2500	1.998	2233371
8	2500	2.093	823877	2500	1.998	2211001
9	2500	2.094	661151	2500	1.997	2221166
10					1.998	2276022
11						
12						
12.5				2500	1.998	2268118
13						
14						
15	2500	2.091	667857	2500	1.998	2290064
30	2500	2.092	651070	2500	1.994	2399600
45						
60	2500	2.092	723930	2500	1.997	2360694
120	2500	2.090	652198	4000	1.997	2496967
180						
240	2500	2.089	645758			
1440	2500	2.085	682654	4000	1.997	1534584
1440	2500	2.007	688118	4000	2.000	1500012
1440	2500	2.003	681328	4000	1.998	1508041

8.2.11. UVS Data

Table 8-2-9. Summary of the data used to build the dissolution curves of **NZC** in EtOH and MeCN at 18°C under 100 rpm.

NZC	**ACETONITRILE**			**ETHANOL**		
Sampling time (min)	Dilution factor	Retention time (min)	Abs_{263}	Dilution factor	Retention time (min)	Abs_{263}
0		-			-	
0.08333333		-			-	
0.16666667	250	-	0.0278	250	-	0.1135
0.25		-			-	
0.33333333		-			-	
0.41666667	250	-	0.0278	250	-	0.1350
0.5		-			-	
0.58333333		-			-	
0.66666667		-		250	-	0.1608
0.75		-			-	
0.83333333	250	-	0.0314		-	
1		-		250	-	0.1359
1.5	250	-	0.033	250	-	0.1544
2	250	-	0.0331	250	-	0.1036
2.5	250	-	0.0337	250	-	0.1237
3		-		250	-	0.1036
3.5	250	-	0.0341	250	-	0.1310
4	250	-	0.0376	250	-	0.1310
4.5	250	-	0.0374	250	-	0.1207
5	250	-	0.0342	250	-	0.1859
6	250	-	0.0328		-	
7	250	-	0.0331	250	-	0.1517
8	250	-	0.0333	250	-	0.1494
9	250	-	0.0326	250	-	0.1652
10	250	-	0.0337	250	-	0.1669
11		-			-	
12		-			-	
12.5	250	-	0.0337		-	
13		-			-	
14		-			-	
15	250	-	0.0337	250	-	0.1451
30		-			-	
45		-			-	
60	250	-	0.0333		-	

120	250	-	0.0333		-	
180		-			-	
240		-			-	
1440	250	-	0.0342	250	-	0.2590
1440	250	-	0.0334	250	-	0.2573
1440	250	-	0.035	250	-	0.2549

8.3. Supporting Information to Chapter 6

8.3.1. Crystal Structure

Table 8-3-1. Main crystallographic data of NRMA and refinement parameters. Crystal Structure resolved from a crystal picked up coming from *a nefiracetam-(RS)-mandelic acid evaporative experiment and * a nefiracetam-(R)-mandelic acid evaporative experiment.

Compound	**NRMA***	**NRMA****
Empirical formula	$C_{22}H_{26}N_2O_5$	$C_{22}H_{26}N_2O_5$
Formula weight ($g.mol^{-1}$)	398.45	398.45
Temperature (K)	295(2)	295(2)
Wavelength (Å)	1.54184	1.54184
Crystal system	Orthorhombic	Orthorhombic
Space group	$P2_12_12_1$	$P2_12_12_1$
a, b, c (Å)	6.01624(12), 9.23442(16), 37.7189(6)	6.01055(9), 9.23597(14), 37.7607(5)
α, β, γ (°)	90, 90, 90	90, 90, 90
Volume ($Å^3$)	2095.53(6)	2096.21(5)
Z	4	4
Density ($g.cm^{-3}$)	1.263	1.263
Absorption coefficient (mm^{-1})	0.737	0.737
F(000)	848	848
Crystal size (mm^3)	0.550 x 0.480 x 0.190	0.470 x 0.330 x 0.270
Theta range for data collection (°)	2.343 to 67.092	4.684 to 67.062
Reflections collected	10110	10293
Completeness to θ = 67.092°	99.1 %	98.8 %
Max. and min. transmission	0.880 and 0.733	0.845 and 0.769
Refinement method	Full-matrix least-squares on F^2	Full-matrix least-squares on F^2
Data / restraints / parameters	3694 / 0 / 271	3690 / 0 / 276
Goodness-of-fit on F^2	1.043	1.068
Final R indices [I>2sigma(I)]	R1 = 0.0375, wR2 = 0.0989	R1 = 0.0303, wR2 = 0.0827
R indices (all data)	R1 = 0.0400, wR2 = 0.1017	R1 = 0.0311, wR2 = 0.0836
Absolute structure parameter	-0.03(10)	-0.07(6)
Δρ (max, min) (e. $Å^{-3}$)	0.150 and -0.139	0.112 and -0.088

8.3.2. Binary Phase Diagram

Table 8-3-2. Data used to build the nefiracetam-mandelic acid Binary Phase diagram.

Ratio N/RSMA	Ratio RMA/SMA	T_{onset} (°C)	T_{endset} (°C)
0.982	0.000	114.10	118.88
1.001	0.103	97.29	114.90
0.961	0.203	96.87	111.93
1.008	0.304	98.25	109.18
1.011	0.401	98.16	104.53
0.983	0.500	97.64	97.64
0.992	0.652	97.79	107.60
1.002	0.704	98.39	108.75
1.006	0.824	97.43	112.88
1.004	0.908	95.68	115.35
0.989	1.000	114.10	118.17

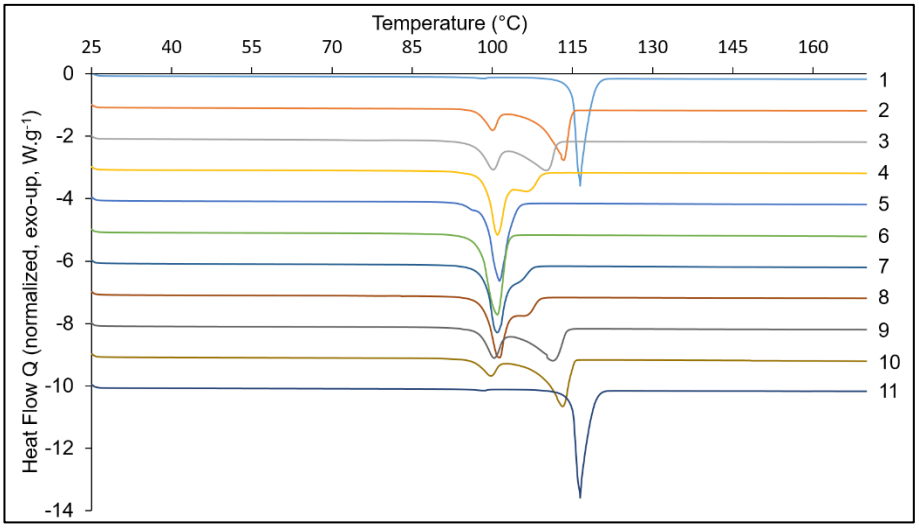

Figure 8-3-1. DSC curves related to each sample prepared for the Binary Phase Diagram construction.

8.3.3. TGA Curves

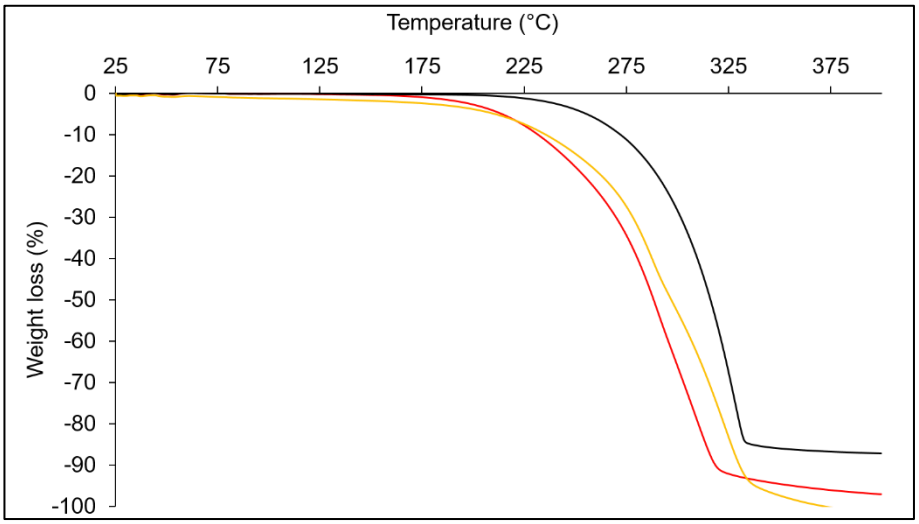

Figure 8-3-2. TGA curves of nefiracetam FI (black), NRSMA (orange) and NRMA (red).

8.3.4. Solubility

$$NRSMA \rightleftarrows N + RSMA \qquad \text{(Eq. 1)}$$

$$K_s = [RSMA] \times [N] \qquad \text{(Eq. 2)}$$

$$\ln K_s = -\frac{\Delta H_{diss}}{RT} + \frac{\Delta S_{diss}}{R} \qquad \text{(Eq. 3)}$$

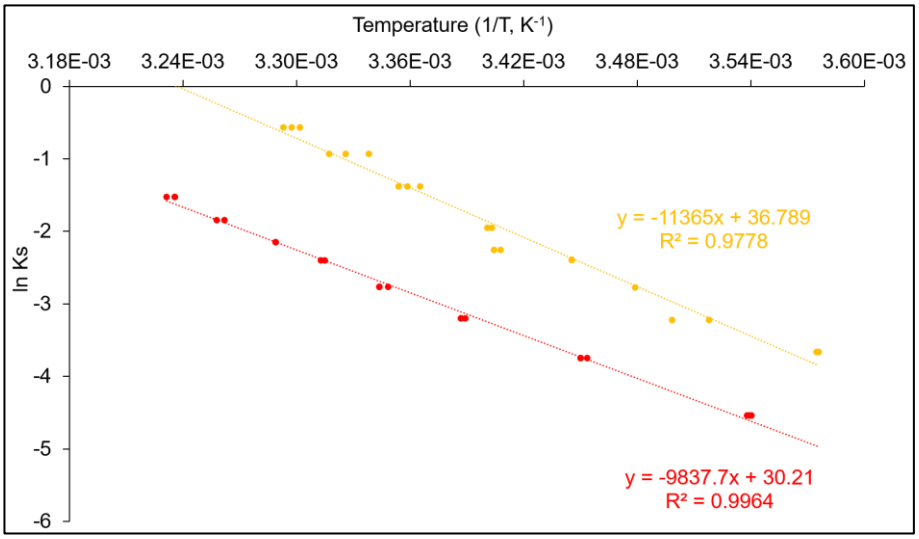

Figure 8-3-3. Van't Hoff plot of the solubility curves of NRSMA (orange) and NRMA (red).

8.3.4. Chiral HPLC

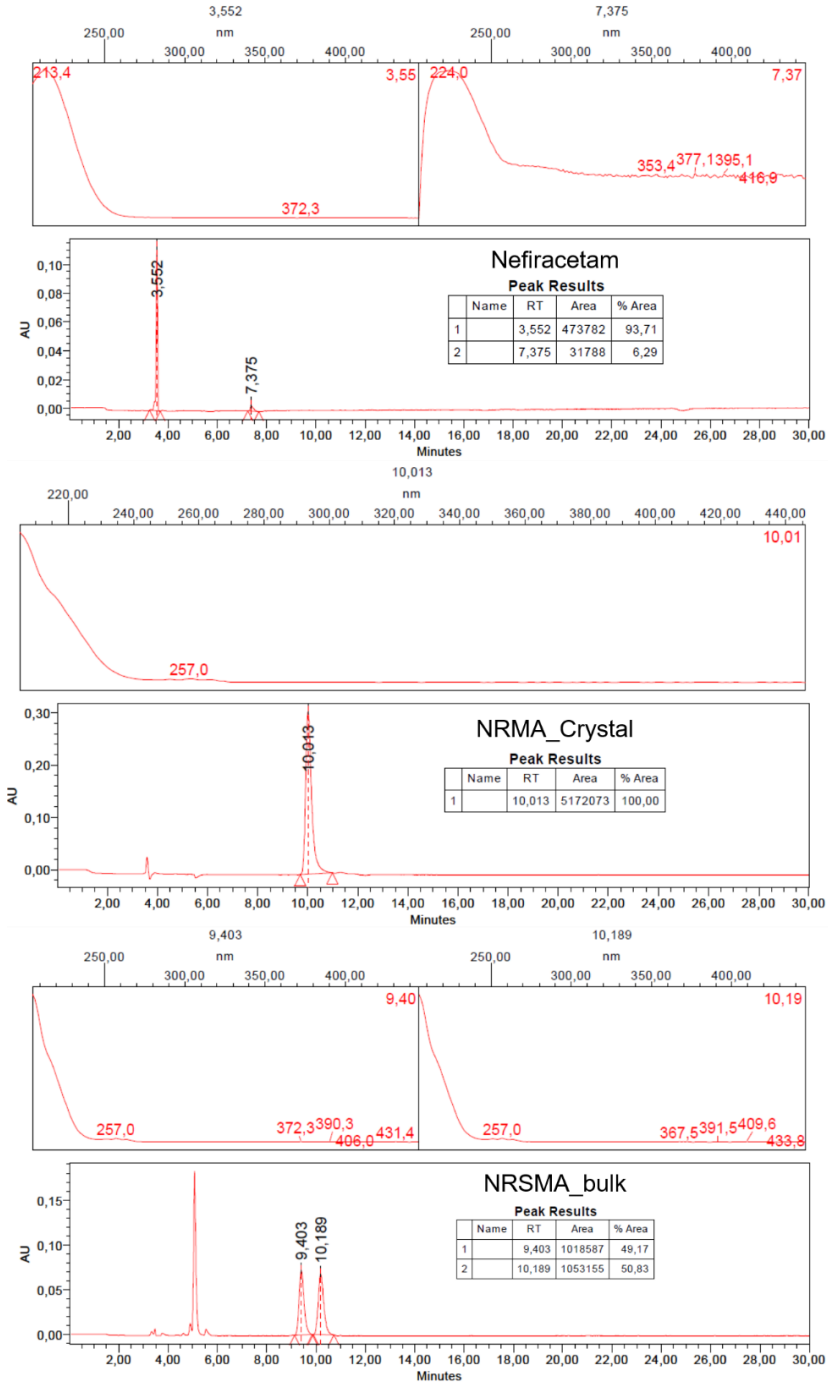

Figure 8-3-4. UV Spectrum index plot and chiral HPLC chromatogram of nefiracetam, NRMA (crystal) and NRSMA (bulk material).

8.3.5. Ternary Phase Diagram

Table 8-3-3. Mass fractions (S, R enantiomer and solvent) calculated to build the Ternary Phase Diagram.

Sample	Mass fraction S	Mass fraction R	Mass fraction Solvent
1	9.60×10^{-2}	0	9.04×10^{-1}
2	1.12×10^{-1}	2.66×10^{-2}	8.61×10^{-1}
3	1.18×10^{-1}	5.66×10^{-2}	8.25×10^{-1}
4	1.07×10^{-1}	1.04×10^{-1}	7.89×10^{-1}
5	1.07×10^{-1}	1.03×10^{-1}	7.90×10^{-1}
6	1.04×10^{-1}	1.02×10^{-1}	7.94×10^{-1}
7	1.10×10^{-1}	1.08×10^{-1}	7.83×10^{-1}
8	1.13×10^{-1}	1.15×10^{-1}	7.72×10^{-1}
9	5.38×10^{-2}	1.05×10^{-1}	8.41×10^{-1}
10	2.34×10^{-2}	1.06×10^{-1}	8.71×10^{-1}
11	0	1.06×10^{-1}	8.94×10^{-1}

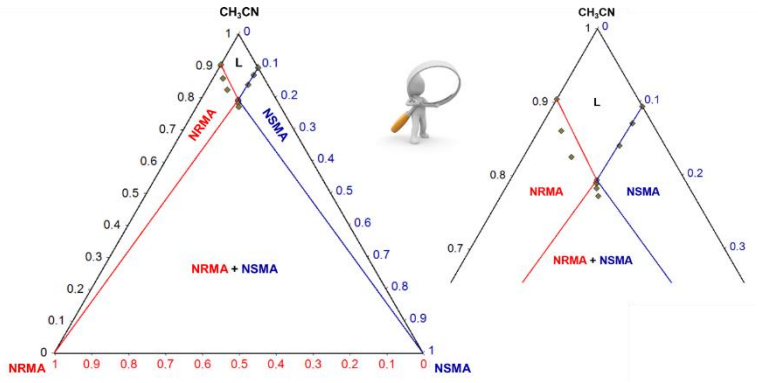

Figure 8-3-5. Ternary Phase Diagram (isothermal cut) of nefiracetam-mandelic acid in MeCN at 23°C.

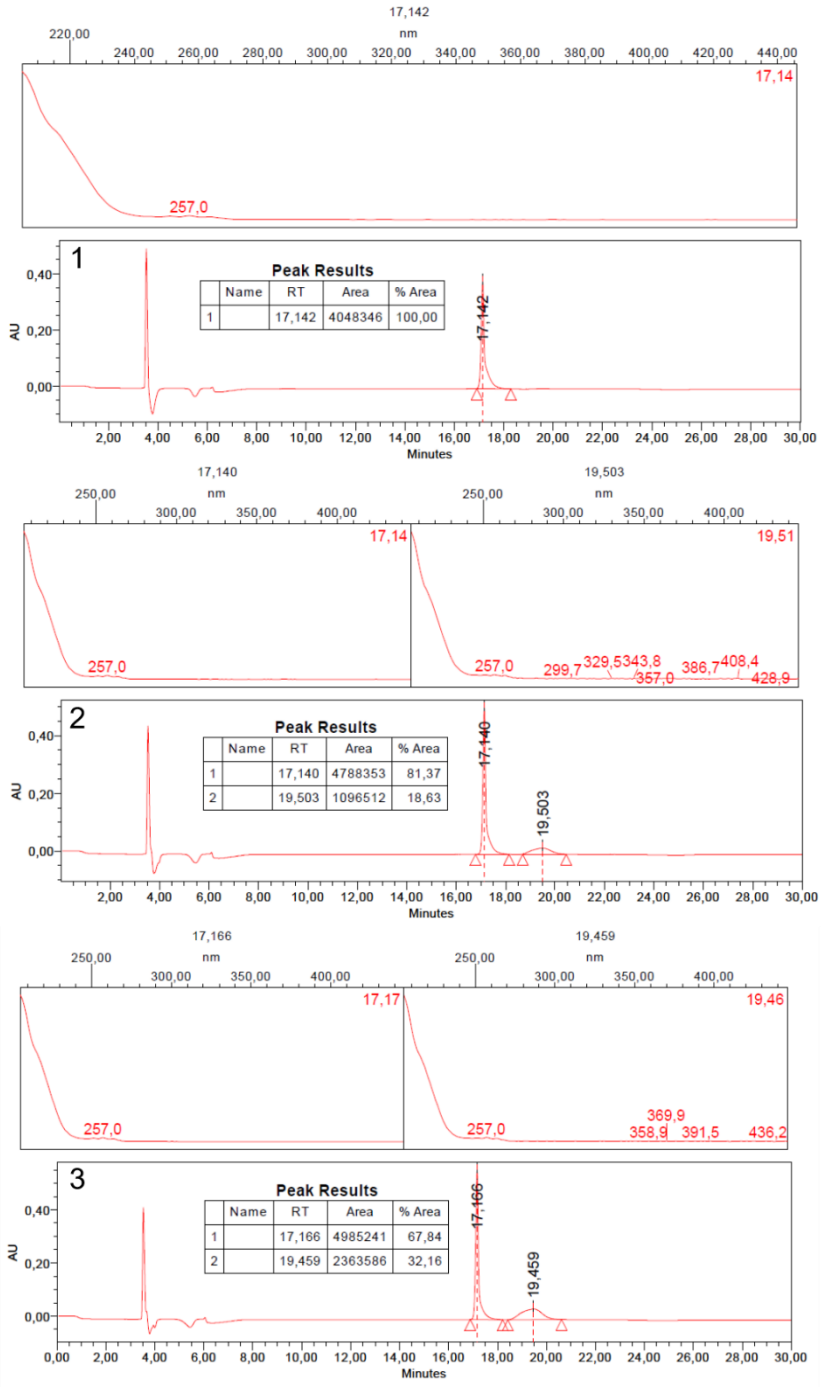

Figure 8-3-6. UV Spectrum index plot and chiral HPLC chromatogram related to the liquid fractions (1, 2 and 3) and required for the Ternary Phase Diagram construction.

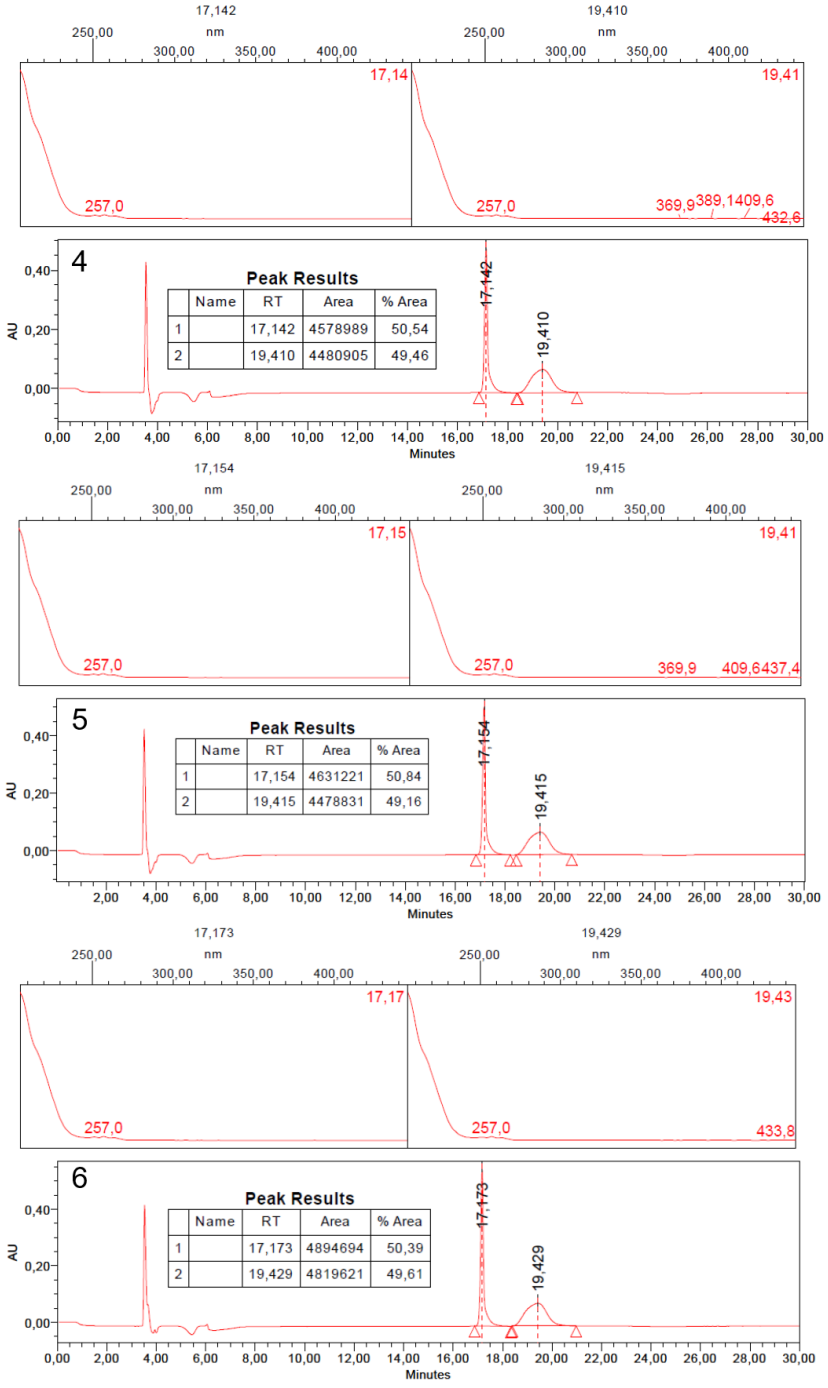

Figure 8-3-7. UV Spectrum index plot and chiral HPLC chromatogram related to the liquid fractions (4, 5 and 6) and required for the Ternary Phase Diagram construction.

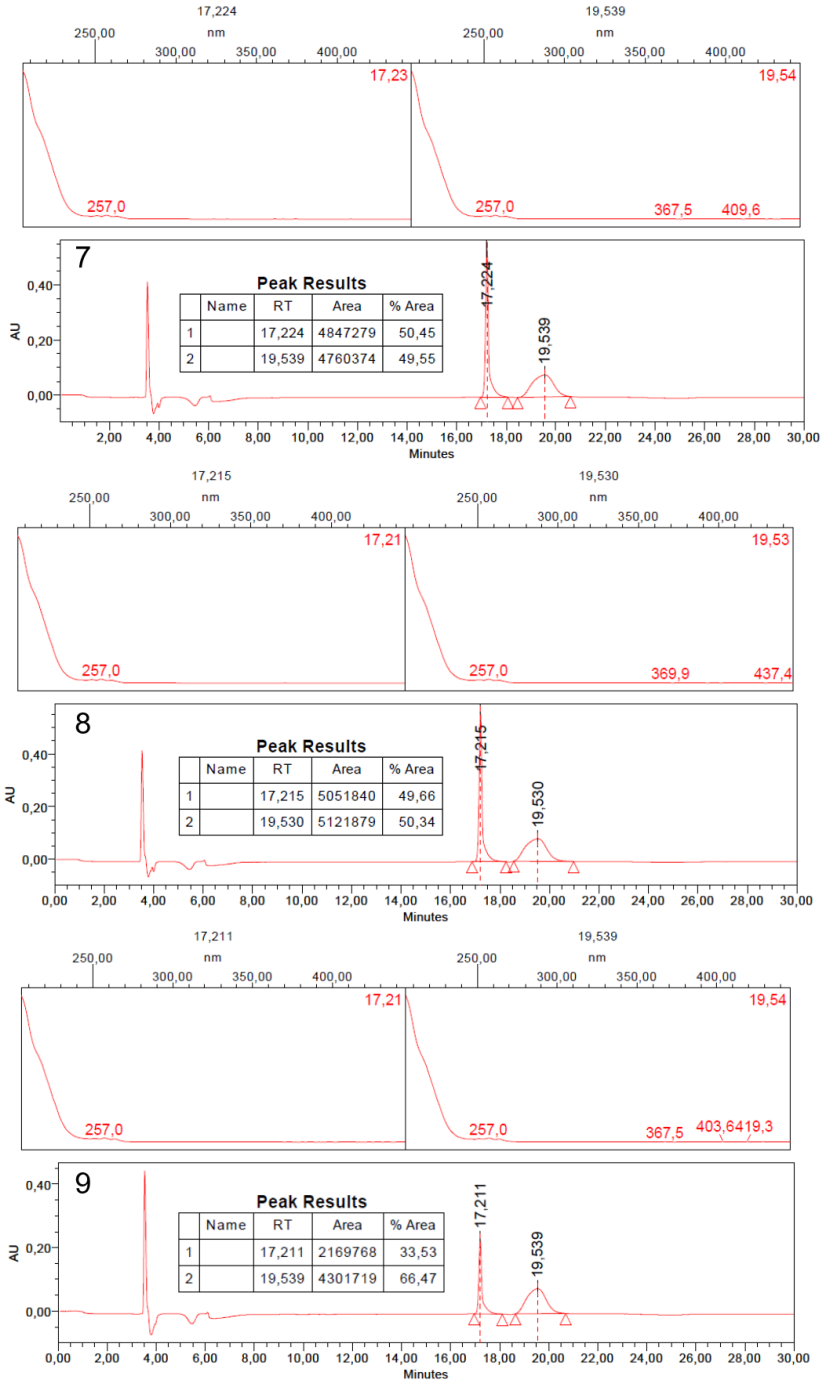

Figure 8-3-8. UV Spectrum index plot and chiral HPLC chromatogram related to the liquid fractions (7, 8 and 9) and required for the Ternary Phase Diagram construction.

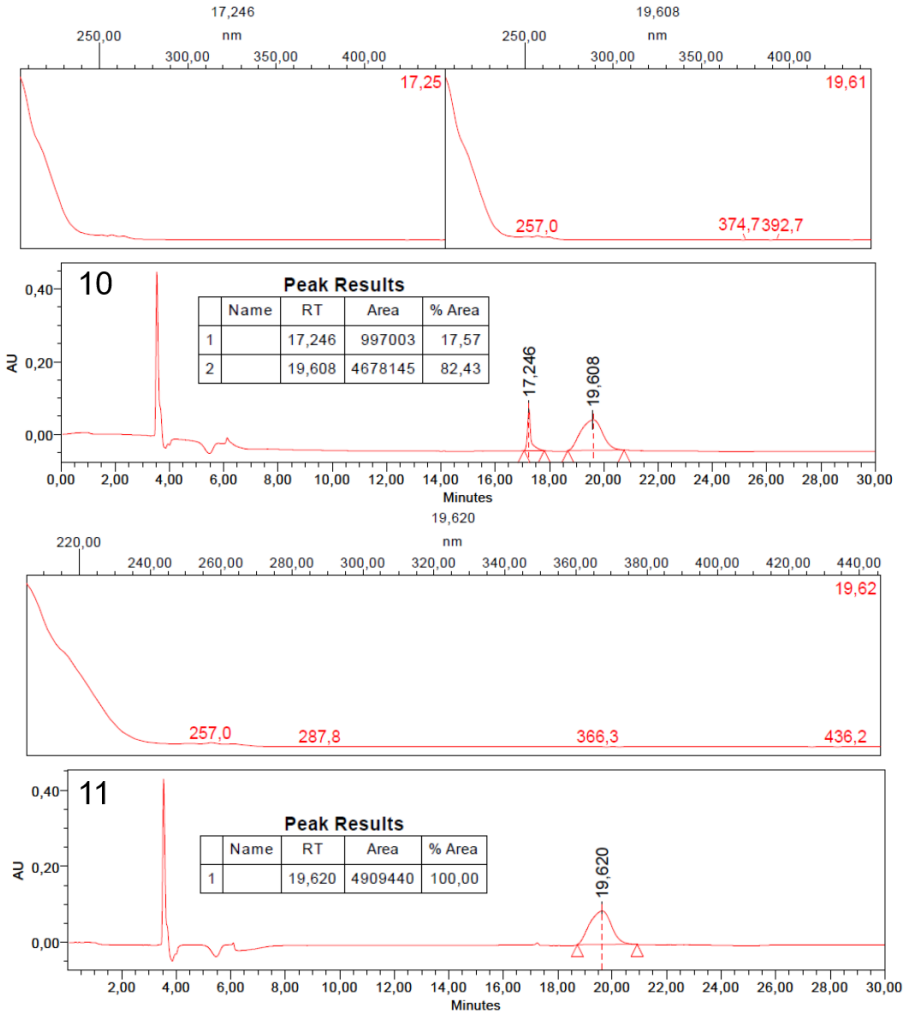

Figure 8-3-9. UV Spectrum index plot and chiral HPLC chromatogram related to the liquid fractions (10 and 11) and required for the Ternary Phase Diagram construction.

8.3.6. Calibration Lines

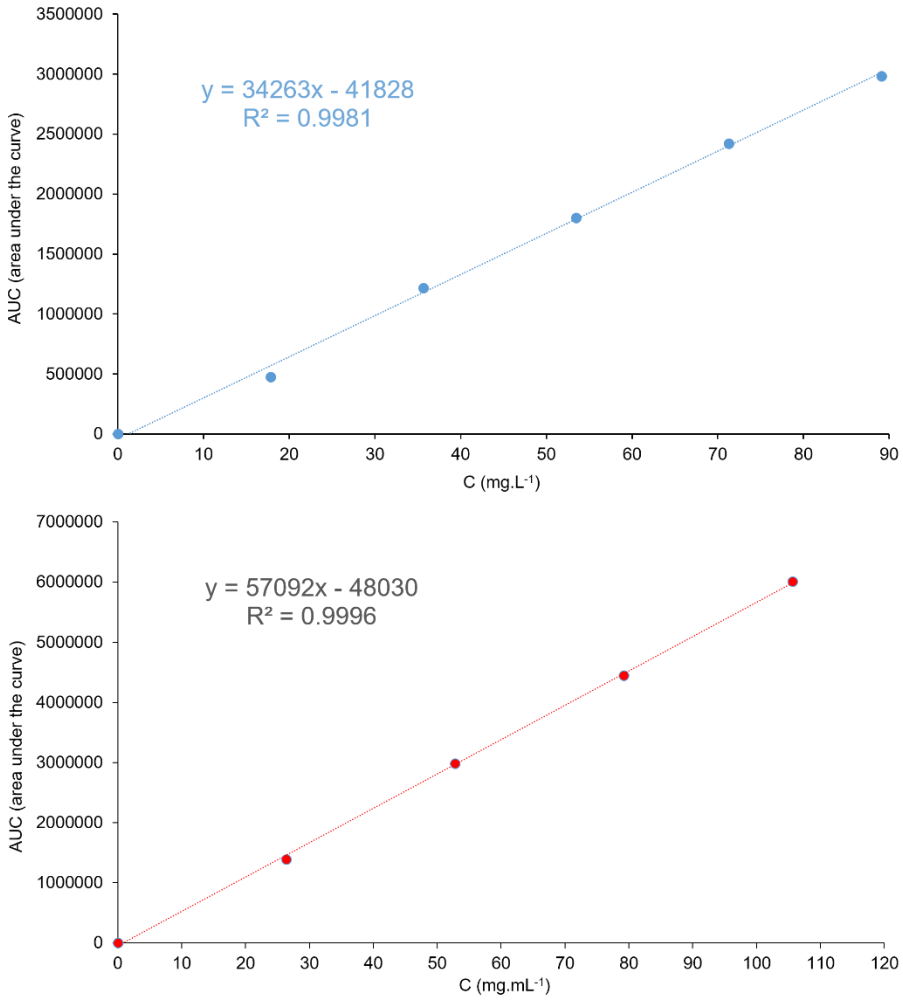

Figure 8-3-10. Calibration lines for nefiracetam dosage in reverse HPLC (top) and RMA/SMA dosage/ratio in chiral HPLC.

8.3.7. Solvent Screen

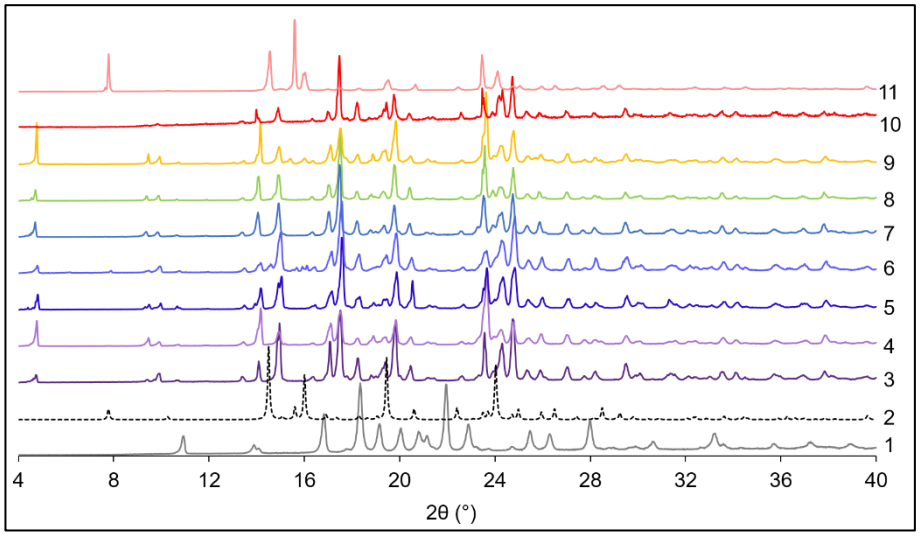

Figure -3-11. XRPD analyses performed on the solid outcomes obtained during the congruency experiments in (3) acetonitrile, (4) chloroform, (5) dichloromethane, (6) diethylether, (7) ethyl acetate, (8) ethanol, (9) water, (10) 2-propanol and (11) tetrahydrofuran. They are compared to the (1) nefiracetam FI simulated pattern and (2) the (RS)-mandelic acid experimental one.

8.3.8. Seeded Isothermal Preferential Crystallization

Table 8-3-4. Process parameters and results of the seven other SIPC trials.

N°	PC Mode	V (mL)	T1 (°C)	T2 (°C)	Cooling rate (°C.min^{-1})	t_{end} (min)	mass NRSMA (g)	mass seed (mg)	m end (mg)
9	SIPC	50	20	17	n/a	120	8.50	52.61	226.40
10	SIPC	50	20	19	n/a	120	8.20	50.41	311.99
11	SIPC	50	20	17	n/a	90	7.50	50.08	358.52
12	SIPC	100	23	17	1.7	60	21.19	50.19	726.96
13	SIPC	100	23	17	1.7	90	16.71	50.24	1435.72
14	SIPC	100	23	17	1.7	120	18.02	50.42	1412.2
15	SIPC	750	23	17.3	0.1	180	120.36	376.83	24902.45

Table 8-3-5. Values of purity, resolution index, productivity and yield for the experiments of Table S4. Those parameters are only calculated for pure **NRMA** outcomes.

N°	Pu NRMA (%)	RI	Pr NRMA (10^{-3} g.g^{-1}.min^{-1})	yield (%)
9	93.82	3.04	0.31	13.08
10	86.68	n/a	n/a	n/a
11	98.46	5.75	0.90	42.00
12	99.32	13.39	1.06	14.81
13	82.07	n/a	n/a	n/a
14	59.89	n/a	n/a	n/a
15	50.19	n/a	n/a	n/a

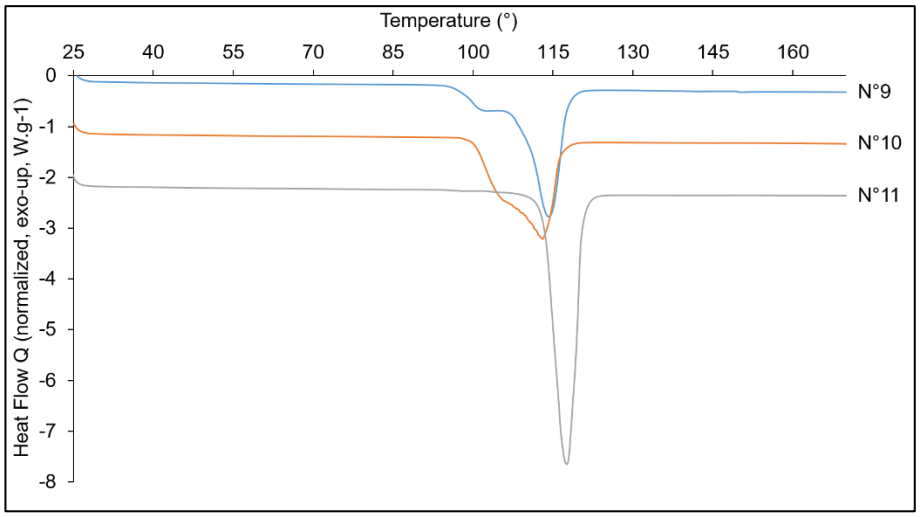

Figure 8-3-12. DSC analyses performed on the solid outcomes of the trials 9 to 11.

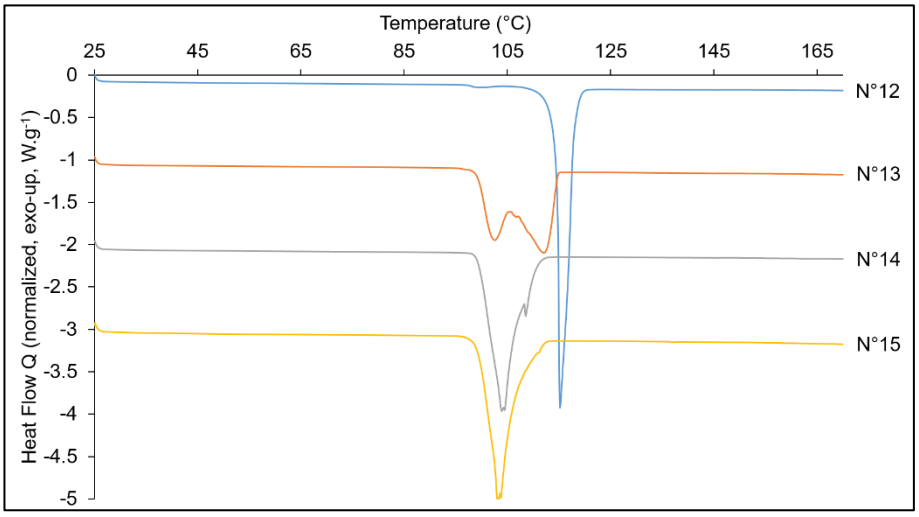

Figure 8-3-13. DSC analyses performed on the solid outcomes of the trials 12 to 15.

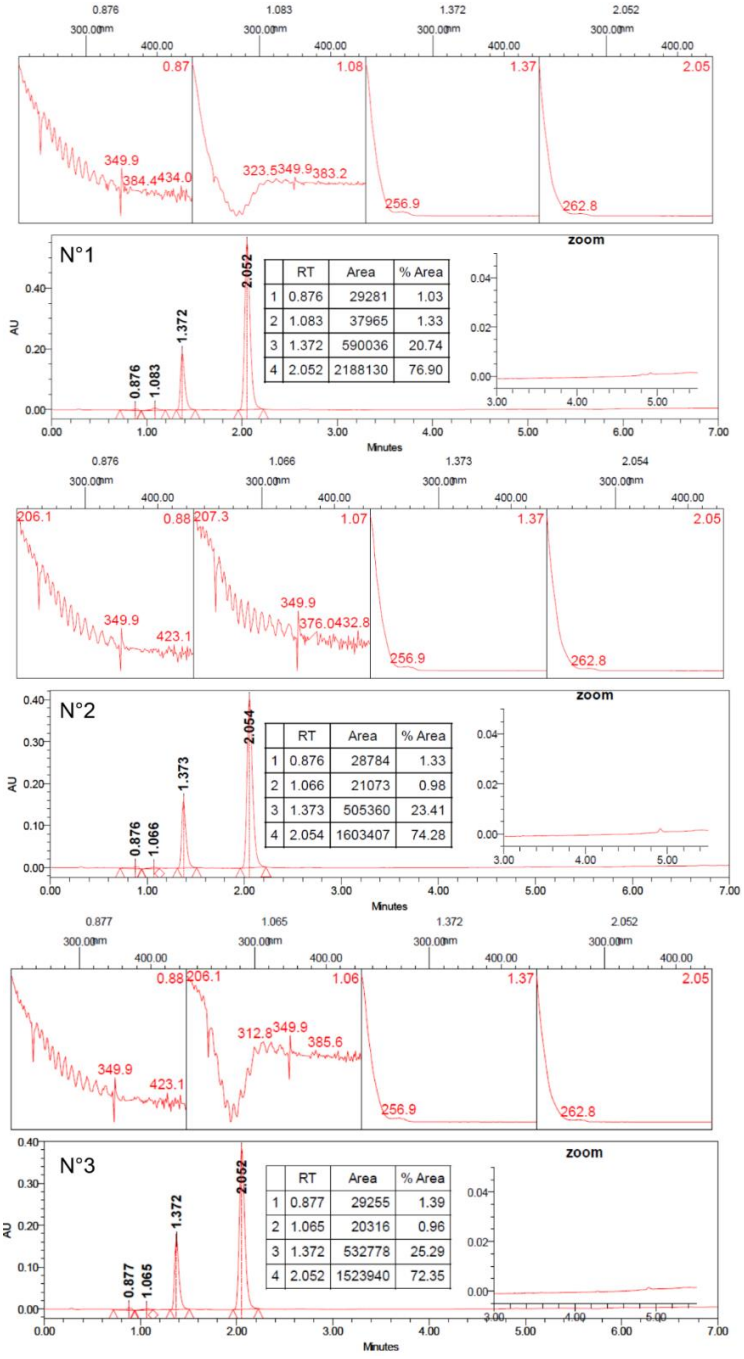

Figure 8-3-14. UV spectrum index plot and reverse HPLC chromatograms used to dose the NRSMA solubility for the trials 1 to 3. The nefiracetam absorption peak goes out around 2.0 min.

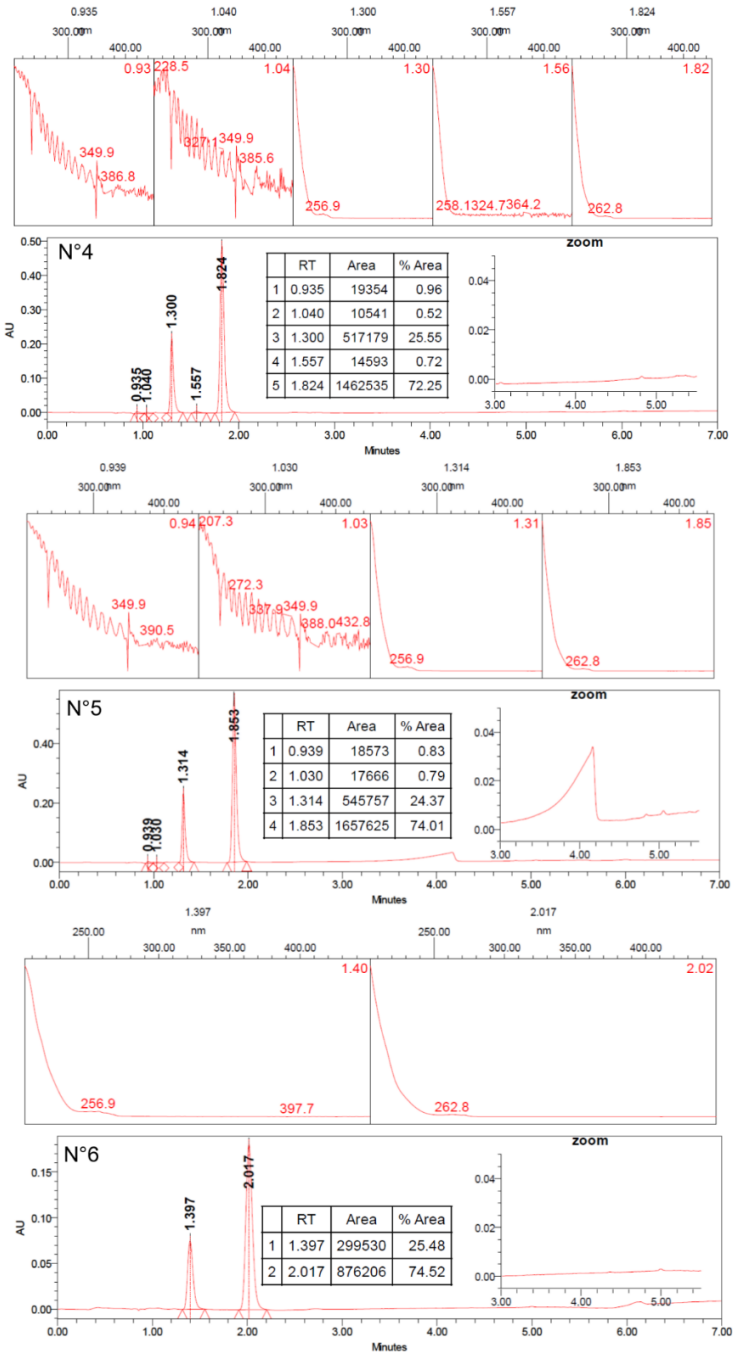

Figure 8-3-15. UV spectrum index plot and reverse HPLC chromatograms used to dose the NRSMA solubility for the trials 4 to 6. The nefiracetam absorption peak goes out around 2.0 min.

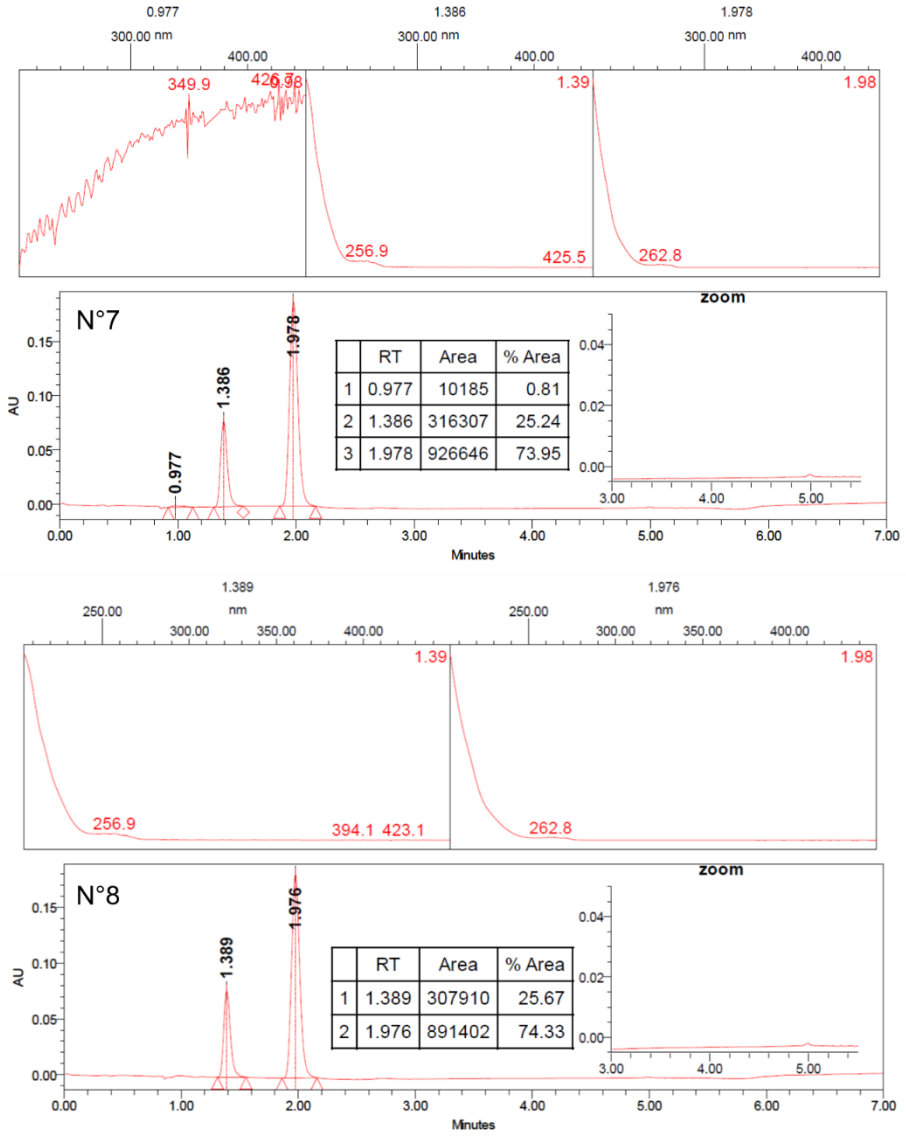

Figure 8-3-16. UV spectrum index plot and reverse HPLC chromatograms used to dose the NRSMA solubility for the trials 7 and 8. The nefiracetam absorption peak goes out around 2.0 min.

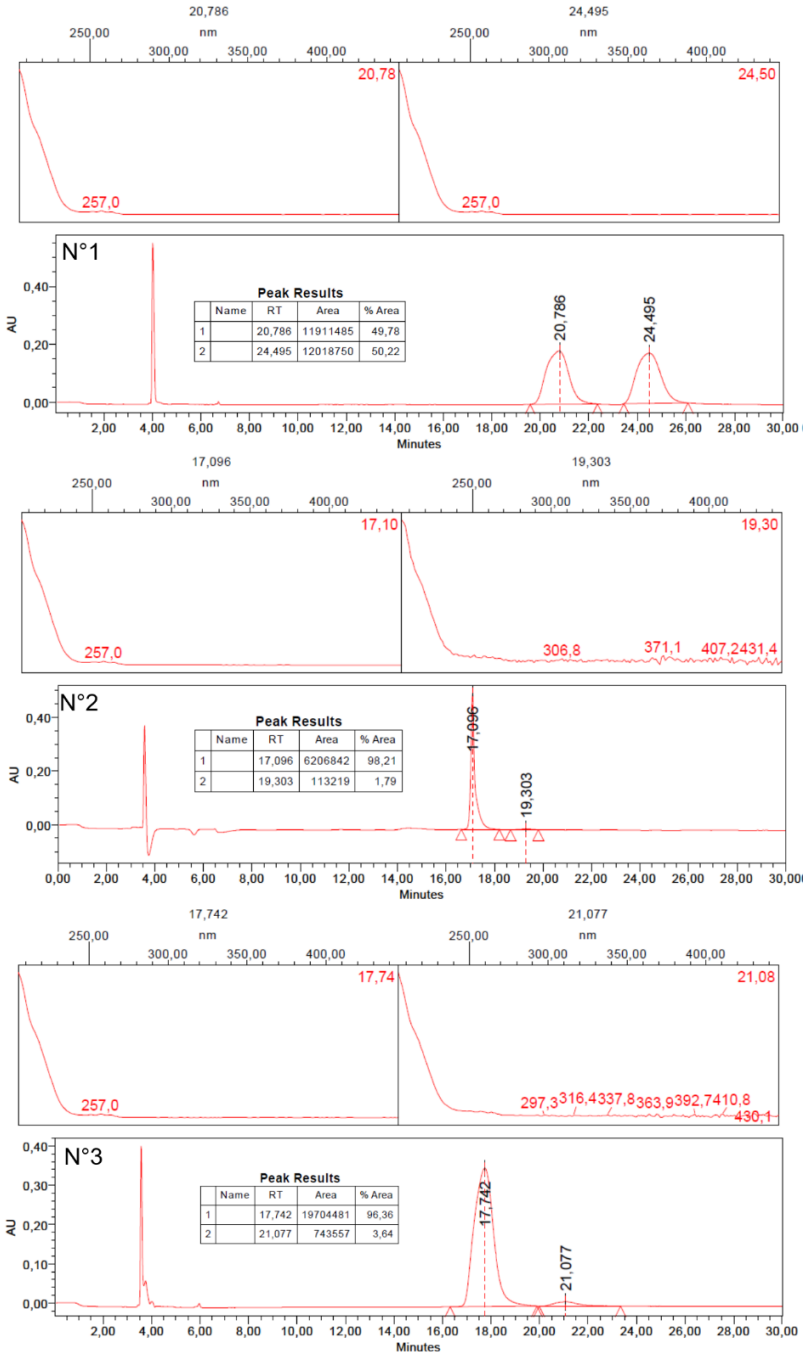

Figure 8-3-17. UV spectrum index plot and chiral HPLC chromatograms of the solid outcomes (trial N°1 to N°3). The first retention peak is associated to the solvent. The R and S-enantiopurity are given by AUC of the two integrated peaks.

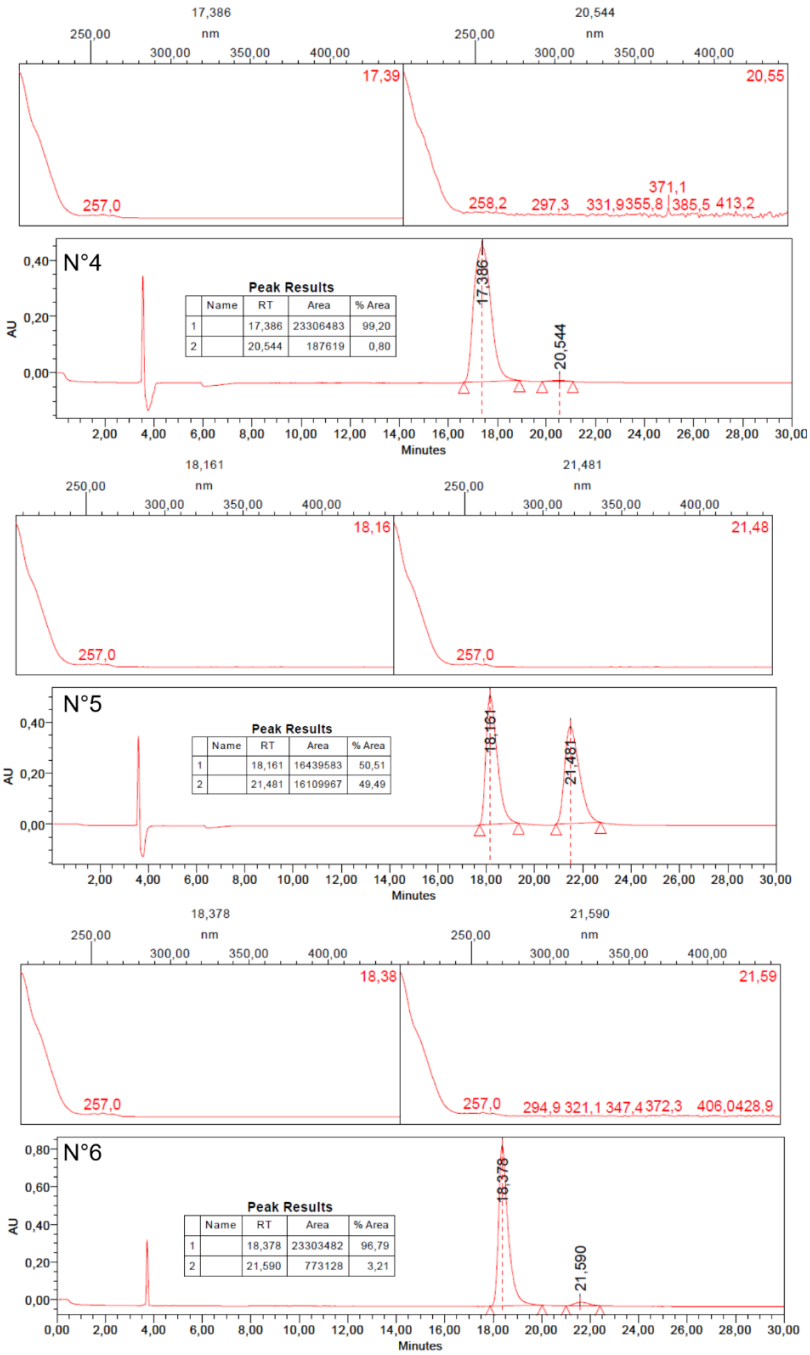

Figure 8-3-18. UV spectrum index plot and chiral HPLC chromatograms of the solid outcomes (trial N°4 to N°6). The first retention peak is associated to the solvent. The R and S-enantiopurity are given by AUC of the two integrated peaks.

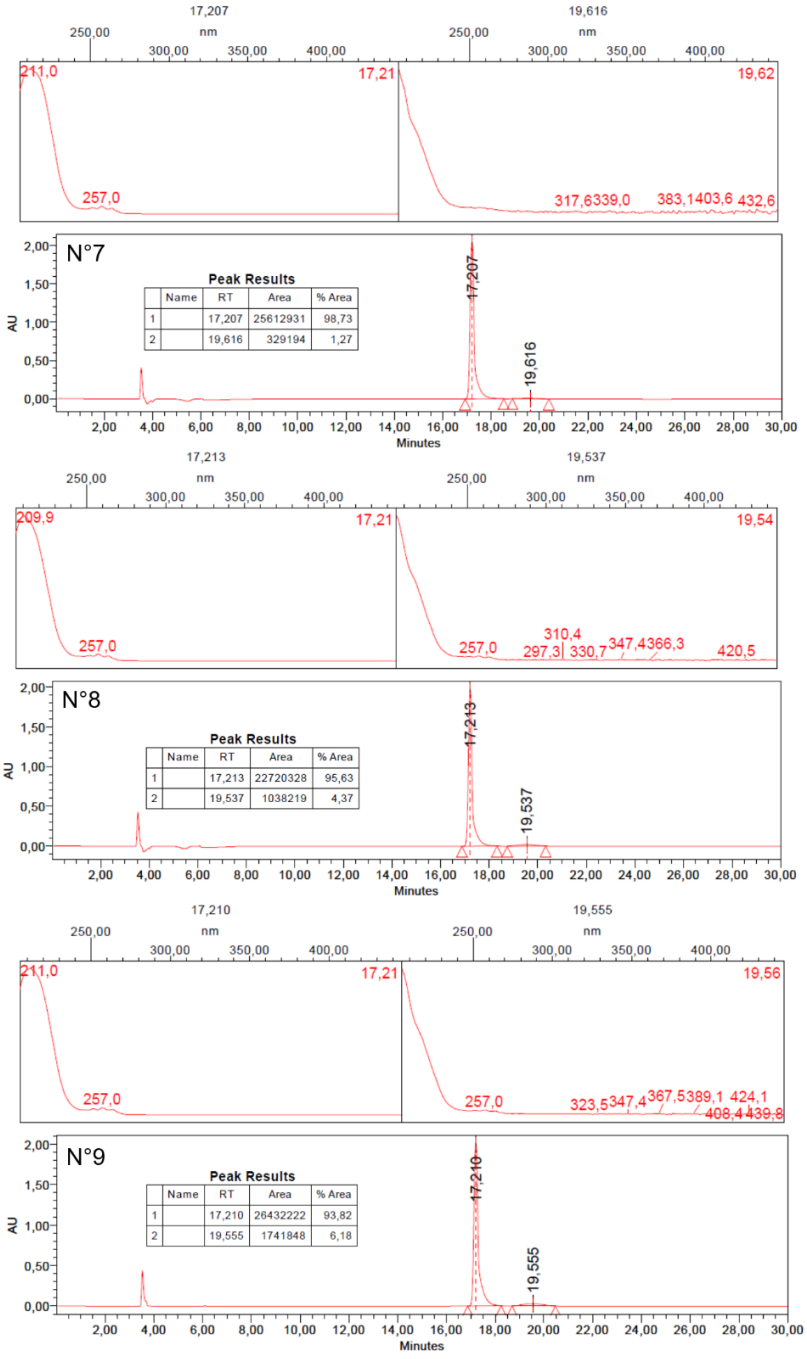

Figure 8-3-19. UV spectrum index plot and chiral HPLC chromatograms of the solid outcomes (trial N°7 to N°9). The first retention peak is associated to the solvent. The R and S-enantiopurity are given by AUC of the two integrated peaks.

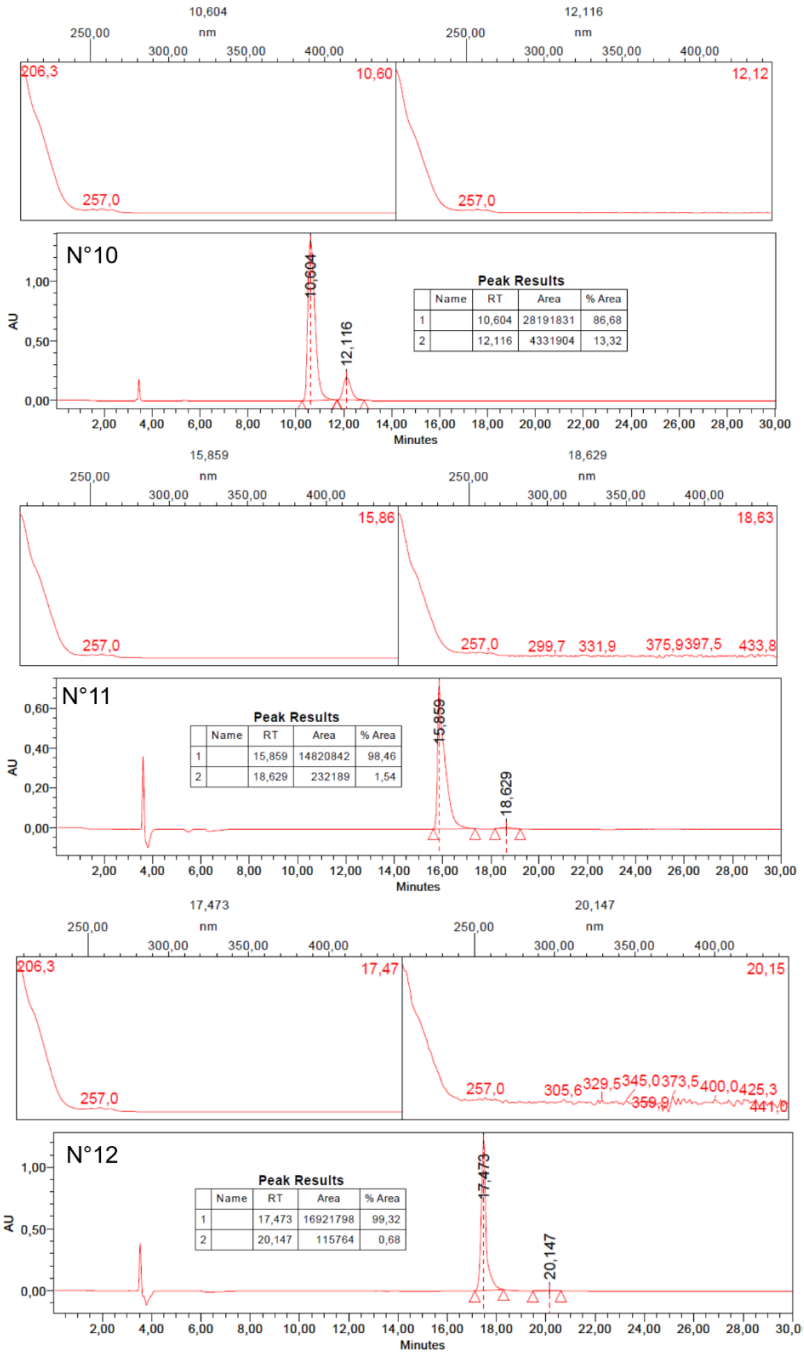

Figure 8-3-20. UV spectrum index plot and chiral HPLC chromatograms of the solid outcomes (trial N°10 to N°12). The first retention peak is associated to the solvent. The R and S-enantiopurity are given by AUC of the two integrated peaks.

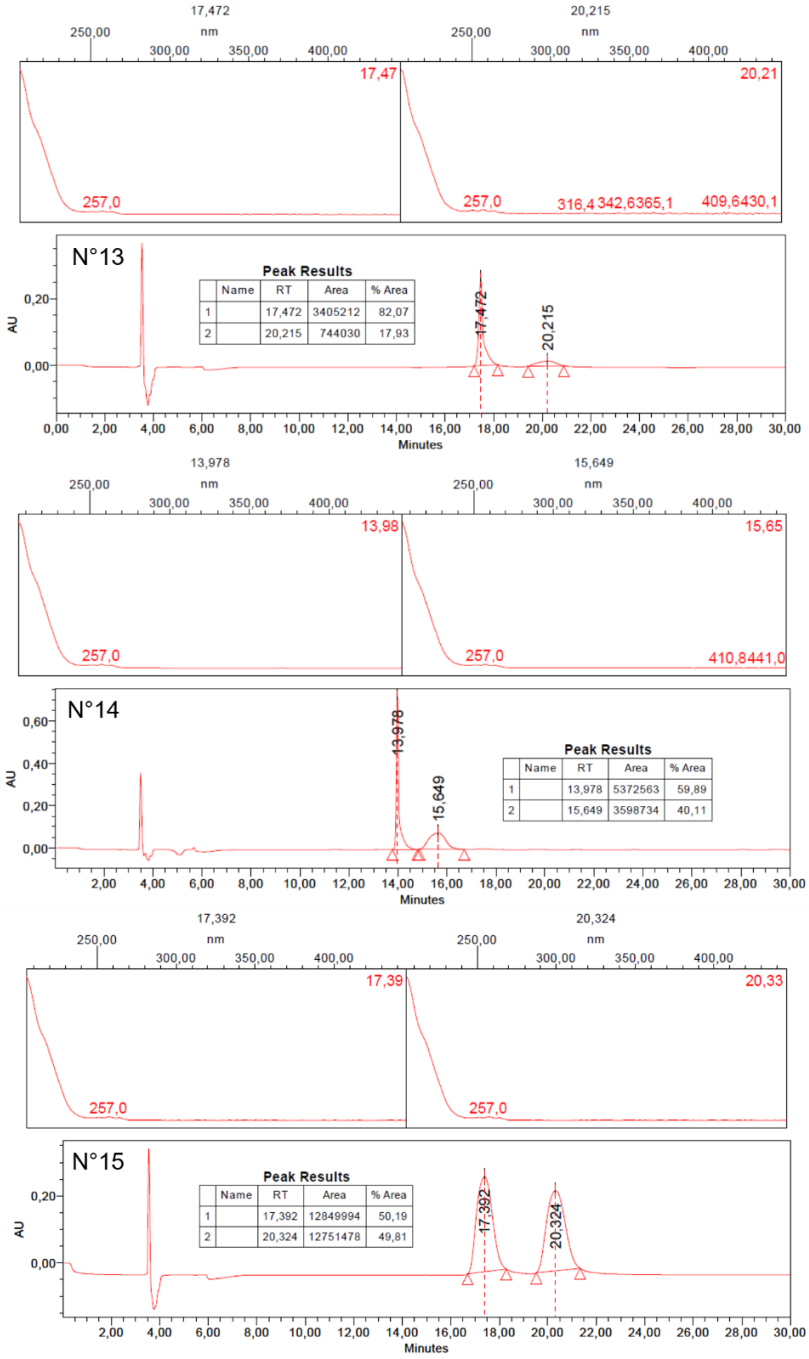

Figure 8-3-21. UV spectrum index plot and chiral HPLC chromatograms of the solid outcomes (trial N°13 to N°15). The first retention peak is associated to the solvent. The R and S-enantiopurity are given by AUC of the two integrated peaks.

8.3.9. Liquid Phase Following-up

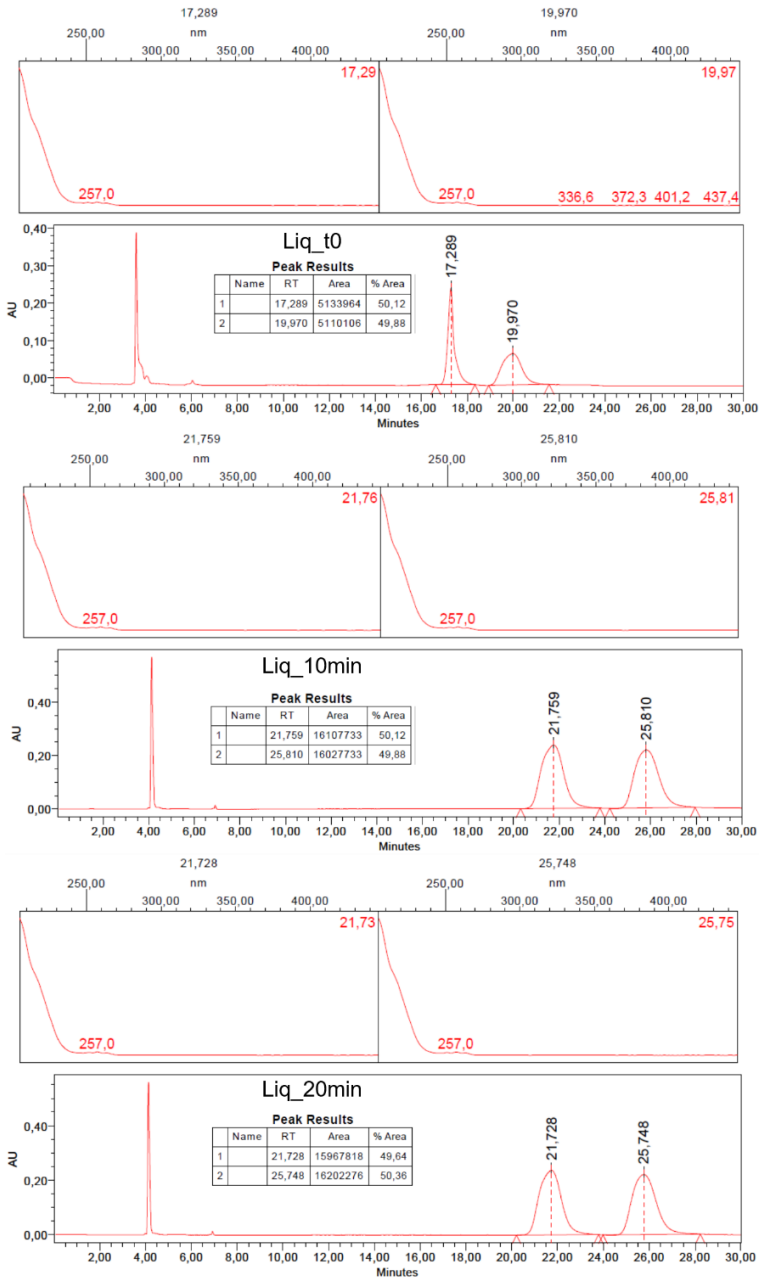

Figure 8-3-22. UV spectrum index plot and chiral HPLC chromatograms of the liquid fractions sampled at t=0, 10 and 20min.

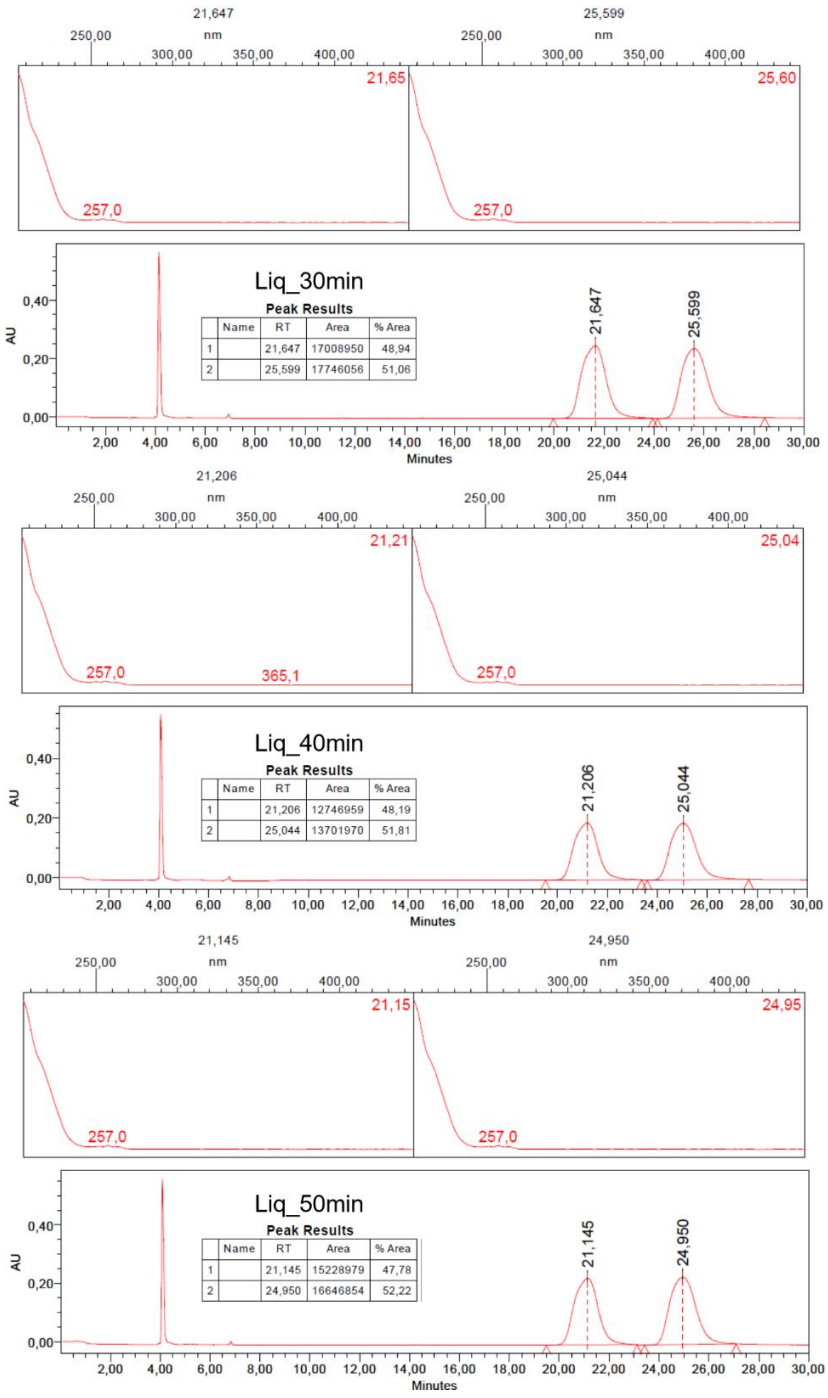

Figure 8-3-23. UV spectrum index plot and chiral HPLC chromatograms of the liquid fractions sampled at t=30, 40 and 50min.

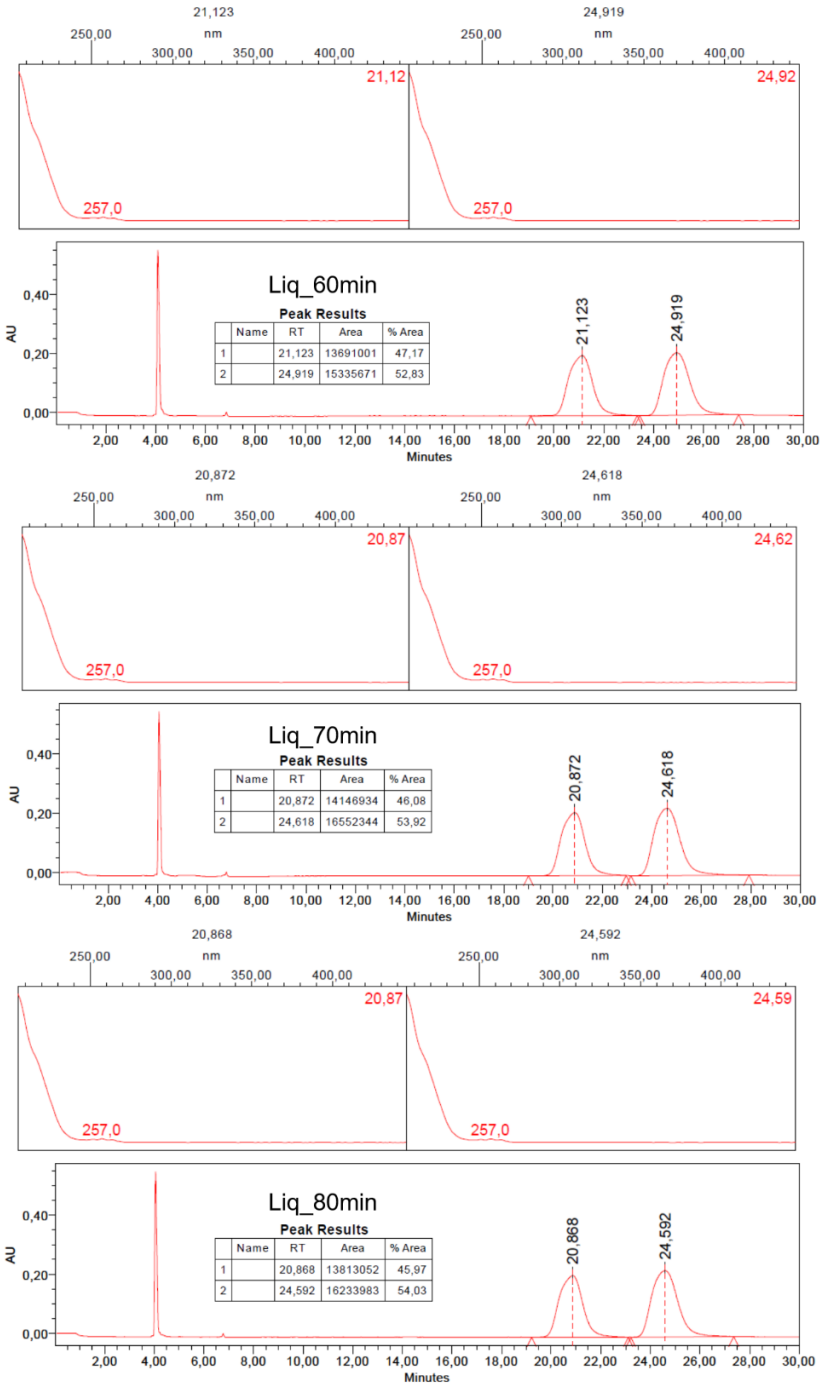

Figure 8-3-24. UV spectrum index plot and chiral HPLC chromatograms of the liquid fractions sampled at t=60, 70 and 80min.

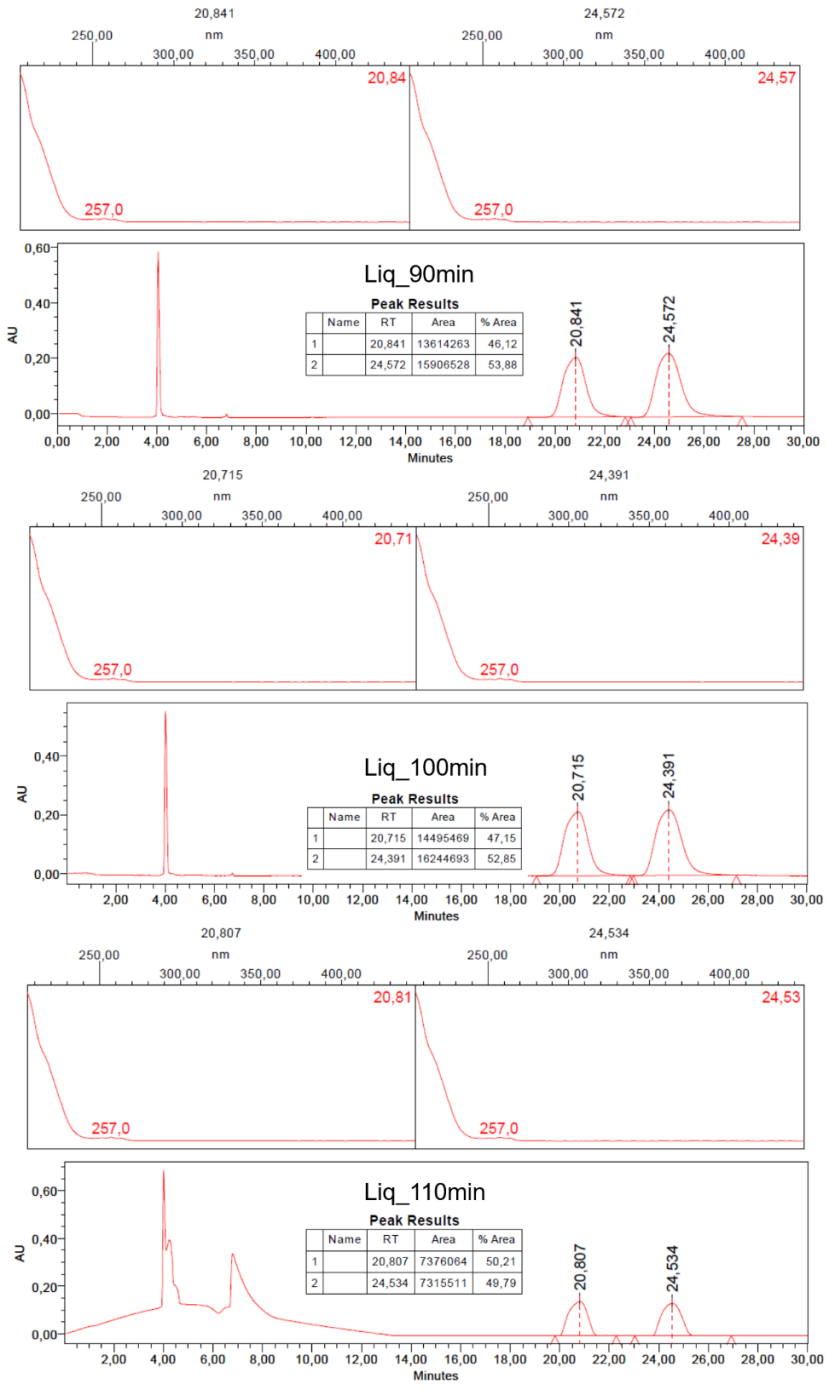

Figure 8-3-25. UV spectrum index plot and chiral HPLC chromatograms of the liquid fractions sampled at t=90, 100 and 110min.

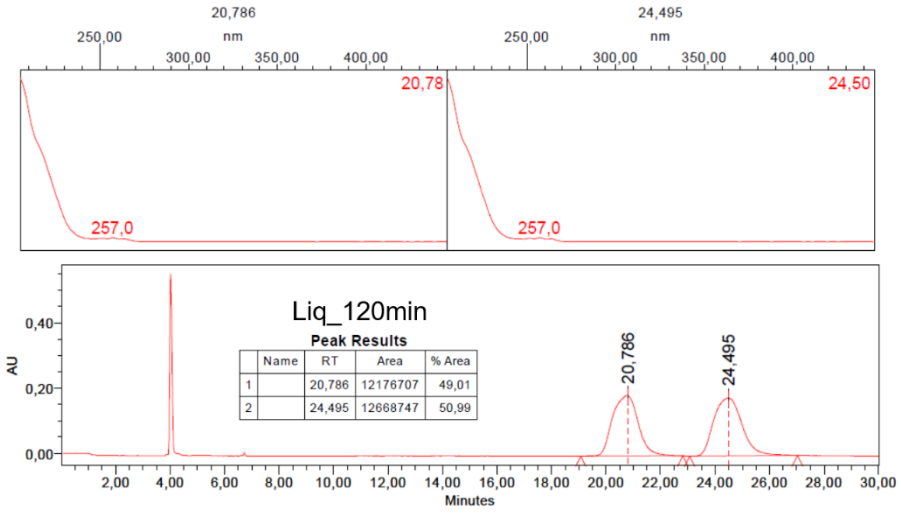

Figure 8-3-26. UV spectrum index plot and chiral HPLC chromatograms of the liquid fractions sampled at t=120min.

8.3.10. Solid Phase Following-up

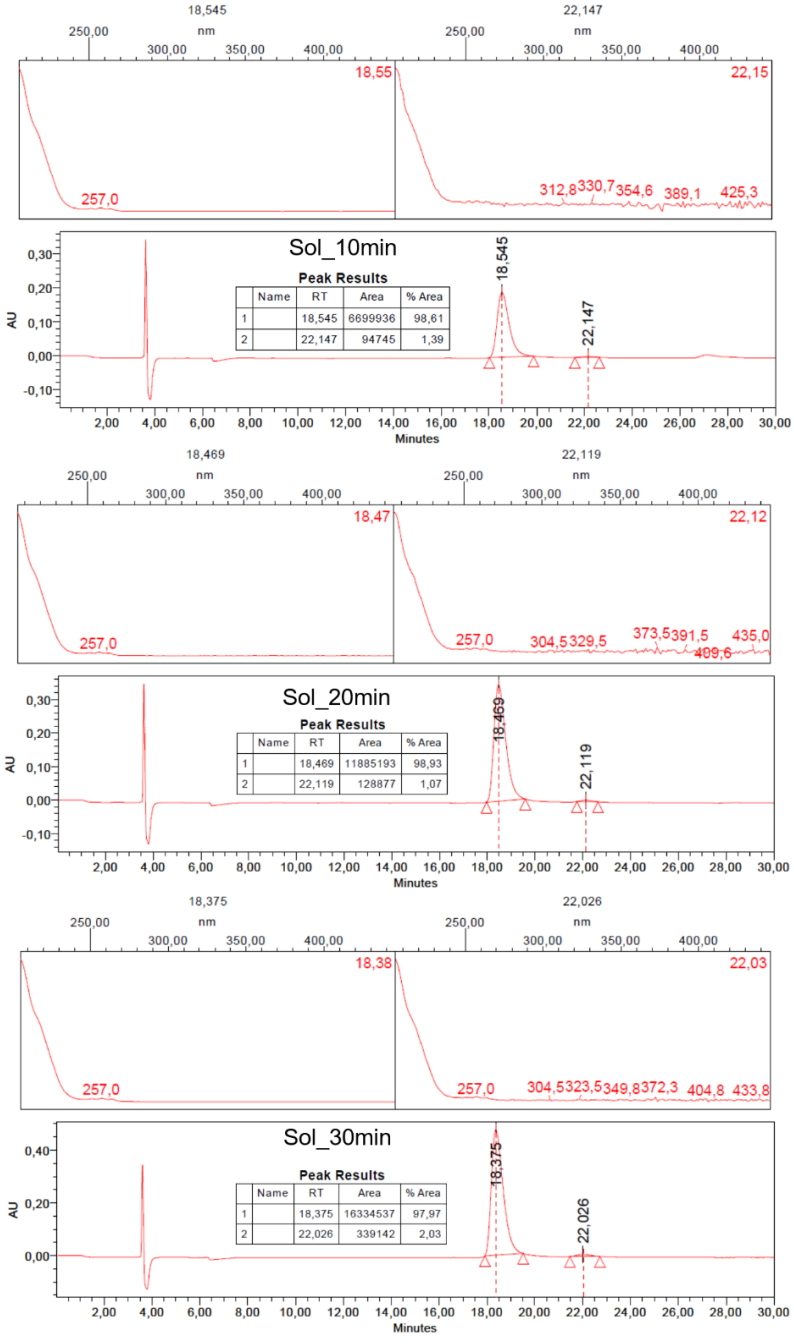

Figure 8-3-27. UV spectrum index plot and chiral HPLC chromatograms of the solids sampled at t=10, 20 and 30min.

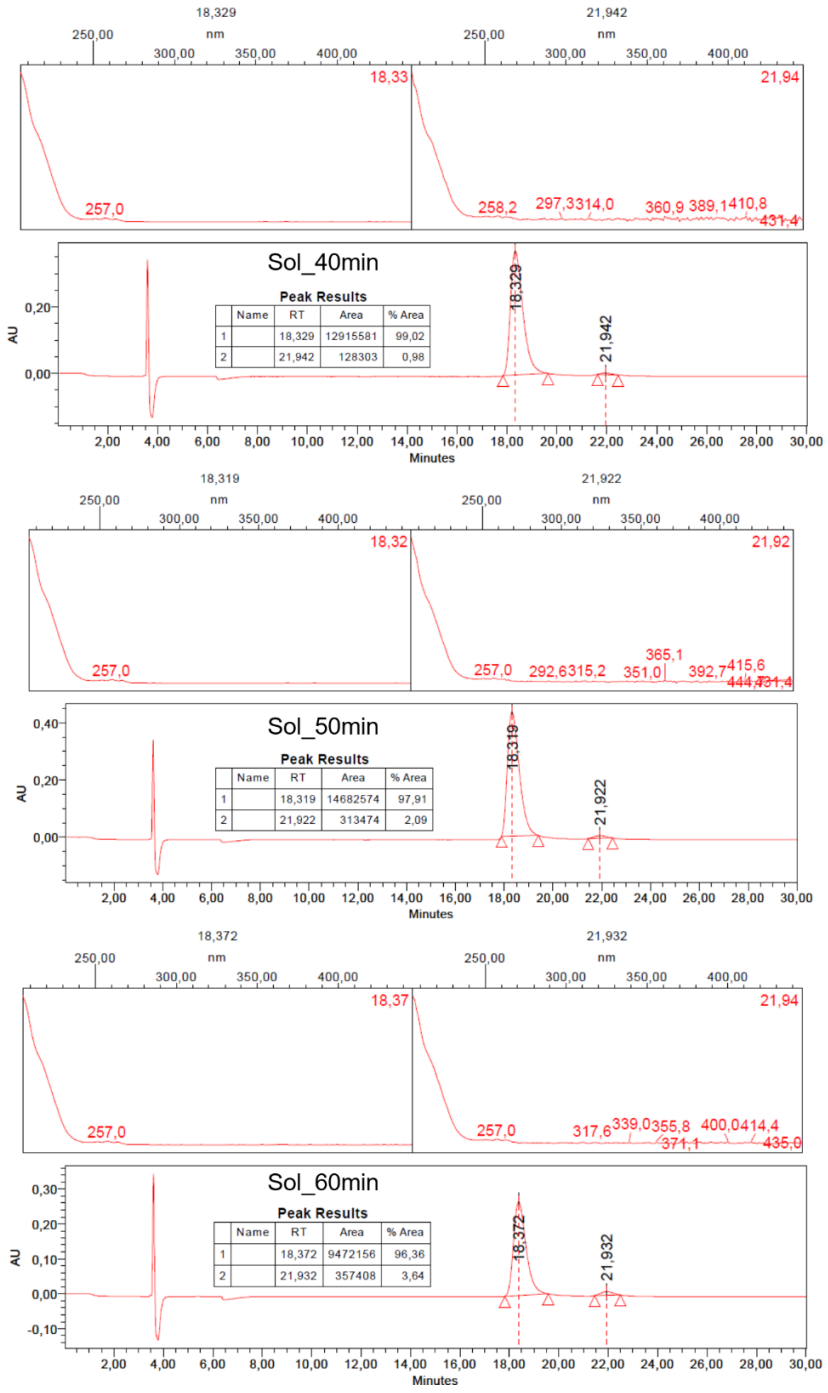

Figure 8-3-28. UV spectrum index plot and chiral HPLC chromatograms of the solids sampled at t=40, 50 and 60min.

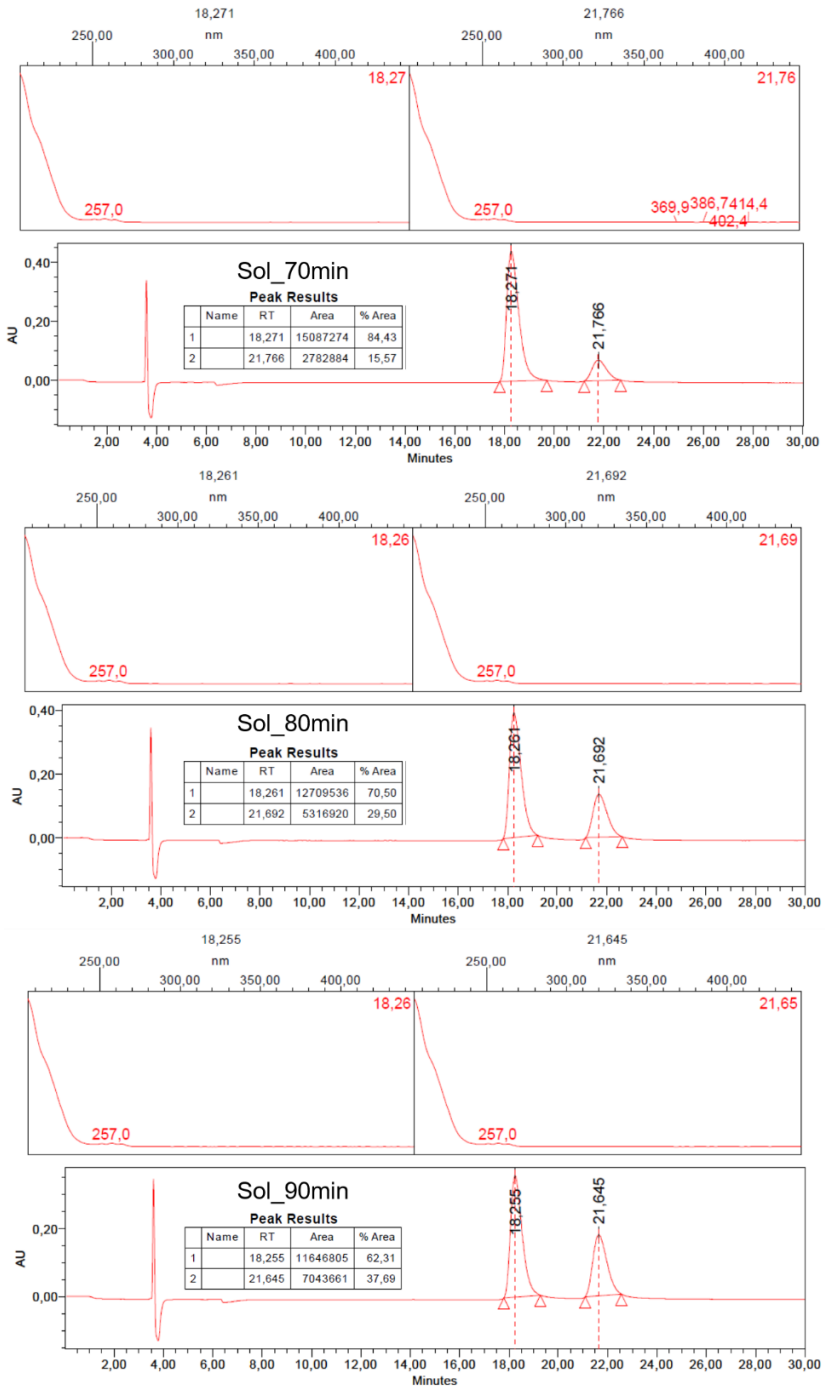

Figure 8-3-29. UV spectrum index plot and chiral HPLC chromatograms of the solids sampled at t=70, 80 and 90min.

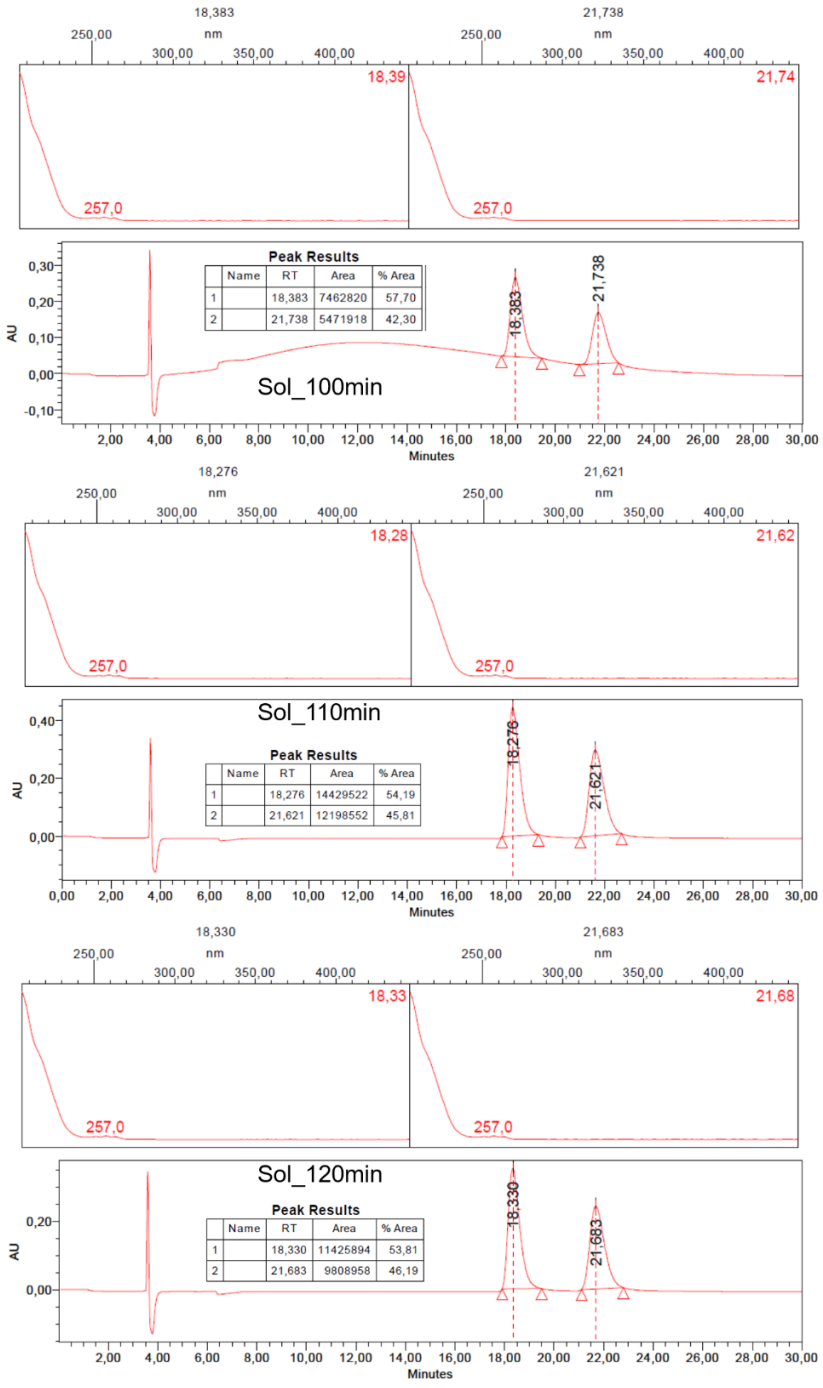

Figure 8-3-30. UV spectrum index plot and chiral HPLC chromatograms of the solids sampled at t=100, 110 and 120min.

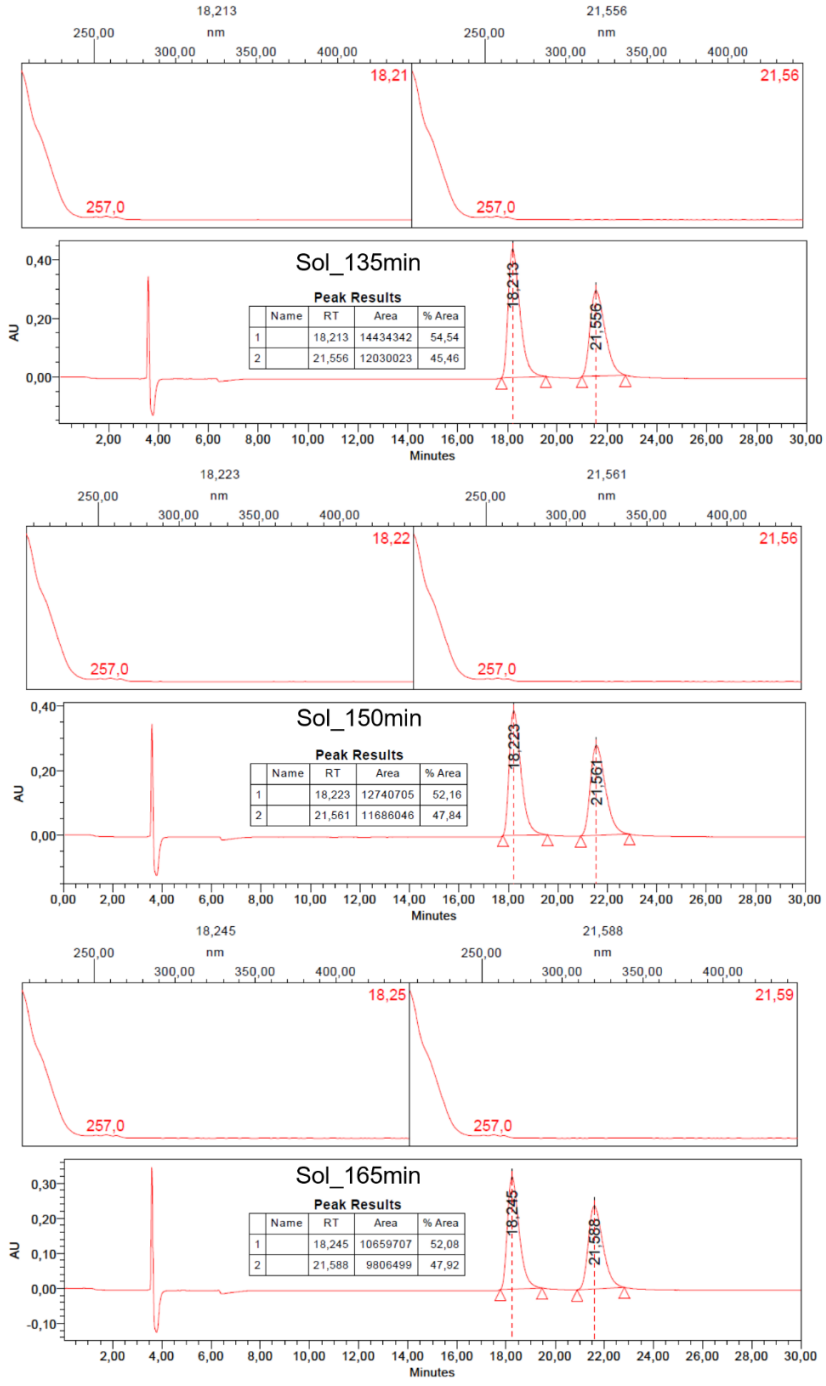

Figure 8-3-31. UV spectrum index plot and chiral HPLC chromatograms of the solids sampled at t=135, 150 and 165min.

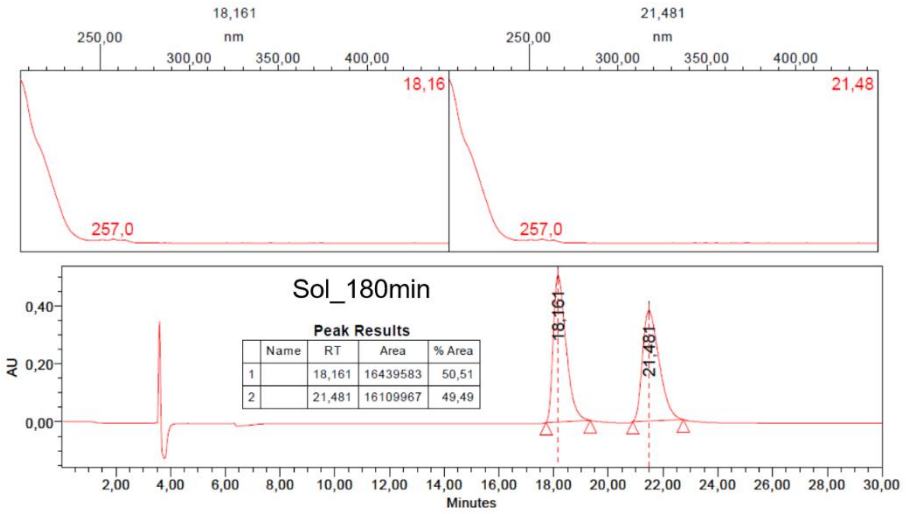

Figure 8-3-32. UV spectrum index plot and chiral HPLC chromatograms of the solids sampled at t=180min.

8.3.11. Continuous Seeded Isothermal Preferential Crystallization

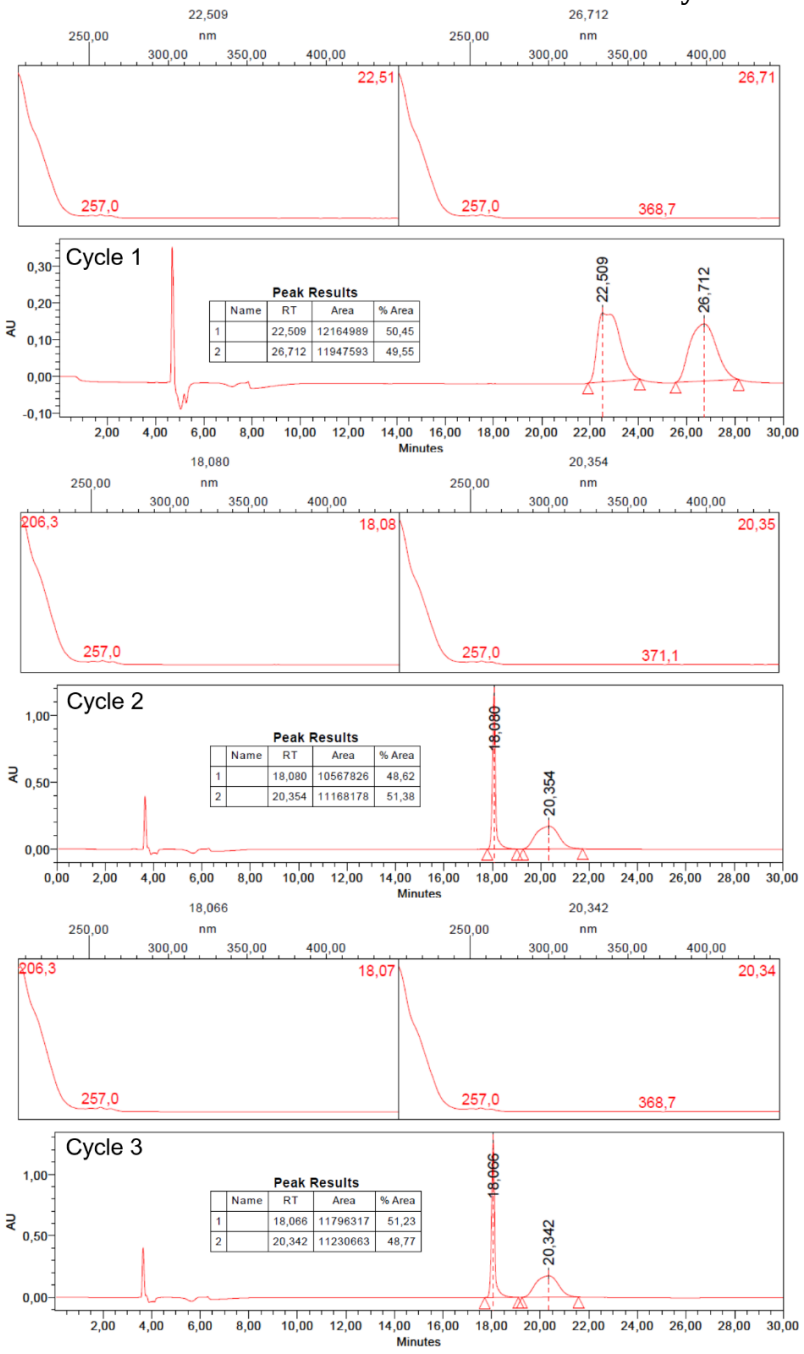

Figure 8-3-33. UV spectrum index plot and chiral HPLC chromatograms of the liquid phase (saturation) related to the cycle 1, 2 and 3.

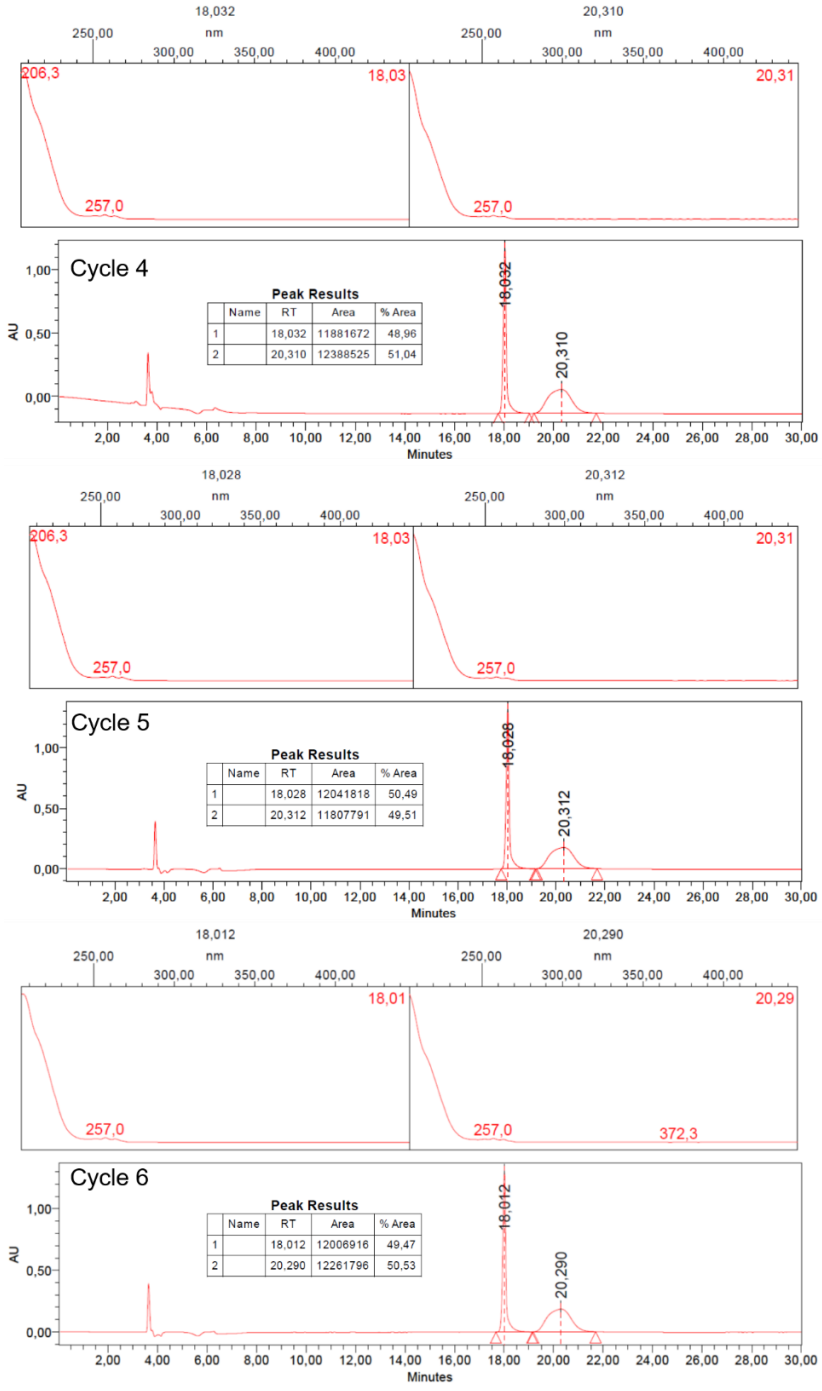

Figure 8-3-34. UV spectrum index plot and chiral HPLC chromatograms of the liquid phase (saturation) related to the cycle 4, 5 and 6.

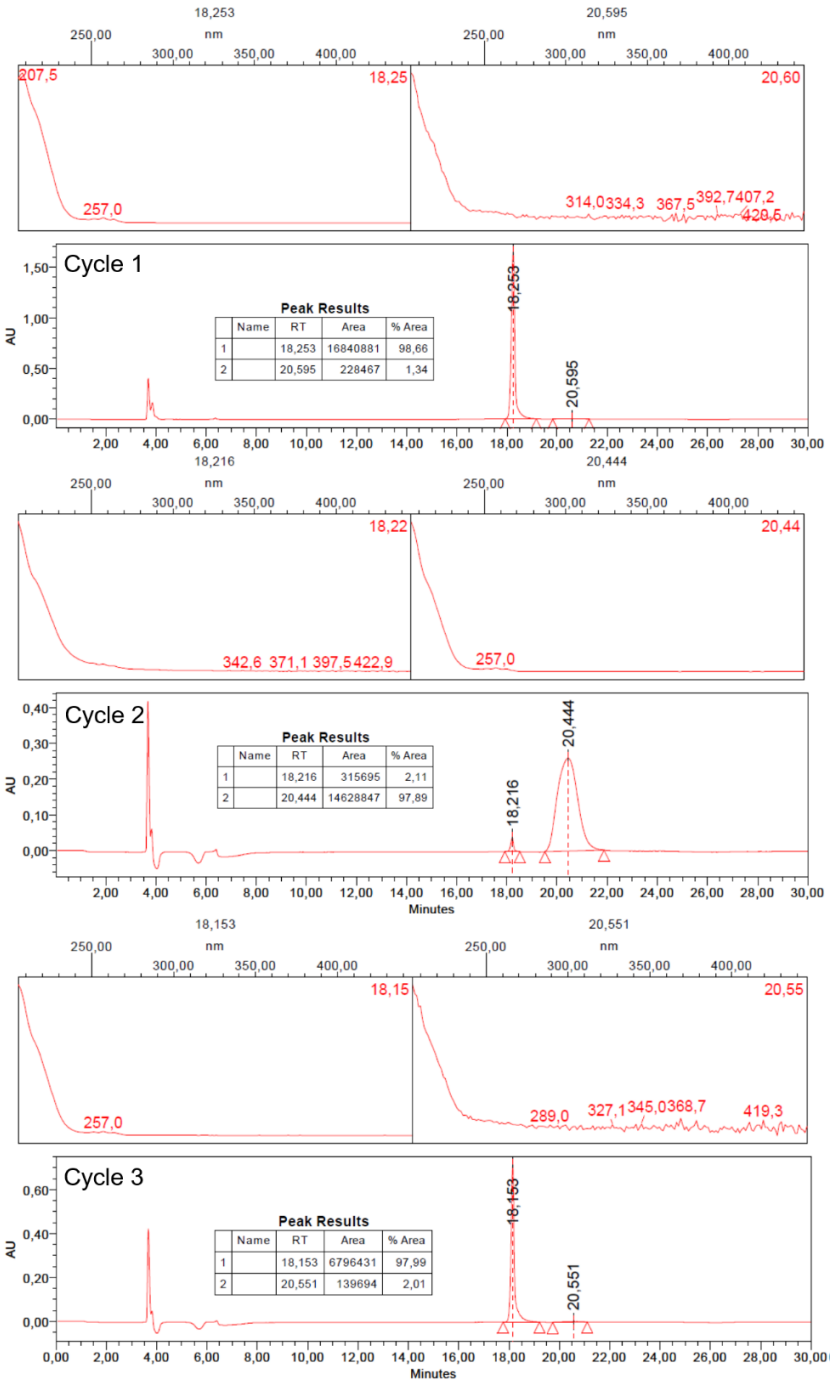

Figure 8-3-35. UV spectrum index plot and chiral HPLC chromatograms of the solid outcomes recovered at the end of the cycle 1, 2 and 3.

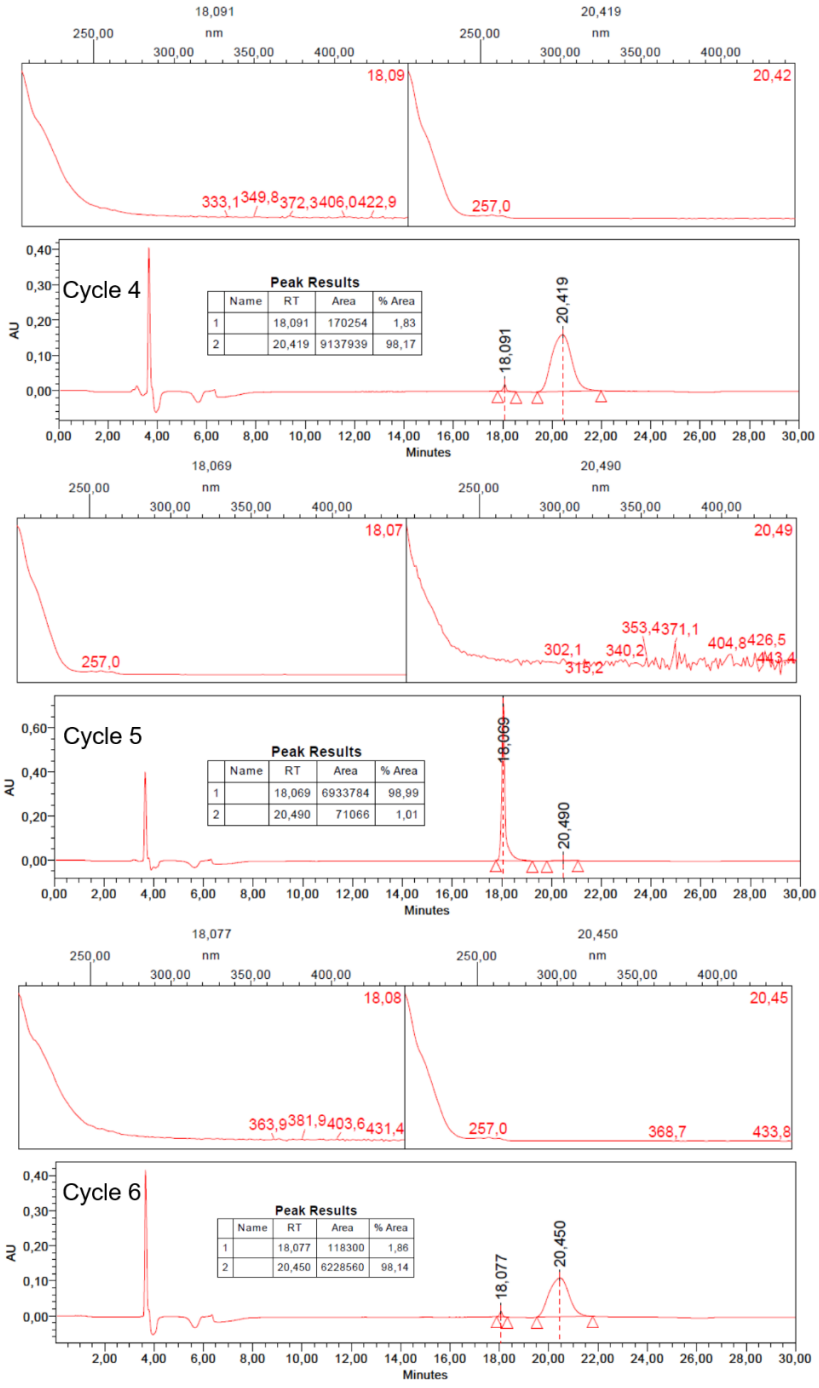

Figure 8-3-36. UV spectrum index plot and chiral HPLC chromatograms of the solid outcomes recovered at the end of the cycle 4, 5 and 6.

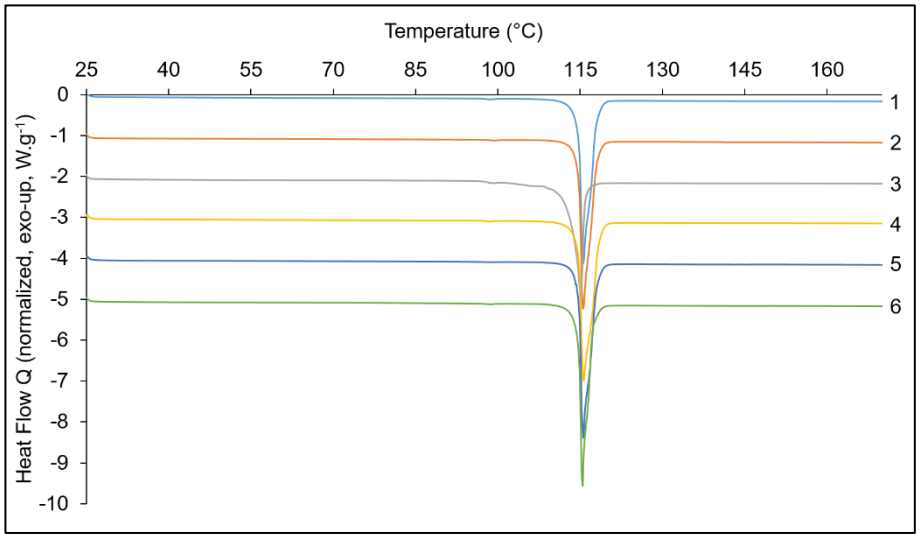

Figure 8-3-37. DSC analyses performed on the solid outcomes of the cycles 1 to 6.

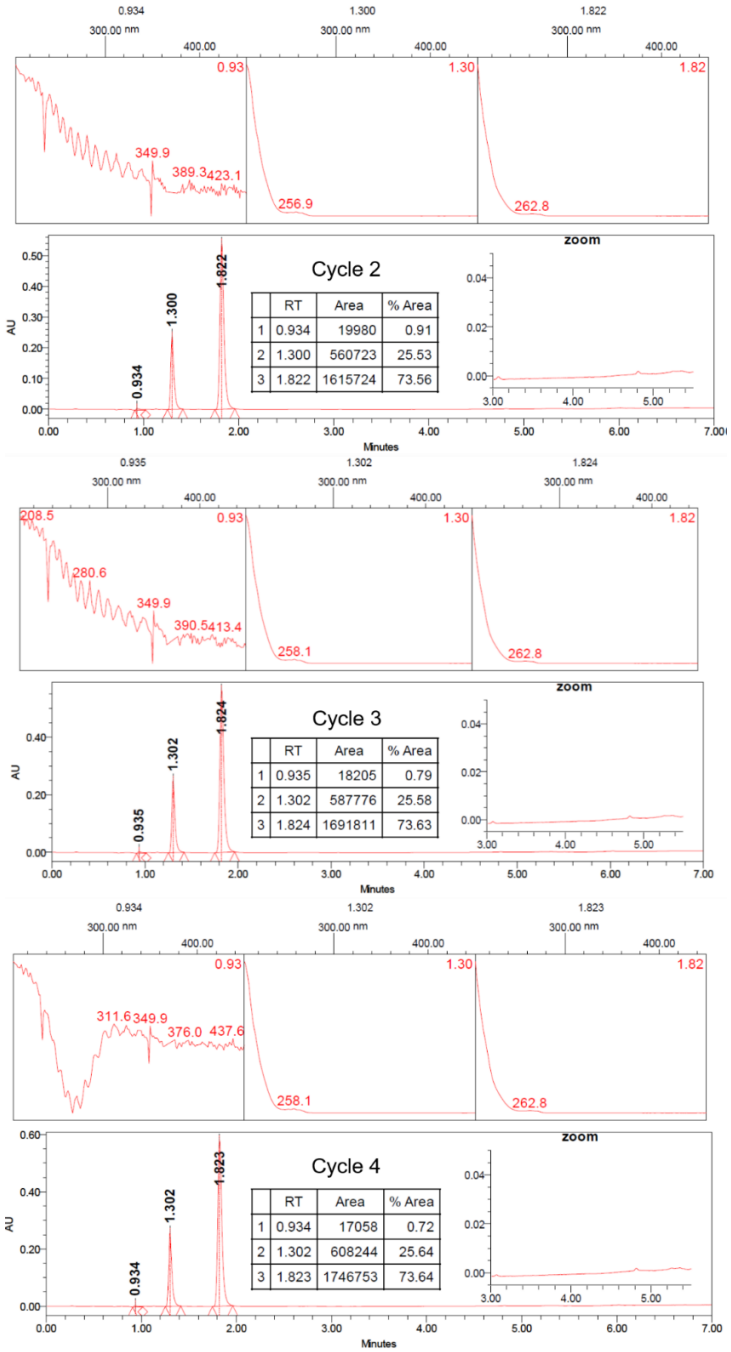

Figure 8-3-38. UV spectrum index plot and reverse HPLC chromatograms used to evaluate the NRSMA concentration for the cycles 2 to 4. The nefiracetam absorption peak goes out around 1.8 min.

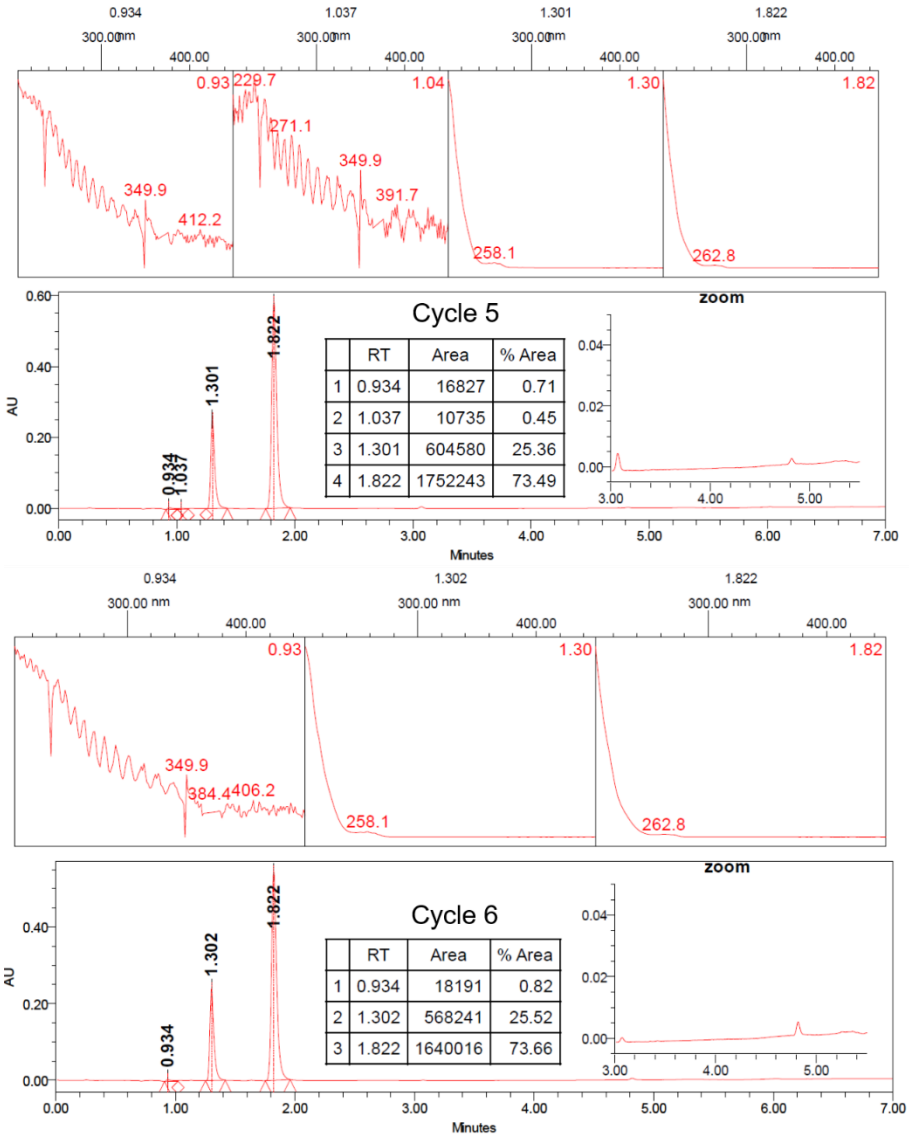

Figure 8-3-39. UV spectrum index plot and reverse HPLC chromatograms used to evaluate the NRSMA concentration for the cycles 5 and 6. The nefiracetam absorption peak goes out around 1.8 min.